COLLECTED PAPERS on Nanophotonics

Vol. 20

August 2004 – July 2005

Prof. Motoichi OHTSU

7 MARCH 2005
Volume 86 Number 10

APPLIED PHYSICS LETTERS

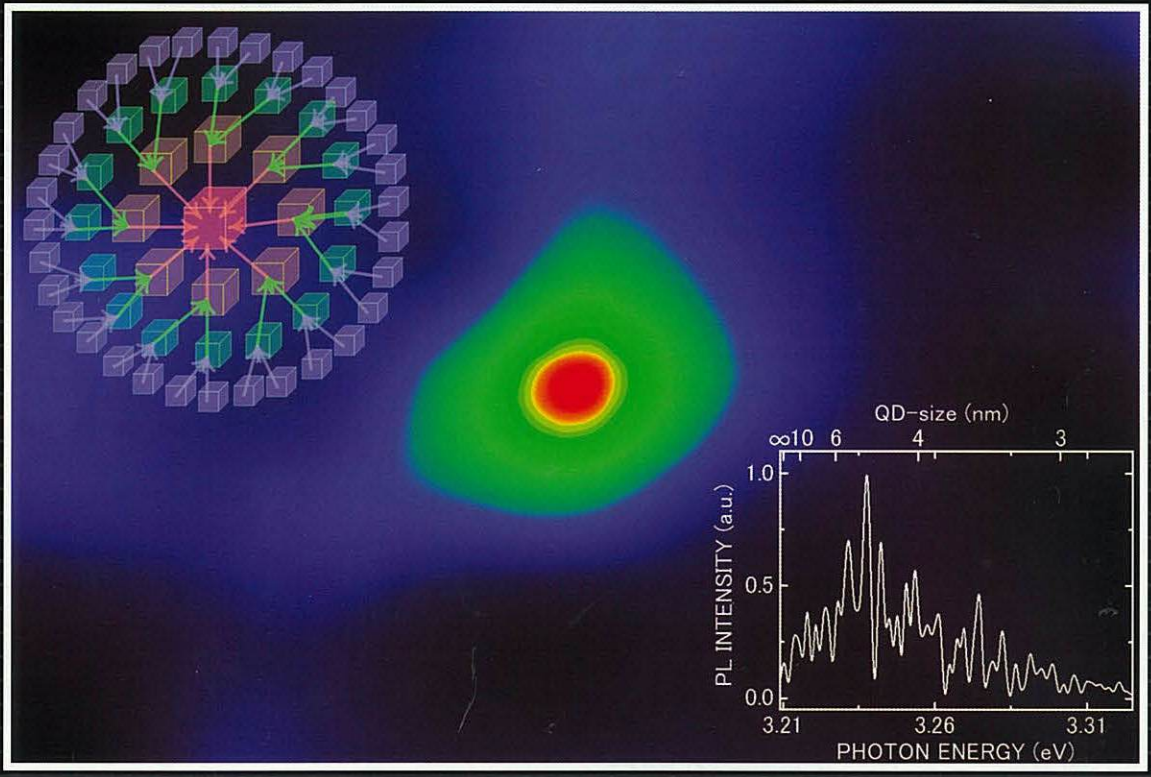

0003-6951(20050307)86:10;1-U

Available online–
See apl.aip.org

AMERICAN INSTITUTE OF PHYSICS

指先に新聞340年分 光と磁気 の奇跡

大容量光ストレージ技術の開発プロジェクト

大量の情報の流通と蓄積に対応できるストレージ技術の発展が求められています。現在のHDDの10倍以上という大容量化を実現するため、1テラビット/inch²の高密度記録を実証する研究開発を行なっています。

トピックス

プラズモンプローブを使った記録用光デバイスを開発

近年、パソコン等に搭載されているHDD(磁気ディスク)などのストレージの記録容量はどんどん大きくなっています。

高密度に情報を記録するために、ディスク上の小さなセルに記録するには記録光スポットもさらに小さくしなければなりません。高効率集光素子(SIM)※と近接場光発光素子※(プラズモンプローブ)※を組み合わせて低浮上スライダに搭載した記録用光デバイスを世界に先がけて試作しました。

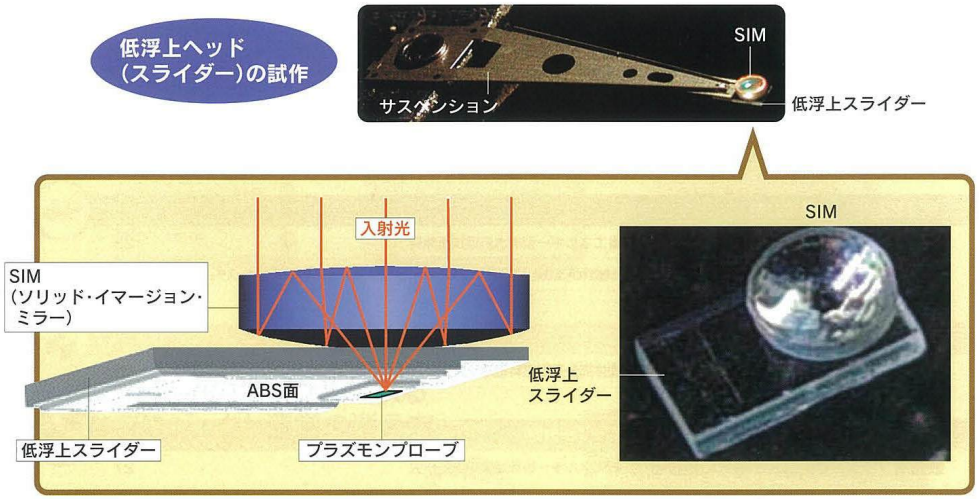

※SIM　入射光を近接場のヘッドまで効率良く集光するミラー。
※近接場光
光の波長よりも小さな物質に光を当てたとき、その物質の表面に発生して、遠くへは伝搬していかない光のこと。あたかも物質表面を覆う光の薄い膜のようなもので、膜の厚みは物質の寸法程度なので、当てる光の波長よりも小さくなる。従って、レンズで光を絞るよりも小さな光スポットとなる。
※プラズモンプローブ　近接場光を発光させる素子　[参考]plasmon:電子波

【図1】

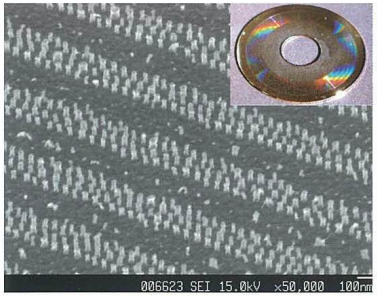

【図2】

光磁気ハイブリッド材料のドット加工配列に成功

光磁気ハイブリット材料(FePtCu)で、80nmピッチ(ドット径<40nm)のドットのナノ加工配列を自己組織化を用いたプロセスで試作しました。2.5インチ径ディスク全面に円周配列できた世界初の成果として期待されています。

背景・意義

情報通信技術のめざましい進展により、ネットワークがすみずみにまで行き渡り、時間や場所の制約を受けずに、必要とする情報や知識を、誰もが自由に創造、流通、共有できる情報通信環境の実現が望まれています。このような情報通信環境においては、ネットワークに情報通信システム・モバイル端末が多数接続された状態での利用が想定されるため、大量の情報の流通・蓄積に対応した大容量のストレージ技術の発展が不可欠です。このプロジェクトでは、高密度と記録・再生の高速性とを実現する光記録技術の実証を目的としています。

研究開発の内容

平成22年頃には1テラビット/inch²のストレージが必要となることが予想されており、高密度の書きこみをするためには記録セルのサイズを小さくすることが必要です。従来の技術の延長では不可能と考えられている技術を、近接場光技術・ナノパターンドメディア等の先進技術を駆使し、大容量の記録ストレージ実現に取り組んでいます。

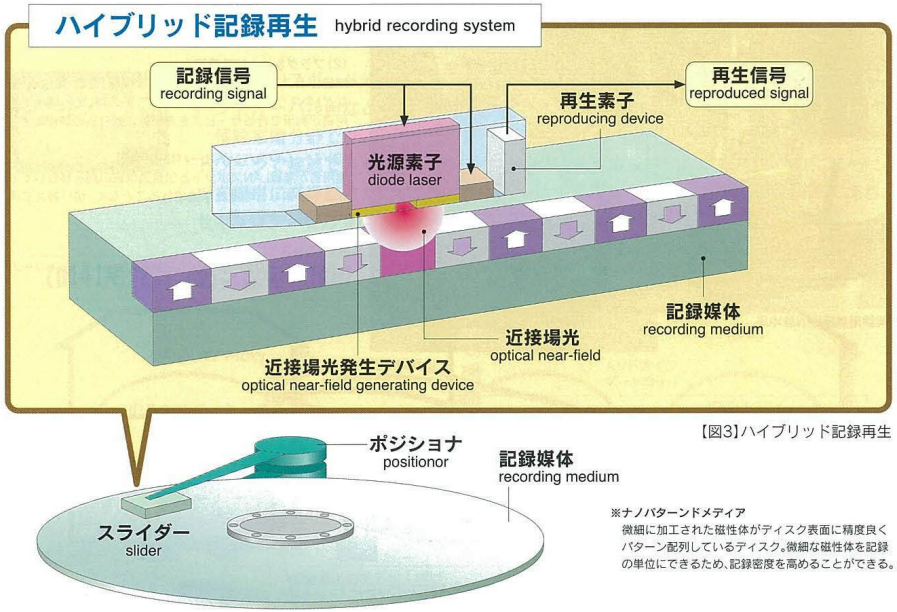

【図3】ハイブリッド記録再生

※ナノパターンドメディア
微細に加工された磁性体がディスク表面に精度良くパターン配列しているディスク。微細な磁性体を記録の単位にできるため、記録密度を高めることができる。

今後の展開

平成16年度までには300ギガビット/inch²級を可能とする各種要素技術を開発し、さらに平成18年度までには、1テラビット/inch²級の高密度と記録・再生の高速性を実証します。

参加組織

PL:大津元一(東京大学教授)
(財)光産業技術振興協会[コニカミノルタオプト(株)/セイコーインスツル(株)/(株)東芝/パイオニア(株)(株)日立製作所/日立マクセル(株)/富士通(株)/(株)リコー]/東京大学/(独)産業技術総合研究所

MEMBERS

(From April 1, 2005)

*[I] THE UNIVERSITY OF TOKYO**

Professor

Motoichi OHTSU[a-e] (Dr. Eng.)

Graduate Student (Doctor Candidate)

Wataru NOMURA

Graduate Students (Master Course)

Kokoro KITAMURA
Hiroki YONEMITSU
Tohru NAKAMATA

Undergraduate Students

Hyungsu JEONG
Nobuaki HIROSE
Takumi YAMAMOTO

Secretary

Sachiyo KOJIMA

a) Also with Kanagawa Academy of Science and Technology
(Director, Ohtsu-Saiki group)
b) Also a director, "Ultrahigh capacity optical storage",
Ministry of Economy, Trade and Industry
c) Also a team leader, "Nanophotonics team", SORST,
Japan Science and Technology Agency
d) Also a leader, "Optical near field lithography project",
Leading Project, Ministry of Education, Culture, Sports, Science, and Technology
e) Also a director, NPO-Research Institute of Nanophotonics

(*)

Department of Electronics Engineering, School of Engineering,
The University of Tokyo
7-3-1 Hongo, Bunkyo-Ku, Tokyo 113-8656
Phone: +81-3-5841-1189, Fax: +81-3-5841-1140
E-mail: ohtsu@ee.t.u-tokyo.ac.jp
URL: http://www. nanophotonics.info/

東京大学大学院工学系研究科電子工学専攻
〒113-8656　東京都文京区本郷 7-3-1
Phone: 03-5841-1189, Fax: 03-5841-1140
E-mail: ohtsu@ee.t.u-tokyo.ac.jp
URL: http://www. nanophotonics.info/

*[II] TOKYO INSTITUTE OF TECHNOLOGY**

Graduate Student (Doctor Candidates)

Jungshik LIM

(*)

Intrdisciplinary Graduate School of Science and Engineering,
Tokyo Insitutute of Technology
4259 Nagatsuta-cho, Midori-ku, Yokohama 226-8502

東京工業大学大学院総合理工学研究科電子機能システム専攻
〒226-8502　横浜市緑区長津田町 4259

*[III] NANOPHOTONICS TEAM**

Researchers

Tadashi KAWAZOE (Dr. Sci.)
Takashi YATSUI (Dr. Eng.)

Manager

Akiyoshi ORIDE

Secretary

Tomoko TOTAKE

(*)
Nanophotonics Team, SORST (Solution Oriented Research for Science and Technology),
Japan Science and Technology Agency
4th Floor, Tenko Building #17
687-1 Tsuruma, Machida-shi, Tokyo 194-0004
Phone: +81-42-788-6030, Fax: +81-42-788-6031

（独）科学技術振興機構、戦略的創造研究推進事業「発展・継続」研究,
ナノフォトニクスチーム
〒194-0004　東京都町田市鶴間 687-1　第 17 天幸ビル 4 階
Phone: 042-788-6030, Fax: 042-788-6031

*[IV] OHTSU-SAIKI GROUP**

Researcher

Shuji MONONOBE (Dr. Eng.)

Secretary

Kazumi NAKAHARA

(*)
Ohtsu-Saiki Group,
Kanagawa Academy of Science and Technology
KSP East, Rm 408,
3-2-1 Sakato, Takatsu-ku, Kawasaki 213-0012
Phone: +81-44-819-2075, Fax: +81-44-819-2072

（財）神奈川科学技術アカデミー　光科学重点研究室
大津斎木グループ
〒213-0012　川崎市高津区坂戸 3-2-1
KSP 東棟　408 号室
Phone: 044-819-2075, Fax: 044-819-2072

*[V] OPTICAL NEAR FIELD LITHOGRAPHY PROJECT**

Researcher

Shunsuke YAMAZAKI

Manager

Masatake KAWANO

Research Assistant

Yuri MIYAGI

Secretary

Kanako CHIBA

(*)

Optical Near Field Lithography Project, Leading Project,
Ministry of Education, Culture, Sports, Science, and Technology
4th Floor, Tenko Building #17
687-1 Tsuruma, Machida-shi, Tokyo 194-0004
Phone: +81-42-788-2211, Fax: +81-42-799-0886

文部科学省　リーディングプロジェクト、
近接場光リソグラフィ　プロジェクト
〒194-0004　東京都町田市鶴間 687-1　第 17 天幸ビル 4 階
Phone: 042-788-2211, Fax: 042-799-0886

*[VI]　RESEARCH INSTITUTE OF NANOPHOTONICS**

Director

Motoichi OHTSU

(*)

Research Insitutute of Nanophotonics,
Nonprofit Organization
1-20-10 Sekiguchi, Bunkyo-ku, Tokyo 112-0014
Phone: +81-3-5225-6432. Fax: +81-3-5225-6435
E-mail: ohtsu-rinps@nanophotonics.t.u-tokyo.ac.jp
URL: http://www.nanophotonics.info/

特定非営利法人　ナノフォトニクス工学推進機構
〒112-0014　東京都文京区関口 1-20-10
Phone: 03-5225-6432. Fax: 03-5225-6435
E-mail: ohtsu-rinps@nanophotonics.t.u-tokyo.ac.jp
URL: http://www.nanophotonics.info/

LIST OF PAPERS

[(pp.XX-XX); pages in this issue of the COLLECTED PAPERS**]**

[I] ORIGINAL PAPERS

(pp.21-25)

[6] A. Neogi, H. Morkoc, T. Kuroda, A. Takeuchi, T. Kawazoe, and M. Ohtsu, "Exciton Localization in Vertically and Laterally Coupled GaN/AlN Quantum Dots", Nano Letters, Vol.5, No.2, February 2005, pp.213-217

(pp.27-31)

[7] K. Yatsui, M. Gunji, S.-C. Yang, H. Suematsu, W. Jiang, T. Yatsui, and M. Ohtsu, "Blue Light Emission from Ultrafine Nanosized Powder of Silicon Produced by Intense Pulsed Ion-Beam Evaporation", Jpn. J. Appl. Phys., Vol.44, No.2, February 2005, pp.L92-L94

(pp.33-35)

[8] T.-W. Kim, T. Kawazoe, S. Yamazaki, and M. Ohtsu, "Low-temperature synthesis and room temperature ultraviolet lasing of nanocrystalline ZnO films", Appl. Phys. A, Vol.80, No.5, February 2005, pp.1049-1051

(pp.37-39)

[9] M. Naruse, T. Miyazaki, F. Kubota, T. Kawazoe, K. Kobayashi, S. Sangu, and M. Ohtsu, "Nanometric summation architecture based on optical near-field interaction between quantum dots", Opt. Lett., Vol.30, No.2, January 2005, pp.201-203

(pp.41-43)

[10] A. Neogi, B.P.Gorman, H. Morkoc, T. Kawazoe, and M. Ohtsu, "Near-field optical spectroscopy and microscopy of self-assembled GaN/AlN nanostructures", Appl. Phys. Lett., Vol.86, No.4, January 2005, pp.043103-1 -3

(pp.45-47)

[11] T. Kawazoe, K. Kobayashi, S. Takubo, and M. Ohtsu, "Nonadiabatic photodissociation process using an optical near field", J. Chem. Phys., Vol.122, No.2, January 2005, pp.024715-1 -5

(pp.49-53)

[12] G.H. Lee, T. Kawazoe, and M. Ohtsu, "Room temperature near-field photoluminescence of zinc-blend and wurtzite ZnO structures", Appl. Surf. Sci., Vol.239, No.3-4, January 2005, pp.394-397

(pp.55-58)

[13] S. Yamazaki, T. Yatsui, M. Ohtsu, T.-W. Kim, and H. Fujioka, "Room-temperature synthesis of ultraviolet-emitting nanocrystalline GaN films using photochemical vapor deposition", Appl. Phys. Lett., Vol.85, No.15, October 2004, pp.3059-3061

(pp.59-61)

[13-1] S. Yamazaki, T. Yatsui, M. Ohtsu, T.-W. Kim, and H. Fujioka, "Erratum: Room-temperature synthesis of ultraviolet-emitting nanocrystalline GaN films using photochemical vapor deposition", Appl. Phys. Lett., Vol.85, No.22, November 2004, p.5471

(p.63)

[14] A. Takamizawa, H. Ito, S. Yamada, and M. Ohtsu, "Observation of cold atom output from an evanescent-light funnel", Appl. Phys. Lett., Vol.85, No.10, September 2004, pp.1790-1792

(pp.65-67)

[15] A. T. Yatsui, J. Lim, M. Ohtsu, S.J. An, and G.-C. Yi, "Evaluation of the discrete energy levels of individual ZnO nanorod single-quantum-well structures using near-field ultraviolet photoluminescence spectroscopy", Appl. Phys. Lett., Vol.85, No.5, August 2004, pp.727-729

(pp.69-71)

[II] PRESENTATIONS IN INTERNATIONAL CONFERENCES

[1] K. H. Yonemitsu, T. Kawazoe, and M. Ohtsu, "Nonadiabatic photochemical reaction and application to photolithography", Abstracts of the International Conference on Luminescence 2005, July 25-29, 2005, Bijing, China (paper number TUE-P-B06)

(p.73)

[2] T. Kawazoe, K. Kobayashi, K. Akahane, N. Yamamoto, N. Ohtani, and M. Ohtsu, "Demonstration of Nanophotonic Devices using Near-Field Optically Coupled Quantum Dots", Abstracts of the International Conference on Luminescence 2005, July 25-29, 2005, Bijing, China (paper number TED-A-E03)

(p.75)

[3] T. Yatsui, and M. Ohtsu, "Fabrication of nanophotonic devices and their integration by optical near-field", Technical Digest of the Pacific Rim Conference on Lasers and Electro-Optics 2005, July 11-15, 2005, Tokyo, Japan (paper number CThN2-5-INV)
[Invited presentation]

(pp.77-78)

[4] T. Yatsui, T. Kawazoe, M. Ohtsu, S.J. An, J. Yoo, and G.-C. Yi, "Evaluating the quantum confinement effect of isolated ZnO nanorod single-quantum-well structures using near-field ultraviolete photoluminescence spectroscopy", Proceedings of 2005 5th IEEE Conference on Nanotechnology, July 11-15, 2005, Nagoya, Japan (paper number TU-A3-5)

(pp.79-81)

[5] T. Kawazoe, K. Kobayashi, K. Akahane, M. Yamamoto, N. Ohtani, and M. Ohtsu, "Demonstration of a Nanophotonic NOT-Gate using Near-Field Optically Coupled Quantum Dots", Proceedings of 2005 5th IEEE Conference on Nanotechnology, July 11-15, 2005, Nagoya, Japan (paper number WE-A2-6)

(pp.83-86)

[6] H. Yonemitsu, T. Kawazoe, and M. Ohtsu, "Nanofabrication using Nonadiabatic Near-Field Photolithography", Proceedings of 2005 5th IEEE Conference on Nanotechnology, July 11-15, 2005, Nagoya, Japan (paper number WE-P2-3)

(pp.87-90)

[7] M. Naruse, T. Yatsui, W. Nomura, and M. Ohtsu, "Hierarchical Optical Memory System Using Near- and Far-field Accesses", Technical Digest of International Symposium on Optical Memory and Optical Data Storage, July 10-14, 2005, Honolulu, USA (paper number MA3)

(pp.91-93)

[8] M. Naruse, T. Kawazoe, S. Sangu, K. Kobayashi, and M. Ohtsu, "Nanophotonic Memory-Based Computation Using Optical Near-Field Interactions", Technical Digest of the OSA Topical Meeting on Information Photonics, June 6-9, 2005, Charlotte, USA (paper number ITuB3)

(pp.95-97)

[9] T. Kawazoe, K. Kobayashi, and M. Ohtsu, "A Nanophotonic NOT-Gate using Near-Field Optically Coupled Quantum Dots", Technical Digest of the Conference on Lasers and Electro-Optics, May 22-27, 2005, Baltimore, USA (paper number CTuF4)

(pp.99-101)

[10] M. Naruse, F. Kubota, T. Kawazoe, S. Sangu, K. Kobayashi, and M. Ohtsu,"Optical Interconnects using Optical Far- and Near-Field Interactins for High-density Data Broadcasting", Technical Digest of the Conference on Lasers and Electro-Optics, May 22-27, 2005, Baltimore, USA (paper number CWF6)

(pp.103-105)

[11] T. Yatsui, J. Lim, T. Kawazoe, M. Ohtsu, S.J. An, J. Yoo, and G.-C. Yi, "Evaluating the quantum confinement effect of isolated ZnO nanorod single-quantum-well structures using near-field ultraviolet photoluminescence spectroscopy", Technical Digest of the Conference on Lasers and Electro-Optics, May 22-27, 2005, Baltimore, USA (paper number CWL2)

(pp.107-109)

[12] T. Yatsui, W. Nomura, and M. Ohtsu, "Size-, position-, and separation-controlled one-dimensional alignment of nanoparticles using an optical near field", Technical Digest of the Conference on Lasers and Electro-Optics, May 22-27, 2005, Baltimore, USA (paper number CThL1)
[Invited presentation]

(pp.111-114)

[13] T. Yatsui, S. Yamazaki, T. Nariga, M. Ohtsu, T.-W. Kim, and H. Fujioka, "Room-temperature synthesis of ultraviolet-emitting nanocrystalline GaN films using photochemical vapor deposition", Absracts of the MRS 2004 Fall Meeting, November 29-December 3, 2004, Boston, USA, p.139 (paper number E11.8)

(p.115)

[14] T. Yatsui, J. Lim, T. Kawazoe, M. Ohtsu, S.J. An, and G.-C. Yi, "Evaluation of the Fine Structures of Isolated ZnO Nanorod Single-Quantum-Well Structures using Near-Field Ultraviolet Photoluminescence Spectroscopy", Absracts of the MRS 2004 Fall Meeting, November 29-December 3, 2004, Boston, USA, p.369 (paper number O3.4)

(p.117)

[15] T. Kawazoe, K. Kobayashi, and M. Ohtsu, "Anti-parallel Coupling of Quantum Dots with an Optical Near-Field Interaction", Abstract Book of the International Symposium on Nano-organization and Function, November 11-12, 2004, Tokyo, Japan, p.27 (paper number 11-A-7)

(p.119)

[16] Y. Saito, S. Mononobe, I. Kato, M. Ohtsu, and H. Honma, "Fabrication of a Near-field Optical Probe by Electroless Plating under Ultrasonic Irradiation", Abstract Book of the International Symposium on Nano-organization and Function, November 11-12, 2004, Tokyo, Japan, p.70 (paper number 12-C-1)

(p.121)

[17] S. Mononobe, I. Kato, H. Honma, and M. Ohtsu, "Surface Activation Based on Oxygen-Reactive Sputtering of Palladium to Plate Near-Field

Optical Fiber Probes", Abstract Book of the International Symposium on Nano-organization and Function, November 11-12, 2004, Tokyo, Japan, p.71 (paper number 12-C-2)

(p.123)

[18] M. Ohtsu, "Nanophotonics: Optical near field phenomena and applications to devices, fabrication, and systems", Abstract of the 4th US-Japan Joint Symposium on Nanophotonics: Beyond the limit of Optical Technology, October 26-27, 2004, Tokyo, Japan (paper number 1)
[Invited presentation]

(pp.125-126)

[19] Y. Saito, S. Mononobe, I. Kato, M. Ohtsu, and H. Honma, "Electroless Nickel Plating under Ultrasonic Irradiation And Its Application to a Scanning Near-Field Optical Microscopy Probe", Meeting Abstracts of the 206th Meeting of The Electrochemical Society, Inc., October 3-8, 2004, Honolulu, USA (paper number A1-57)

(p.127)

[20] Y. Saito, S. Mononobe, M. Ohtsu, and H. Honma, "Fabrication of a SNOM probe using electroless nickel plating with ultrasonic irradiation", Book of Abstracts II of the 55th Annual Meeting of the International Society of Electrochemistry, September 19-24, 2004, Thessaloniki, Greece, p.1281 (paper number S10FP9)

(p.129)

[21] K. Kobayashi and M. Ohtsu, "Quasi-Particle Model for Optical Near-Field Interaction with Single Atom, Molecule and Nanomaterials", Technical Digest of the 8th International Conference on Near-field Nano Optics & Related Techniques, September 5-9, 2004, Seoul, Korea, p.97 (paper number MoO48)

(p.131)

[22] S. Mononobe, I. Kato, Y. Saito, H. Honma, and M. Ohtsu, "Fabrication of a Near-Field Optical Fiber Probe Based on Size-Dependent Electroless Nickel Plating", Technical Digest of the 8th International Conference on Near-field Nano Optics & Related Techniques, September 5-9, 2004, Seoul, Korea, p.123 (paper number MoP24)

(p.133)

[23] V. Polonski, B. Martin, R. Netterfield, T. Yatsui, T. Kawazoe, and M. Ohtsu, "Optical near-field-assisted dry etching of silica in a sulfur hexafluoride atmosphere", Technical Digest of the 8th International Conference on Near-field Nano Optics & Related Techniques, September 5-9, 2004, Seoul, Korea, p.184 (paper number TuO15)

(p.135)

[24] M. Naruse, T. Kawazoe, S. Sangu, K. Kobayashi, T. Miyazaki, F. Kubota, and M. Ohtsu, "Nanometric Summation Architecture Using Optical Near-field Coupling Between Quantum Dots", Proceedings Vol.2 of the 30th European Conference on Optical Communications, September 5 - 9, 2004, Stockholm, Sweden, pp.202-203 (paper number Tu3.4.5)

(pp.137-138)

[III] REVIEW PAPERS

[1] M. Ohtsu, "Nanophotonics and materials: Beyond the diffraction limit of light", Engineering Materials, Vol.53, No.7, July 2005, pp.18-21
【大津元一、「光の回折限界を超えるナノフォトニクスとその材料」、工業材料、第 53 巻、第 7 号、2005 年 7 月、pp.18-21】

(pp.139-142)

[2] M. Ohtsu, "What is nanophotonics?: Its needs and seeds", Engineering Materials, Vol.53, No.6, June 2005, pp.78-81
【大津元一、「ナノフォトニクスとは：そのニーズとシーズ」、工業材料、第 53 巻、第 6 号、2005 年 6 月、pp.78-81】

(pp.143-146)

[3] S. Mononobe, Y. Saito, H. Honma, and M. Ohtsu, "Fabrication of a near-field optical probe based on electroless plating under ultrasonic irradiation", Material Integration, Vol.18, No.4, April 2005, pp.29-32
【物部秀二、斉藤裕一、本間英夫、大津元一、「超音波照射下無電解めっきによる近接場光学顕微鏡プローブの作製」、マテリアルインテグレーション、第 18 巻、第 4 号、2005 年 4 月、pp.29-32】

(pp.147-150)

[4] T. Kawazoe, K. Kobayashi, and M. Ohtsu, "Investigation and Development of Optical Near-field Interaction between Nano-materials", Solid State Physics, Vol. 40, No.4, April 2005, pp.227-238
【川添忠、小林潔、大津元一、「ナノ物質間の近接場光相互作用の研究と展開」、固体物理、第 40 巻、第 4 号、2005 年 4 月、pp.227-238】

(pp.151-162)

[5] T. Yatsui and M. Ohtsu, "Nanofabrication using optical near-field", Vol.71, No.3, March 2005, pp.311-314
【八井崇、大津元一、「近接場光による微細加工」、精密工学会誌、第 71 巻、第 3 号、2005 年 3 月、pp.311-314】

(pp.163-166)

[IV] PUBLISHED BOOKS

[1] M. Ohtsu (ed.), *Progress in Nano-Electro-Optics IV*, Springer Verlag, Berlin, 2005, (206 pages)

(pp.167-172)

[2] M. Ohtsu (ed.), *Progress in Nano-Electro-Optics III*, Springer Verlag, Berlin, 2005, (224 pages)

(pp.173-178)

[3] M. Ohtsu, "Physics and Applications of Nanophotonics", Chapter 6 in *New Photonics Technologies for the Information Age*, ed. by S.Sudo and K. Okamoto, Artech House, Boston, 2004, pp.93-137

(pp.179-181)

[V] AWARDS

[1] M. Ohtsu, *The 30th Harushige INOUE Award*, Japan Science and Technology Agency, July 13, 2005
【大津元一、「第 30 回井上春成賞」、（独）科学技術振興機構、2005 年 7 月 13 日】

[2] M. Ohtsu, *The Purple Ribbon Medal*, The Cabinet Office, Government of Japan, November 3, 2004
【大津元一、「紫綬褒章」、内閣府、2004 年 11 月 3 日】

[I] ORIGINAL PAPERS

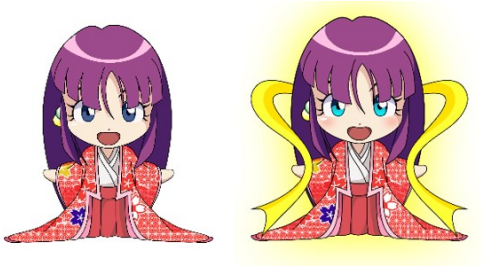

Near-field measurement of spectral anisotropy and optical absorption of isolated ZnO nanorod single-quantum-well structures

Takashi Yatsui[a)] and Motoichi Ohtsu[b)]
Solution-Oriented Research for Science and Technology, Japan Science and Technology Agency, Machida, Tokyo, 194-0004 Japan

Jinkyoung Yoo, Sung Jin An, and Gyu-Chul Yi
National CRI Center for Semiconductor Nanorods and Department of Materials Science and Engineering, Pohang University of Science and Technology (POSTECH), San 31 Hyoja-dong, Pohang, Gyeongbuk 790-784, Korea

(Received 3 February 2005; accepted 10 June 2005; published online 11 July 2005)

We report low-temperature near-field spectroscopy of isolated ZnO/ZnMgO single-quantum-well structures (SQWs) on the end of ZnO nanorod to define their potential for nanophotonics. First, absorption spectra of isolated ZnO/ZnMgO nanorod SQWs with the Stokes shift as small as 3 meV and very sharp photoluminescent peaks indicate that the nanorod SQWs are of very high optical quality. Furthermore, we performed polarization spectroscopy of isolated ZnO SQWs, and observed valence-band anisotropy of ZnO SQWs in photoluminescence spectra directly. Since the exciton in a quantum structure is an ideal two-level system with long coherence times, our results provide criteria for designing nanophotonic devices. © *2005 American Institute of Physics*.
[DOI: 10.1063/1.1990247]

ZnO nanocrystallites are a promising material for realizing nanometer-scale photonic devices,[1] i.e., nanophotonic devices, at room temperature, owing to their large exciton binding energy[2–4] and large oscillator strength.[5] Furthermore, the recent demonstration of semiconductor nanorod quantum-well structures enables us to fabricate nanometer-scale electronic and photonic devices on single nanorods.[6–9] Recently, ZnO/ZnMgO nanorod heterostructures were fabricated and the quantum confinement effect even from the single-quantum-well structures (SQWs) was observed.[10] Near-field spectroscopy has made a remarkable contribution to investigations of the optical properties in nanocrystallite,[11] and has resulted in the observation of nanometer-scale optical images, such as the local density of exciton states.[12] However, reports on semiconductor quantum structure are limited to naturally formed quantum dots (QDs).[12–14] Here we report low-temperature near-field spectroscopy of artificially fabricated ZnO SQWs on the end of a ZnO nanorod.

ZnO/ZnMgO SQWs were fabricated on the ends of ZnO stems with a mean diameter of 40 nm and a length of 1 μm using catalyst-free metalorganic vapor phase epitxy, in which the ZnO nanorods were grown in the *c* orientation.[10,15] They were grown vertically from a sapphire (0001) substrate using catalyst-free metalorganic vapor phase epitaxy, in which the ZnO nanorods were grown vertically from a sapphire (0001) substrate in the *c* orientation.[10,15] The Mg concentration in the ZnMgO layers averaged 20 at. %. Two samples were prepared for this study: their ZnO well layer thickness L_w, were 2.5 and 3.75 nm, while the thicknesses of the ZnMgO bottom and top barrier layers in the SQWs were fixed at 60 and 18 nm, respectively. After growing the ZnO/ZnMgO nanorod SQWs, they were dispersed so that they were laid down on a flat sapphire substrate to isolate them from each other [Fig. 1(a)].

The far-field photoluminescence (PL) spectra were obtained using a He–Cd laser ($\lambda = 325$ nm) before dispersion of the ZnO/ZnMgO nanorod SQWs. The emission signal was collected with the acromatic lens ($f = 50$ mm). To confirm that the optical qualities of individual ZnO/ZnMgO SQWs were sufficiently high, we used a collection-mode near-field optical microscope (NOM) using a He–Cd laser ($\lambda = 325$ nm) for excitation, and a UV fiber probe with an aperture diameter of 30 nm. The excitation source was focused on a nanorod sample laid on the substrate with a spot size approximately 100 μm in diameter. The PL signal was collected with the fiber probe, and detected using a cooled charge coupled device through a monochromator. The fiber

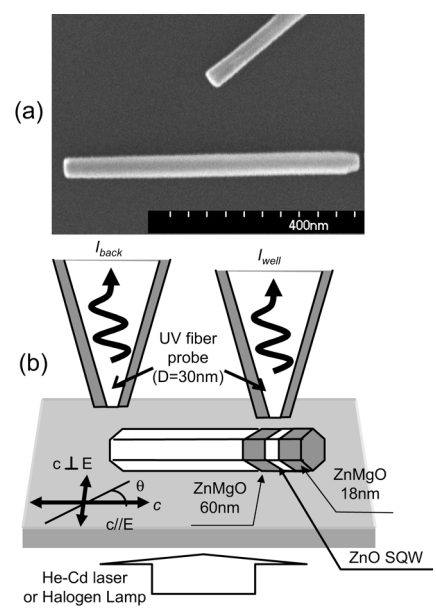

FIG. 1. Schematic of experimental setup for near-field PL spectroscopy. (a) Scanning electron micrographic image of the dispersed ZnO/ZnMgO SQWs. (b) Schematic of ZnO/ZnMgO SQWs on the ends of ZnO nanorods. *c*: *c* axis of the ZnO stem. θ: angle between the ZnO stem and the direction of incident light polarization.

[a)]Electronic mail: yatsui@ohtsu.jst.go.jp
[b)]Also at: School of Engineering, The University of Tokyo, Bunkyo-ku, Tokyo, 113-8656 Japan.

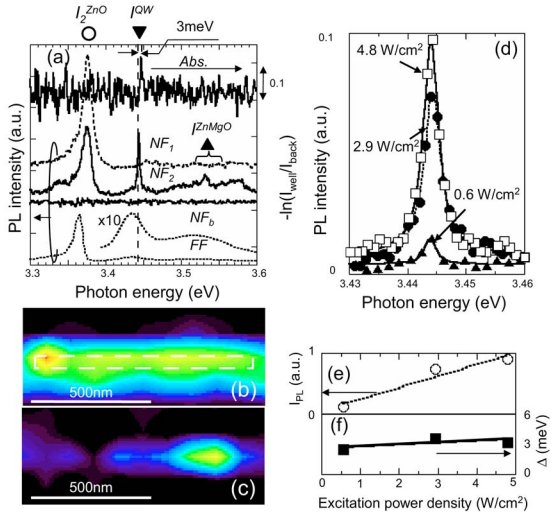

FIG. 2. (Color online) Near-field PL and absorption spectroscopy of isolated ZnO SQWs (L_w=3.75 nm) at 15 K. (a) NF_1, NF_2: near-field PL spectra. NF_b: background noise. Abs.: near-field absorption spectrum. FF: far-field PL spectrum of vertically aligned ZnO SQWs (L_w=3.75 nm). NOM images of isolated ZnO SQWs obtained at (b) 3.375 and (c) 3.444 eV. The rectangle shown in dashed white lines indicates the position of the ZnO stem. (d) Near-field PL spectra of isolated ZnO SQWs at excitation densities ranging from 0.6 to 4.8 W/cm^2. The integrated PL intensity I_{PL} (e) and homogeneous linewidths Δ (f) as a function of the excitation power density.

probe was kept in close proximity to the sample surface (~5 nm) using the shear-force feedback technique. The polarization of the incident light was controlled with a λ/2 wave plate. In contrast to the naturally formed QD structure (a high monolayer island formed in a narrow quantum well), the barrier and cap layers laid on the substrate allowed the probe tip access to the PL source, which reduced carrier diffusion in the ZnO SQWs and the subsequent linewidth broadening, thereby achieving a high spatial and spectral resolution. In addition to the PL measurements, absorption spectra were obtained using a halogen lamp, where the absorption was defined by the ratio I_{well}/I_{back} between the signal intensities transmitted through the well layer (I_{well}) and substrate (I_{back}, 50 nm apart from the well layer) [Fig. 1(b)]. The absorption signal was collected with the same fiber probe with an aperture diameter of 30 nm. Since the ZnMgO layers are much thicker than that of the well layer (~3 nm), any difference in the transmission signals between I_{well} and I_{back} was not detected, which resulted in no detection of the absorption peak originating from the ZnMgO layers.

As a preliminary near-field spectroscopy experiment of the ZnO SQWs, we obtained near-field PL spectra of the ZnO SQWs with L_w=3.75 nm [Fig. 2(a)] obtained with polarization perpendicular to the *c* axis [θ=90° in Fig. 1(b)]. Two typical spectra are shown, one with a single peak at 3.375 eV (NF_1) and the other with several sharp peaks around 3.375, 3.444, and 3.530 eV (NF_2), while NF_b is a background spectra [Fig. 2(a)]. Several conclusions can be drawn from these spectral profiles. First, comparison with the far-field PL spectrum [FF: dashed curve in Fig. 2(a)] showed that the emission peak I_2^{ZnO} at 3.375 eV was suppressed, and I^{QW} (3.444 eV) and I^{ZnMgO} (3.530 eV) were enhanced in NF_2, indicating that peaks I_2^{ZnO} and I^{ZnMgO} originated from the ZnO stem and ZnMgO layers, respectively. Second, since the peak position of I^{QW} was consistent with the theoretical prediction (3.430 eV) using the finite square-well potential of the quantum confinement effect in the ZnO well layer for L_w=3.75 nm, we concluded that peak I^{QW} originated from the ZnO SQWs. The theoretical calculation used $0.28m_0$ and $1.8m_0$ as the effective masses of an electron and hole in ZnO, respectively, at a ratio of conduction- and valence-band offsets ($\Delta E_c/\Delta E_v$) of 9, and a band-gap offset (ΔE_g) of 250 meV.[10] The spatial distributions of the near-field PL intensity of peaks I_2^{ZnO} and I^{QW} [Figs. 2(b) and 2(c)] supported the postulate that the blueshifted emission was confined to the end of the ZnO stem. Third, the spectral width (3 meV) of peak I^{QW} was much narrower than those of the far-field PL spectra (40 meV). To estimate the homogeneous linewidth of isolated ZnO SQWs, we observed the power dependence of the near-field PL spectra [Fig. 2(d)] by varying the excitation power densities from 0.6 to 4.8 W/cm^2. The shape of each spectrum was fitted using the Lorentzian function indicated by the solid curve. Figures 2(e) and 2(f) show the integrated PL intensity (I_{PL}) and linewidth (Δ) of the fitted Lorentzian, which increased linearly and remained constant around 3 meV, respectively. These results indicate that emission peak I^{QW} represented the emission from a single-exciton state in ZnO SQWs and that the linewidth was governed by the homogeneous broadening. Fourth, the Stokes shift of 3 meV [Fig. 2(a)] was much smaller than the reported value (50 meV) in ZnO/ZnMgO superlattices.[16,17] The small Stokes shift may result from the decreased piezoelectric polarization effect by the fully relaxed strain for the ZnO/ZnMgO nanorod quantum structures in contrast to the two-dimensional (2D) ZnO/ZnMgO heteroepitaxial multiple layers are strongly supported by the theoretical calculation on the double barrier lnAs/lnP nanorod heterostructures.[18]

Based on these experiments, a major investigation of the optical properties of isolated ZnO SQWs was performed by analyzing the polarization-dependent PL spectrum of isolated ZnO SQWs (L_w=3.75 nm). As shown in Fig. 3(a), NF_0 is a near-field PL spectrum obtained with parallel polarization with respect to the *c* axis, θ=0°, and this exhibits a new peak I_{1b}^{QW} at 3.483 eV, which is out of peak in the far-field spectrum (3.435 eV±20 meV). Peak I_{1a}^{QW} is the same as I^{QW} in Fig. 2(a).

As the ZnO has valence-band anisotropy owing to the wurtzite crystal structure, the operator corresponds to the $\Gamma_5(\Gamma_1)$ representation when the electric vector $\boldsymbol{E}$ of the incident light is perpendicular (parallel) to the crystalline *c* axis, respectively. By considering the energy difference between Γ_5 and Γ_1 in the center of the zone around 40 meV for bulk material,[5,19,20] and the direction of the incident light polarization with respect to the *c* axis, emission peaks I_{1a}^{QW} and I_{1b}^{QW} in Fig. 3(a) are allowed for the exciton from Γ_5 and Γ_1, respectively. This observation of a Γ_1 exciton in a PL spectrum originates from the enhancement of the exciton binding energy owing to the quantum confinement effect[4] because the exciton binding energy of the emission from Γ_1 (50–56 meV) (see Refs. 20 and 21) is comparable to that from Γ_5 (60 meV). Furthermore, in contrast to the bulk ZnO film, our sample configuration using laid ZnO nanorod SQWs has realized π polarization (θ=0°), allowing the detection of the emission from the Γ_1 exciton. The homogeneous linewidth of emission peak I_{1a}^{QW} (Γ_5) is in the range 3–5 meV, while that of I_{1b}^{QW} (Γ_1) is 9–11 meV [Fig. 3(b)]. This difference is attributed to the degeneracy of the transi-

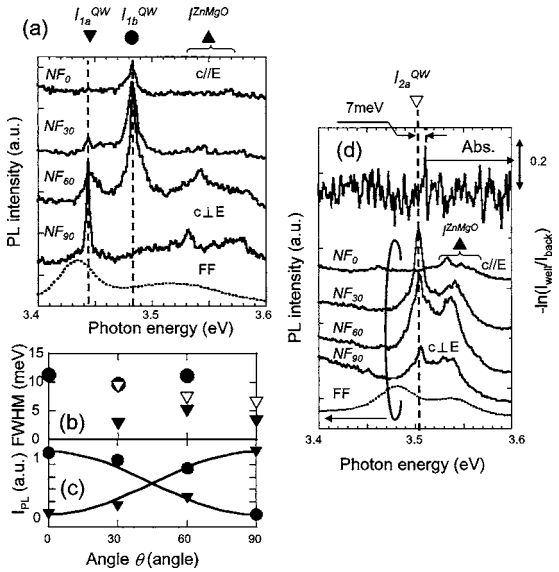

FIG. 3. Polarization dependence of near-field PL spectra of isolated ZnO SQWs obtained at 15 K. (a) NF_θ, FF: near-field and far-field PL spectra of isolated ZnO SQWs (L_w=3.75 nm) for θ=0°, 30°, 60°, and 90°. (b) Solid triangles and circles are the polarization dependence of the linewidth of I_{1a}^{QW} and I_{1b}^{QW}, respectively in (a). Open triangles are the polarization dependence of linewidth of I_{2a}^{QW} in (d). (c) Solid triangles and circles are the integrated PL intensities (I_{PL}) of I_{1a}^{QW} and I_{1b}^{QW}, respectively, normalized to the total PL intensities ($I_{1a}^{QW}+I_{1b}^{QW}$). (d) NF_θ, FF: near-field and far-field PL spectra, respectively, of isolated ZnO SQWs (L_w=2.5 nm). Abs.: absorption spectrum.

tion of the Γ_1 exciton with continuum and to the contribution of the residual strain field, and results in sensitive dependence of the Γ_1 exciton on the strain, as reported in the GaN.[22] The solid triangles and circles in Fig. 3(c) shows the respective normalized integrated PL intensity at I_{1a}^{QW} and I_{1b}^{QW}, respectively, which are in good agreement with the sine-squared and cosine-squared functions represented by the solid curves. These results indicate that emission peaks I_{1a}^{QW} and I_{1b}^{QW} originate from unidirectional transition dipoles that are orthogonal to each other.

To study the linewidth broadening mechanism, Fig. 3(d) shows the polarization-dependent near-field PL spectra (NF_0–NF_{90}) and absorption spectrum obtained for isolated ZnO SQWs with a thinner well layer (L_w=2.5 nm). In NF_0–NF_{90}, the emission peaks I^{ZnMgO} around 3.535 eV originate from the ZnMgO layers. Emission peak I_{2a}^{QW} originates from the Γ_5 exciton in the SQWs, as was the case for I_{1a}^{QW} in Fig. 3(a), since the position of peak I_{2a}^{QW} (3.503 eV) is comparable to that of the dominant peak in the far-field PL spectra (3.480 eV) and the theoretical prediction (3.455 eV) using the finite square-well potential of the quantum confinement effect in the ZnO well layer. In comparison to ZnO SQWs with L_w=3.75 nm, however, emission peak I_{2a}^{QW} had a broader linewidth (7–10 meV), which is attributed to the shorter exciton dephasing time. In the nanocrystallite where the excitons are quantized, the linewidth should be determined by the exciton dephasing time. Such dephasing arises from the collisions of the excitons at the irregular surface, so that the linewidth is d^{-2} (d is the effective size of the quantum structure).[23] The observed well-width dependence of the spectral linewidth, $3.75^{-2}/2.5^{-2}\sim 3/7$, and the Stokes shift of 7 meV [see Fig. 3(c)] larger than that for L_w=3.75 nm (3 meV) are supported by this dephasing mechanism quantitatively. Although emission peak I_{2a}^{QW} was suppressed for θ=0°, no peaks corresponding to the Γ_1 exciton in SQWs were detected owing to the reduction of the exciton binding energy, since the peak energy of Γ_1 for the ZnO SQWs with L_w=2.5 nm is comparable with that of ZnMgO.

The results shown here provide criteria for realizing nanophotonic devices using a two-level system.[24,25] As a representative device, a nanophotonic switch can be realized by controlling the dipole forbidden optical energy transfer among resonant energy levels in nanometer-scale QD via an optical near field.[26] Since the switching dynamics was already confirmed using CuCl quantum cubes,[26] the success of near-field PL and absorption measurement of isolated SQWs described above is a promising step toward designing a nanophotonic switch and related devices.

The authors are grateful to Drs. I. Banno (Yamanashi University) and S. Sangu (Ricoh Company, Ltd.) for many fruitful discussions. The work at POSTECH was supported by the National Creative Research Initiative Project, Korea and the AOARD 04–49 (Quotation No. FA5209–04–T0254).

[1] M. Ohtsu, K. Kobayashi, T. Kawazoe, S. Sangu, and T. Yatsui, IEEE J. Sel. Top. Quantum Electron. **8**, 839 (2002).
[2] A. Ohtomo, K. Tamura, M. Kawasaki, T. Makino, Y. Segawa, Z. K. Tang, G. K. L. Wong, Y. Matsumoto, and H. Koinuma, Appl. Phys. Lett. **77**, 2204 (2000).
[3] M. H. Huang, S. Mao, H. Feick, H. Yan, Y. Wu, H. Kind, E. Weber, R. Russo, and P. Yang, Science **292**, 1897 (2001).
[4] H. D. Sun, T. Makino, Y. Segawa, M. Kawasaki, A. Ohtomo, K. Tamura, and H. Koinuma, J. Appl. Phys. **91**, 1993 (2002).
[5] D. C. Reynolds, D. C. Look, B. Jogai, C. W. Litton, G. Cantwell, and W. C. Harsch, Phys. Rev. B **60**, 2340 (1999).
[6] Y. Wu, R. Fan, and P. Yang, Nano Lett. **2**, 83 (2002).
[7] M. T. Björk, B. J. Ohlsson, C. Thelander, A. I. Persson, K. Deppert, L. R. Wallenberg, and L. Samuelson, Appl. Phys. Lett. **81**, 4458 (2003).
[8] M. S. Gudiksen, L. J. Lauhon, J. Wang, D. C. Smith, and C. M. Lieber, Nature (London) **415**, 617 (2002).
[9] W. I. Park, G.-C. Yi, M. Kim, and S. J. Pennycook, Adv. Mater. (Weinheim, Ger.) **15**, 526 (2003).
[10] W. I. Park, S. J. An, J. L. Yang, G.-C. Yi, S. Hong, T. Joo, and M. Kim, J. Phys. Chem. B **108**, 15457 (2004).
[11] K. Matsuda, T. Saiki, S. Nomura, M. Mihara, and Y. Aoyagi, Appl. Phys. Lett. **81**, 2291 (2002).
[12] K. Matsuda, T. Saiki, S. Nomura, M. Mihara, Y. Aoyagi, S. Nair, and T. Takagahara, Phys. Rev. Lett. **91**, 177401 (2003).
[13] J. R. Guest, T. H. Stievater, G. Chen, E. A. Tabak, B. G. Orr, D. G. Steel, D. Gammon, and D. S. Katzer, Science **293**, 2224 (2001).
[14] T. Guenther, C. Lienau, T. Elsaesser, M. Glanemann, V. M. Axt, T. Kuhn, S. Eshlaghi, and A. D. Wieck, Phys. Rev. Lett. **89**, 057401 (2002).
[15] W. I. Park, D. H. Kim, S.-W. Jung, and G.-C. Yi, Appl. Phys. Lett. **80**, 4232 (2002).
[16] A. Ohtomo, M. Kawasaki, I. Ohkubo, H. Koinuma, T. Yasuda, and Y. Segawa, Appl. Phys. Lett. **75**, 980 (1999).
[17] T. Makino, A. Ohtomo, C. H. Chia, Y. Segawa, H. Koinuma, and M. Kawasaki, Physica E (Amsterdam) **21**, 671 (2004).
[18] M. Zervos and L.-F. Feiner, J. Appl. Phys. **95**, 281 (2004).
[19] M. Zamfirescu, A. Kavokin, B. Gil, G. Malpuech, and M. Kaliteevski, Phys. Rev. B **65**, 161205 (2002).
[20] S. F. Chichibu, T. Sota, G. Cantwell, D. B. Eason, and C. W. Litton, J. Appl. Phys. **93**, 756 (2003).
[21] D. C. Reynolds, C. W. Litton, D. C. Look, J. E. Hoelscher, B. Claflin, T. C. Collins, J. Nause, and B. Nemeth, J. Appl. Phys. **95**, 4802 (2004).
[22] M. Tchounkeu, O. Briot, B. Gil, J. P. Alexis, and R.-L. Aulombard, J. Appl. Phys. **80**, 5352 (1996).
[23] T. Wamura, Y. Masumoto, and T. Kawamura, Appl. Phys. Lett. **59**, 1758 (1991).
[24] A. Zrenner, E. Beham, S. Stufler, F. Findeis, M. Bichler, and G. Abstreiter, Nature (London) **418**, 612 (2002).
[25] Z. Yuan, B. E. Kardynal, R. M. Stevenson, A. J. Shields, C. J. Lobo, K. Cooper, N. S. Beattie, D. A. Ritchie, and M. Pepper, Science **295**, 102 (2002).
[26] T. Kawazoe, K. Kobayashi, S. Sangu, and M. Ohtsu, Appl. Phys. Lett. **82**, 2957 (2003).

Nanodot coupler with a surface plasmon polariton condenser for optical far/near-field conversion

Wataru Nomura[a] and Motoichi Ohtsu[b]
School of Engineering, The University of Tokyo, 7-3-1 Hongo, Bunkyo-ku, Tokyo, Japan 113-8656

Takashi Yatsui
Solution-Oriented Research for Science and Technology (SORST), Japan Science and Technology Agency, 687-1 Tsuruma, Machida, Tokyo, Japan 194-0004

(Received 8 November 2004; accepted 11 March 2005; published online 28 April 2005)

To transmit an optical signal to a nanophotonic device, a nanodot coupler was fabricated from a linear array of closely spaced metallic nanoparticles. To increase the optical far- to near-field conversion efficiency for transmission, a surface plasmon polariton (SPP) condenser was also fabricated from hemispherical metallic nanoparticles so that it worked as a "phased array". The SPP was focused with a spot size as small as 400 nm at $\lambda = 785$ nm. When the focused SPP was incident into the nanodot coupler, its transmission length through the nanodot coupler was confirmed to be 4.0 μm, which is three times longer than that of a metallic core waveguide owing to the efficient near-field coupling between the localized surface plasmon of neighboring nanoparticles. Furthermore, the transmission length through a zigzag-shaped nanodot coupler was as long as that through a linear one. © *2005 American Institute of Physics*.
[DOI: 10.1063/1.1920419]

Future optical transmission and data processing systems will require advanced photonic devices, and their integration, in order to increase data processing rates and capacity. Consequently, these devices will have to be significantly smaller than conventional diffraction-limited photonic devices. To meet this requirement, we have proposed nanometer-scale photonic integrated circuits (nanophotonic ICs) that are composed of nanometer-sized elemental devices (nanophotonic devices).[1]

For use in future photonic systems, the nanophotonic devices and ICs must be connected to conventional diffraction-limited photonic devices. This connection requires a far/near-field conversion device, such as a nanometer-scale optical waveguide. The performance parameters required of this device include:

(a) High conversion efficiency.
(b) A guided beam width of less than 100 nm for efficient coupling of the converted optical near-field to sub-100 nanometer-sized dots.
(c) A transmission length that is longer than the optical wavelength to avoid direct coupling of the propagating far-field light to the nanophotonic device consisted of nanometer-scale dots. [The transmission length ℓ_t is defined as $I(z) = I(0)\exp(-z/\ell_t)$, where $I(z)$ is the optical intensity and z is the longitudinal position measured from the input terminal $(z=0)$].

One candidate device that meets these performance requirements is a plasmon waveguide using a metallized silicon wedge structure that converts propagating far-field light to an optical near-field.[2] In this device, a one-dimensional transverse magnetic (TM) plasmon mode is excited efficiently via a metallic core waveguide along the plateau. However, the ℓ_t of the TM plasmon mode is still in the order of 700 nm (at $\lambda = 830$ nm) for a metallic core waveguide with a gold core (diameter $D = 10$ nm) insulated using air.[3] To increase ℓ_t, a more promising candidate is a nanodot coupler consisting of an array of closely spaced metallic nanoparticles, because higher transmission efficiency is expected owing to the plasmon resonance in the closely spaced metallic nanoparticles.[4] Energy transfer along the nanodot coupler relies on the near-field coupling between the plasmon-polariton mode of the neighboring nanoparticles.

To increase in the efficiency of exciting localized surface plasmon in the nanodot coupler than that excited by propagating far-field light, we equipped the nanodot coupler with a surface plasmon polariton (SPP) condenser for efficient far/near-field conversion. Figure 1(a) shows the proposed optical far/near-field conversion device. Incoming far-field light is first transformed into the two-dimensional SPP mode on the

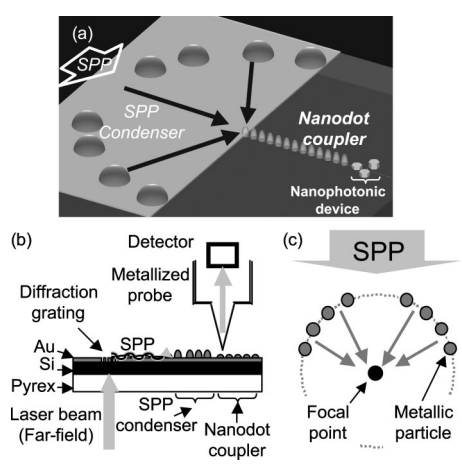

FIG. 1. (a) Bird's eye view of a nanodot coupler with a SPP condenser. (b) Experimental system. (c) Schematic illustration of the SPP condenser.

[a]Electronic mail: nomura@nanophotonics.t.u-tokyo.ac.jp
[b]Also with Japan Science Technology Agency, 687-1 Tsuruma, Machida, Tokyo, Japan 194-0004.

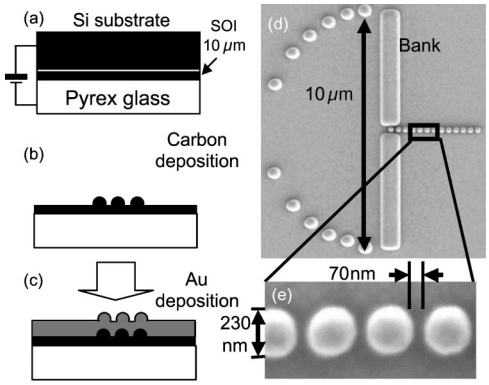

FIG. 2. Fabrication of the nanodot coupler and SPP condenser: (a) Anodic bonding [step (i)], (b) carbon hemisphere deposition using FIB [step (ii)], (c) 120 nm gold film deposition using sputtering [step (iii)], (e) and (d) SEM images of the fabricated nanodot coupler and SPP condenser.

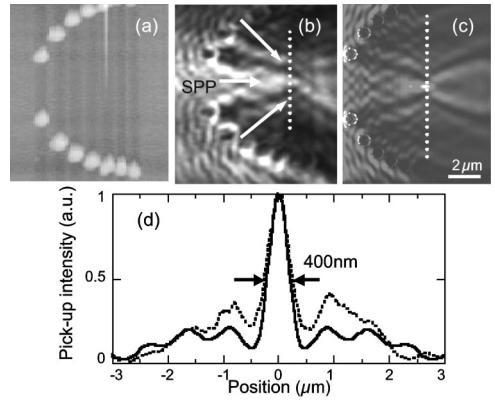

FIG. 3. (a) Shear-force image of the SPP condenser. (b) The near-field energy distribution of (a) taken at $\lambda = 785$ nm. (c) Calculated spatial distribution of the electric-field energy using the FDTD method. The dashed and solid curves in (d) are cross-sectional profiles along the dashed white lines in (b) and (c), respectively.

gold film [see Fig. 1(b)]. Then, the SPP mode is scattered and focused by the SPP condenser, which consists of several hemispherical metallic submicron particles that are arranged in an arc and work as a "phased array" [Fig. 1(c)].[5] The input terminal of the nanodot coupler is fixed at the focal point of the SPP. Finally, after the localized surface plasmon transmits through the nanodot coupler, it is converted into an optical near-field so that it couples to the nanophotonic device.

The advantages of this device are that it has;

(1) A high conversion efficiency, from the SPP mode to the localized surface plasmon in the nanodot coupler, owing to coupling the scattering at the inlet metallic nanoparticle.[6]
(2) No cut-off diameter of the metallic nanoparticle array, i.e., the beam width decreases with the diameter because the electric-field vector, which is dominant in the nanodot coupler, involves only a Förster field.[4]
(3) Long-distance propagation of the TM-plasmon mode. For example, the calculation using the finite-difference time domain (FDTD) method estimated a transmission length of $\ell_t = 2\ \mu$m (at $\lambda = 785$ nm) for a plasmon-polariton mode with linearly aligned 50 nm dots with 10 nm separation.[7,8]

Advantages (1) to (3) are compatible with meeting requirements (A) to (C), respectively.

To fabricate the nanodot coupler and SPP condenser using a focused ion beam (FIB), we used a silicon-on-insulator wafer to avoid ion beam drift. The fabrication process was as follows:

(i) A (100)-oriented SOI wafer was bonded to a glass substrate by anodic bonding [Fig. 2(a)].[9]
(ii) After removing the silicon substrate and SiO_2 layer from the SOI wafer by wet etching, carbon hemispheres were deposited using FIB [Fig. 2(b)].
(iii) To excite SPP mode and enhance the optical near-field energy, a 120 nm thick gold film was applied using sputtering [Fig. 2(c)]. The number of hemispheres, their positions, and their sizes were optimized using the FDTD method in order to minimize the focused spot size.[8]
(iv) Finally, a diffraction grating was fabricated using a FIB milling technique 50 μm below the condenser in order to excite the SPP by the incident optical far field.

Figures 2(d) and 2(e) show scanning electron microscopic (SEM) images of the SPP condenser and nanodot coupler. Two banks were fabricated, in order to avoid illumination of the nanodot coupler by the satellite spots (originating from higher-order diffraction) [Fig. 2(d)]. The nanodot coupler consisted of a linear array of nanoparticles with diameters of 230 nm separated by 70 nm. The SPP condenser consisted of twelve scatterers 350 nm in diameter, aligned on an arc with a diameter of 10 μm.

The spatial distribution of the optical near-field energy was observed using a collection mode near-field optical microscope [see Fig. 1(b)]. A light source with a wavelength of $\lambda = 785$ nm light was used. A sharpened fiber probe with 20 nm thick gold film was used to enhance the collection efficiency.[10]

First, we checked whether the SPP condenser led to efficient scattering and resultant focusing of the SPP by exciting the SPP mode through the grating coupler. Figures 3(a) and 3(b) show a shear-force image of the SPP condenser and the spatial distribution of the optical near-field energy, respectively. As shown in the cross-sectional profile [dashed curve in Fig. 3(d)] through the focal point of the SPP [white dotted line in Fig. 3(b)], the full width at half maximum (FWHM) of the spatial distribution of the SPP was as narrow as 400 nm. Figure 3(c) shows the spatial distribution of the optical near-field energy in the SPP condenser calculated using the FDTD method, where each cell was $50 \times 50 \times 25$ nm and the model consisted of $240 \times 240 \times 80$ cells. Considering the tip diameter (50 nm) of the metallized fiber probe used for collection mode, the observed distribution [Fig. 3(b) and dashed curve in Fig. 3(d)] was in good agreement with the calculated results [FWHM = 380 nm, solid curve in Fig. 3(d)]. These results imply that our device works as an efficient phased array.

Second, we measured the spatial distribution of the optical near-field energy on a linear nanodot coupler, the input terminal of which was fixed at the focal point of the SPP. Figures 4(a) and 4(b) show an SEM image and the spatial distribution of the optical near-field energy on the nanodot coupler, respectively. The black dots in Fig. 4(c) show cross-

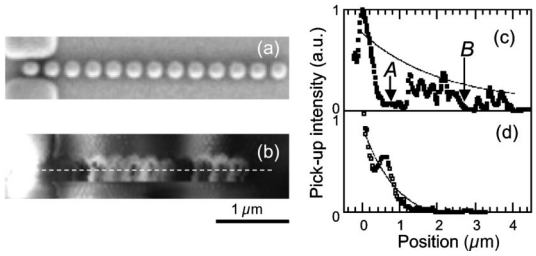

FIG. 4. SEM image (a) and the near-field energy distribution (b) of a linearly chained nanodot coupler. (c) Solid circles show the cross-sectional profiles along the white dashed line in (b). The solid curve shows the fitted exponential envelope. A and B indicate dips resulting from the length of the nanodot coupler. (d) Open circles show the cross-sectional profiles along metallic core waveguide and the solid curve shows the fitted exponential envelope.

sectional profiles along the white broken line in Fig. 4(b). Position $x=0$ corresponds to the focal point of the SPP condenser. Although not all of the energy couples to the nanodot coupler owing to mode mismatch, the optical near-field intensity has a maximum at each edge of the nanoparticles. This is due to an artifact resulting from the fiber probe at constant height mode. The dips indicated by arrows *A* and *B* originate from interference of the localized surface plasmon in the nanodot coupler that arises from reflection at the output terminal. However, the exponential envelope [solid curve of Fig. 4(c)] fitted by neglecting these influences indicates that the transmission length ℓ_t was 4.0 μm. ℓ_t was five times longer than the wavelength, which meets requirement (C). The beam width was 250 nm, which is comparable to the nanoparticle size. As the size of the nanoparticles was determined by the resolution of FIB for carbon hemisphere deposition, the beam width can be decreased to sub-50 nm scale using electron-beam lithography, which will meet requirement (B).

Third, we checked whether near-field coupling between the neighboring nanoparticles resulted in lower propagation loss by comparing our device with a metallic core waveguide. For this purpose, we fabricated a gold core waveguide the same width as the diameter of the nanoparticles in the nanodot coupler, with its input terminal also fixed at the focal point of the SPP. The open circles in Fig. 4(d) show the cross-sectional profile of the metallic core waveguide and the exponential envelope [solid curve in 4(d)] indicates that the transmission length ℓ_t was 1.2 μm. To evaluate the observed transmission length, we calculated the theoretical value of our metallic core waveguide. Since the Au core waveguide is placed on a Si substrate, we calculated one-dimensional TM plasmon mode[11] in the cylindrical Au core waveguide with an diameter of 250 nm ($\varepsilon_{\mathrm{Au}}=(0.174+i4.86)^2=-23.59+i1.69$) (Ref. 12) surrounded by the medium with an average dielectric constant of Si and air,[13] $\varepsilon_{cl}=\{(3.705+i0.007)^2+1\}/2=7.36+i0.03$.[12] Based on these assumptions, the calculated transmission length of our Au core waveguide is 1.4 μm. Since this is in good agreement with the observed value (1.2 μm).

Finally, we also observed the spatial distribution of the optical near-field energy for a zigzag-shaped nanodot coupler [see Figs. 5(a) and 5(b)]. Corners A to D in Fig. 5(c) represent the profiles at locations A to D in Fig. 5(d), respectively. Comparing adjacent curves, we found that the energy loss at

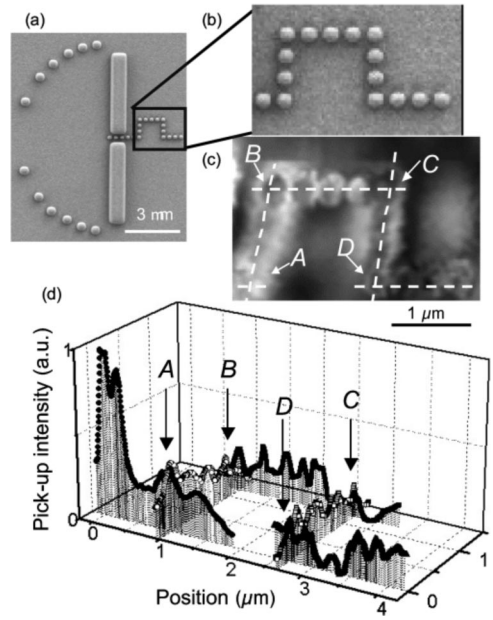

FIG. 5. (a) and (b) SEM images and the near-field intensity distribution (c) of a zigzag-shaped nanodot coupler. (d) The cross-sectional profiles along the dashed white lines in (c). The arrows A to D indicate the corners.

corners A–D was negligible. This is attributed to efficient coupling of the TM and transverse electric localized surface plasmon at the corners. As a result, the transmission length through this zigzag-shaped nanodot coupler was equivalent to that through a linear one.

In summary, we proposed and fabricated an optical far/near-field conversion device that consisted of a nanodot coupler and an SPP condenser. The FWHM of the spatial distribution of the optical near-field energy at the focal point of the SPP was as small as 400 nm at $\lambda=785$ nm. Furthermore, installing a linear nanodot coupler at the focal point of the SPP realized efficient excitation of plasmon-polariton mode with a transmission length of 4.0 μm. Equivalent energy transfer was observed in zigzag-shaped nanodot couplers. These results confirm that a nanodot coupler with an SPP condenser can be used as the optical far/near-field conversion device required by future systems.

[1] M. Ohtsu, K. Kobayashi, T. Kawazoe, S. Sangu, and T. Yatsui, IEEE J. Sel. Top. Quantum Electron. **8**, 839 (2002).
[2] T. Yatsui, M. Kourogi, and M. Ohtsu, Appl. Phys. Lett. **79**, 4583 (2001).
[3] J. Takahara, S. Yamagishi, H. Taki, A. Morimoto, and T. Kobayashi, Opt. Lett. **22**, 475 (1997).
[4] M. L. Brongersma, J. W. Hartmanm, and H. A. Atwater, Phys. Rev. B **62**, R16356 (2000).
[5] I. I. Smolyaninov, D. L. Mazzoni, J. Mait, and C. C. Davis, Phys. Rev. B **56**, 1601 (1997).
[6] T. Yatsui, M. Kourogi, and M. Ohtsu, Appl. Phys. Lett. **71**, 1756 (1997).
[7] M. Quinten, A. Leitner, J. R. Krenn, and F. R. Aussenegg, Opt. Lett. **23**, 1331 (1998).
[8] The computer simulations in this paper are performed by a FDTD-based program, *Poynting for Optics*, a product of Fujitsu, Japan.
[9] T. R. Anthony, J. Appl. Phys. **58**, 1240 (1998).
[10] T. Yatsui, K. Itsumi, M. Kourogi, and M. Ohtsu, Appl. Phys. Lett. **80**, 2257 (2002).
[11] L. Novotny and C. Hafner, Phys. Rev. E **50**, 4094 (1994).
[12] *Handbook of Optical Constants of Solids*, edited by E. D. Palik (Academic, New York, 1985).
[13] H. Kuwata, H. Tamaru, K. Esumi, and K. Miyano, Appl. Phys. Lett. **83**, 4625 (2003).

Available online at www.sciencedirect.com
SCIENCE DIRECT®
Journal of Luminescence 112 (2005) 117–121
JOURNAL OF LUMINESCENCE
www.elsevier.com/locate/jlumin

Exciton dynamics and logic operations in a near-field optically coupled quantum-dot system

K. Kobayashi[a,*,1], S. Sangu[b], T. Kawazoe[a], M. Ohtsu[a,c]

[a]*Japan Science and Technology Agency, 687-1 Tsuruma, Machida, Tokyo 194-0004, Japan*
[b]*Research and Development Center, Ricoh Company Limited, 16-1 Shinei-cho, Tsuzuki-ku, Yokohama, Kanagawa 224-0035, Japan*
[c]*Department of Electronics Engineering, University of Tokyo, 7-3-1 Hongo, Bunkyo-ku, Tokyo 133-8656, Japan*

Available online 24 November 2004

Abstract

High spatial localization of an optical near field allows us to access and excite individual nanometric materials that are much smaller than the diffraction limit of light, while propagating or far-field light can only excite the system globally. This difference, as an initial condition, provides the new exciton dynamics by effective use of a dark state, or a dipole-forbidden state in a quantum-dot (QD) system coupled by the optical near field. We show theoretically and experimentally excitation energy transfer between CuCl quantum cubes, using temporally and spatially resolved near-field spectroscopy. In addition, we report another new feature of the exciton dynamics inherent in a similar system, or characteristic functional (AND/XOR-logic) operations, depending on the initial excitation as well as symmetry of the spatial arrangement of the QDs.

PACS: 71.35.Gg; 73.21.La; 78.67-n; 42.79.Ta

Keywords: Dipole-forbidden energy transfer; Optical near field; Quantum coherence

Owing to the spatial localization of the field beyond the diffraction limit of light, optical near-field techniques allow us to control the states of nanometric materials as well as to observe nanometric structures such as a single molecule and quantum dots (QDs) [1,2]. They also provide, as an initial condition, a distinct difference from global excitation of the system by the far field to individual excitation of the system by the near field, which leads to the new exciton dynamics by effective use of a dark state or a dipole-forbidden state, for example. This kind of characteristic dynamics is expected to open up a new way to realize novel nanophotonic functional devices [3]. Towards this direction, we theoretically show

*Corresponding author. Tel./fax: +81 3 5734 2136.
E-mail address: kkoba@phys.titech.ac.jp (K. Kobayashi).
[1]Present address: Department of Physics, Tokyo Institute of Technology, 2-12-1-H79 O-okayama, Meguro-ku, Tokyo 152-8551, Japan.

0022-2313/$ - see front matter
doi:10.1016/j.jlumin.2004.09.008

excitation energy transfer between CuCl quantum cubes, followed by experimental verification using temporally and spatially resolved near-field spectroscopy [4]. Moreover, we numerically demonstrate XOR- and AND-gate operations, using the dynamics of a three-QD system coupled via optical near fields that depends on the initial excitation as well as symmetry of the spatially arranged QDs [5].

We first outline the formulation of a near-field optical coupling between two nanometric quantum dots, using the multipolar QED Hamiltonian in the dipole approximation [6], $-\vec{\mu}\cdot\vec{D}$, where $\vec{\mu}$ and $\vec{D}$ represent the transition dipole moment and electric displacement field, respectively. It has the advantage that no explicit interdot Coulomb interactions are included in the interaction Hamiltonian and entire contribution to the fully retarded result originates from exchange of transverse photons. Basic ideas of the formulation are to express internal electronic structures in a QD in terms of a collection of local dipoles, and to investigate the interactions between nanometric QDs and spatially varying optical near fields, on the basis of the projection operator method [7].

When we assume Frenkel excitons, the excitonic states in a quantum dot specified by the quantum number m and μ can be expressed by superposition of excitons in the Wannier representation as [8]

$$|\phi_{m\mu}\rangle = \sum_{\vec{R},\vec{R}'} F_m\left(\vec{R}_{\mathrm{CM}}\right)\varphi_\mu\left(\vec{\beta}\right)\hat{c}^\dagger_{\mathrm{c}\vec{R}'}\hat{c}_{\mathrm{v}\vec{R}}|\phi_{\mathrm{g}}\rangle, \tag{1}$$

where $F_m\left(\vec{R}_{\mathrm{CM}}\right)$ and $\varphi_\mu\left(\vec{\beta}\right)$ denote the envelope functions for the center of mass (CM) and relative motions of excitons, respectively. Here $\vec{R}_{\mathrm{CM}}$ is the CM position, and $\vec{\beta}$ is defined as $\vec{\beta}=\vec{R}'-\vec{R}$ with the atomic sites $\left(\vec{R},\vec{R}'\right)$. The creation and annihilation operators of electrons at site $\vec{R}$ in the energy band $\mathrm{b}=(\mathrm{c},\mathrm{v})$ are $\hat{c}^\dagger_{\mathrm{b}\vec{R}}$ and $\hat{c}_{\mathrm{b}\vec{R}}$, respectively. According to Ref. [5], the near-field optical coupling strength $\hbar U'$ between two excitonic states $\left|\phi^{\mathrm{A}}_{m\mu}\right\rangle$ in QD-A and $\left|\phi^{\mathrm{C}}_{m'\mu'}\right\rangle$ in QD-C can be written in the lowest order as

$$\begin{aligned}\hbar U' = {} & \varphi^A_\mu(0)\varphi^{C*}_{\mu'}(0)\\ & \times\iint F^A_m\left(\vec{R}_A\right)F^{C*}_{m'}\left(\vec{R}_C\right)\\ & \times\left[Y_A\left(\vec{R}_A-\vec{R}_C\right)+Y_C\left(\vec{R}_A-\vec{R}_C\right)\right]\mathrm{d}\vec{R}_A\,\mathrm{d}\vec{R}_C,\end{aligned} \tag{2}$$

where the functions $Y_{\mathrm{A(C)}}\left(\vec{R}_{\mathrm{A}}-\vec{R}_{\mathrm{C}}\right)$ connect two spatially isolated envelope functions of the CM motions of excitons, and can be expressed as the sum of two Yukawa functions with short and long interaction ranges [5,7].

For later use, we give typical values of the coupling strength in Eq. (2), using a Z_3-exciton state of CuCl quantum cubes embedded in a NaCl matrix [9]. Calculation results are plotted in Fig. 1 as a function of the intercube distance. The solid curve represents the coupling strength between two dipole-active levels $m=m'=(1,1,1)$ of QDs with a width of 5 nm, while the dotted curve is the result for $m=(1,1,1)$ of QD with a width of 5 nm and $m'=(2,1,1)$ of QD with a width of 7 nm.For conventional far field light, $m'=(2,1,1)$ is the dipole-forbidden exciton level, but it is allowed via a near-field optical interaction that is schematically illustrated in the inset of Fig. 1. Alternatively, a propagating far field constructs a symmetric state from two resonant exciton levels of inter-QDs by global coupling, while an optical near field allows producing an antisymmetric state by its steep gradient field to excite either one of QDs

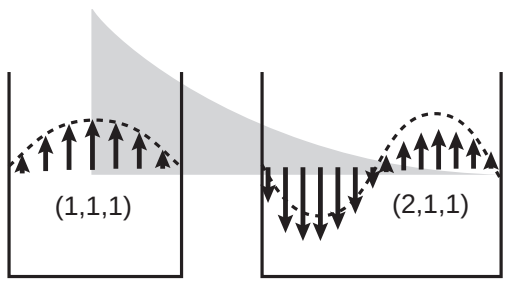

Fig. 1. Near-field optical coupling between two quantum cubes as a function of the intercube distance. Inset: schematic illustration of the QD-coupling via a gradient optical field.

individually. The antisymmetric coupling strength is estimated as $\hbar U' = 5.05\,\mu\text{eV}$ ($U'^{-1} = 130\,\text{ps}$) for intercube distance of 6.1 nm, which is approximately a quarter of the symmetric case at the same intercube distance.

Now we consider an antisymmetric coupling in a two-quantum dot system consisting of QD-A (two-level) and QD-C (three-level) in order to investigate exciton dynamics, especially a transient response from a steady state (see Fig. 2). Resonant exciton states (E_2-level) are coupled via near-field optical interaction $\hbar U_{\text{AC}} \equiv \hbar U'$, and note that this coupling is usually forbidden, as mentioned above. In addition, E_2-level in QD-A and E_1-level in QD-C are coupled with a free photon reservoir while E_2-level in QD-C is coupled with a phonon reservoir. Suppose that E_1-level in QD-C is, for simplicity, incoherently excited at $t = 0$ by pulse-laser photons with a rate of $A_{\text{p}}(t)$, after the system reaches a steady state by the weak continuous CW excitation of QD-A. Then the following terms

$$\alpha\left\{\left[\hat{A}\hat{\rho}(t),\ A^{\dagger}\right] + \left[A^{\dagger},\ \hat{\rho}(t)\hat{A}\right]\right\} + A_{\text{p}}(t)\left\{\left[\hat{C}_1\hat{\rho}(t),\ \hat{C}_1^{\dagger}\right] + \left[\hat{C}_1^{\dagger},\ \hat{\rho}(t)\hat{C}_1\right]\right\} \quad (3)$$

are added to the equations of motion analogous to Eq. (5), which will be discussed below. Here α is the rate of weak CW excitation of upper levels in QD-A than E_2-level to achieve a steady state, while the annihilation and creation operators of excitons are $\left(\hat{A}, \hat{A}^{\dagger}\right)$, $\left(\hat{C}_1, \hat{C}_1^{\dagger}\right)$, and the density operator is $\hat{\rho}(t)$. In the numerical calculation, we use the same parameters [9] as before, and restrict ourselves to the one- and two-exciton dynamics.

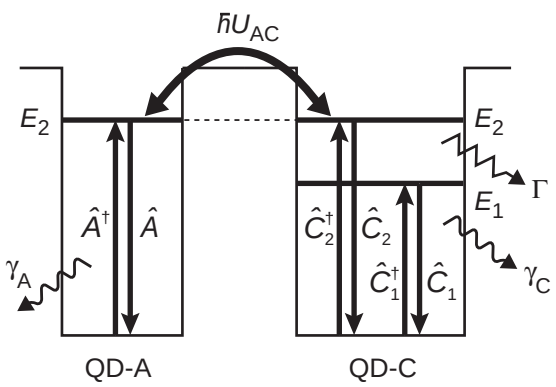

Fig. 2. Theoretical result on the transient exciton population in QD-A (solid curve) and experimental photoluminescence data (circles). The inset schematically depicts the system configuration.

Fig. 2 shows a theoretical result on the transient exciton population dynamics, together with experimental data on the temporally and spatially resolved near-field optical spectroscopy. The solid curve depicts the theoretical values, and the filled circles represent the experimental data. Here, we use $U'^{-1} = 130\,\text{ps}$ which was estimated above. The excitation rate by the pulse laser was set as $A_{\text{p}}(t)^{-1} = 1\,\text{ps}$, and the pulse width was assumed to be 10 ps, while the rate $\alpha^{-1} = 10\,\text{ns}$ was employed. The relaxation constants (γ_{A}, γ_{C}) due to e–h recombination in isolated QDs, and the nonradiative relaxation constant Γ due to the exciton-phonon coupling were set as $\gamma_{\text{A}}^{-1} = 5.9\,\text{ns}$, $\gamma_{\text{C}}^{-1} = 2.1\,\text{ns}$, and $\Gamma^{-1} = 20\,\text{ps}$, respectively.It follows from Fig. 2 that temporal evolution of exciton population in QD-A proportional to experimental photoluminescence exhibits a damped oscillation for a relatively long time. It is due to the nutation at E_2-levels of QD-A and QD-C that originates from the state-filling of E_1-level of QD-C by pulse-laser photons. The oscillation period in Fig. 2 is determined by the near-field optical coupling U'. The damping rate is governed by the radiative relaxation constant of QD-C, though the oscillation amplitude depends on that of QD-A to become larger as γ_{A} becomes smaller. Without taking quantum coherence into account, the calculated damping rate is twice as fast as the experimental one. Theoretical predictions are consistent with experimental data, which indicates the importance of quantum coherence between resonant energy levels in a QD system coupled via the near-field optical interaction.

Here we suppose a three-quantum dot system, as shown in Fig. 3, in order to apply the above discussion to logic and functional operations using a near-field optically coupled QD system. Two identical dots (QD-A and -B) are resonantly coupled with each other via an optical near field, while a three-level dot (QD-C) is loosely coupled with a pair of QD-A and -B, and serves as an

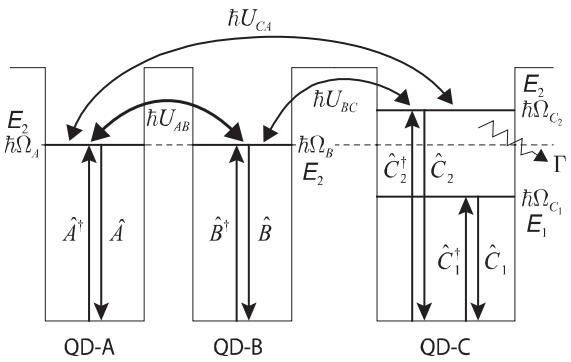

Fig. 3. Schematic drawing of a three-quantum dot system coupled via optical near fields.

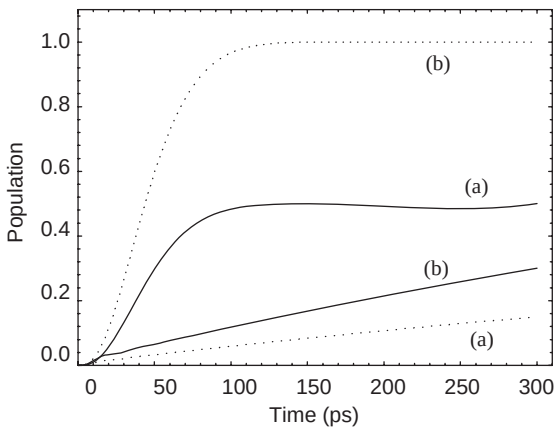

Fig. 4. Temporal evolution of output population in QD-C for $\Delta\Omega = U$ (solid curves) and $\Delta\Omega = -U$ (dotted curves). (a) QD-A is only populated, and (b) both QD-A and -B are populated. As the coupling strengths, $\hbar U = 89\,\mu\text{eV}$ (size:10 nm, intercube distance: 5 nm) and $\hbar U' = 14\,\mu\text{eV}$ (size: 10 and 14.1 nm, intercube distance: 15 nm) were used.

output part with a dissipation process. A model Hamiltonian for the system, $\hat{H}$, is given by

$$\hat{H} = \hat{H}_0 + \hat{H}_{\text{int}},$$
$$\hat{H}_0 = \hbar\Omega\left(\hat{A}^\dagger\hat{A} + \hat{B}^\dagger\hat{B}\right) + \hbar\sum_{i=1}^{2}\Omega_{C_i}\hat{C}_i^\dagger\hat{C}_i,$$
$$\hat{H}_{\text{int}} = \hbar U\left(\hat{A}^\dagger\hat{B} + \hat{B}^\dagger\hat{A}\right) + \hbar U'\left(\hat{A}^\dagger\hat{C}_2 + \hat{C}_2^\dagger\hat{A} + \hat{B}^\dagger\hat{C}_2 + \hat{C}_2^\dagger\hat{B}\right), \quad (4)$$

where the creation and annihilation operators of excitons, $\left(\hat{A}^\dagger, \hat{A}\right)$, $\left(\hat{B}^\dagger, \hat{B}\right)$, and $\left(\hat{C}_i^\dagger, \hat{C}_i\right)$, are illustrated in Fig. 3. The eigenfrequencies for the symmetric system are denoted by $\Omega_A = \Omega_B \equiv \Omega$, while the near-field optical couplings are designated by $U_{AB} \equiv U$ and $U_{BC} = U_{CA} \equiv U'$. Then the temporal evolution of the exciton occupation in the QD system, $\hat{\rho}(t)$, is described by the following master equation within the Born–Markov approximation [10] as

$$\dot{\hat{\rho}}(t) = \frac{1}{i\hbar}\left[\hat{H}, \hat{\rho}(t)\right] - \frac{\Gamma}{2}\left[\left\{\hat{C}_2^\dagger\hat{C}_1\hat{C}_1^\dagger\hat{C}_2, \hat{\rho}(t)\right\} - 2\hat{C}_1^\dagger\hat{C}_2\hat{\rho}(t)\hat{C}_2^\dagger\hat{C}_1\right]. \quad (5)$$

It follows from the system's symmetry that the symmetric and antisymmetric-state representation gives the smallest number of density-matrix elements for describing the dynamics [11]. The equations of motion for the density matrix, or the exciton dynamics can be classified by the number of excitons in the system, and the energy difference $\hbar\Delta\Omega$ from the upper level of QD-C to E_2-level of QD-A (or -B) oppositely contributes to the one- and two-exciton dynamics, respectively. It indicates that the resonance conditions for selective energy transfer in the one- and two-exciton states are given by $\Delta\Omega = U$ and $-U$, respectively, and that such energy transfers allow us to selectively pick up information about the initial exciton populations in a pair of QD-A and -B. The result can be utilized for logic operations in the system.

We show some numerical results for XOR- and AND-logic operations, solving Eq. (5) for the one-exciton and two-exciton dynamics in a CuCl quantum cube system. The solid and dotted curves in Fig. 4, respectively, show the temporal evolution of the output population in QD-C for $\Delta\Omega = U$ and $-U$. It shows that the system behaves as an XOR-like-logic gate when $\Delta\Omega = U$ while it behaves as an AND-logic gate when $\Delta\Omega = -U$. Since the equally populated antisymmetric state is decoupled from the symmetric-state dynamics, the population in the XOR only reaches a half of the maximum. In an asymmetrically arranged system,

however, it is no longer decoupled, nor has it no radiation within a lifetime of the state. This fact may be applied to a buffer memory, and it will be possible to access quantum entangled states if the initial excitation is appropriately prepared.

References

[1] N. Hosaka, T. Saiki, J. Microsc. 202 (2001) 362.
[2] K. Matsuda, T. Saiki, S. Nomura, M. Mihara, Y. Aoyagi, S. Nair, T. Takagahara, Phys. Rev. Lett. 91 (2003) 177401.
[3] M. Ohtsu, K. Kobayashi, T. Kawazoe, S. Sangu, T. Yatsui, IEEE J. Sel. Top. Quant. Electron. 8 (2002) 839.
[4] T. Kawazoe, K. Kobayashi, J. Lim, Y. Narita, M. Ohtsu, Phys. Rev. Lett. 88 (2002) 067404.
[5] S. Sangu, K. Kobayashi, A. Shojiguchi, M. Ohtsu, Phys. Rev. B 69 (2004) 115334.
[6] D.P. Craig, T. Thirunamachandran, Molecular Quantum Electrodynamics, Academic Press, London, 1984.
[7] K. Kobayashi, S. Sangu, H. Ito, M. Ohtsu, Phys. Rev. A 63 (2001) 013806.
[8] E. Hanamura, Phys. Rev. B 37 (1988) 1273.
[9] N. Sakakura, Y. Masumoto, Phys. Rev. B 56 (1997) 4051.
[10] H.J. Carmichael, Statistical Methods in Quantum Optics 1, Springer, Berlin, Heidelberg, 1999.
[11] B. Coffey, Phys. Rev. A 17 (1978) 1033.

Available online at www.sciencedirect.com
SCIENCE DIRECT®
Journal of Luminescence 114 (2005) 315–316
JOURNAL OF LUMINESCENCE
www.elsevier.com/locate/jlumin

Erratum

Erratum to: "Exciton dynamics and logic operations in a near-field optically coupled quantum-dot system" [J. Lumin. 112 (2005) 117]

K. Kobayashi[a,*,1], S. Sangu[b], T. Kawazoe[a], M. Ohtsu[a,c]

[a]*Japan Science and Technology Agency, 687-1 Tsuruma, Machida, Tokyo 194-0004, Japan*
[b]*Research and Development Center, Ricoh Company Limited, 16-1 Shinei-cho, Tsuzuki-ku, Yokohama, Kanagawa 224-0035, Japan*
[c]*Department of Electronics Engineering, University of Tokyo, 7-3-1 Hongo, Bunkyo-ku, Tokyo 133-8656, Japan*

Received 1 May 2005

Available online 1 July 2005

The Publisher apologizes that Figs. 1 and 2 were reproduced incorrectly. The correct figures are given below.

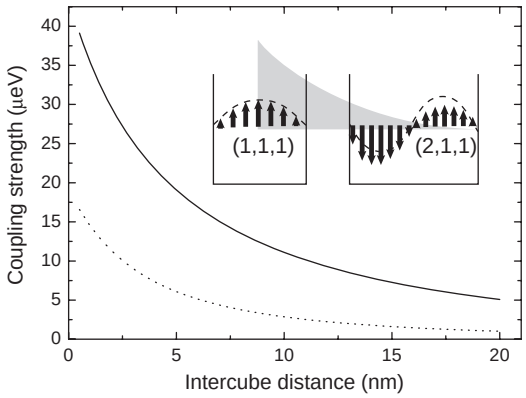

Fig. 1. Near-field optical coupling between two quantum cubes as a function of intercube distance. Inset: schematic illustration of the QD-coupling via a gradient optical field.

DOI of original article: 10.1016/j.jlumin.2004.09.008
*Corresponding author. Tel./fax: +81 3 5734 2136.
E-mail address: kkoba@phys.titech.ac.jp (K. Kobayashi).
[1]Present address: Department of Physics, Tokyo Institute of Technology, (H79) 2-12-1 O-okayama, Meguro-ku, Tokyo 152-8551, Japan.

doi:10.1016/j.jlumin.2005.05.007

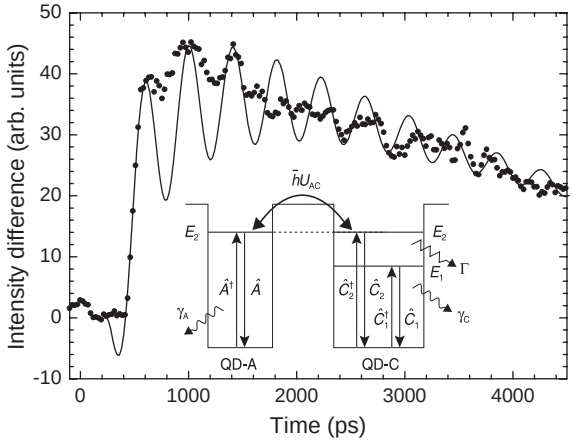

Fig. 2. Theoretical result on the transient exciton population dynamics (solid curve) and experimental photoluminescence data (circles). The inset schematically depicts the system configuration.

7 MARCH 2005
Volume 86 Number 10

APPLIED PHYSICS LETTERS

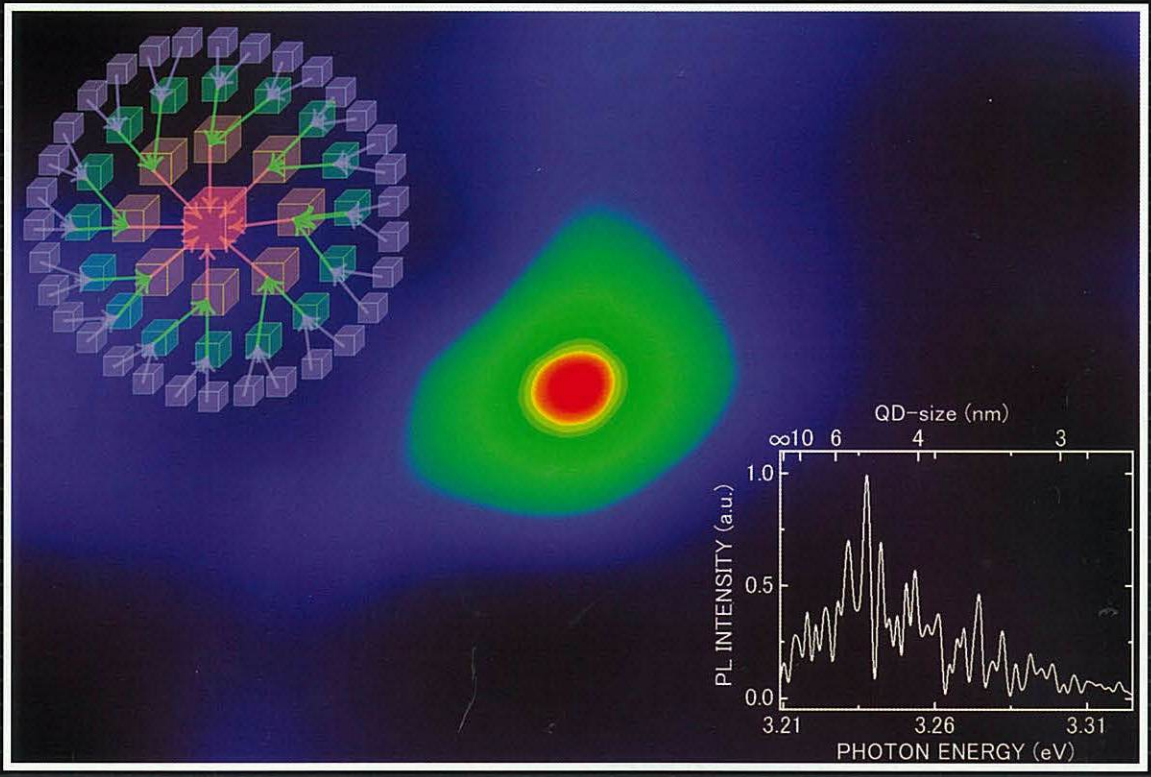

0003-6951(20050307)86:10;1-U

Available online–
See apl.aip.org

AMERICAN INSTITUTE OF PHYSICS

Optical nanofountain: A biomimetic device that concentrates optical energy in a nanometric region

Tadashi Kawazoe[a)] and Kiyoshi Kobayashi[b)]
SORST, Japan Science and Technology Agency, 687-1 Tsuruma, Machida, Tokyo 194-0004, Japan

Motoichi Ohtsu[c)]
Interdisciplinary Graduate School of Science and Engineering, Tokyo Institute of Technology, 4259 Nagatsuta, Midori-ku, Yokohama 226-8502, Japan

(Received 4 June 2004; accepted 11 January 2005; published online 28 February 2005)

We have proposed and demonstrated a nanophotonic device, which concentrates optical energy in a nanometric region. We call this device an "*optical nanofountain*," which uses the energy transfer among quantum dots and acts like a light-harvesting photosynthetic system. We experimentally concentrated optical energy in a nanometric area less than 20 nm by using the optical nanofountain which was composed of CuCl quantum dots embedded in a NaCl matrix. Its focal diameter of 20 nm corresponds to the numerical aperture of 12. © *2005 American Institute of Physics*.
[DOI: 10.1063/1.1875734]

Optical fiber communication systems are the key to data transmission between central processing units or other electronic devices owing to their large capacity and high speed. Currently, it is difficult to integrate optical devices with electronic devices to support such systems, owing to the diffraction limit of light. That is, optical devices cannot be smaller than the wavelength of light, while electronic devices, such as switches, logic gates, and memories, are already less than 100 nm in size. In order to exceed this limit, we have proposed nanophotonic devices[1] and demonstrated the operation of a nanophotonic switch less than 20 nm in size based on the optical near-field energy transfer among quantum dots (QDs).[2,3] Although the internal efficiency of nanophotonic devices is very high,[2,4] for efficient operation of the system an interconnection device needs to be developed to collect the incident propagating light and drive the nanophotonic device.[1,5] Conventional far-field optical devices, such as convex lenses and concave mirrors, cannot be used for this interconnection because of their diffraction-limited operation. In this letter, we propose and demonstrate an optical device that we call an "*optical nanofountain*," which concentrates optical energy in a nanometric region by using optical near-field energy transfer among QDs. This nanometric optical device enables not only highly efficient interconnection to nanophotonic devices but also other nanometric optical operations and measurements, e.g., nanometric optical tweezers, highly sensitive nanometric resolution microscopes, and so on.

The energy transfer from smaller to larger QDs have been studied by the spectrally, spatially, and time resolved experiment. Kagan *et al.*[6] observed the energy transfer among CdSe QDs coupled by dipole-dipole interdot interaction. We proposed the model for the unidirectional resonant energy transfer between QDs via optical near-field interaction and observed the energy transfer among randomly dispersed CuCl QDs using the optical near-field spectrometer. The theoretical analysis and time evolution of the energy transfer via optical near-field interaction were also discussed.[7,8] Crooker *et al.*[9] studied the dynamics of exciton energy transfer in close-packed assemblies of monodisperse and mixed-size CdSe nanocrystal QDs, and reported the energy-dependent transfer rate of excitons from smaller to larger dots.[9]

As we and other research groups mentioned,[3,9] the principle of the energy transfer among QDs is equivalent to that of the light-harvesting photosynthetic system, which skillfully concentrates and harvests optical energy in nanometric photosynthetic systems. The photosynthetic purple bacteria *Rhodopseudomonas acidophila* (Refs. 10 and 11) has two light-harvesting antennae: LH1 and LH2. LH1 contains a 32-bacteriochlorophyll (BChl) ring, and LH2 contains a B800 ring with 9 BChls and a B850 ring with 18 BChls. They harvest photons and efficiently transfer the excitation energy from B800 to LH1, where the excitonic energy of B800 is higher than that of LH1. This unidirectional energy transfer is due to the nanometric dipole-dipole interaction, i.e., an optical near-field interaction,[12] among BChl rings with low energy dissipation.[13] The optical energy concentrator *optical nanofountain*, which we propose, operates in the same manner as the light harvesting system in the photosynthetic bacteria.

The optical nanofountain is operated using this energy transfer, as shown in Fig. 1(a), together with the energy transfer between QDs via an optical near-field interaction.[3,7,8] When closely spaced QDs with quantized energy levels resonate with each other, near-field energy transfer occurs between them. Assuming that an effective size ratio between closely located QD-A and QD-B is $1:\sqrt{2}$, the quantized energy levels (1,1,1) in QD-A and (2,1,1) in QD-B resonate with each other, so that almost all of the excitation energy in QD-A is transferred to the (1,1,1) level in QD-B via near-field energy transfer and successive intersublevel relaxation.[14] This unidirectional energy transfer from smaller to larger QDs concentrates the optical energy in a nanometric region in a biomimetic manner. When different sized QDs with resonant energy sublevels are distributed as shown in

[a)]Electronic mail: kawazoe@ohtsu.jst.go.jp
[b)]Current affiliation: Department of Physics, Tokyo Institute of Technology, 2-12-1 Ookayama, Meguro-ku, Tokyo 152-8551, Japan.
[c)]Also at: SORST, Japan Science and Technology Agency, 687-1 Tsuruma, Machida, Tokyo 194-0004, Japan.

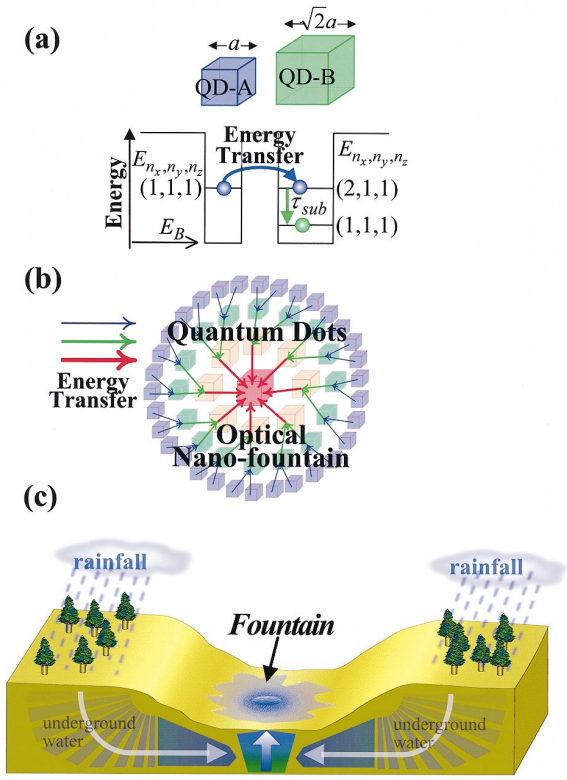

FIG. 1. (Color) (a) Schematic explanation of the energy transfer between QDs via an optical near-field interaction. E_{nx}, E_{ny}, E_{nz} $(n_x,n_y,n_z)=(1,1,1)$ or (2,1,1) is the quantum number representing the excitonic energy level in a QD. (b) Schematic explanation of the optical nanofountain and unidirectional energy transfer. (c) Schematic drawing of a fountain in a basin.

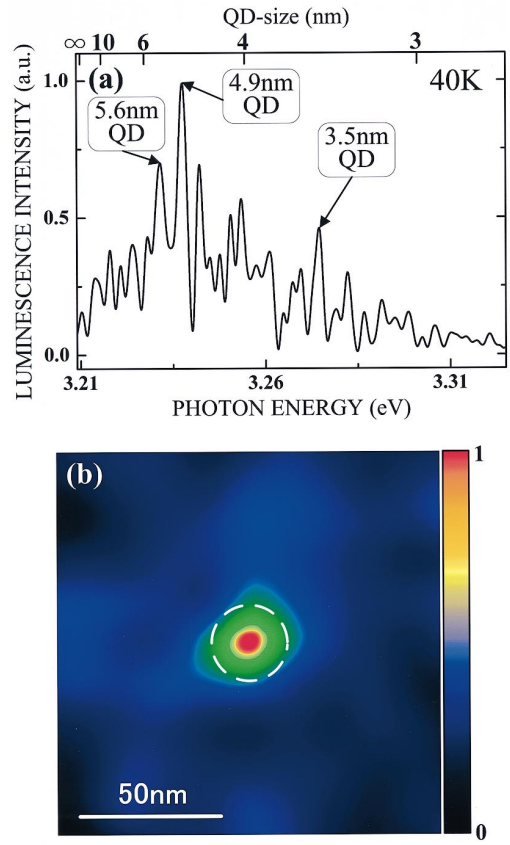

FIG. 2. (Color) (a) Near-field luminescence spectrum of CuCl QDs at 40 K. The relationship between the photon energy of luminescence and the size of the QDs is shown above and below the horizontal axes. (b) Spatial distribution of the luminescence intensity in an optical nanofountain. The bright spot surrounded by a broken circle is the focal spot.

Fig. 1(b), energy transfer occurs via the optical near field, as illustrated by the arrows. Light incident to the QD array is ultimately concentrated in the largest QD. The size of the area of light concentration corresponds to that of the QD. Therefore, this device realizes nanometric optical concentration. Since the mechanism of the optical nanofountain is similar to that of the light-trapping system in photosynthetic bacteria, the operation of the optical nanofountain is a biomimetic action. The device proposed here is called an optical nanofountain because light spurts from the largest QD after it is concentrated by stepwise energy transfer from smaller neighboring QDs. In action, the device looks like a fountain in a basin, as shown schematically in Fig. 1(c). From previous experimental tests of nanophotonic switch operation,[2,4] it is expected that the concentration efficiency of this device will be close to 1 because there are no other possible relaxation paths in the nanometric system.

To demonstrate the operation of an optical nanofountain, we used CuCl cubic QDs embedded in a NaCl matrix with an average QD size of 4.2 nm and an average separation of less than 20 nm.[15] Although, the QDs have an inhomogeneous size distribution and are randomly arranged in the matrix, the operation can be confirmed if an appropriate QD group is found using nanometric resolution luminescence spectrometer, i.e., near-field spectrometer. For the operation, we maintained a sample at the optimum temperature T(40 K). At $T<40$ K, the resonant condition becomes tight due to narrowing of the homogeneous linewidth of the quantized energy sublevels, while at $T>40$ K, the unidirectional energy transfer is obstructed by the thermal activation of excitons in the QDs. A 325 nm He–Cd laser was used as the excitation light source. A double-tapered UV fiber probe with an aperture 20 nm in diameter was fabricated using chemical etching and coated with a 150 nm thick Al film to ensure sufficiently high detection sensitivity.[16] Figure 2(a) shows a

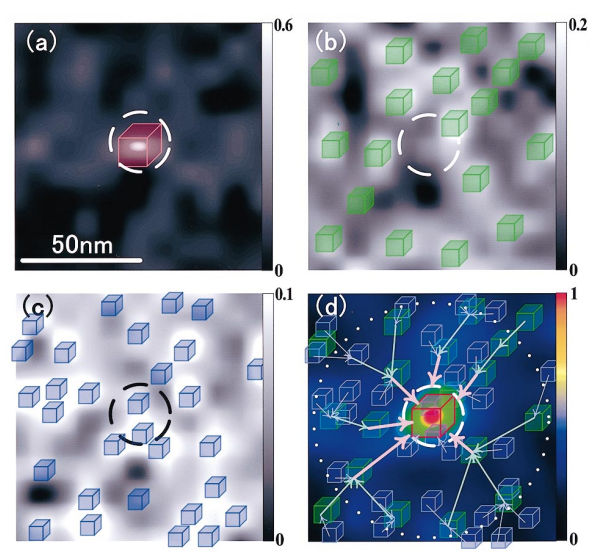

FIG. 3. (Color) Spatial distribution of the luminescence intensity of CuCl QDs of: (a) 6 nm$\leqslant L\leqslant$10 nm (3.215 eV$\leqslant E_p\leqslant$3.227 eV), (b) 4 nm$\leqslant L\leqslant$6 nm (3.227 eV$\leqslant E_p\leqslant$3.254 eV), (c) 2.5 nm$\leqslant L\leqslant$4 nm (3.254 eV$\leqslant E_p\leqslant$3.350 eV), and (d) the total for 2.5 nm$\leqslant L\leqslant$10 nm (3.215 eV$\leqslant E_p\leqslant$3.350 eV) for the same area as in Fig. 2(b). The cubes represent the positions estimated from the luminescence intensity distribution.

typical near-field luminescence spectrum of the sample in the correction-mode operation.[17] It is inhomogeneously broadened due to the quantum size effect and the size distribution of the QDs. We have never observed luminescence of the exciton molecules due to the low excitation density of less than $1\ \mathrm{W/cm^2}$. The spectral curve includes several fine peaks, which are the luminescence that comes from different sized QDs. Since we can obtain the size-selective QD position from the spatial distribution of the luminescence peak intensity, the two-dimensional scanning measurement of the luminescence intensity collected by the photon energy allows us to search for QDs acting as optical nanofountains. At 40 K, it is not so difficult to find the QD array acting as an optical nanofountain. We found about one optical nanofountain in the $5\times 5\ \mu\mathrm{m}^2$ region on the sample surface experimentally.

Figure 2(b) shows the typically spatial distribution of the luminescence emitted from QDs that operates well as an optical nanofountain. Here, the collected luminescence photon energy, E_p, was $3.215\ \mathrm{eV} \leqslant E_p \leqslant 3.350\ \mathrm{eV}$, which corresponded to the luminescence from QDs of size $2.5\ \mathrm{nm} \leqslant L \leqslant 10\ \mathrm{nm}$. The bright spot inside the broken circle corresponds to a spurt from an optical nanofountain, i.e., the focal spot of the nanometric optical condensing device. The diameter of the focal spot was less than 20 nm, which was limited by the spatial resolution of the near-field spectrometer. From the Rayleigh criterion (i.e., resolution$=0.61\cdot\lambda/\mathrm{NA}$),[18] we obtained its numerical aperture (NA) of 12 for $\lambda=385$ nm.

To demonstrate the detailed operating mechanism of the optical nanofountain, we show the size-selective luminescence intensity distribution, i.e., by photon energy, in Figs. 3(a)–3(c). The broken circles and the areas scanned by the probe are equivalent to that in Fig. 2(b). The luminescence intensity distribution is displayed using a grey scale, whose normalized scales are 0–0.6, 0–0.2, 0–0.1, and 0–1 for Figs. 3(a)–3(d), respectively. Cubes represent QDs whose positions were estimated from the luminescence intensity distribution. In Fig. 3(a), a single QD of $6\ \mathrm{nm} \leqslant L \leqslant 10\ \mathrm{nm}$ was observed at the focal position. In Figs. 3(b) and 3(c), the observed QDs are $4\ \mathrm{nm} \leqslant L \leqslant 6\ \mathrm{nm}$ and $2.5\ \mathrm{nm} \leqslant L \leqslant 4\ \mathrm{nm}$, respectively, and are located around the broken circles. Figure 3(d) shows the total luminescence intensity distribution obtained as the integral of Figs. 3(a)–3(c). The bright spot in this figure agrees with the position of the largest QD in Fig. 3(a) and the smaller QDs are distributed around it. This means that the optical energy is concentrated to the largest QD. The luminescence intensity at the bright spot is more than five times greater than that from a single isolated QD of $L=10$ nm. While the luminescence intensities of the smaller surrounding QDs are lower than those of the isolated QDs. This indicates that optical energy is transferred from smaller to larger QDs and is concentrated in the largest QD, as shown by arrows in Fig. 3(d). This device can also be used as a frequency selector, based on the resonant frequency of the QDs, which can be applied to frequency domain measurements, multiple optical memories, multiple optical signal processing, frequency division multiplexing, and so on.

In summary, we propose a nanophotonic device, the optical nanofountain, which uses energy transfer among QDs, and demonstrated its operation using CuCl QDs embedded in a NaCl matrix. This device concentrated the optical field energy and focused it within a 20 nm spot.

[1] M. Ohtsu, K. Kobayashi, T. Kawazoe, S. Sangu, and T. Yatsui, IEEE J. Sel. Top. Quantum Electron. **8**, 839 (2002).
[2] T. Kawazoe, K. Kobayashi, S. Sangu, and M. Ohtsu, Appl. Phys. Lett. **82**, 2957 (2003).
[3] T. Kawazoe, K. Kobayashi, J. Lim, Y. Narita, and M. Ohtsu, Phys. Rev. Lett. **88**, 067404 (2002).
[4] T. Kawazoe, K. Kobayashi, S. Sangu, and M. Ohtsu, J. Microsc. **209**, 261 (2003).
[5] M. N. Islam, X. K. Zhao, A. A. Said, S. S. Mickel, and C. F. Vail, Appl. Phys. Lett. **71**, 2886 (1997).
[6] C. R. Kagan, C. B. Murray, M. Nirmal, and M. G. Bawendi, Phys. Rev. Lett. **76**, 1517 (1996).
[7] S. Sangu, K. Kobayashi, A. Shojiguchi, T. Kawazoe, and M. Ohtsu, J. Appl. Phys. **93**, 2937 (2003).
[8] K. Kobayashi, S. Sangu, T. Kawazoe, and M. Ohtsu, J. Lumin. (to be published).
[9] S. A. Crooker, J. A. Hollingsworth, S. Tretiak, and V. I. Klimov, Phys. Rev. Lett. **89**, 186802 (2002).
[10] G. McDermott, S. M. Prince, A. A. Freer, A. M. Hawthornthwaite-Lawless, M. Z. Papiz, R. J. Cogdell, and N. W. Isaacs, Nature (London) **374**, 517 (1995).
[11] P. Jordan, P. Fromme, H. T. Witt, O. Klukas, W. Saenger, and N. Krauss, Nature (London) **411**, 909 (2001).
[12] K. Kobayashi, S. Sangu, H. Ito, and M. Ohtsu, Phys. Rev. A **63**, 013806 (2001).
[13] K. Mukai, S. Abe, and H. Sumi, J. Phys. Chem. B **103**, 6096 (1999).
[14] T. Suzuki, T. Mitsuyu, K. Nishi, H. Ohyama, T. Tomimasu, S. Noda, T. Asano, and A. Sasaki, Appl. Phys. Lett. **69**, 4136 (1996).
[15] N. Sakakura and Y. Masumoto, Phys. Rev. B **56**, 4051 (1997).
[16] T. Saiki, S. Mononobe, M. Ohtsu, N. Saito, and J. Kusano, Appl. Phys. Lett. **68**, 2612 (1996).
[17] *Near-Field Nano/Atom Optics and Technology*, edited by M. Ohtsu (Springer, Tokyo, 1998).
[18] M. Born and E. Wolf, *Principles of Optics*, 6th Ed. (Pergamon, Oxford, 1983).

e-J. Surf. Sci. Nanotech. Vol. 3 (2005) 74-78 Conference - Nano-org. & Func. -

Anti-parallel coupling of Quantum Dots with an Optical Near-Field Interaction*

Tadashi Kawazoe†
Solution Oriented Research for Science and Technology (SORST), Japan Science and Technology Agency (JST), 687-1 Tsuruma, Machida, 194-0004, Japan

Kiyoshi Kobayashi
Department of Physics, Tokyo Institute of Technology 2-12-1 O-okayama, Meguro-ku, Tokyo 152-8551, Japan

Motoichi Ohtsu
Department of Electronics Engineering, University of Tokyo 7-3-1 Hongo, Bunkyo-ku, Tokyo 113-8656, Japan
(Received 2 November 2004; Accepted 29 January 2005; Published 1 March 2005)

We report the direct observation of optically forbidden energy transfer between cubic CuCl quantum dots via an optical near-field interaction using time-resolved near-field photoluminescence (PL) spectroscopy. The energy transfer time and exciton lifetime were estimated from the rise and decay times of the PL pump-probe signal, respectively. We found that the exciton lifetime increased as the energy transfer time fell, which strongly supports the notion that near-field interaction between QD makes the anti-parallel dipole coupling. Namely, a quantum-dots pair coupled by an optical near field has a long exciton lifetime and optically forbidden features due to its anti-parallel electric dipole pair. [DOI: 10.1380/ejssnt.2005.74]

Keywords: Photoluminescence; Nano-scale imaging, measurement, and manipulation technology; Alkali halides; Nano-particles, quantum dots, and supra-molecules; Coupled quantum dots

I. INTRODUCTION

The unique optical properties of a quantum dot (QD) system, *i.e.*, the quantum size effect that originates from the electronic state in QDs, are of major research interest. A coupled QD system has more properties that are unique than a single QD system, including the Kondo effect [1, 2], Coulomb blockade [3], spin interaction [4], and so on. Furthermore, it is possible to control the coupling strength of QDs by using the optical near-field interaction, and to realize unique optical device operation. Recently, we observed an optically forbidden energy transfer between neighboring cubic CuCl QDs via an optical near field [5]. The breaking of the dipole selection rule in the nanometric region has been discussed theoretically [6]. It is based on the fact that the point dipole description of a QD is not suitable for the system that the dots approach each other in a nanometric region. The magnitude of this nanometric dipole-dipole interaction, *i.e.*, the optical near-field interaction, can be estimated by measuring the energy transfer time [7].

The energy transfer between QDs is not only of physical interest, but is also applicable to the novel technology of nanophotonics [8]. We have proposed and demonstrated a nanometric all-optical switch using an optical near field, *i.e.*, the nanophotonic switch [9, 10]. Since the switching time depends strongly on the energy transfer time, observations of the energy transfer time are important for designing nanophotonic switches, and for understanding the phenomenon of energy transfer via an optical near field. It is also important to measure the lifetime of the excitons in a coupled QD pair, because the optical near-field interaction influences the exciton lifetime, and the repetitive switching speed depends on the exciton lifetime [7].

For a coupled QD system, the carrier lifetime is expected to differ from that of an isolated QD. Figure 1 shows schematic drawings of the typical states of coupled QDs. When their electric dipoles are parallel, the carrier lifetime decreases due to the increase in the total oscillator strength, *i.e.*, Dicke's superradiance [11], as shown in Fig.1 (a). Conversely, when their electric dipoles are anti-parallel, their carrier lifetime increases, because the total oscillator strength decreases, and they ultimately become optically forbidden, as shown in Fig.1 (b).

In this letter, we report the observed energy transfer time from the exciton state in a CuCl QD to the optically forbidden exciton state in another CuCl QD, using time-resolved optical near-field spectroscopy. We also show the nature of the anti-parallel dipole-coupling feature of the optical near-field interaction experimentally.

II. EXPERIMENTAL

Cubic CuCl QDs, *i.e.*, quantum cubes (QCs), embedded in NaCl are suitable for studying the optical near-field interaction, because the possibility of energy transfer due to carrier tunneling and Coulomb coupling can be neglected, since the potential depth exceeds 4 eV and the binding energy of exciton is more than 200 meV with its Bohr radius of 0.68 nm [12]. We fabricated CuCl QCs embedded in a NaCl matrix using the Bridgman method and successive annealing, and found that the average size of the QCs was $L = 4.2$ nm [13]. A 325-nm CW He-Cd laser and 385-nm SHG of CW and mode-locked Ti-sapphire lasers (repetition rate: 80MHz) were used as the light sources. To achieve the selective excitation of the discrete energy levels in the QCs, the duration of the transform-limited pulse of the mode-locked laser was set at 10 ps. A double-tapered fiber probe with a 150-nm aluminum coating and a 40-nm diameter aperture was fabricated by chemical etching and the pounding method [14, 15]. After

*This paper was presented at International Symposium on Nano-organization and Function, Tokyo, Japan, 11-12 November, 2004.
†Corresponding author: kawazoe@ohtsu.jst.go.jp

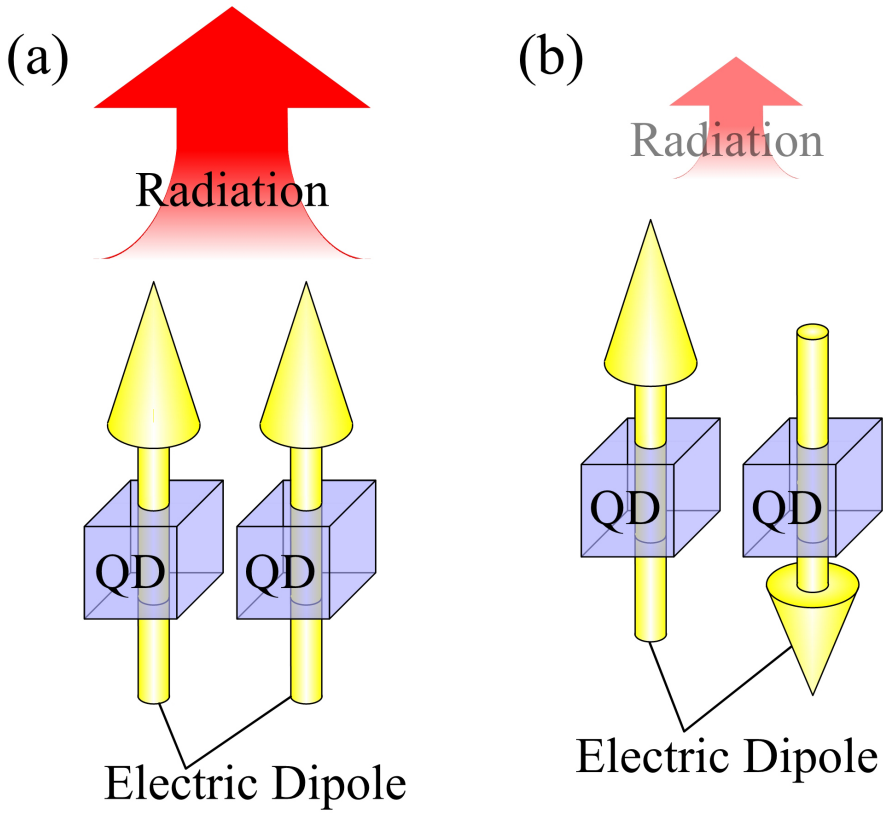

FIG. 1: Schematic drawing of a quantum dot (QD) pair and its electric dipoles. (a) The electric dipoles are parallel to each other, *i.e.*, the superradiant state. (b) The dipoles are anti-parallel, *i.e.*, the dipole forbidden state.

the QC pairs in the inhomogeneous size-dispersed sample were found using an optical near-field microscope, the temporal evolution of the photoluminescence (PL) pump-probe signal was detected using the time correlation single photon counting method with a 15-ps time resolution.

III. RESULTS AND DISCUSSIONS

Figures 2(a) and (b) show the near-field PL spectrum of the sample and the spatial distribution of the luminescence intensity from a 6.3-nm QC at 15 K, respectively, with the 325-nm CW probe light only, which excited the band-to-band transition in the sample. The inset in Fig. 2(b) shows the energy transfer between the observed QCs, *i.e.*, from 4.6- to 6.3-nm QCs, where τ_i, τ_{sub}, and τ_{ex} are the energy transfer time, inter-sub-level transition time, and exciton lifetime, respectively. The energy eigenvalues for the quantized Z_3 exciton energy level in a CuCl QC with side length of L are given by $E_{n_x,n_y,n_z} = E_B + \hbar^2\pi^2(n_x^2+n_y^2+n_z^2)/2M(L-a_B)^2$, where E_B is the bulk Z_3 exciton energy, M is the translational mass of the exciton, a_B is its Bohr radius, n_x, n_y, and n_z are quantum numbers (n_x, n_y, n_z=1, 2, 3,...), and $d = (L - a_B)$ corresponds to the effective side length found after considering the dead layer correction [16]. There was resonance between the quantized exciton energy level of quantum number (1,1,1) in the 4.6-nm QCs and the quantized exciton energy level of quantum number (2,1,1) in the 6.3-nm QCs. Note that the transition, induced by the propagating light, between ground state to (2,1,1) excited state is dipole-forbidden. However, optical near-field energy transfer is allowed with the coupling energy represented by the following Yukawa function: $V(r) = A\exp(-\mu \cdot r)/r$ [17, 18]. Here, r is the separation between the two QCs, A is the coupling coefficient, and μ is the inverse decay length of the Yukawa function, which correspond to the effective mass of our published effective interaction theory [17, 18]. For the $L = 4.6$- and 6.3-nm QC pair with 10-nm separation, the estimated τ_i is 50 ps, which is much shorter than τ_{ex}, which is a few ns. Since τ_{sub} is generally less than a few ps and is much shorter than τ_i [19], luminescence of a 4.6-nm QC decreases due to competitive inhibition and that of a 6.3-nm QCs increases due to the supply of the excitation energy from the neighboring 4.6-nm QC. As a result, the PL signal from the 6.3-nm QC was observed as the spectral peak indicated by the arrow in Fig. 2(a).

Figures 3(a) and (b) show the differential PL spectrum and the spatial distribution of the luminescence intensity from the 4.6-nm QC at 15 K, respectively taken with the 325-nm CW probe light and the 385-nm 10-ps pump pulse. Here, the differential PL spectral intensity is defined as (the PL spectrum with pump and probe light)-(the PL spectrum with the probe light only)- (the PL spectrum with the pump light only). The upward pointing arrow shows the photon energy of the pump pulse tuned to the (1,1,1) exciton energy level in the 6.3-nm QC. The inset in Fig. 3(b) shows the energy transfer between the QCs when the pump pulse excites the 6.3-nm QC. In this case, because the exciton energy in the 4.6-nm QC cannot be transferred to the (1,1,1) exciton

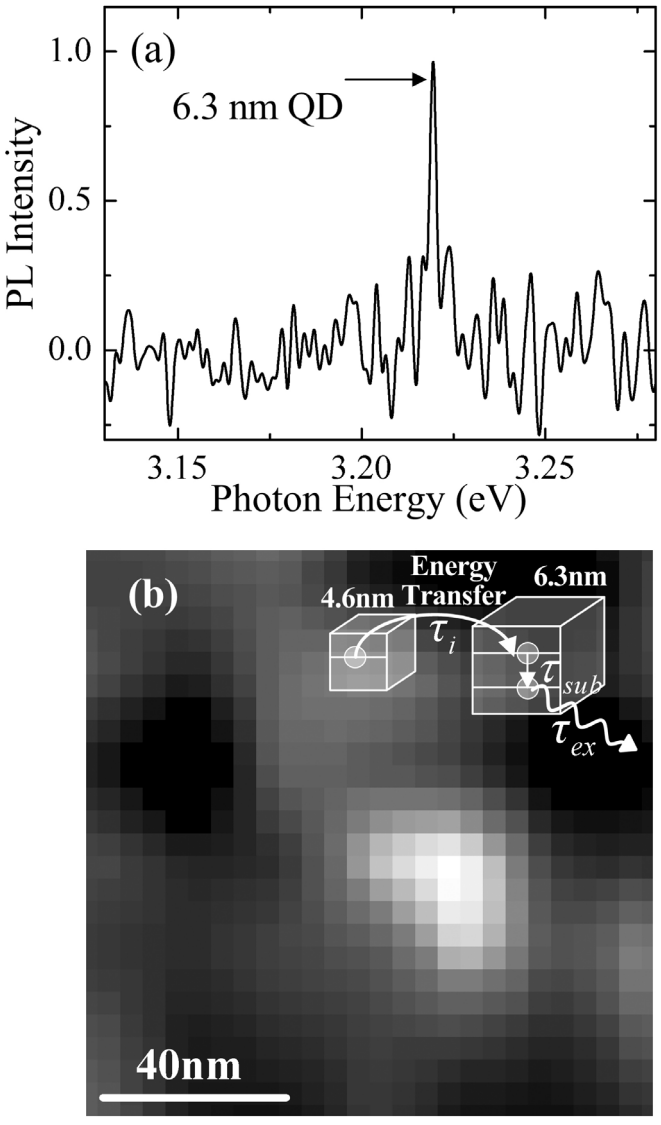

FIG. 2: (a) The near-field PL spectrum. (b) The spatial distribution of the luminescence intensity from the 6.3-nm QC (luminescence peak in (a)) with the 325-nm CW probe light only. The inset shows the observed QC pair and the energy flow.

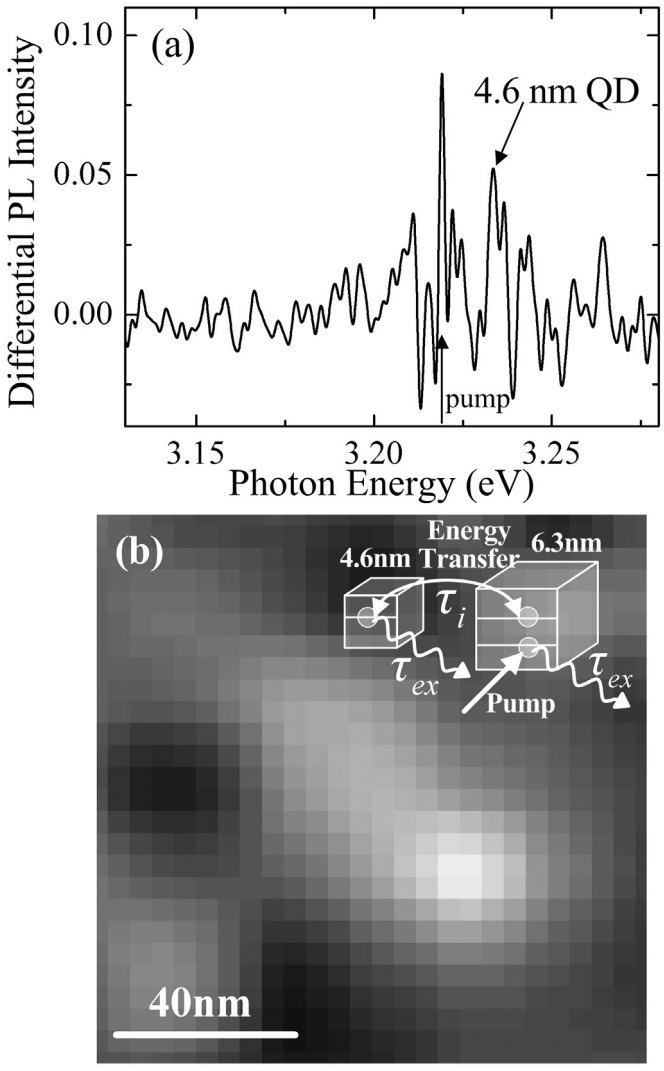

FIG. 3: (a) The differential PL spectrum. (b) The spatial distribution of the luminescence intensity from the 4.6-nm QC with the 325-nm CW probe light and the 385-nm 10-ps pump pulse. Here we used the narrow band-pass filter (FWHM:8 meV), whose optical density in the stop-band is more than 6. The inset shows the observed QC pair and the energy flow.

energy level in the 6.3-nm QC due to the state filling effect, the exciton energy flows back and forth between the (1,1,1) exciton energy level in the 4.6-nm QC and (2,1,1) exciton energy level in the 6.3-nm QC[20, 21], and some excitons recombine in the 4.6-nm QC. Therefore, the PL signal from the 4.6-nm QC was detected as the spectral peak indicated by the arrow in Fig. 3(a). The temporal evolution of this PL signal strongly depends on the τ_i and τ_{ex} of the coupled QC system.

Figures 4(a) and (b) show the temporal evolution of the PL peak intensity from 4.6-nm QCs on different time scales: (a) from −70 ps to 350 ps, (b) from −400 ps to 4000 ps. The open squares (P1), circles (P2), and triangles (P3) correspond to the experimental results observed for three different 4.6- and 6.3-nm QC pairs. In Fig. 4(a), the longitudinal axis has a linear scale. The solid, broken, and dotted curves are fitted to the experimental values using the rate equation, which is given by

$$\begin{aligned} \frac{dI_{4.6}}{dt} &= I_0 - \frac{I_{4.6}}{\tau_i} - \frac{I_{4.6}}{\tau_{ex\_4.6}} + \frac{I_{6.3}}{\tau_i} + I_{probe}, \\ \frac{dI_{6.3}}{dt} &= I_0 - \frac{I_{6.3}}{\tau_i} - \frac{I_{6.3}}{\tau_{ex\_6.3}} + \frac{I_{4.6}}{\tau_i} + I_{probe}. \end{aligned} \quad (1)$$

Here, $I_{4.6}$ and $I_{6.3}$ are the exciton populations in the 4.6- and 6.3-nm QCs, respectively and I_0 and I_{probe} are the *a priori* population and the exciton population created by the probe laser. The exciton population in the 6.3-nm QC is increased due to the pump pulse at $t = 0$. The exciton population in the 4.6-nm QC is also increased due to the prohibited energy transfer to the 6.3-nm QC with the filling effect. This increase in the exciton population of the 4.6-nm QC corresponds to the increase in the PL intensity from the 4.6-nm QC. The rise-time of the PL intensity from the 4.6-nm QC strongly depends on the energy transfer time τ_i. The energy transfer times

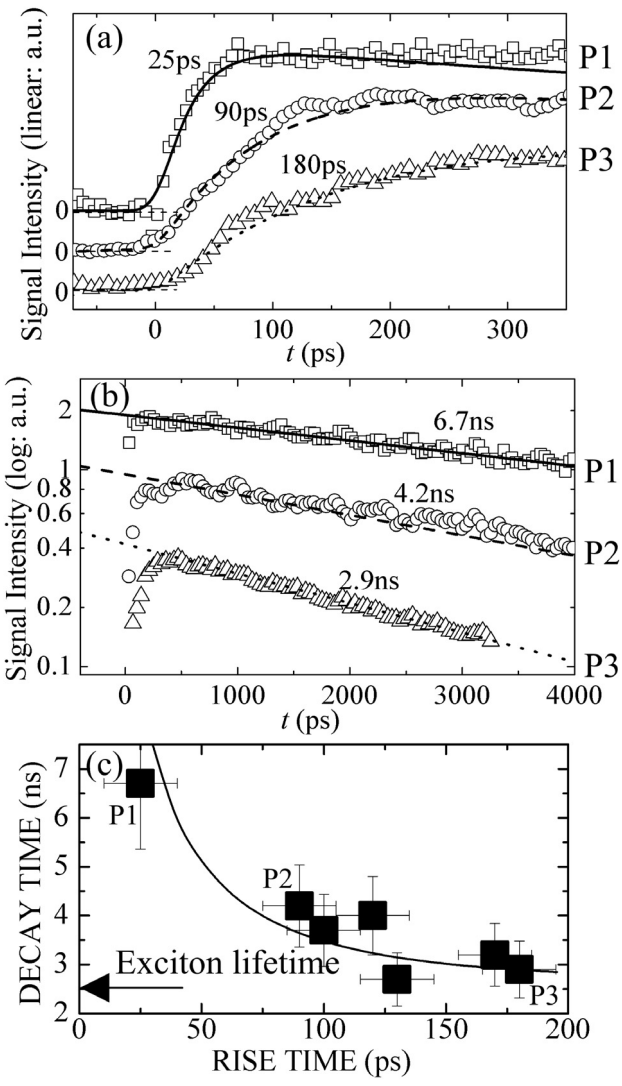

FIG. 4: Time evolutions of the PL peak signal intensity in Fig. 3(a) observed at different positions in the sample, *i.e.*, different QC pairs, (P1:□, P2:○, and P3:△). (a) Evolution in the range -70 ps $\leq t \leq 350$ ps with a linear longitudinal axis. (b) Evolution in the range -400 ps $\leq t \leq 4000$ ps with a logarithmic longitudinal axis. (c) Relationship between the energy transfer and decay times for the PL pump-probe signal. Closed squares show the experimental results, which were fitted using the solid curve.

(τ_i) for P1, P2, and P3 were estimated from the fitting curves to be 25, 90, and 180 ps, respectively, as shown in Fig. 4(a). This is the first direct measurement of the energy transfer time between QDs, and the values agree with the values estimated using our proposed near-field interaction theory [18]. In addition, when we consider scaling by $1/r^3$ (dipole-dipole interaction) or e^{-r}/r (near-field interaction), these estimated values are reasonable as compared with the theoretical energy transfer time of 0.8 ps obtained in the light-harvesting antenna complex of photosynthetic purple bacteria [6], whose system is about one fifth the size of the CuCl QC system. Differences in the rise times of P1, P2, and P3 are attributed to the differences in the separations of the 4.6- and 6.3-nm QCs.

The decay time of the PL intensity from the 4.6-nm QC also differed with the QC pair, as demonstrated in Fig. 4(b), which has a logarithm-scale longitudinal axis. The solid, broken, and dotted lines show the decay time of the PL for QC pairs P1, P2, and P3, respectively, and the respective values are 6.7, 4.2, and 2.9 ns. The solid squares in Fig. 4(c) are the experimental results for the relation between the decay and rise times of the PL from the 4.6-nm QC for several QC pairs including P1, P2, and P3. The decay time exceeds the exciton lifetime of the isolated 6.3-nm QC measured experimentally, and increases as the rise time falls. Rate Equation (1) indicates that the decay time is determined by the exciton lifetimes (*i.e.*, physical properties constant) in the 6.3-nm and 4.6-nm QC. The other dissipative pathways can be negligible small in consideration of the exciton luminescence efficiency. Therefore the experimental result in Fig. 4(c) means that the exciton lifetime in the QCs increases with the optical near-field interaction. This increase in the exciton lifetime due to the optical near-field interaction can be understood using the feature of the anti-parallel dipole-dipole coupling of an optical near field. The difference in the total oscillator strength, F, of the excitons in the coupled QD system can be approximated to the lowest order as being inversely proportional to the optical near-field interaction due to its anti-parallel coupling characteristics. Then, the decay time of the PL intensity from the 4.6-nm QC, which equals the exciton lifetime τ_{ex}, is given by $\tau_{ex} \propto 1/F \propto 1/\{F_0?F_0 \cdot \exp(-a\tau_i)\}$; then, $\tau_{ex} = \tau_0/\{1 - \exp(-a\tau_i)\}$, where τ_0, F_0, and a are the exciton lifetime of an isolated QC, its oscillator strength, and the fitting parameter, respectively. The solid curve in Fig. 4(c) is the fitted result based on this assumption, and it agrees well with the experimental results.

Next, we discuss the origins of the anti-parallel coupling features of the optical near-field interaction between QDs. In the experiment, we detected the PL signal from QCs, which means that only the transverse exciton was detected, because the longitudinal exciton is optically forbidden and its dispersion differs from that of the transverse exciton, *i.e.*, it has a different energy in the QCs. Since, the direction of the electric dipole in the transverse exciton is perpendicular to the direction of propagation, the dipole never becomes aligned with the direction of propagation after the energy is transferred to the neighboring QC. Although there are two possible eigenstates of the mutual arrangements of the dipoles in excitons, *i.e.*, parallel and anti-parallel, as shown in Figs. 1(a) and 1(b), the occurrence probability of the anti-parallel state exceeds that of the parallel state because the total energy of the system for the anti-parallel state is lower than that for the parallel state. This anti-parallel feature of the optical near-field coupled QCs reduces the recombination of excitons. Consequently, the exciton lifetime increases with the optical near-field interaction.

IV. CONCLUSION

We measured the optically forbidden energy transfer time between cubic CuCl QCs via the optical near-field interaction directly using a PL pump-probe technique. The signal rise time, which corresponds to the energy transfer time, was from 25 to 180 ps. We also showed that the

decay time increased as the energy transfer time fell; this was attributed to the anti-parallel dipole-coupling feature of the near-field interaction between the QDs. These features are of interest physically and are applicable to photonic devices, such as optical nanometric sources, long phosphorescence devices, and optical battery cells.

[1] D. Goldhaber-Gordon, H. Shtrikman, D. Mahalu, D. Abusch-Magder, U. Meirav, and M. A. Kastner, Nature **391**, 156 (1998).

[2] D. Goldhaber-Gordon, J. Göres, M. A. Kastner, H. Shtrikman, D. Mahalu, and U. Meirav, Phys. Rev. Lett. **81**, 5225 (1998).

[3] F. R. Waugh, M. J. Berry, D. J. Mar, R. M. Westervelt, K. L. Campman, and A. C. Gossard, Phys. Rev. Lett. **75**, 705 (1995).

[4] G. Burkard, G. Seelig, and D. Loss, Phys. Rev. B **62**, 2581 (2000).

[5] T. Kawazoe, K. Kobayashi, J. Lim, Y. Narita, and M. Ohtsu, Phys. Rev. Lett. **88**, 067404 (2002).

[6] K. Mukai, S. Abe, and H. Sumi, J. Phys. Chem. B **103**, 6096 (1999).

[7] S. Sangu, K. Kobayashi, T. Kawazoe, A. Shojiguchi, M. Ohtsu, Trans. Mat. Res. Soc. Jpn., in press (2005).

[8] M. Ohtsu, K. Kobayashi, T. Kawazoe, S. Sangu, and T. Yatsui, IEEE J. Sel. Top. Quant. Electron **8**, 839 (2002).

[9] T. Kawazoe, K. Kobayashi, S. Sangu, and M. Ohtsu, Appl. Phys. Lett. **82**, 2957 (2003).

[10] T. Kawazoe, K. Kobayashi, S. Sangu, and M. Ohtsu, J. Microscopy **209**, 261 (2002).

[11] R. H. Dicke, Phys. Rev. **93**, 99 (1954).

[12] A. D. Yoffe, Adv. Phys. **50**, 1 (2001).

[13] T. Itoh, Y. Iwabuchi, and M. Kataoka, phys. status solidi (b) **145**, 567 (1988).

[14] T. Saiki, S. Mononobe, M. Ohtsu, N. Saito, J. Kusano, Appl. Phys. Lett. **68**, 2612 (1996).

[15] T. Saiki and K. Matsuda, Appl. Phys. Lett. **74**, 2773 (1999).

[16] N. Sakakura and Y. Masumoto, Phys. Rev. B **56**, 4051 (1997).

[17] K. Kobayashi, S. Sangu, H. Ito, and M. Ohtsu, Phys. Rev. A **63**, 013806 (2000).

[18] S. Sangu, K. Kobayashi, A. Shojiguchi, T. Kawazoe, and M. Ohtsu, J. Appl. Phys. **93**, 2937 (2003).

[19] T. Suzuki, T. Mitsuyu, K. Nishi, H. Ohyama, T. Tomimasu, S. Noda, T. Asano, A. Sasaki, Appl. Phys. Lett. **69**, 4136 (1996).

[20] S.Sangu, K. Kobayashi, T. Kawazoe, A. Shojiguchi and M. Ohtsu, Trans. Mater. Reserch Soc. of Jpn. **28**, 1035 (2003).

[21] K. Kobayashi, S. Sangu, T. Kawazoe, and M. Ohtsu, J. Luminescence, in press (2005).

NANO LETTERS

2005
Vol. 5, No. 2
213−217

Exciton Localization in Vertically and Laterally Coupled GaN/AlN Quantum Dots

A. Neogi*

Department of Physics, University of North Texas, Denton, Texas 76203

H. Morkoç

Department of Electrical Engineering, Virginia Commonwealth University, Richmond, Virginia 23284

T. Kuroda and A. Tackeuchi

Department of Applied Physics, Waseda University, Okubo 3-4-1, Tokyo 169-8555, Japan

T. Kawazoe and M. Ohtsu

Department of Physics, University of Tokyo, Japan

Received September 13, 2004; Revised Manuscript Received December 2, 2004

ABSTRACT

Near-field and time-resolved photoluminescence measurements show evidence of exciton localization in vertically and laterally coupled GaN quantum dots (QDs). The binding energies in multiple period QDs (MQDs) are observed to be stronger by more than six times compared to single period QDs (SQDs). Excitons in MQDs have a short (450 ps) lifetime and persist at room temperature, while SQDs exhibit extraordinarily long (>5 ns) lifetime at 10 K due to reduced spatial overlap of electron and hole wave functions in strained QDs.

The most spectacular property of quantum-confined nitride-based quantum well (QW) or dots (QD) lie in the huge electric fields along their growth axes as this material system normally has wurtzite symmetry.[1−6] The study of nitride QDs is particularly interesting as it depicts the interplay of built-in strain-dependent electric fields and quantum confinement in the nitride-based material system. When the dot size is of the order of the exciton Bohr radius, the quantum confinement effects on both the exciton binding energy and the optical band gap allow tailoring of the optical properties of the system.[3,6] In self-organized GaN QDs, the quantum confinement effect observed in the "classical" GaAs-based QD or QW, is offset by the large piezoelectric and spontaneous polarization fields, resulting in a red shift of the ground-state optical transition below the bulk band gap by about 0.5 eV.[3] This enormous shift is attributed to the piezoelectric field exceeding 5 MV/cm. The dot size and built-in strain fields can be engineered to tune the emission wavelength from the visible to the ultraviolet light regime in GaN-QD based optical emitters. QD layers are expected to effectively decouple the active layers from the substrate and the buffer layer and, thus reduce the defect density.[6]

We have recently reported the growth of GaN QDs grown on relatively thin AlN spacer layers (2 nm). A large blue-shift in the exciton emission energy indicates a strong carrier confinement, despite the reduction in the effective stress within the GaN QD layers.[7−9] In this paper, we compare the carrier recombination dynamics in single period laterally coupled QD (SQD) and multiple period vertically stacked QD (MQD) for investigating the emission mechanism in GaN QDs by time-resolved photoluminescence (PL) measurements. The stacking of multiple layers is expected to influence the optical properties due the strain-induced realignment of dots in one level with respect to the adjacent level. The main motivation is to isolate pure dimensionality effects in the MQDs from the influence of the giant polarization (piezoelectric and spontaneous) induced electric fields present in the SQD system.[10−12] We present the first report on exciton localization in vertically correlated GaN MQDs in the presence of built-in strain field.

* Corresponding author. E-mail: arup@unt.edu.

10.1021/nl048511x CCC: $30.25
Published on Web 12/24/2004

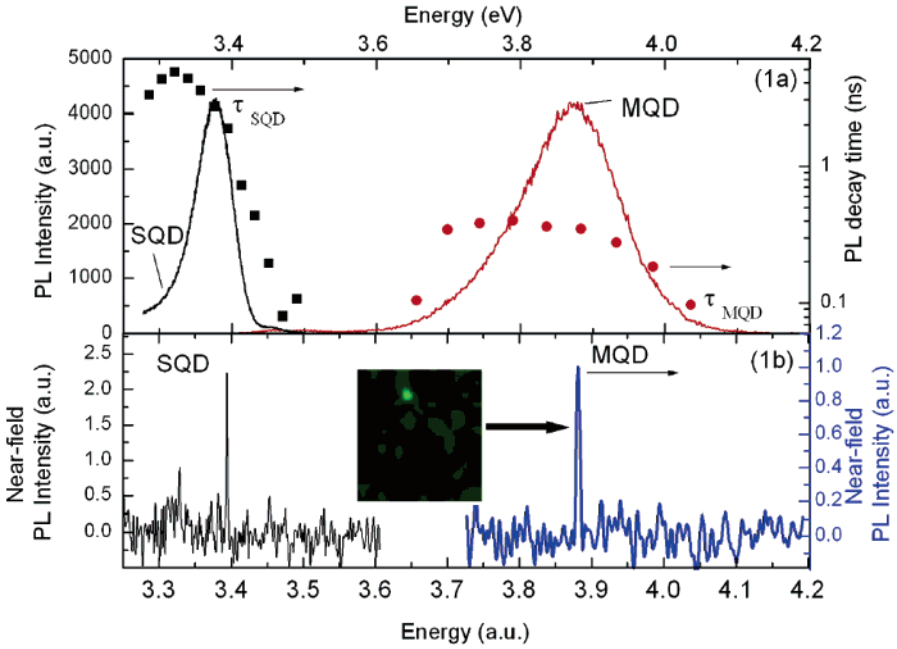

Figure 1. Comparison of PL spectra in single and stacked GaN QDs at 10 K: (a) time-integrated far-field PL, (b) near-field PL of a 450 nm × 450 nm scanned area, with spatial resolution of 40 nm, inset showing the spatially resolved PL of a MQD at 3.88 eV.

GaN dots were self-assembled on a 2 nm thin AlN layer over AlN/GaN superlattice buffer layer grown on sapphire substrate using molecular beam epitaxy.[8] Dots were self-assembled by nitridation using RF plasma in a nitrogen atmosphere. The dot size and density depend on the growth condition, deposition time, and post growth treatment.[9] The SQDs were allowed to ripen, unlike the MQDs, which were covered with a thin AlN spacer layer immediately after the nucleation of self-assembled GaN structures. The ripening of the dots in the SQDs leads to coupling in the lateral direction. AFM images show that SQDs has a relatively larger dot size (height/width − 20/150 nm) compared to the MQDs (8/40 nm). It is observed from high-resolution transmission electron microscopy that in SQDs, the lateral separation is about 2−4 nm, whereas in MQDs, the lateral separation is ∼ 4−5 nm in the cap layer and 5−8 nm in the underlying layers. Due to the narrower AlN spacer layers between the dots (∼2 nm), a stronger coupling exists between the dots in the vertical direction. Time-integrated PL (TI−PL) and time-resolved PL (TR−PL) measurements were performed using a frequency tripled Ti:sapphire laser mode-locked at 100 MHz with an excitation energy at 4.66 eV, and the PL signal was detected using a streak camera with a resolution of 15 ps. A near-field scanning optical microscope is used for studying exciton localization in single QD.

The recombination of the excitons has been investigated by TRPL measurements performed using a 100 MHz Kerr-lens mode-locked, frequency tripled Ti:sapphire laser with a typical temporal width of 80 fs and an average incident pump power of 0.3 mW (0.4 μJ/cm^2). The excitation wavelength was 270 nm (4.6 eV) and the PL signal was dispersed through a grating spectrometer (600 gr/mm) and measured using a Hamamatsu streak camera with a resolution of 15 ps.

The time integrated PL spectrum from a single QD layer was compared to a MQD sample measured 2−10 ns after the excitation of the pump laser pulse at 10 K (Figure 1a). The PL emission energy depends on the size of quantum dots. For MQDs with relatively smaller dots, the PL peak is at 3.86 eV, nearly 400 meV blue-shifted with respect to the bulk GaN bandedge. In SQDs, which are composed of larger dots due to the ripening effect, the PL peak is centered at 3.37 eV and is significantly red shifted from the MQD PL peak and lies 90 meV below the bulk GaN bandedge (3.46 eV). This red shift is a clear manifestation of the internal polarization-induced electric field present in wurtzite GaN QDs, which induces a red-shift in the QD transition energy due to quantum confined Stark effect. It appears in case of the single layer QDs owing to the relatively larger structural dimension, the induced electric field dominates the quantum confinement effect in larger QDs. The line width in SQDs is also considerably narrower due to the reduced dot distribution in a single period QD compared to that in the multilayered structure in MQDs. The line width in MQD is ≈200 meV compared to 70 meV for the SQDs, which clearly indicates that the dominant inhomogeneous broadening mechanism in the MQDs results from dot size variations from period to period. TEM images show vertical correlation in MQDs.[13] Figure 1b shows the near-field PL spectra of SQDs and MQDs consisting of dominant sharp spectral features respectively at 3.37 and 3.88 eV. The PL from a 450 nm × 450 nm area of MQD sample (inset of Figure 1b) shows that the emission area is less than 50 nm. The line width in SQD has a fwhm ∼ 0.9 meV compared to 2.3 meV in the MQD samples. The near-field PL peaks correspond to the central far-field emission energy from both SQDs and MQDs and indicates exciton localization in a cluster of few QDs. It is observed that the near-field PL line width shown in

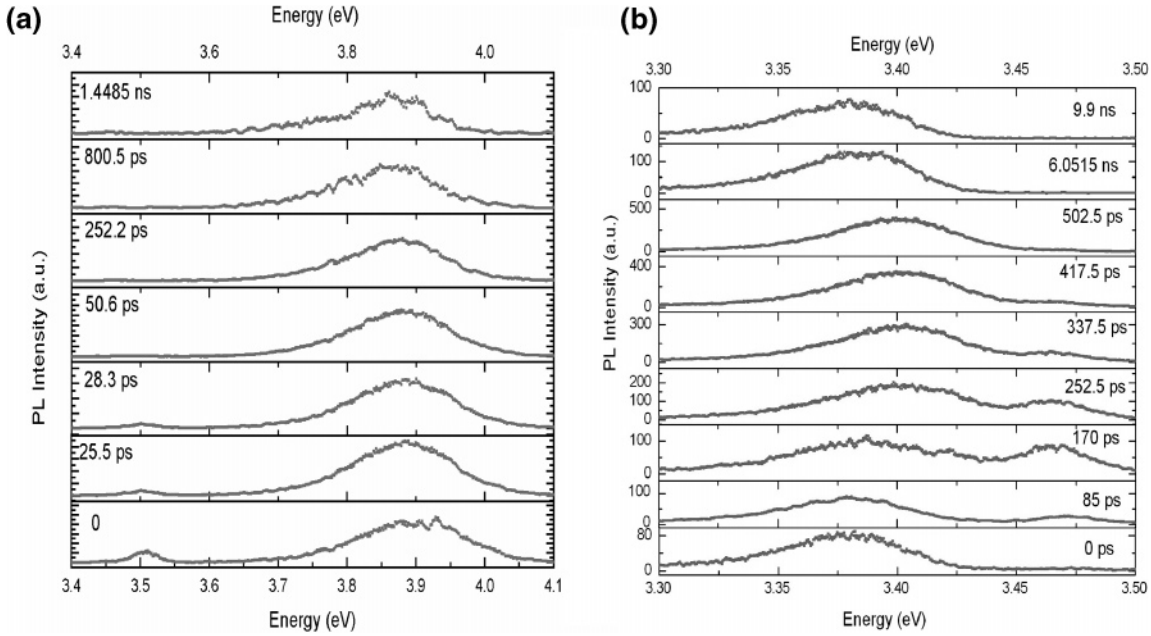

Figure 2. Time integrated photoluminescence spectra in (a) 20 period MQD and (b) SQD.

Figure 1b is significantly narrower than the far-field PL line width shown in Figure 1a. The narrow near-field PL spectrum (∼ few meV) is presumably due to the emission from a cluster of 2−5 dots, which are excited by the narrow NSOM probe with 5 nm diameter and are 10−20 nm from the surface. The far-field PL is significantly broader (> 100 meV) as it is influenced by inhomogeneous broadening due to emission from a large ensemble of QDs, which are simultaneously excited by a beam with relatively larger spot diameter. The near-field PL spectrum yields information on carrier recombination and exciton emission from single quantum dots with minimal inhomogeneous broadening due to lateral coupling. The far-field PL spectrum is strongly influenced by the lateral coupling in the GaN/AlN QD system with high dot density.

In MQDs, the lifetime is relatively steady (290−390 ps) across the PL peak as a result of the stronger carrier confinement in smaller QDs. Emission at lower energies arises from larger QDs with reduced wave function overlap and longer recombination times. Therefore, the decrease in τ_D at low emission energies is likely to be caused by nonradiative relaxation from the QDs. However, the decay from SQD is more complex due to the presence of a strain-induced piezoelectric polarization field. In SQDs, the lifetime varies by nearly 2 orders of magnitude (∼70 ps to 5 ns), which indicates the presence of large intrinsic strain. At high emission energies, the GaN buffer layer at ∼3.46 eV acts as nonradiative recombination center. The strained and larger dots emitting at lower energies (<3.3 eV) also contribute to nonradiataive recombination and result in a decrease in the PL decay time in SQDs.

Figure 2a shows the temporal evolution of the PL spectrum from the 20-period QD sample measured at 10 K. A small peak emanates from the GaN buffer layer at 3.49 eV and decays within 25−30 ps. The PL spectrum is asymmetric and the decay constant shows a weak biexponential feature in all regions of this spectrum. With an increase in the delay time, a red shift of the PL peak exceeding 35 meV is observed, which indicates the collective effect of polarization fields and photoexcited carrier screening. QDs grown under reduced strain still have appreciable polarization fields present in the dot regions of the GaN/AlN MQDs. Under the influence of piezoelectric and spontaneous fields, optically excited carriers drift apart. The electrons (holes) move toward the direction opposed to (along) the piezoelectric/spontaneous field and the field induced by these spatially separated charge carriers will screen the piezoelectric/spontaneous field. On the other hand, the screening field due to spatially separated charge carriers decreases with the delay time due to the radiative recombination of electrons and holes. At $t_d = 0$, the screening field induced by the photoexcited electron and holes is the strongest, which reduces or partially balances out the piezoelectric and spontaneous field. As the delay time increases, carriers recombine radiatively and the screening field gradually diminishes and the original piezoelectric/spontaneous field is restored. Thus the total amount of shift from $t_d = 0$ to $t_d \rightarrow \infty$ effectively corresponds to the variation of the electron and hole levels in the presence of the piezoelectric/spontaneous field with and without carrier screening, respectively. The PL spectra from MQDs also show a strong confinement as indicated by the relatively small shift in the peak PL energy with temperature.[9]

Figure 2b shows the time-resolved spectra of the SQDs measured at various delay times at 10 K. Initially at $t = 0$, the time-integrated PL spectra show a single peak at 3.37 eV emitting from the single-period GaN QD dots at an energy below the GaN bandedge (Figure 1). The excitonic peak from the 3D-GaN buffer layers appears due to carrier relaxation from smaller dots relaxing carriers from higher energy states. Within 100 ps, carrier relaxation occurs from the bulk GaN states either due to the presence of shallow-

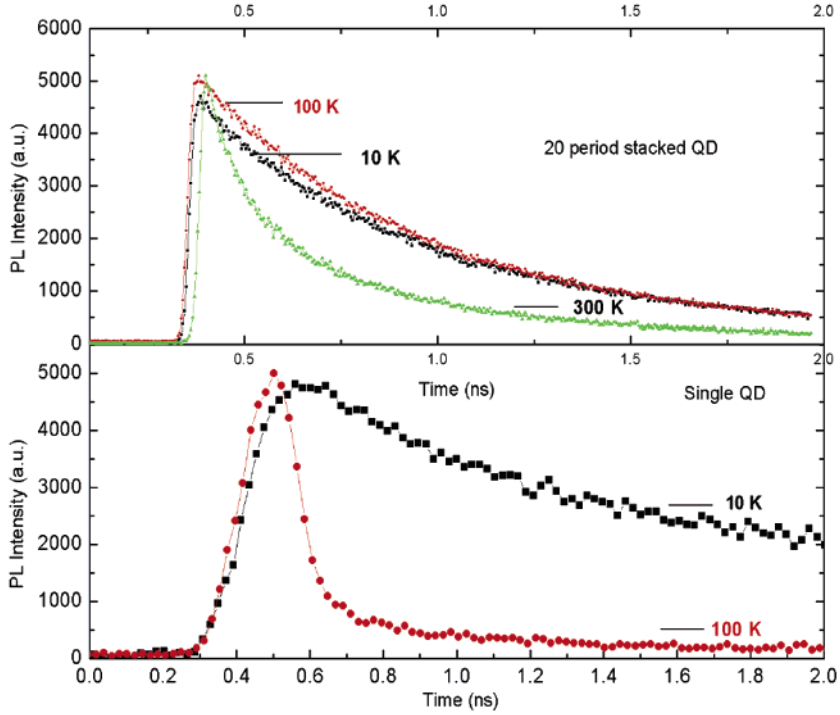

Figure 3. Comparison of temperature dependence of decay times in single and multiple quantum dots.

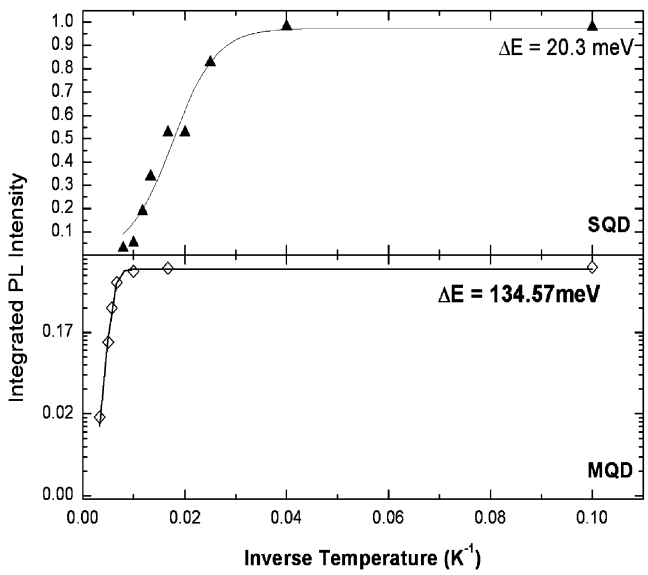

Figure 4. Spectrally integrated intensities and time-integrated data plotted as a function of inverse temperature.

level defect states or through the smaller GaN dots with size comparable to GaN bandedge emission energy. The TRPL decay time constant of the carriers at this energy (~3.45 eV) is extremely fast and occurs within 100 ps even at low temperature. This enhancement of the recombination rate is possibly due to the increase in the nonradiative recombination center that occurs due to this particular growth technique. We also observe an initial blue shift due to the band filling of the QDs and screening of the photoexcited followed by the gradual restoration of the large built-in piezoelectric field.[14] This time evolution also shows that the piezoelectric field is considerably larger in SQDs compared to MQDs. The relatively long decay time in single layer QDs at low temperature is a signature of the spatial separation of electron hole wave functions due to the strained induced by the ripening of the QDs during the growth process.[15]

A comparison of the temperature dependent spectrally integrated decay characteristics of the SQDs and MQDs been shown in Figure 3. In MQDs there is no significant difference in the decay constants from 10 to 100 K, and even at 300 K the nonradiative recombination rate is lower than that in a single period QD at 100 K. It is observed that in SQDs the nonradiative recombination process is dominant as the temperature increases and the PL intensity drops exponentially, unlike the temperature insensitive feature in MQDs.

To compare the effective binding energies of the excitonic states in confined QDs in the stacked MQDs and highly strained SQDs, we show in Figure 4 the normalized intensities of the time integrated spectral features as a function of inverse temperature. These intensities are successfully modeled with the activated behavior,

$$I(T) = I_o/[1 + C\exp(-\Delta E/k_B T)] \qquad (1)$$

where ΔE is the activation energy.

The exciton recombination time in the GaN SQDs at 10 K is single exponential with an extraordinarily long exciton recombination time, ~5 ns and $\Delta E = \Delta E_{sqd}$ ~20 meV, while in MQDs $\Delta E = \Delta E_{mqd}$ ~ 134 meV for the broad emission states. This shows that the emission associated with these QDs, whose activation energies differ by 6-fold, are significantly different. The intensities obtained from fits of the exponential decays in Figure 3 and Figure 1 also shows that the short-lifetime component corresponds to the broad emission feature in MQDs, while the long-lifetime component corresponds to the relatively narrower spectral feature

in SQDs. The PL spectra in SQD clearly result from excitons confined to the QDs. However, this state is only weakly bound (20 meV) and thermally depopulates by 150 K. The extraordinarily long lifetime of this state ($\sim$ 5.0 ns) indicates that the overlap of the electron (e) and hole (h) wave functions is significantly weaker than for the short-lived states in strongly confined smaller QDs in the stacked MQD system, suggesting that this excitonic state in SQD may result from spatially indirect e−h transitions. In contrast, these spectra and lifetimes indicate that the state responsible for the broad emissions in MQDs is strongly bound (134 meV) and persists nearly to room temperature. Moreover, the short lifetime of this PL emission indicates that the electron and hole overlap is large and the radiation recombination process is dominant.[17] The relatively long radiative lifetime in SQDs can also be attributed to the lack of additional decay channels induced by vertical correlation in MQDs.

The presence of a piezoelectric field in these larger clusters of SQDs is further supported by optical power dependence of the luminescence spectra. It has been observed (which is not shown here) that as excitation power density increases, the PL peak blue shifts significantly. This behavior is typical of piezoelectric nanostructures and is due to partial screening of the piezoelectric field by the photoexcited e−h pair.[16] A 25 meV blue shift is observed as the power density varies from 1 to 10 μJ/cm^2.

In conclusion, we have compared the carrier recombination dynamics in SQD and MQDs. It is observed that at low temperatures the recombination time in SQDs is over an order of magnitude longer than the nonradiative recombination process at 100 K. The vertical correlation among the adjoining stacked layer leads to enhanced PL efficiency in MQDs and results in an efficient emission at room temperature. At low temperature, the luminescence decay is dominated by radiative recombination with relatively shorter lifetimes (250−500 ps), which indicates a potential for device applications. In SQDs, nonradiative processes resulting in an extremely short total decay time constants at high temperatures dominate exciton recombination.

Acknowledgment. The authors are thankful to Dr. Brian P. Gorman for transmission electron microscopy of the quantum dot structures. This research was supported by the University of North Texas "Faculty Research Grants Program".

References

(1) Morkoç, H. *Nitride Semiconductors and Devices*; Springer-Verlag: Heidelberg, 1999. Nakamura, S.; Fasol, G. *The Blue Laser Diode*; Springer-Verlag: Heidelberg, 1997.
(2) Widmann, F.; Simon, J.; Daudin, B.; Feuillet, G.; Rouvière, J. L.; Pelekanos, N.; Fishman, G. *Phys. Rev. B* **1998**, *58*, R15989; Widmann, F.; Simon, J.; Pelekanos, N. T.; Daudin, B.; Feuillet, G.; Rouviere, J. L.; Fishman, G. *Microelectronic J.* **1999**, *30*, 353.
(3) Widmann, F.; et al. *Phys. Rev. B* **1998**, *58*, R15989. Widmann, F.; et al. *Microelectron. J.* **1999**, *30*, 353.
(4) Arakawa, Y.; Someya, T.; Tachibana, K. *Phys. Status Solidi B* **2001**, *224*, 1.
(5) Tanaka, S.; Takeuchi, M.; Aoyagi, Y. *Jpn. J. Appl. Phys.* **2000**, *39*, L831.
(6) Huang, D.; Fu, Y.; Morkoç, H. "Preparation, Structural and Optical Properties of GaN based quantum dots" in *Optoelectronic Properties of Semiconductor Nanostructures*; Steiner, T., Ed.; Artech House: Boston, 2004.
(7) Reshchikov, M. A.; Cui, J.; Yun, F.; Visconti, P.; Nathan, M. I.; Molnar, R.; Morkoç, H. *Mater. Res. Soc. Symp. Proc.* **2001**, *639*, G11.2.
(8) Morkoç, H.; Neogi, A.; Kuball, M. *Mater. Res. Soc. Proc.* **2004**, *749*, T6.5.1/N8.5.1/Z6.5.1.
(9) Neogi, A.; Everitt, H. O.; Morkoç, H.; Kuroda, T.; Tackeuchi, A. *IEEE Trans. Nanotechnol.* **2004**, *2*, 450.
(10) Woggon, U. *Optical Properties of Semiconductor QDs*; Springer: Berlin, 1997.
(11) Lipsanen, H.; Sopanen, M.; Ahopelto, J. *Phys. Rev. B* **1995**, *51*, 13868.
(12) Chamard, V.; Metzger, T. H.; Daudin, B.; Adelmann, C.; Mula, G. *Appl. Phys. Lett.* **2001**, *79*, 1971.
(13) Neogi, A.; Gorman, B. P.; Morkoç, H.; Kawazoe, T.; Ohtsu, M. Near-field Optical Spectroscopy and Microscopy of Self-assembled GaN/AlN Nanostructures. *Appl. Phys. Lett.* **2005**, in press.
(14) Talierco, T.; Lefebvre, P.; Gallart, M.; Morel, A. *J. Condens. Matter Phys.* **2001**, *13*, 7027.
(15) Andreev, A.; Reily, E. O. *Appl. Phys. Lett.* **2001**, *79*, 521.
(16) Shin, E.; Li, J.; Lin, J. Y.; Jiang, H. X. *Appl. Phys. Lett.* **2000**, *77*, 1170.
(17) Reale, A.; Massari, G.; Di Carlo, A.; Lugli, P.; Vinattieri, A.; Alderighi, D.; Colocci, M.; Semond, F.; Grandjean, N.; Massies, J. Comprehensive description of the dynamical screening of the internal electric fields of AlGaN/GaN quantum wells in time-resolved photoluminescence experiments. *J. Appl. Phys.* **2003**, *93*, 400.

NL048511X

Japanese Journal of Applied Physics
Vol. 44, No. 2, 2005, pp. L 92–L 94

Blue Light Emission from Ultrafine Nanosized Powder of Silicon Produced by Intense Pulsed Ion-Beam Evaporation

Kiyoshi YATSUI, Michiharu GUNJI, Sung-Chae YANG, Hisayuki SUEMATSU, Weihua JIANG, Takashi YATSUI[1] and Motoichi OHTSU[1]

Extreme Energy-Density Research Institute, Nagaoka University of Technology, Nagaoka, Niigata 940-2188, Japan
[1]*SORST, Tokyo Institute of Technology, Nagatsuta, Midori-ku, Yokohama, Kanagawa 226-8503, Japan*

(Received May 13, 2004; accepted November 9, 2004; published December 17, 2004)

Blue light emission has been observed from ultrafine nanosized powder of silicon, which was synthesized by rapid cooling of high-density ablation plasma produced by intense pulsed light-ion beam interaction with a silicon target, called pulsed ion-beam evaporation. The emission appears from the powder without heat treatment after being synthesized. Furthermore, the emission is found to be very stable; neither red- nor blue-shift is observed. In fact, the spectrum from the powder four months after the synthesis is the same as those from as-synthesized powder. The rapid heat cooling inherent to ion-beam evaporation seems to be essential for emission. [DOI: 10.1143/JJAP.44.L92]

KEYWORDS: blue light emission, photoluminescence, nanosized powder of silicon, ion-beam evaporation, high-density ablation plasma, rapid heat cooling

Recently, visible photoluminescence has been observed from ultarfine nanosized powder (UFP) of silicon[1–6] due to quantum-size confinement, although, in principle the light emission is not possible from bulk silicon because of indirect transition. UFP can be produced by either wet or dry processes. The former, such as chemical reaction, has the advantage of mass production, whereas there is a problem of poor quality. The latter, such as pulsed laser ablation, results in powder of good purity, although the production rate is very poor.

In 1995, we proposed and successfully experimentally demonstrated the synthesis of UFP[7] by rapid cooling of high-density ablation plasma produced by the interaction of an intense pulsed light-ion beam (LIB) with the target, called pulsed ion beam evaporation (IBE).[8–10] Here, the plasma density of approximately 10^{18}–10^{20} cm^{-3} can be obtained by the IBE, which is more than 10–12 orders of magnitude higher than those in conventional methods of plasma production. Later, it was shown theoretically,[11] using equations of moment, lognormal distribution of the UFP and an ion beam-target interaction, that the UFP can be synthesized mainly by coagulation of monomers. Here, high-density aluminum plasma is rapidly cooled by ambient nitrogen gas to synthesize UFP of AlN. In fact, mono-dispersed size distribution has been observed for AlN. Here, rapid heat cooling at a rate of 10^8 K/s plays an important role in synthesis of UFP.

In our previous paper, we reported the preparation of 0.18-μm-thick silicon thin films within 20 μs.[12] In the process, heat associated with the plasma promoted the crystallization of the deposited silicon thin films on substrates in vacuum at room temperature. Since the average grain size of silicon in the thin films was 27–56 nm, it is natural to conclude that silicon UFP might be synthesized by IBE by adopting conditions under which the quenching rate is high, i.e. synthesis in atmospheric gas and/or at low temperature. On the basis of the above consideration concerning the UFP associated with IBE, we attempted the synthesis of silicon UFP in He gas at −10°C.

The experiment was carried out using the pulsed power generator, "ETIGO-II",[13] at the Nagaoka University of Technology. Basically, it consists of capacitor banks (Marx generator), a pulse-forming network, switches, an impedance-conversion line, and load (i.e., ion-beam diode). The Marx generator consists of numerous capacitors, which are initially charged in parallel and discharged in series by closing the vacuum switches. The high-voltage pulse, with the pulse width on the order of 1 μs, is compressed to 50 ns by the pulse-forming network via a combination of switches. The electric power can be converted into an intense pulsed light-ion beam by using an ion-beam diode. In the experiment, we have used a magnetically insulated diode (MID),[14] which prevents the motion of electrons due to the presence of a transverse magnetic field.

Typically, the experiment was carried out under the following conditions: proton beam energy (peak) ∼1 MeV, ion current on target ∼3 kA/cm^2, and pulse width ∼50 ns. The ion species of the beam is mainly protons, typically more than 75%, and the rest is carbon, because a polyethylene sheet was used as the flashboard anode of the MID. Since the range, the distance from the surface in which the energy of protons is dissipated due to interactions with free electrons, bound electrons, and ions, can be estimated to be 14 μm for protons with the energy of 1 MeV, extremely high energy density, typically on the order of 100 J/cm^2, can be obtained on the target surface with an area of 100 cm^2. Under these conditions, the energy per atom on the target can be estimated to be typically 15 eV/atom, which is sufficient to ionize silicon. Thus, a high-density ablation plasma can be produced.

Figure 1 shows the experimental setup of the ion-beam diode and the chamber used to synthesize the UFP of silicon. The distance between the anode of the MID and the target was 170 mm, where the geometric focal point of the MID is 160 mm. The substrate of quartz glass was placed 90 mm downstream of the target. The substrate was kept at room temperature or −10°C. The atmosphere was helium gas with a purity of 99.9999% at 1 Torr, or residual gas evacuated to 10^{-4} Torr. In both atmospheres, oxygen partial pressure should be 10^{-4} Torr. The UFP was collected on the substrate. The photoluminescence was measured by illuminating the UFP with a He-Cd laser of a wavelength of 325 nm. The intensity of visible light depended on the position on the substrate. The UFP in a visible-light-emitting

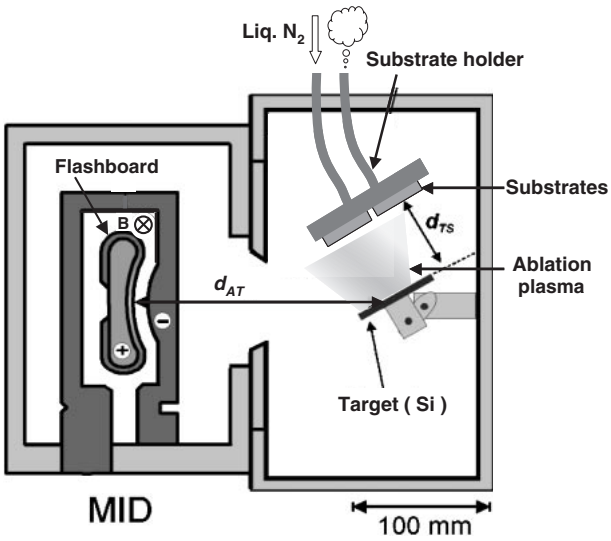

Fig. 1. Schematic of magnetically insulated ion beam diode and vacuum chamber used to synthesize nanosize powder of silicon.

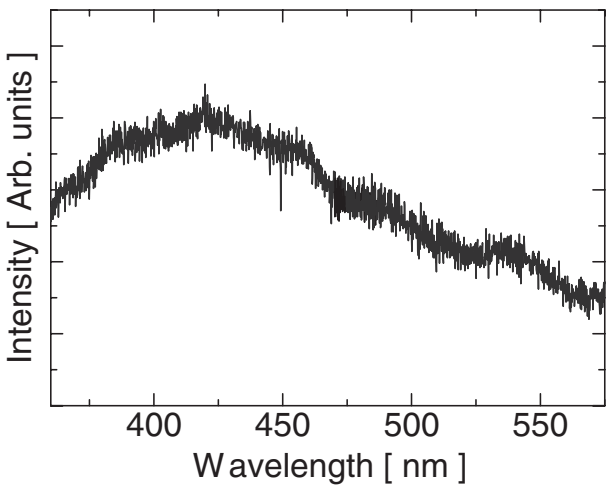

Fig. 2. Photoluminescence spectrum obtained from nanosized powder of silicon, where the substrate was kept at −10°C and the ambient gas was helium at 1 Torr.

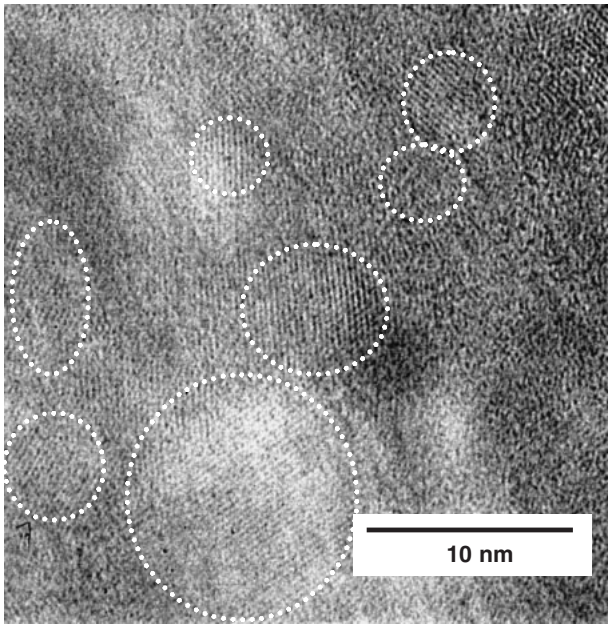

Fig. 3. HR-TEM image of the silicon powder. White dotted circles show grain boundaries of silicon. Experimental conditions are the same as those described in Fig. 2.

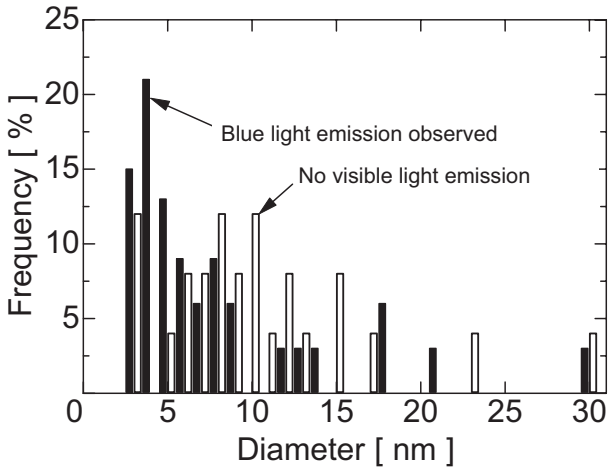

Fig. 4. Size distribution of nanosized powder of silicon obtained from HR-TEM images. Experimental conditions are the same as those described in Fig. 2.

portion was separated from the rest. Both portions of UFP were observed using a high-resolution, transmission electron microscope (HR-TEM). From the HR-TEM images, the grain size distributions for the UFP with and without visible light emission were obtained.

Figure 2 shows the PL spectrum obtained from the UFP of silicon. We can clearly see a broad emission from the blue to green wavelength region. The blue emission at around 420 nm is the strongest in the spectrum. It is noted here that the PL spectrum is very stable, and that neither blue- nor red-shift is observed. In fact, the spectrum of the UFP exposed to air for four months after synthesis is observed to be very similar to that of as-deposited UFP of silicon.

Figure 3 shows a HR-TEM image of the UFP of silicon exhibiting visible light emission. White dotted lines indicate grain boundaries of the silicon. Although a large grain 10 nm in diameter exists, it is found that most of the grains are less than 5 nm in diameter. The UFP of silicon was successfully synthesized by rapid quenching of plasma in He gas with the substrate at −10°C.

Figure 4 shows the size distribution of the UFP, which was determined from the HR-TEM image (see Fig. 3). It can be seen that the sample emitting blue light emission consists mostly of small particles, particularly those less than 4 nm in diameter. In addition, it is seen that larger UFP particles emit no visible light. From these results presented above, such an emission seems to be due to the quantum size confinement of silicon.

In summary, the ultrafine nanosized powder of silicon was successfully synthesized by intense pulsed light-ion beam evaporation. The emission was seen from the powder obtained without heat treatment after being synthesized. Blue light emission was clearly observed, with peaks at around 420 nm. Furthermore, the emission was found to be very stable, and neither red- nor blue-shift in the wavelength

was observed. In fact, the spectrum obtained from the powder four months after synthesis was very similar to that of as-synthesized powder. Rapid heat cooling inherent to ion-beam evaporation seems to be essential for emission.

This work was partly supported by 21st Century COE program from the Ministry of Education, Culture, Sports, Science and Technology of Japan.

1) L. T. Canham: Appl. Phys. Lett. **57** (1990) 1046.
2) E. Werwa, A. A. Seraphin, L. A. Chiu, C. Zhou and K. D. Kolenbrander: Appl. Phys. Lett. **64** (1994) 1821.
3) H. Mizuno, H. Koyama and N. Koshida: Thin Solid Films **297** (1997) 61.
4) K. Murakami, T. Makimura, N. Ono, T. Sakuramoto, A. Miyashita and O. Yoda: Appl. Surf. Sci. **127–129** (1998) 368.
5) L. Patrone, D. Nelson, V. Safarov, M. Sentis and W. Marine: J. Lumin. **80** (1999) 217.
6) X. Y. Chen, Y. F. Lu, Y. H. Wu, B. J. Cho, M. H. Liu, D. Y. Dai and W. D. Song: J. Appl. Phys. **93** (2003) 6311.
7) K. Yatsui, C. Grigoriu, H. Kubo, K. Masugata and Y. Shimotori: Appl. Phys. Lett. **67** (1995) 1214.
8) K. Yatsui: Laser & Part. Beams **7** (1989) 733.
9) K. Yatsui, X. D. Kang, T. Sonegawa, T. Matsuoka, K. Masugata, Y. Shimotori, T. Satoh, S. Furuuchi, Y. Ohuchi, T. Takeshita and H. Yamamoto: Phys. Plasmas **1** (1994) 1730.
10) K. Yatsui, C. Grigoriu, K. Masugata, W. Jiang and T. Sonegawa: Jpn. J. Appl. Phys. **36** (1997) 4928.
11) Q. Zhu, W. Jiang and K. Yatsui: J. Appl. Phys. **86** (1999) 5279.
12) S. C. Yang, A. Fazlat, H. Suematsu, W. Jiang and K. Yatsui: IEEE Trans. Plasma Sci. **30** (2002) 1816.
13) A. Tokuchi, N. Nakamura, T. Kunimatsu, N. Ninomiya, M. Den, Y. Araki, K. Masugata and K. Yatsui: *Proc. 2nd Int. Symp. Inertial Confinement Fusion by High-Power Particle Beams, Nagaoka, 1986*, ed. K. Yatsui (Nagaoka Univ. of Tech., Nagaoka, 1986) p. 430.
14) K. Yatsui, A. Tokuchi, H. Tanaka, H. Ishizuka, A. Kawai, E. Sai, K. Masugata, M. Ito and M. Matsui: Laser & Part. Beams **3** (1985) 119.

Appl. Phys. A 80, 1049–1051 (2005)
DOI: 10.1007/s00339-004-3044-9

Applied Physics A
Materials Science & Processing

T.-W. KIM[1,*,✉]
T. KAWAZOE[1]
S. YAMAZAKI[2]
M. OHTSU[1,2,**]

Low-temperature synthesis and room temperature ultraviolet lasing of nanocrystalline ZnO films

[1] Japan Science and Technology Corporation, 687-1, Tsuruma, Machida, Tokyo, 194-0004, Japan
[2] Interdisciplinary Graduate School of Science and Engineering, Tokyo Institute of Technology, Yokohama, Kanagawa, 226-8502, Japan

Received: 4 March 2004/Accepted: 20 September 2004
Published online: 18 November 2004 •

ABSTRACT Nanocrystalline ZnO films were fabricated via a simple method involving the oxidation of Zn films at a remarkably low temperature of 380 °C. X-ray diffraction study confirmed that the Zn films were completely oxidized even at the low temperature of 380 °C and the ZnO films fabricated were of polycrystalline wurtzite structure. Room temperature optical pumping using a frequency-quintupled Q-switched Nd:YAG laser ($\lambda = 213$ nm) exhibited that sharp peaks at around 3.12 eV emerged above excitation powers of $\sim 7\ \mathrm{MW/cm^2}$, demonstrating lasing in the ZnO films. These results represent that the process is a simple, promising approach for fabricating ZnO of sufficient optical performance for use as ultraviolet (UV) light emitters and an alternative UV laser source; both are key components in short-wavelength photonic devices.

PACS 81.07.Bc; 61.46.+w; 68.55.-a; 78.55.Et; 42.55.Px

ZnO, which has a room temperature bandgap of 3.37 eV and an exciton binding energy of ~ 60 meV, is a promising wide bandgap semiconductor for applications with photonic devices in ultraviolet (UV) region [1–3]. In particular, the high exciton binding energy is feasible for fabricating the photonic devices emitting UV light or laser at room temperature (RT) via an exciton recombination process. Few researchers have report the room temperature observation of UV emission and/or lasing in epitaxially grown ZnO films fabricated by using several methods such as pulsed laser deposition [4, 5], plasma-assisted molecular beam epitaxy [6], and metalorganic vapor phase epitaxy [7]. Recently, it was reported that UV lasing were demonstrated in ZnO nanowires synthesized at a relatively high temperature of about 1000 °C using a vapor phase transport process [8].

However, requirements of epitaxial growth of the film or a high growth temperature might restrict an available substrate material due to their lattice mismatches and higher endurance against heat. Therefore, development of a low temperature process for preparing high-quality ZnO films with reliable optical performances is strongly required to manufacture a variety of ZnO-based optical devices. In the previous report, we have showed that ZnO nanocrystallites fabricated by the same low temperature oxidation of metallic Zn precursors, exhibited strong UV emission peak around 3.27 eV at room temperature [9]. In addition, for fabricating a high-quality ZnO nanodots, we have developed a technique with control over the size and position, using near-field optical chemical vapor deposition (NFO-CVD) [10]. Furthermore, the photoluminescence properties of a single ZnO nanodot fabricated using the method were reported [11]. ZnO nanodots can be a promising material for a nanophotonic switching device that is indispensable for the realization of nanophotonic integrated circuits (ICs) we proposed [12]. In this study, we report the low temperature growth of nanocrystalline ZnO films and the observation of UV lasing in the films.

We employed a simple method for fabricating nanocrystalline ZnO films via the oxidation of Zn films at a remarkably low temperature of 380 °C; Zn films with a nominal thickness of 500 nm were deposited on CaF_2 (111) substrate by thermal evaporation of pure metallic Zn powder (99.999%), and then the sample was placed in a thermal furnace under a constant flow of high-purity oxygen gas. The crystal structure and morphology of the samples were characterized using X-ray diffraction (XRD) and scanning electron microscopy (SEM), respectively. Optical pumping was carried out using a frequency quintupled Q-switched Nd:YAG laser ($\lambda = 213$ nm, 20 Hz, 4 ns pulse width) at room temperature. The pump beam was focused to a spot of 0.5 mm diameter on the film with the 45° oblique direction and the emission light were detected in the normal direction to the film.

Figure 1 shows XRD patterns of as-deposited metallic Zn films (a) and ZnO (b) obtained by the oxidation at 380 °C for 6 h. For the as-deposited Zn thin films, a strong peak is observed at $2\theta = 36.39°$, which corresponds to the (002) diffraction of hexagonal phase Zn (Fig. 1(a)). Annealing the sample at 380 °C transformed the Zn into ZnO, as shown in Fig. 1(b). Diffraction peaks are observed at $2\theta = 31.88°$, 34.56°, and 36.29°, which correspond to (100), (002), and (101) of ZnO with wurtzite structure, respectively. Simple estimation of the lattice constants with the position of each diffraction peak provides lattice constants of $a = 0.324$ and $c = 0.519$ nm, which are in good agreement with those of bulk ZnO. In contrast,

✉ Fax: +81-44-819-2053, E-mail: twkim90@ksp.or.jp
*Present address: Kanagawa Academy of Science and Technology (KAST), 3-2-1, Sakado, Takatsu-ku, Kawasaki, Kanagawa, 213-0012 Japan
**Present address: School of Engineering, The University of Tokyo, 7-3-1 Hongo, Bunkyo-ku, Tokyo 113-8656, Japan

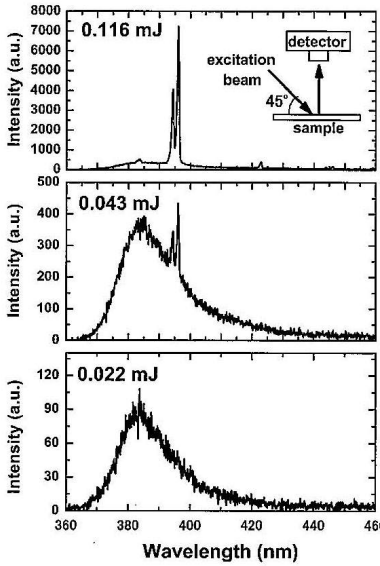

FIGURE 3 Emission spectra from the nanocrystalline ZnO films when the pump pulse energy is 0.022, 0.043, and 0.116 mJ (*from bottom to top*). The *inset* illustrates the measurement configuration

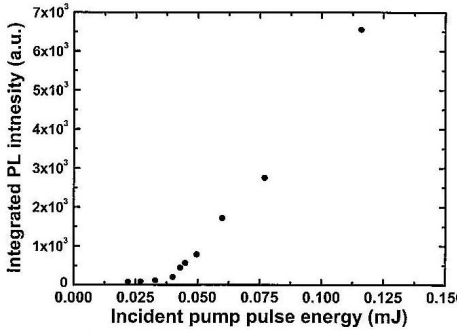

FIGURE 4 Integrated emission intensity of the ZnO films as a function of the incident pump pulse energy

$\sim 7\,\mathrm{MW/cm^2}$. Recently, there were a few reports on the lasing from polycrystalline ZnO film. For instance, H. Cao et al. investigated the lasing in ZnO polycrystalline films composed of fine ZnO nanoparticles with sizes of 50–150 nm [14]. According to their report, lasing action can be achieved in polycrystalline ZnO films by 'self-formed cavities' due to strong optical scattering in the films. And the threshold intensity was $\sim 0.4\,\mathrm{MW/cm^2}$. We believe that lasing in our sample resulted from the same mechanism. However, it should be noted that their samples were prepared with pulsed laser deposition at a relatively high temperature (500–700 °C) comparing with that in our case (380 °C). Meanwhile, S. Cho et al. reported the observation of lasing in ZnO polycrystalline films fabricated at 1000 °C [15]. The threshold intensity of their sample was $\sim 9\,\mathrm{MW/cm^2}$. Here, it may be worthy to notice that there is a difference in the threshold intensities between the samples. We think that the threshold intensity can be affected by several parameters such as size of ZnO nanocrystals, film thickness, and compactness of sample. In our case, the laser action can be achieved using ZnO films fabricated at a remarkable low temperature of 380 °C.

In conclusion, we have fabricated nanocrystalline ZnO films via a simple method involving the oxidation of Zn films at a remarkably low temperature of 380 °C. Room temperature optical pumping using a frequency-quintupled Q-switched Nd:YAG laser ($\lambda = 213$ nm) exhibited that sharp peaks at around 3.12 eV emerged above excitation powers of $\sim 7\,\mathrm{MW/cm^2}$, demonstrating lasing in the ZnO films. These results represent that the process is a simple, promising approach for fabricating ZnO of sufficient optical performance for use as ultraviolet (UV) light emitters and an alternative UV laser source; both are key components in short-wavelength photonic devices.

ACKNOWLEDGEMENTS We gratefully acknowledge Dr. T. Yatsui for his useful discussions.

REFERENCES

1 R.E. Dietz, J.J. Hopfield, D.G. Thomas: J. Appl. Phys. **32**, 2282 (1961)
2 D.M. Bagnall, Y.F. Chen, Z. Zhu, T. Yao, S. Koyama, M.Y. Shen, T. Goto: Appl. Phys. Lett. **70**, 2230 (1997)
3 Z.K. Tang, P. Yu, G.K.L. Wong, M. Kawasaki, A. Ohtomo, H. Koinuma, Y. Segawa: Solid State Commun. **103**, 459 (1997)
4 Z.K. Tang, G.K.L. Wong, P. Yu, M. Kawasaki, A. Ohtomo, H. Koinuma, Y. Segawa: Appl. Phys. Lett. **72**, 3270 (1998)
5 J.F. Muth, R.M. Kolbas, A.K. Sharma, S. Oktyabrsky, J. Narayan: J. Appl. Phys. **85**, 7884 (1999)
6 Y. Chen, N.T. Tuan, Y. Segawa, H-J. Ko, S-K. Hong, T. Yao: Appl. Phys. Lett. **78**, 1469 (2001)
7 S.W. Jung, W.I. Park, H.D. Cheong, Gyu-Chul Yi, Hyun M. Jang, S. Hong, T. Joo: Appl. Phys. Lett. **80**, 1924 (2002)
8 M.H. Huang, S. Mao, H. Feick, H. Yan, Y. Wu, H. Kind, E. Weber, R. Russo, P. Yang: Science **292**, 1897 (2001)
9 T-W. Kim, T. Kawazoe, S. Yamazaki, J. Lim, T. Yatsui, M. Ohtsu: Solid State Comm. **127**, 21 (2003)
10 Y. Yamamoto, M. Kourogi, M. Ohtsu, V. Polonski, G.H. Lee: Appl. Phys. Lett. **76**, 2173 (2000)
11 T. Yatsui, T. Kawazoe, M. Ueda, Y. Yamamoto, M. Kourogi, M. Ohtsu: Appl. Phys. Lett. **81**, 3651 (2002)
12 M. Ohtsu, K. Kobayashi, T. Kawazoe, S. Sangu, T. Yatsui: IEEE J. Sel. Top. Quantum Electron. **8**, 839 (2002)
13 T.-W. Kim, T. Kawazoe, S. Yamazaki, M. Ohtsu: Appl. Phys. Lett **84**, 3358 (2004)
14 H. Cao, Y.G. Zhao, H.C. Ong, S.T. Ho, J.Y. Dai, J.Y. Wu, R.P.H. Chang: Appl. Phys. Lett. **73**, 3656 (1998)
15 S. Cho, J. Ma, Y. Kim, Y. Sun, G.K.L. Wong, J.B. Ketterson: Appl. Phys. Lett. **75**, 2761 (1999)

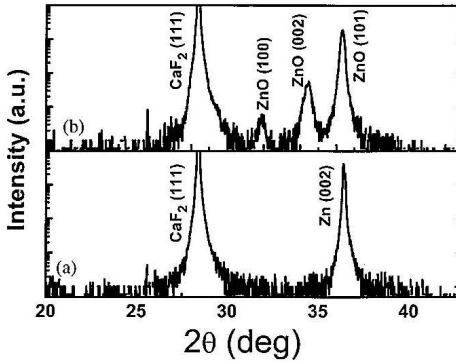

FIGURE 1 XRD patterns of as-prepared Zn films and the ZnO fabricated at 380 °C. For the as-prepared Zn films, a strong peak is observed at $2\theta = 36.39°$, which corresponds to the (002) diffraction of hexagonal phase Zn. After oxidation at 380 °C, diffraction peaks are observed at $2\theta = 31.88°$, 34.56°, and 36.29°, which correspond to (100), (002), and (101) of ZnO with wurtzite structure, respectively

no peak of Zn was observed for the sample. These indicate that the Zn films are completely transformed into crystalline ZnO at a temperature as low as 380 °C. We have oxidized the samples at various temperatures. According to the results, above 420 °C single crystalline ZnO nanowires were obtained instead of polycrystalline ZnO nanocrystallites. We could not observe the laser action in the samples composed of nanowires. We think that the result was caused by the thin film thickness. The detailed experimental results on these were given in our previous work [13]. In addition, we have also tried to fully oxidize the sample below 380 °C, but the samples oxidized below 380 °C for 6 hrs were not fully oxidized. This fact was confirmed by the XRD and X-ray photoelectron spectroscopy measurements.

Figure 2 shows typical SEM images of as-prepared Zn films with a different film thickness (a and b) and ZnO films (c and d) formed after oxidation at 380 °C for 6 h; a nominal film thickness of 50 nm for a and c, and 500 nm for b and d. Lots of separated hexagonal Zn plates, of which diameters range from 100 to 900 nm with thicknesses from 20 to 50 nm, are seen in Fig. 2a. We believe that the characteristic hexagonal shape is indicative of the formation of single-crystal pure metal Zn. As the film thickness increases, layer structure of Zn plates are seen in Fig. 2b. After oxidation, the hexagonal Zn plates somewhat swelled due to the increase of the cell volume caused by the incorporation of oxygen (see Fig. 2c,d).

We carried out optical pumping for the sample at room temperature. Figure 3 shows the emission spectra observed with the different pulse energies. And the inset illustrates the measurement configuration. For the pulse energy of 0.022 mJ, a broad emission peak is observed at around 385 nm, which is attributed to a spontaneous emission of ZnO. As the excitation energy increases, the emission intensity rapidly increases and sharp peaks emerge in the spectra, when the excitation energy exceeded 0.043 mJ, showing the onset of laser action. The full-width half maximum (FWHM) of the sharp peaks is less than 0.6 nm, which is much smaller than that of the spontaneous emission peak. Figure 4 shows the integrated emission intensity as a function of incident pump pulse energy. The threshold intensity for the lasing was determined to be

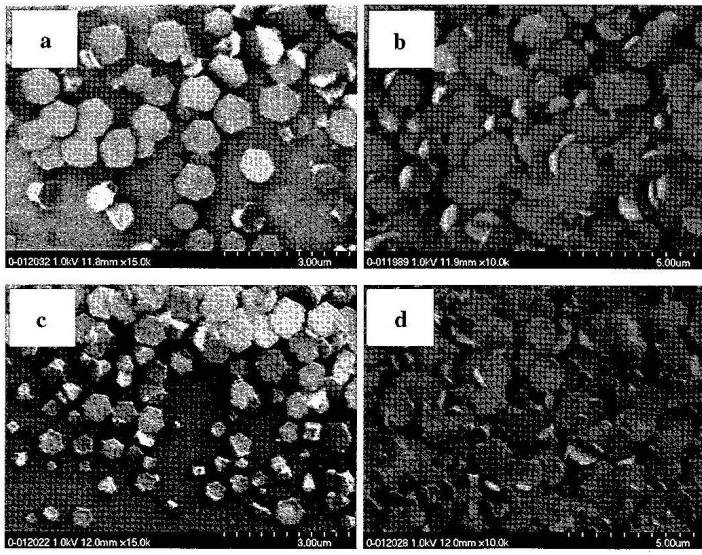

FIGURE 2 SEM images of as-prepared Zn films with a different film thickness ((**a**) and (**b**)) and the ZnO films ((**c**) and (**d**)) formed after oxidation at 380 °C for 6 h; a nominal film thickness of 50 nm for (**a**) and (**c**), and 500 nm for (**b**) and (**d**)

Nanometric summation architecture based on optical near-field interaction between quantum dots

Makoto Naruse, Tetsuya Miyazaki, and Fumito Kubota

National Institute of Information and Communications Technology, 4-2-1 Nukui-kita, Koganei, Tokyo 184-8795, Japan

Tadashi Kawazoe

Japan Science and Technology Agency, 687-1 Tsuruma, Machida, Tokyo 194-0004, Japan

Kiyoshi Kobayashi

Tokyo Institute of Technology, 2-12-1 Ookayama, Meguro-ku, Tokyo 152-8551, Japan

Suguru Sangu

Ricoh Co., Ltd., 16-1 Shinei-cho, Tsuzuki-ku, Yokohama, Kanagawa 224-0035, Japan

Motoichi Ohtsu

University of Tokyo, 7-3-1 Hongo, Bunkyo-ku, Tokyo 184-8795, Japan

Received July 22, 2004

A nanoscale data summation architecture is proposed and experimentally demonstrated based on the optical near-field interaction between quantum dots. Based on local electromagnetic interactions between a few nanometric elements via optical near fields, we can combine multiple excitations at a certain quantum dot, which allows construction of a summation architecture. Summation plays a key role for content-addressable memory, which is one of the most important functions in optical networks. © 2005 Optical Society of America

OCIS codes: 200.3050, 270.0270, 070.6020.

To meet future bandwidth requirements, a huge amount of computation must be performed at the nodes in optical networks and in data centers. Performing such computations in the optical domain[1] is expected to enhance overall system performance. However, integration of a large amount of optical hardware[2] is essentially constrained by the diffraction limit of light, which severly limits the overall capability.

Nanophotonics, on the other hand, is not restricted by the diffraction limit since it is based on local electromagnetic interactions between a few nanometric elements via optical near fields.[3] Consequently, suitable architectures should be built to exploit this capability of the physical layer. In this Letter we propose a data summation mechanism based on nanophotonics, which is, for instance, the basis for optical data matching or content-addressable memory (CAM).

We first describe architectural considerations regarding data matching and its optical implementation. CAM has an architecture in which the input signal content serves as a query to a database and the output is the address of data matching the input. CAM plays an important role in various applications, such as routers,[4] translation look-aside buffers, image processing, and data compression.

We can relate the CAM architecture to an inner product operation. We assume an N-bit input signal $\mathbf{S} = (s_1, \cdots, s_N)$ and reference data $\mathbf{D} = (d_1, \cdots, d_N)$. Here the inner product $\mathbf{S} \cdot \mathbf{D} = \sum_{i=1}^{N} s_i d_i$ will provide a maximum value when the input perfectly matches the reference data. The multiplication of two bits, namely, $x_i = s_i d_i$, has already been demonstrated by a combination of three quantum dots.[5] Therefore the key operation remaining is the summation $\sum x_i$, where all data bits x_i $(i = 1, \cdots, N)$ should be taken into account; this is shown schematically in Fig. 1(a). The existing ways of realizing such a data-gathering scheme include focusing lenses, optical waveguide couplings, and photodetector arrays; however, such methods impose yet another barrier to integration and miniaturization. In nanophotonics, on the other hand, optical energy is attracted to a certain quantum dot by optical near-field couplings between quantum dots, as described below.

The exclusiveness of the operations should be noted. The inner product $\mathbf{S} \cdot \mathbf{D}$ is, in fact, not enough to determine the correct matching of input $\mathbf{S}$ and reference $\mathbf{D}$; the inner product of the inverted input signal and reference data is also required. Inversion is, however, a difficult function to implement optically. One possible option is to properly design the modulation format,[6] for instance, by representing a logical level with two digits, for example, Logic 1 ="10" and Logic 0 ="01". Then, an N-bit logical input is physically represented by $2N$ bits, which makes the inner product equivalent to the matching operation. For the purpose of implementing the longest prefix matching, which is important for packet data transfer,[7] a "don't care" status is also required, and it can be coded as "11" in this scheme. Then, the resultant multiplication of a don't care bit to an incoming bit will be 1 for either Logic 0 or 1. Suppose that the reference data in memory $\mathbf{D}_1, \cdots, \mathbf{D}_M$ and input $\mathbf{S}$ are represented in the format described above. Then, the function of the CAM will be to derive the value j that maximizes $\mathbf{S} \cdot \mathbf{D}_j$ $(j = 1, \cdots, M)$.

In such a system each of the inner products is realized on the nanoscale, and therefore the overall CAM is realized in an extremely compact volume

0146-9592/05/020201-03$15.00/0

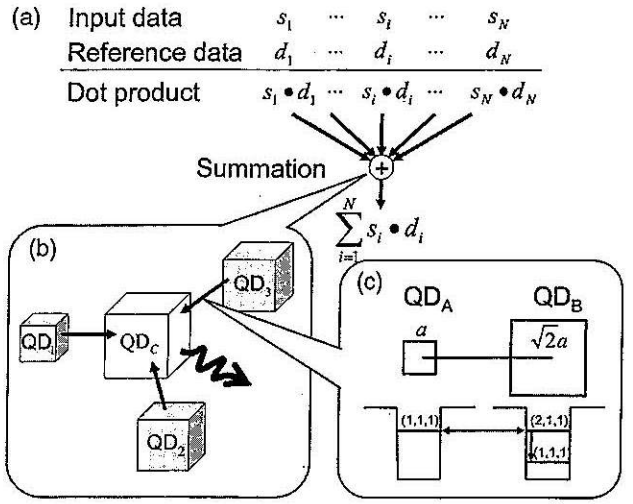

Fig. 1. (a) Inner product operation. (b) Summation mechanism in quantum dots. (c) Interdot interaction via an optical near field.

compared with its conventional counterpart. Moreover, conventional CAM VLSI chips consume lots of energy, whereas nanophotonic devices can be operated with extremely low energy.[5]

Here we describe the implementation of the summation architecture. It is based on interdot interaction via an optical near field, as shown schematically in Fig. 1(b) where excitations are transferred toward a certain quantum dot (QD_C at the center). As a fundamental case, we assume two quantum dots, QD_A and QD_B, as shown in Fig. 1(c). The ratio of the sizes of QD_A and QD_B is $1:\sqrt{2}$. There is a resonant quantized energy sublevel between these two dots, which are coupled by an optical near-field interaction.[5,8–10] Therefore the exciton population in the (1, 1, 1) level in QD_A is transferred to the (2, 1, 1) level of QD_B.[8–10] Note that this interaction is forbidden for far-field light.[9–11] Since the intrasublevel relaxation via exciton–phonon coupling is fast, the population is quickly transferred to the lower (1, 1, 1) level in QD_B. Similar energy transfers may take place in the dots surrounding QD_B among the resonant energy levels so that energy flow can occur. One could worry that, if the lower energy level of QD_B is occupied, another exciton cannot be transferred to that level because of the Pauli exclusion principle. Here, again because of the nature of the optical near-field interaction, the exciton population goes back and forth in the resonant energy level between QD_A and QD_B, which is called optical nutation.[9,10] Finally, both excitons can be transferred to QD_B. The lowest energy level in each quantum dot is coupled to a free photon bath to sweep out the excitation radiatively. The output signal is proportional to the (1, 1, 1)-level population in QD_B. Numerical calculations were performed based on quantum master equations in the density matrix formalism. The model Hamiltonian of the two dots is given by

$$H = \hbar\begin{bmatrix} \Omega_A & U \\ U & \Omega_B \end{bmatrix}, \tag{1}$$

where $\hbar U$ is the optical near-field interaction and $\hbar\Omega_A$ and $\hbar\Omega_B$ refer to the eigenenergies of QD_A and QD_B, respectively. For a two-exciton system we can prepare seven bases as summarized in Fig. 2(a), where one or two excitons occupy either one or two levels among the (1, 1, 1) level in QD_A (denoted by A), the (2, 1, 1) level in QD_B (denoted by B2), and the (1, 1, 1) level in QD_B (denoted by B1). These seven states are interconnected either by interdot near-field coupling (U), exciton–phonon coupling (Γ), or relaxation to the radiation photon bath (γ_A for QD_A and γ_B for QD_B). Within the Born–Markov approximation of the Liouville equation,[12,13] we can derive multiple differential equations. In the following we assume that $U^{-1} = 50$ ps, $\Gamma^{-1} = 10$ ps, $\gamma_A{}^{-1} = 2\sqrt{2}$ ns, and $\gamma_B{}^{-1} = 1$ ns as a typical parameter set.

First we consider an initial condition where there are two excitons in the system: one in QD_A and the other in QD_B (two-exciton system). The population of the (1, 1, 1) level in QD_B corresponds to the output signal, which is composed of three bases specified by (i), (ii), and (iii) in Fig. 2(a). The populations for those three bases, which are diagonal elements of the density matrix, are denoted by $\rho_{A,B1}(t)$, $\rho_{B1,B2}(t)$, and $\rho_{B1}(t)$, respectively; $\rho_{A,B1}(t)$ and $\rho_{B1,B2}(t)$ are related to

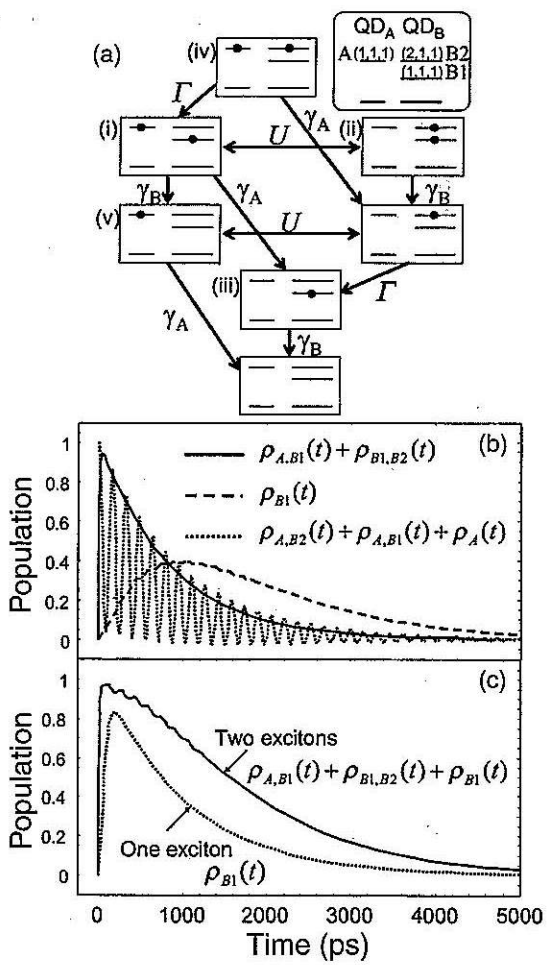

Fig. 2. (a) Bases of the two-exciton system in two quantum dots coupled by optical near fields. (b) Time evolution of the population in a two-exciton system. (c) Population comparison between one- and two-exciton systems.

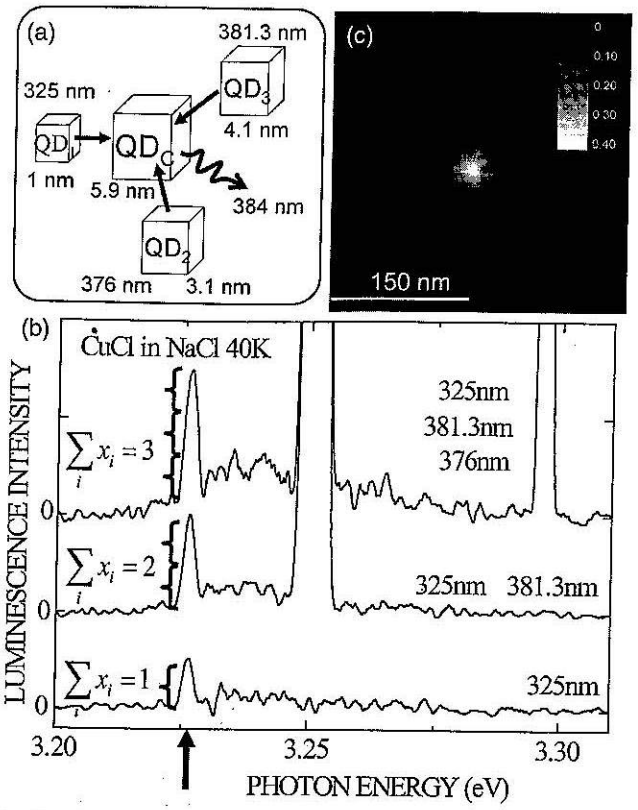

Fig. 3. Experimental results of the nanometric summation. (a) Quantum dot arrangement. (b) Luminescence intensity for three different numbers of excited QDs. (c) Spatial intensity distribution of the output photon energy.

two-exciton dynamics of the system. They show the time evolution of the one-exciton population in QD_A and in the upper level of QD_B, respectively, in addition to an exciton in the lower level of QD_B. The time evolution of $\rho_{A,B1}(t) + \rho_{B1,B2}(t)$ is shown by the solid curve in Fig. 2(b). The other population, $\rho_{B1}(t)$, has just one exciton in B1, and so it represents the output evolution of the one-exciton system, which is shown by the dashed curve in Fig. 2(b). Incidentally, the population when QD_A has an exciton, namely, the sum of the populations related to bases (i), (iv), and (v) in Fig. 2(a), is denoted by the dotted curve in Fig. 2(b). Nutation is observed as expected since the lower level of QD_B is likely to be busy and the interdot near-field interaction is faster than the relaxation bath coupling at each dot.

Next we compare the population dynamics between one- and two-exciton systems. The dotted curve in Fig. 2(c) shows the time evolution of the population in the lower level of QD_B, where, as initial conditions, one exciton exists only in QD_A. The solid curve in Fig. 2(c) is that for the two-exciton system. Physically the output signal is related to the integration of the population in the lower level of QD_B. Numerically integrating the population between 0 and 5 ns, we can obtain the ratio of the output signals between the two- and one-exciton systems as 1.86:1, which reflects the number of initial excitons, or the summation mechanism.

A proof-of-principle experiment was performed to verify the nanoscale summation using CuCl quantum dots in a NaCl matrix, which has also been employed for demonstrating nanophotonic switches[5] and optical nanofountains.[14] We choose a quantum dot arrangement in which small QDs (QD_1–QD_3) surrounded a large QD (QD_C), as shown schematically in Fig. 3(a). Here we irradiate at most three light beams with different wavelengths, 325, 376, and 381.3 nm, which excite QD_1, QD_2, and QD_3, respectively, with sizes of 1, 3.1, and 4.1 nm. The excited excitons are transferred to QD_C, and its radiation is observed by a near-field fiber probe. Notice the output signal intensity at a photon energy level of 3.225 eV in Fig. 3(b), which corresponds to a wavelength of 384 nm or a QD_C size of 5.9 nm. The intensity varies approximately as 1:2:3, depending on the number of excited QDs in the vicinity. The spatial intensity distribution was measured by scanning the fiber probe, as shown in Fig. 3(c), where the energy is converged at the center. Hence the architecture works as a summation mechanism based on exciton energy transfer via optical near-field interactions.

In summary, an architecture for data summation has been presented, and proof of principle has been demonstrated based on near-field coupling between quantum dots.

M. Naruse's e-mail address is naruse@nict.go.jp.

References

1. M. J. O'Mahony, D. Simeonidou, D. K. Hunter, and A. Tzanakaki, IEEE Commun. Mag. **39,** 128 (2001).
2. P. C. Teh, P. Petropoulos, M. Ibsen, and D. J. Richardson, IEEE J. Lightwave Technol. **19,** 1352 (2001).
3. M. Ohtsu, K. Kobayashi, T. Kawazoe, S. Sangu, and T. Yatsui, IEEE J. Sel. Topics Quantum Electron. **8,** 839 (2002).
4. H. Liu, IEEE Micro **22,** 58 (2002).
5. T. Kawazoe, K. Kobayashi, S. Sangu, and M. Ohtsu, Appl. Phys. Lett. **82,** 2957 (2003).
6. M. Naruse, H. Mitsu, M. Furuki, I. Izumi, Y. Sato, S. Tatsuura, M. Tian, and F. Kubota, Opt. Lett. **29,** 608 (2004).
7. K. Kitayama and M. Murata, IEEE J. Lightwave Technol. **21,** 2753 (2003).
8. T. Kawazoe, K. Kobayashi, J. Lim, Y. Narita, and M. Ohtsu, Phys. Rev. Lett. **88,** 067404 (2002).
9. S. Sangu, K. Kobayashi, A. Shojiguchi, T. Kawazoe, and M. Ohtsu, J. Appl. Phys. **93,** 2937 (2003).
10. S. Sangu, K. Kobayashi, A. Shojiguchi, and M. Ohtsu, Phys. Rev. B **69,** 115334 (2004).
11. Z. K. Tang, A. Yanase, T. Yasui, Y. Segawa, and K. Cho, Phys. Rev. Lett. **71,** 1431 (1993).
12. L. Mandel and E. Wolf, *Optical Coherence and Quantum Optics* (Cambridge U. Press, Cambridge, England, 1995).
13. H. J. Carmichael, *Statistical Methods in Quantum Optics I* (Springer-Verlag, Berlin, 1999).
14. T. Kawazoe, K. Kobayashi, and M. Ohtsu, in *Conference on Lasers and Electro-Optics (CLEO) 2004*, Vol. 96 of OSA Trends in Optics and Photonics Series (Optical Society of America, Washington, D.C., 2004), paper IFC1.

Near-field optical spectroscopy and microscopy of self-assembled GaN/AlN nanostructures

A. Neogi[a] and B. P. Gorman
Department of Physics and Materials Science and Engineering, University of North Texas, Denton, Texas 76203

H. Morkoç
Department of Electrical and Computer Engineering, Virginia Commonwealth University, Richmond, Virginia 23284

T. Kawazoe and M. Ohtsu
Department of Electrical Engineering, University of Tokyo, Tokyo, Japan

(Received 14 July 2004; accepted 30 November 2004; published online 19 January 2005)

The spatial distribution and emission properties of small clusters of GaN quantum dots in an AlN matrix are studied using high-resolution electron and optical microscopy. High-resolution transmission electron microscopy reveals near vertical correlation among the GaN dots due to a sufficiently thin AlN spacer layer thickness, which allows strain induced stacking. Scanning electron and atomic force microscopy show lateral coupling due to a surface roughness of ~50–60 nm. Near-field photoluminescence in the illumination mode (both spatially and spectrally resolved) at 10 K revealed emission from individual dots, which exhibits size distribution of GaN dots from localized sites in the stacked nanostructure. Strong spatial localization of the excitons is observed in GaN quantum dots formed at the tip of self-assembled hexagonal pyramid shapes with six $[10\bar{1}1]$ facets. © *2005 American Institute of Physics*. [DOI: 10.1063/1.1851005]

The successful development of short wavelength light-emitting diodes and the most recent realization of nitride-based quantum dot lasers have stimulated great interest in the application of quantum confined structures for blue and ultraviolet optoelectronic devices.[1,2] In particular, III-nitride-based self-assembled quantum dots (QDs) are very promising for a wide range of commercial applications.[3–7]

The study of self-assembled GaN quantum dots presents a challenge, as the placement of individual dots is difficult to control during the epitaxial growth process, and the dot density can be quite high.[8,9] Thus traditional experimental techniques often only allow simultaneous observation of large ensembles of quantum dots where inhomogeneous broadening washes out many of the interesting features. We have investigated the optical properties of GaN QD and have observed that the built-in strain fields significantly influence the radiative recombination lifetime.[10–12] The role of size distribution of the QDs on the radiative emission process is not yet clear.[12]

Recent reports on the near-field optical properties of GaN QD studied using illumination mode are limited by the low spatial resolution due to carrier diffusion accentuated by a large dot size inhomogeneity.[13,14] The contribution from individual dots or coupled QD clusters exhibiting narrow near-field photoluminescence (PL) line shape (~ few milli-electron-volts) from high-spatial resolution is yet to be reported. The PL line shape of individual dots in the GaN system is expected to be significantly broader than GaAs- or InP-based QDs due to broadening induced by a significantly larger LO phonon scattering rate. In this letter we present the near-field optical emission characteristics from a cluster of a few GaN QDs with very high spatial resolution. This letter will also discuss the lateral and vertical electronic coupling of dots caused by interdot scattering of carriers.

The sample consisted of 40-stacked planes of GaN QDs in AlN matrix, grown on a sapphire substrate by molecular beam epitaxy.[10,11] The buffer layer consisted of alternating layers of AlN and GaN grown on a thin layer of initiation AlN buffer. Quantum dots were formed by growing a GaN layer at just above the critical thickness, which allows it to maintain its pseudo-coherence with the AlN lattice. The QD planes were separated by 2-nm-thick AlN barriers and capped by an AlN layer 3 nm thick. The thin AlN spacer layer in the presence of self-assembly process led to the formation of GaN QDs embedded within two-dimensional GaN/AlN quantum-well-like structures.

The surface morphology of GaN nanostructures was studied using scanning electron (SEM) and atomic force microscopy (AFM). Shown in Fig. 1(a) is a topographical map of an area of 1×1 μm^2 measured using AFM, which exhibits a honeycomb feature at the surface due to modulation of the AlN cap layer by the underlying GaN QDs. Due to the thin cap layer, a high density (3×10^{10} dots/cm^2) of the QDs as well as a strong inhomogeneity of their lateral dimensions, ranging from 30 up to 50 nm, is clearly evidenced. The height of these capped QDs range from 7 to 10 nm. This nonuniform surface topology induces inhomogeneous broadening in the far-field emission spectrum due to lateral coupling. It was shown by Widmann *et al.*[8] that the QD size varies significantly depending on whether the QDs are allowed to evolve under vacuum before covering with AlN, or not, as a result of a ripening mechanism. This variation in size can lead to a large variation in the piezoelectric effect in the self-assembled GaN layers. Our experiments indicate that ripening leads to reduced footprint and increased height for a larger aspect ratio, as the dots are not spherical.[11]

[a]Author to whom correspondence should be addressed; electronic mail: arup@unt.edu

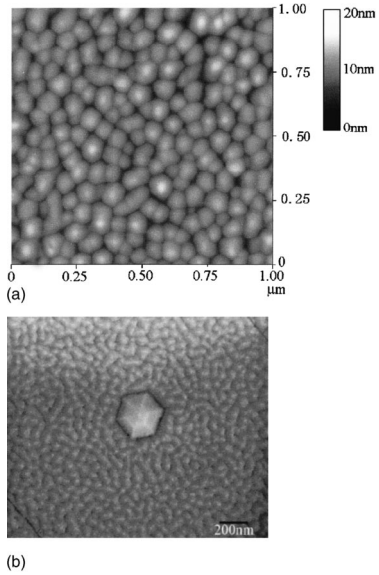

FIG. 1. (Color online) (a) AFM image showing the surface of GaN dots covered with 2 nm AlN cap layer. (b) SEM images showing the surface morphology and self-assembly of a hexagonal pyramid shape GaN structure with ~300 nm diameter.

The modulations at the surface are also observed in the high magnification SEM images [Fig. 1(b)]. The SEM spatial patterns of the capped GaN QDs showing island-like features can be correlated with the sample morphology as measured by AFM. A large hexagonal GaN pyramid is self-assembled on the AlN cap on the surface of the GaN QD layers with a radius of curvature no more than 300 nm. The faces of the pyramids are the $\{10\bar{1}1\}$ planes as evidenced by the angle between the inclined edge and the base of the pyramid. The measured angle of around 58°–60° is in good agreement with the calculated angle of 58.4° using the GaN lattice parameters of $c=5.185$ Å and $a=3.189$ Å. The formation of the pyramids indicates that the $\{10\bar{1}1\}$ surfaces are self-assembled preferentially compared to the $[000\bar{1}]$ surface. Thus it can be inferred that $\{10\bar{1}1\}$ surfaces have the lowest surface potential with respect to the self-assembly process. The tip of the pyramid is very sharp with a diameter measured to be less than 20 nm.

The optical emission properties were investigated by studying the PL characteristics in the far-field and near-field limit. Figure 2 shows the time-integrated far-field PL spectrum of QDs at room temperature, measured using a frequency tripled Ti:sapphire laser delivering pulses of 10 ps duration at 267 nm (photon energy 4.655 eV). The peak emission energy was close to 3.67 eV, with a broad linewidth of ~250 meV arising due to the inhomogeneous strain and also the lateral and vertical coupling amongst the QDs in the various layers. The PL peaks from the QD layers are shifted to a higher energy as compared to the underlying bulk GaN for the wurtzite phase (band gap energy $E_g=3.45$ eV). The inhomogeneously broadened PL line shape can be attributed to the emission from optically pumped carriers thermalized in the statistically distributed ground states of the probed QD, which vary in energy because of small variations in size, composition, and strain. The inset shows the temperature dependence of the PL intensity and emission linewidth. The relatively temperature-insensitive PL emission below 125 K occurs as the radiative decay of excited carriers dominates the recombination process.[12] However, above 125 K the PL intensity decreases more severely with increasing temperature due to increase in nonradiative recombination. The relatively small change in thermally induced PL peak energy shift (0.168 meV/K) is due to strong carrier confinement in the QDs with the redshift at higher temperatures likely due to a reduction of the exciton-Bohr radius that makes the excitons less polar.[9] The photoluminescence excitation spectrum measured using a Xe lamp shows absorption from the GaN nanostructures from higher energies. A large Stark shift exceeding 400 meV is observed to the built-in strain in the QD layers.

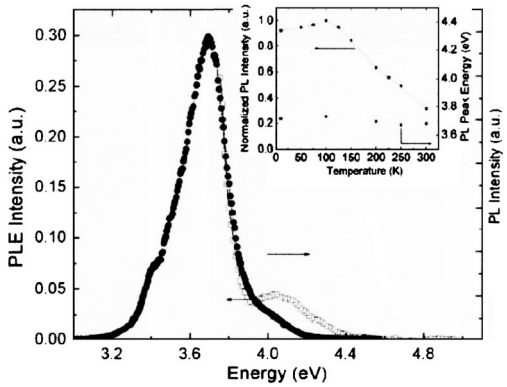

FIG. 2. (Color online) Far-field PL spectrum of GaN QDs with temperature dependence of PL intensity and PL emission energy shown in the inset.

Compared to bulk or GaN/AlN quantum well, a larger PL efficiency has been observed for this QD system despite a relatively shorter radiative lifetime of ~500 ps.[12] The role of inhomogeneity in the far-field PL spectra due to spatial QD distribution has been investigated via near-field PL spectroscopy. We have used a commercial (NSOM)[6] operating in illumination mode at 10 K for measuring the spatially and spectrally resolved PL spectra. A tapered, metal-coated optical fiber having a nominal apical aperture of 30 nm was exploited as the nanosource through which the sample was irradiated with UV light (325 nm delivered by a He–Cd cw laser). Figures 3(a)–3(c) show monochromatic PL images within a 450 nm^2 area, in which the detection wavelengths are 343 ± 1, 345 ± 1.5, and 355 ± 1 nm, respectively. The NSOM-PL in Figs. 3(a) and 3(c), which originates from a much smaller number of QDs compared to dot density obtained from surface features in Fig. 1, consists of a number of sharp spectral features of similar amplitude with full width at half maximum ranging from 500 μeV to 2 meV. We observe that the bright areas in Figs. 3(a) and 3(c) are larger than the dark ones. It may be that the honeycomb-like QD features observed at the surface are not entirely optically active and larger islands or smaller QDs presumably act as nonradiative recombination centers. The nucleation of relatively larger dots emitting at lower energies, i.e., ~3.49 eV [Fig. 3(c)] is more prevalent compared to the smaller dots emitting at higher energies ~3.62 eV [Fig. 3(a)]. The brighter regions A, B, C, E, F in Figs. 3(a) and 3(c) are an indication of strong confinement and a correlation in the vertical direction.

As the optically active part of our sample consists of 40 QD or QW planes, several layers with varying QD spatial distribution are excited simultaneously. So even if the NSOM probe is located above a region of the first QD layer

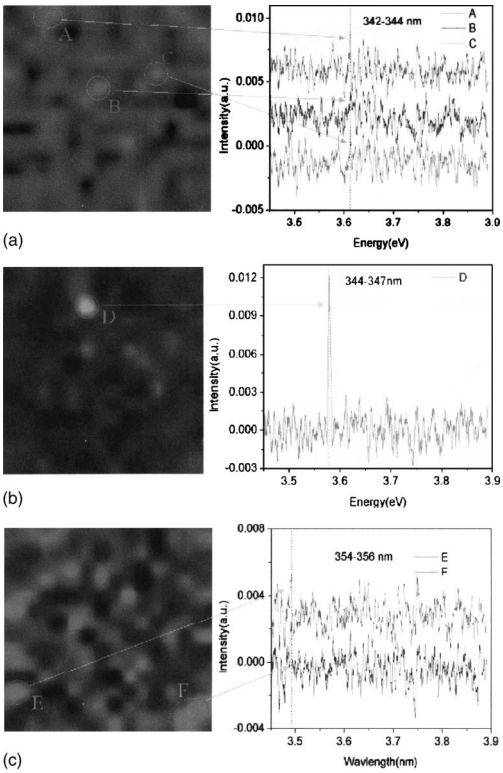

FIG. 3. Near-field luminescence spectra from GaN QD. (a) Spatial and spectrally resolved PL measured at 342–344 nm. (b) Spatial and spectrally resolved PL measured at 344–347 nm. (c) Spatial and spectrally resolved PL measured at 354–356 nm.

containing large dots, luminescence at high energy still originated from the underlying QD planes. This suggests that, while the intense background signal is due to the luminescence of a large part of the active region that cannot be spatially resolved, the localized modulations are due only to the morphology of the dots located on the outermost layer, which can be stronger in the presence of vertical correlation.

To gain insight into the origin of the light emission and the influence of spatial variation of GaN QDs and quantum wells on the intensity, we performed cross-sectional transmission electron microscopy (TEM). Samples were processed in a dual-beam SEM/FIB (FEI Nova 600) using a Ga ion beam accelerating voltage of 5 kV, followed by examination in a Tecnai F20 analytical HRTEM. A near vertical correlation of the GaN dots ~30 nm in width is observed from STEM-HAADF image (not shown here), with some dot assemblies being correlated at an angle slightly off vertical. It is also observed that the width of these dots and their period correspond to the surface texture observed in AFM and SEM images (Fig. 1). A HRTEM image shown in Fig. 4 illustrates that 1.1- to 2-nm-high GaN QD-like clusters are embedded in GaN/AlN QW-like structures.

It is reasonable to assign the high energy PL spectrum (Fig. 2) to the superposition of blueshifted near-band-gap excitonic emissions arising from clusters of dots with size smaller than the excitonic Bohr radius for GaN ($a_B \sim 3$ nm), at least in the growth direction (3 nm). The distribution of the dots in the vertically stacked layers also explains the background emission from spatially unresolved underlying QD and QW layers. The strong room-temperature PL is due to the vertical correlation of the dots, while the lateral coupling at the surface and underlying layers results in nonradiative recombination. Contrast observed in the NSOM images (Fig. 2) may be due to stronger emission from dot clusters correlated more closely to the vertical direction, as opposed to dot clusters correlated off-axis observed in Fig. 4.

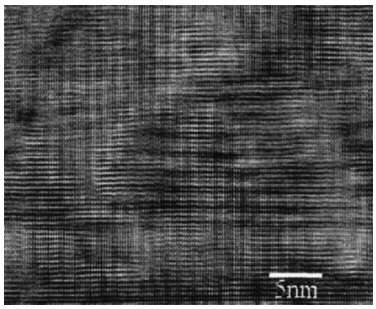

FIG. 4. HRTEM image showing $\langle 1-1-1-0 \rangle$ cross section of stacked layers GaN dots.

An intense emission is observed from a 20-nm-diam area "D" at an intermediate energy regime 3.59 eV (~345 nm), with a small background emission [Fig. 3(b)], implying that the source of this strong PL is significantly different from the emission of larger QDs or smaller QDs shown in Figs. 3(a) and 3(c). The emission at 3.39 eV is particularly strong in the vicinity of the hexagonal pyramid structure shown in Fig. 1(b). The emission is likely due to the localization of excitons in GaN QD formed at the tip of the hexagonal pyramid. The strong room-temperature PL is due to the vertical correlation of the dots, while the lateral coupling at the surface and underlying layers results in nonradiative recombination resulting in reduced PL emission at higher temperatures.

In conclusion we have studied the luminescence features of a sample of GaN quantum dots with a spatial resolution of 50 nm. The luminescence spatial patterns near the peak energy were measured, showing island-like features that can be correlated with the sample morphology as measured by AFM and SEM techniques. Cross-sectional TEM investigations revealed 1.1- to 2-nm-thick QD-like GaN layers correlated vertically or slightly off-axis, which may affect the vertical NSOM intensity data.

[1] H. Morkoç, *Nitride Semiconductors and Devices* (Springer, Heidelberg, 1999); S. Nakamura and G. Fasol, *The Blue Laser Diode* (Springer, Heidelberg, 1997).
[2] D. Huang, Y. Fu, and H. Morkoç, in *Optoelectronic Properties of Semiconductor Nanostructures*, edited by T. Steiner (Artech House, Boston, 2004).
[3] A. D. Yoffe, Adv. Phys. **42**, 173 (1993).
[4] K. Shimada, T. Sota, and K. Suzuki, J. Appl. Phys. **84**, 4951 (1998).
[5] F. Widmann, B. Daudin, G. Feuillet, Y. Samson, J. L. Rouvière, and N. Pelekanos, J. Appl. Phys. **83**, 7618 (1998).
[6] M. Ohtsu, K. Kobayahsi, T. Kawazoe, and S. Sangu, IEEE J. Sel. Top. Quantum Electron. **8**, 1 (2002).
[7] Y. Arakawa, T. Someya, and K. Tachibana, Phys. Status Solidi B **224**, 1 (2001).
[8] F. Widmann, J. Simon, N. T. Pelekanos, B. Daudin, G. Feuillet, J. L. Rouviere, and G. Fishman, Microelectron. J. **30**, 353 (1999).
[9] P. Ramvall, P. Riblet, S. Nomura, Y. Aoyagi, and S. Tanaka, J. Appl. Phys. **87**, 3883 (2000).
[10] H. Morkoc, A. Neogi, and M. Kuball, Mater. Res. Soc. Symp. Proc. **749**, 56743 (2004).
[11] A. Neogi, H. Everitt, and H. Morkoc, IEEE Trans. Nanotechnol. **2**, 10 (2003).
[12] A. Neogi, H. Everitt, and H. Morkoc, IEEE Trans. Nanotechnol. (in press).
[13] G. Salviati, F. Rossi, N. Armani, V. Grillo, O. Martinez, A. Vinattieri, B. Damilano, A. Matsuse, and N. Grandjean, J. Phys.: Condens. Matter **16**, S115 (2004).
[14] P. G. Gucciardi, A. Vinattieri, M. Colocci, B. Damilano, N. Grandjean, F. Semond, and J. Massies, Phys. Status Solidi B **224**, 53 (2001).

THE JOURNAL OF CHEMICAL PHYSICS **122**, 024715 (2005)

Nonadiabatic photodissociation process using an optical near field

Tadashi Kawazoe[a] and Kiyoshi Kobayashi[b]
SORST, Japan Science and Technology Agency, 687-1 Tsuruma, Machida, Tokyo 194-0004, Japan

Satoru Takubo
Interdisciplinary Graduate School of Science and Engineering, Tokyo Institute of Technology, 4259 Nagatsuta, Midori-ku, Yokohama 226-8502, Japan

Motoichi Ohtsu
SORST, Japan Science and Technology Agency, 687-1 Tsuruma, Machida, Tokyo 194-0004, Japan and Interdisciplinary Graduate School of Science and Engineering, Tokyo Institute of Technology, 4259 Nagatsuta, Midori-ku, Yokohama 226-8502, Japan

(Received 13 April 2004; accepted 12 October 2004; published online 23 December 2004)

We demonstrated the deposition of nanometric Zn dots using photodissociation with gas-phase diethylzinc and an optical near field under nonresonant conditions. To explain the experimental results, we proposed an exciton-phonon polariton model, and discuss the quantitative experimental dependence of the deposition rate on the optical power and photon energy based on photodissociation involving multiple-step excitation via molecular vibration modes. The physical basis of this process, which seems to violate the Franck-Condon principle, is the optically nonadiabatic excitation of the molecular vibration mode due to the steep spatial gradient of the optical near-field energy. © *2005 American Institute of Physics.* [DOI: 10.1063/1.1828034]

Optical near fields (ONF) have been applied to high-resolution optical microscopy, high-density optical memory, atom manipulation, and so on.[1] We have studied the application of ONF to nanostructure fabrication by applying the novel properties of ONF to photochemical reactions, and have demonstrated the feasibility of the chemical vapor deposition (CVD) of Zn dots using ONF techniques.[2–4] We have used the high spatial resolution capability of ONF to deposit 20 nm wide Zn wires[2] and 25 nm wide Zn dots.[4]

Conventional optical CVD utilizes a two-step process; photodissociation and adsorption. For photodissociation, far-field light must resonate the reacting molecular gasses in order to excite molecules from the ground state to an excited electronic state.[5,6] The Franck-Condon principle holds that this resonance is essential for excitation.[5] The excited molecules then relax to the dissociation channel, and the dissociated Zn atoms adsorb to the substrate surface. For near-field optical CVD (NFO-CVD), photodissociation can take place even under nonresonant conditions. Recently, we succeeded in the photodissociation of metal organic molecules and the deposition of Zn dots using a nonresonant ONF with a photon energy lower than the energy gap of the electronic state of the molecule.[7] This photochemical reaction is one of the unique phenomena of ONF, and we have presented several processes that may produce the photochemical reaction. In addition to optical CVD, these phenomena are applicable to many other photochemical nanotechnologies. Therefore, it is very important to clarify their physical origin. In this paper, we report the incident optical-power and photon energy dependencies of the deposition rate of Zn in NFO-CVD, and explain the experimental results based on the features of ONF and the exciton-phonon polariton (EPP) model.

In the EPP model, the ONF is able to excite the molecular vibration mode due to the steep spatial gradient of the ONF. Figure 1 illustrates schematics the excitation of the molecular vibration mode by ONF and EPP schematically. For an optical far field, the field intensity is uniform in a neutral molecule smaller than the wavelength. Only the electrons in the molecule respond to the electric field with the same phase and intensity. Therefore, an optical far field cannot excite the molecular vibration. By contrast, the field intensity is not uniform in a molecule for an ONF with a steep spatial gradient. The electrons respond nonuniformly, and the molecular vibration modes are excited because the molecular orbital changes and the molecule is polarized as a result of this nonuniform response of the electrons, as shown in Fig. 1(a). We propose the EPP model to quantify this excitation process. The EPP is a quasiparticle, which is an exciton polariton trailing the phonon (lattice vibration) generated by the steep spatial gradient of its optical filed, as shown in Fig. 1(b). The EPP model is formulated below.

Details of the experiment have been reported previously.[3,7] The cone angle and apex diameter of the fiber probe used for NFO-CVD were 30° and less than 30 nm, respectively.[1] Since a bare fiber probe without an opaque coating was used for deposition, far-field light leaked to the circumference of the fiber probe and an ONF was generated at the apex. This allowed us to investigate the deposition by an optical far field and ONF simultaneously. The optical power from the fiber probe was measured with a photodiode placed behind the sapphire substrate. The deposited Zn dots were measured using a shear-force microscope with the fiber probe used for deposition. The buffer gas was ultrahigh purity argon (Ar) at 3 Torr and the gas source of reactant mol-

[a]Electronic mail: kawazoe@ohtsu.jst.go.jp
[b]Present address: Department of Physics, Tokyo Institute of Technology, 2-12-1 O-okayama, Meguro-ku, Tokyo 152-8551, Japan.

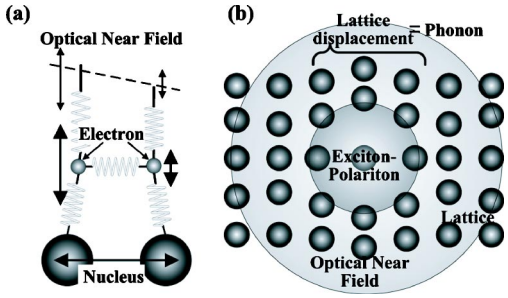

FIG. 1. Schematic explanations of the excitation of molecular vibration mode by ONF (a) and EPP (b).

ecules was diethylzinc (DEZn) at 100 mTorr at room temperature. A He-Cd laser ($\hbar\nu$=3.81 eV) was used as a nearly resonant light source with the absorption band edge E_{abs} (4.13 eV) of DEZn.[8] Ar^+ (2.54 eV) and diode (1.81 eV) lasers were used as nonresonant light sources.

Figure 2 shows shear-force topographical images of the sapphire substrate after NFO-CVD using the ONF for 3.81 eV (a), 2.54 eV (b), and 1.81 eV (c). The laser power and irradiation time were (a) 2.3 μW and 60 s, (b) 360 μW and 180 s, and (c) 1 mW and 180 s, respectively. While the previous work using conventional far-field optical CVD has claimed that a Zn film cannot be grown using nonresonant light ($\hbar\nu$<4.13 eV),[9] we observed the deposition of Zn dots

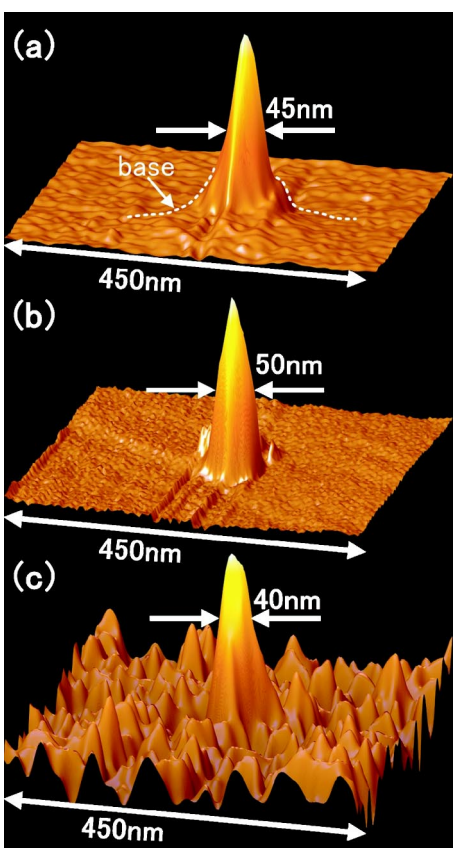

FIG. 2. Shear-force topographical images after NFO-CVD at photon energies of $\hbar\nu$=3.81 eV (a), 2.54 eV (b), and 1.81 eV (c). The scanning area are 450×450 nm^2. The observed laser output power and the irradiation time for deposition were 2.3 μW and 60 s (a), 360 μW and 180 s (b), and 1 mW and 180 s (c), respectively.

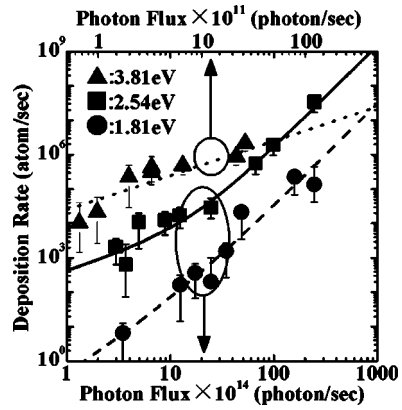

FIG. 3. The optical power (photon-flux: I) dependency of the rate R of Zn deposition. The dotted, solid, and broken curves fit the results using $R = aI + bI^2 + cI^3$.

on the substrate just below the apex of the fiber probe using NFO-CVD, even with nonresonant light. The chemical composition of the deposited material was confirmed by x-ray photoelectron spectroscopy. Moreover, we observed luminescence from nanometric ZnO dots, which were prepared by oxidizing the Zn dots fabricated by NFO-CVD.[4] These experimental results imply that the Zn was very pure.

In Fig. 2(a), the photon energy exceeds the dissociation energy (E_d=2.26 eV) of DEZn and is close to the E_{abs} of DEZn, i.e., $\hbar\nu > E_d$ and $\hbar\nu \approx E_{abs}$.[8] The diameter (full width at half maximum) and height of the topographical image were 45 and 26 nm, respectively. This image has a wide base, as shown by the dotted curves. This base is a Zn layer, less than 2 nm thick, which is deposited by far-field light leaking from the bare fiber probe. This deposition is possible because DEZn absorbs a small amount of light with $\hbar\nu$ =3.81 eV. The very high peak in the image suggests that ONF enhances the photodissociation rate, because ONF intensity increases rapidly near the apex of the fiber probe.

In Fig. 2(b), the photon energy still exceeds the dissociation energy of DEZn, but it is lower than the absorption edge, i.e., $\hbar\nu > E_d$ and $\hbar\nu < E_{abs}$.[8,10] The diameter and height of the image were 50 and 24 nm, respectively. While high intensity far-field light leaked from the bare fiber probe, it did not deposit a Zn layer, so there is no foot at the base of the peak. This confirmed that the photodissociation of DEZn and Zn deposition occurred only with an ONF of $\hbar\nu$=2.54 eV.

In Fig. 2(c), $\hbar\nu < E_d$ and $\hbar\nu < E_{abs}$. Even with such low photon energy, we succeeded in depositing of Zn dots. The topographical image had a diameter and height of 40 and 2.5 nm, respectively. We hardly claim that these depositions of Zn dots, in Fig. 2, are peculiar phenomena to an ONF, because while high intensity far-field light leaked from the bare fiber probe, the Zn dots are deposited on the substrate just below the apex of the fiber probe.

To quantify this novel photodissociation process, we examine the relationship between the photon-flux I and the deposition rate of Zn R in Fig. 3. For $\hbar\nu$=3.81 eV (▲), R is proportional to I. For $\hbar\nu$=2.54 (■) and 1.81 (●) eV, higher-order dependencies appear and are fitted by the third-order

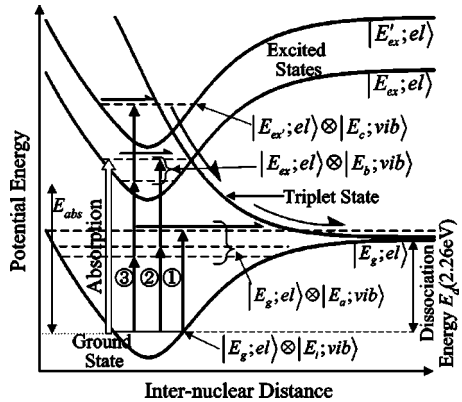

FIG. 4. Schematic drawing of potential curves of an electron in DEZn molecular orbitals. The relevant energy levels of the molecular vibration modes are indicated by the horizontal broken lines.

function $R=aI+bI^2+cI^3$. The respective values of $a_{\hbar\nu}$, $b_{\hbar\nu}$, and $c_{\hbar\nu}$ are $a_{3.81}=5.0\times10^{-6}$ and $b_{3.81}=c_{3.81}=0$ for $\hbar\nu=3.81$ eV; $a_{2.54}=4.1\times10^{-12}$, $b_{2.54}=2.1\times10^{-27}$, and $c_{2.54}=1.5\times10^{-42}$ for $\hbar\nu=2.54$ eV; $a_{1.81}=0$, $b_{1.81}=4.2\times10^{-29}$, and $c_{1.81}=3.0\times10^{-44}$ for $\hbar\nu=1.81$ eV. These values are used to investigate the physical origin of nonresonant NFO-CVD below.

Figure 4 schematically shows the potential curves of an electron in a DEZn molecular orbital drawn as a function of the internuclear distance of the C–Zn bond, which is involved in photodissociation.[8] The relevant energy levels of the molecular vibration mode are indicated by the horizontal broken lines in each potential curve. When a far-field light is used, photoabsorption (indicated by the white arrow in this figure) triggers the dissociation of DEZn.[11] By contrast, when nonresonant ONF is used, there are three possible origins of photodissociation, as we have already proposed.[7] They are (1) the multiple photon absorption process, (2) a multiple step transition process via the intermediate energy level induced by the fiber probe, and (3) the multiple step transition via an excited state of the molecular vibration mode. Possibility (1) is negligible, because the optical power density in the experiment was less than 10 kW/cm^2, which is too low for multiple photon absorption.[12] Possibility (2) is also negligible, because NFO-CVD was observed for the light in the ultraviolet~near-infrared region, although DEZn lacks relevant energy levels for such a broad region. As a result, our experimental results strongly supported possibility (3), i.e., the physical origin of the photodissociation caused by nonresonant ONF is a transition to an excited state via a molecular vibration mode. The three multiple-step excitation processes in Fig. 4, labeled by ①, ②, and ③ contributed to this.

To evaluate these contributions, we propose the EPP model, which describes the ONF generated at the nanometric probe tip.[13] An ONF is a highly mixed state with material excitation rather than a propagating light field; particularly, electronic excitation near the probe tip driven by photons incident into the fiber probe causes mode-mode or anharmonic couplings of phonons. They are considered renormalized phonon which allow multiple-phonon transfer from the tip to a molecule simultaneously.

The model Hamiltonian for the ONF probe can be diagonalized using the conventional theory,[14] and expressed in such a quasiparticle (EPP) representation as $H=\Sigma_p\hbar\omega(p)\xi_p^\dagger\xi_p$. Here, the creation (annihilation) operator for EPP and the frequency are denoted $\xi_p^\dagger(\xi_p)$ and $\omega(p)$, respectively. Therefore, in this model, a molecule located near the probe tip does not absorb simple photons, but absorbs EPP, the energies of which are transferred to the molecule, exciting molecular vibrations or inducing electronic transitions.

We will now discuss the dissociation probability of a molecule, assuming that the deposition rate of the metal atoms is proportional to the molecular dissociation rate. The transitions from the initial to the final states can be formulated accordingly to the conventional perturbation method for the interaction Hamiltonian that is given by the multipolar quantum electrodynamics Hamiltonian in the dipole approximation[15] for an optical near-field-molecule interaction as

$$H_{\text{int}}=-\int \boldsymbol{\mu}(\mathbf{r})\cdot\mathbf{D}^{\perp}(\mathbf{r})d^3r,$$

$$\mathbf{D}^{\perp}(\mathbf{r})=i\sum_p\left(\frac{2\pi\hbar\omega_p}{V}\right)^{1/2}\boldsymbol{\epsilon}_{\mathbf{p}}[a_p\exp(i\mathbf{pr})-a_p^\dagger\exp(-i\mathbf{pr})].$$

Here $\boldsymbol{\mu}(\mathbf{r})$ and $\mathbf{D}^{\perp}(\mathbf{r})$ denote the electric dipole operator and the electric displacement vector at position $\mathbf{r}$, respectively. The polarization unit vector of a photon is designated as $\boldsymbol{\epsilon}_{\mathbf{p}}$. Rewriting the photon operators $(a_p,a_p^\dagger)$ in terms of the exciton-phonon polariton operators $(\xi_p,\xi_p^\dagger)$ discussed above, and noticing that the electric dipole operator consists of two components (electronic and vibrational), we have the interaction Hamiltonian expressed in terms of EPP as

$$H_{\text{int}}=i\{\mu^{\text{el}}(e+e^\dagger)+\mu^{\text{nucl}}(v+v^\dagger)\}\times\sum_{\mathbf{p}} i\sqrt{\frac{2\pi\hbar\omega_p}{V}}\{v_pv_p'(\xi_p+\xi_p^\dagger)\}e^{i\mathbf{pr}}.$$

Here μ^{el} and μ^{nucl} are the electronic and vibrational dipole moments, respectively, and the creation (annihilation) operators of the electronic and vibrational excitations are denoted by $e^\dagger(e)$ and $v^\dagger(v)$, respectively. The incident photon frequency and transformation coefficients are ω_p and $v_p(v_p')$, respectively. Then, the transition probability of one-, two-, and three-step excitation (labeled ①, ②, and ③ in Fig. 4, and denoted by the corresponding final states as $|f_{\text{first}}\rangle$, $|f_{\text{second}}\rangle$, and $|f_{\text{third}}\rangle$) can be written as

$$P_{\text{first}}(\omega_p)=\frac{2\pi}{\hbar}|\langle f_{\text{first}}|H_{\text{int}}|i\rangle|^2=\frac{(2\pi)^2}{\hbar d}v_p^2v_p'^2u_p'^2(\mu^{\text{nucl}})^2I_0(\omega_p),$$

$$P_{\text{second}}(\omega_p)=\frac{2\pi}{\hbar}|\langle f_{\text{second}}|H_{\text{int}}|i\rangle|^2=\frac{(2\pi)^3}{\hbar d^2}\frac{v_p^4 v_p'^6 u_p'^2}{|\hbar\omega(p)-(E_a-E_i+\mathrm{i}\gamma_m)|^2}(\mu^{\text{el}})^2(\mu^{\text{nucl}})^2 I_0^2(\omega_p),$$

$$P_{\text{third}}(\omega_p)=\frac{2\pi}{\hbar}|\langle f_{\text{third}}|H_{\text{int}}|i\rangle|^3=\frac{(2\pi)^4}{\hbar d^3}\frac{v_p^6 v_p'^{10} u_p'^2}{|\hbar\omega(p)-(E_a-E_i+\mathrm{i}\gamma_m)|^2|\hbar\omega(p)-(E_{ex}-E_g+i\gamma_m')|^2}(\mu^{\text{el}})^4(\mu^{\text{nucl}})^2 I_0^3(\omega_p),$$

where du_p', and $I_0(\omega_p)$ represent the probe tip transformation coefficient and incident light intensity, respectively. Energy conservation is assumed in each transition probability. For this purpose, the following initial and three final states of a system consisting of the optical near-field probe and a molecule are prepared:

$$|i\rangle=|\text{probe}\rangle\otimes|E_g;\text{el}\rangle\otimes|E_i;\text{vib}\rangle,$$

$$|f_{\text{first}}\rangle=|\text{probe}\rangle\otimes|E_g;\text{el}\rangle\otimes|E_a;\text{vib}\rangle,$$

$$|f_{\text{second}}\rangle=|\text{probe}\rangle\otimes|E_{ex};\text{el}\rangle\otimes|E_b;\text{vib}\rangle,$$

$$|f_{\text{third}}\rangle=|\text{probe}\rangle\otimes|E_{ex'};\text{el}\rangle\otimes|E_c;\text{vib}\rangle,$$

where $|\text{probe}\rangle$, $|E_\alpha;\text{el}\rangle$, and $|E_\beta;\text{vib}\rangle$ represent a probe state, molecular electronic state, and vibrational state, respectively. In addition, $E_a(\alpha=g,ex,ex')$ and $E_\beta(\beta=i,a,b,c)$ represent the molecular electronic and vibrational energies, respectively, as schematically shown in Fig. 4, and γ_m and γ_m' are the inewidth of the vibrational and electronic states, respectively. It follows that these near-resonant transition probabilities have the following ratio:

$$\frac{P_{\text{second}}(\omega_p)/I_0^2(\omega_p)}{P_{\text{first}}(\omega_p)/I_0(\omega_p)}=\frac{P_{\text{third}}(\omega_p)/I_0^3(\omega_p)}{P_{\text{second}}(\omega_p)/I_0^2(\omega_p)}=\frac{\hbar}{2\pi}\frac{P_{\text{first}}(\omega_p)}{|\gamma_m|^2 I_0(\omega_p)}\left(\frac{v_p'^2}{u_p'^2}\right)\left(\frac{\mu^{\text{el}}}{\mu^{\text{nucl}}}\right)^2.$$

Here we assume $\gamma_m=\gamma_m'$, for simplicity. Using this ratio, we analyze the experimental intensity dependence of the deposition rate to clarify possibility (3). For $\hbar\nu=2.54$ eV, all the processes (①, ②, and ③) depicted in Fig. 4 are possible because $\hbar\nu>E_d$ (although $\hbar\nu<E_{abs}$). Fitting the experimental value of $P_{\text{first}}(\omega_{2.54})=a_{2.54}I_0(\omega_{2.54})=10^2$ events/s with reasonable values of $\mu^{\text{nucl}}=1$ D, $\mu^{\text{el}}=10^{-3}$ D, $\gamma_m=10^{-1}$ eV, and $v_p'^2/u_p'^2=0.01$, and $d=30$ nm, we obtain the following value for the ratio:

$$\frac{P_{\text{second}}(\omega_{2.54})/I_0^2(\omega_{2.54})}{P_{\text{first}}(\omega_{2.54})/I_0(\omega_{2.54})}=\frac{P_{\text{third}}(\omega_{2.54})/I_0^3(\omega_{2.54})}{P_{\text{second}}(\omega_{2.54})/I_0^2(\omega_{2.54})}=\frac{\hbar}{2\pi}\frac{P_{\text{first}}(\omega_{2.54})}{|\gamma_m|^2 I_0(\omega_{2.54})}\left(\frac{v_p'^2}{u_p'^2}\right)\left(\frac{\mu^{\text{el}}}{\mu^{\text{nucl}}}\right)^2\simeq 10^{-15},$$

which is in good agreement with the experimental values $b_{2.54}/a_{2.54}\simeq c_{2.54}/b_{2.54}\simeq 10^{-15}$. For $\hbar\nu=1.81$ eV, dissociation occurs via either ② or ③ shown in Fig. 4, because $\hbar\nu<E_d(E_{obs})$. The ratio can be evaluated as

$$\frac{P_{\text{third}}(\omega_{1.81})/I_0^3(\omega_{1.81})}{P_{\text{second}}(\omega_{1.81})/I_0^2(\omega_{1.81})}=\frac{\hbar}{2\pi}\frac{P_{\text{first}}(\omega_{1.81})}{|\gamma_m|^2 I_0(\omega_{1.81})}\left(\frac{v_p'^2}{u_p'^2}\right)\left(\frac{\mu^{\text{el}}}{\mu^{\text{nucl}}}\right)^2\simeq 10^{-15},$$

which is also in good agreement with the experimental value $c_{1.81}/b_{1.81}\simeq 10^{-15}$. For the theoretical estimation, we use the experimental value for $P_{\text{first}}(\omega_{1.81})\simeq a_{2.54}I_0(\omega_{2.54})=10^2$ events/s because both transitions for light with photon energies of 1.84 and 2.54 eV are attributed to the coupling between phonons in the probe and molecular vibrations. The overall agreement between the theoretical and experimental results suggests that the EPP model provides a way to understand the physical origin of the near-field photodissociation process. For $\hbar\nu=3.81$ eV, the direct absorption by the electronic state is much stronger than in other cases, because the light is near resonant for DEZn. This is why we did not observe higher-order power dependence of the deposition rate in the optical power region that we observed.

In conclusion, we demonstrated NFO-CVD of nanometric Zn dots based on the photodissociation of gas-phase diethylzinc using ONF under nonresonant conditions. To clarify the physical origin of this process, the optical power and photon energy dependencies of the deposition rates were measured. We explain the dependencies using a multiple-step excitation process via the molecular vibration mode and the EPP model. In this model, the enhanced coupling between the optical field and molecular vibration originates from the steep spatial gradient of the optical power of ONF. Such a nonadiabatic photochemical process violates the Franck-Condon principle that assumes an adiabatic process, and is applicable to other photochemical phenomena. The process involved in the photochemical reaction based on ONF reported here will open new methods in nanotechnology.

[1] See, for example, edited by M. Ohtsu, *Near-Field Nano/Atom Optics and Technology* (Springer, Tokyo, 1998).
[2] V. V. Polonski, Y. Yamamoto, M. Kourogi, H. Fukuda, and M. Ohtsu, J. Microsc. **194**, 545 (1999).
[3] Y. Yamamoto, M. Kourogi, M. Ohtsu, V. Polonski, and G. H. Lee, Appl. Phys. Lett. **76**, 2173 (2000).
[4] T. Yatsui, M. Ueda, Y. Yamamoto, T. Kawazoe, M. Kourogi, and M. Ohtsu, Appl. Phys. Lett. **81**, 3651 (2002).
[5] J. G. Calvert and J. N. Patts, Jr., *Photochemistry* (Wiley, New York, 1966).
[6] R. L. Jackson, J. Chem. Phys. **96**, 5938 (1992).
[7] T. Kawazoe, Y. Yamamoto, and M. Ohtsu, Appl. Phys. Lett. **79**, 1184 (2001).
[8] R. L. Jackson, J. Chem. Phys. **96**, 5938 (1992).

[9] M. Shimizu, H. Kamei, M. Tanizawa, T. Shiosaki, and A. Kawabata, J. Cryst. Growth **89**, 365 (1988).
[10] R. L. Jackson, Chem. Phys. Lett. **163**, 315 (1989).
[11] H. Okabe, *Photochemistry* (Wiley, New York, 1978).
[12] A. Yariv, *Introduction to Optical Electronics*, 3rd ed. (Holt, Rinehart and Winston, New York, 1985).
[13] K. Kobayashi, S. Sangu, H. Ito, and M. Ohtsu, Phys. Rev. A **63**, 013806 (2001).
[14] J. J. Hopfield, Phys. Rev. **112**, 1555 (1958); A. L. Ivanov, H. Haug, and L. V. Keldysh, Phys. Rep. **296**, 237 (1998).
[15] D. P. Craig and T. Thirunamachandran, *Molecular Quantum Electrodynamics* (Dover, New York, 1998).

Available online at www.sciencedirect.com
SCIENCE DIRECT®
Applied Surface Science 239 (2005) 394–397
applied surface science
www.elsevier.com/locate/apsusc

Room temperature near-field photoluminescence of zinc-blend and wurtzite ZnO structures

G.H. Lee[a,*], T. Kawazoe[b], M. Ohtsu[b,c]

[a]*Department of Information Materials Engineering, Dong-Eui University, 995 Eomgwangno, Busanjin-gu, Busan 614-714, South Korea*
[b]*Japan Science and Technology Corporation, 687-1 Tsuruma, Machida, Tokyo 194-0004, Japan*
[c]*Interdisciplinary Graduate School of Science and Engineering, Tokyo Institute of Technology, 4259 Nagatsuda, Midori-ku, Yokohama 226-8502, Kanagawa, Japan*

Accepted 2 June 2004
Available online 3 August 2004

Abstract

Near-field photoluminescence (PL) was measured from ZnO film, composed of nanocrystallites with zinc-blend (ZB) and wurtzite (W) structures, on a sapphire (0 0 0 1) substrate at room temperature (RT). The size of nanocrystallites was in the range of 30–50 nm. Using a fiber probe with aperture size of 80 nm, two near-field emission peaks attributed to one ZB and one W structures were observed. The difference in the emission energies was 0.10 eV close to the calculated bandgap difference between ZB and W structures. The intensity of emission peak from ZB structure with lower energy was stronger than that from W structure, which is supposed to be resulted from the quenched excitonic effect of W structure.

PACS: 42.70.−a; 73.61.Tm; 78.55.−m; 81.05.Dz

Keywords: ZnO; Wurtzite; Zinc-blend; Near-field photoluminescence

1. Introduction

ZnO is an interesting material in optoelectronics due to its wide bandgap energy of 3.27 eV at room temperature (RT) and the large exciton binding energy of 60 meV. The exciton binding energy is larger than the thermal energy at RT of 24 meV, which results in not only the ultraviolet (UV) excitonic emission with high efficiency, but also the optically pumped excitonic lasing with low threshold even at the temperature higher than RT [1,2]. Owing to these features, ZnO has become one of the most promising materials for blue and ultraviolet light emitting diode and diode lasers.

ZnO can have zinc-blend (ZB) structure of cubic phase or wurtzite (W) structure of hexagonal phase. However, since W structure is predominant, the formation of ZB-ZnO structure on sapphire substrate, which has been widely used as the substrate due to its thermal stability and high transparency, has not been yet reported. On the other hand, it is well known that W–ZnO induces piezoelectric field effects by residual strain, which tends to quench the excitonic effects, while the ⟨0 0 1⟩ direction in ZB structure is free from the piezoelectric field. This implies that more effective

* Corresponding author. Tel.: +82 51 890 1722; fax: +82 51 890 1619.
E-mail address: ghl@deu.ac.kr (G.H. Lee).

0169-4332/$ – see front matter
doi:10.1016/j.apsusc.2004.06.004

UV excitonic emission and lasing are expected from ZnO with ZB structure. Thus, it is of considerable importance to fabricate ZB-ZnO and observe its optical properties.

Since the conventional far-field spectroscope measures an ensemble of nanocrystallites with size fluctuation, it results in inhomogeneous broadened spectral features, which makes it impossible to evaluate the precise intrinsic crystallographic contribution from the nanocrystallites. In contrast to this, near-field optical microscope has nanoscale resolution, which enables us to evaluate the optical properties of nanometer scale structure and nanocrystallite. Recently we have succeeded in evaluating optical spectra and quantum size effect of individual ZnO nanocrystallite using an optical near-field technique [3,4].

In this letter, we report on the characteristic optical bandgap difference between W and ZB-ZnO structures through the PL spectra observed by near-field spectroscope at RT as well as the comparison of excitonic effect on emission. The PL spectra of a nanocrystallite with W structure and one with ZB structure were observed by employing a high throughput fiber probe with an aperture of 80 nm.

2. Experimental procedure

The ZnO film was prepared by oxidizing ZB-ZnS film deposited epitaxially on a sapphire (0 0 0 1) substrate. The ZnS film was deposited at 800 °C under working pressure of 7×10^{-7} Torr by pulsed laser deposition (PLD) method. KrF excimer laser (λ = 248 nm, duration time: 20 ns, energy density: 5 J/cm^2) was used as a light source for the ablation of the single crystal ZB-ZnS target. In the initial growth, ZnS with ZB structure was grown on sapphire substrate. Thus ZnS was deposited with the thickness of 3 nm and oxidized at 900 °C under oxygen stream for 2 h. After the oxidation, any ZnS peaks were not obtained and predominant peaks from (0 0 0 2) of W-ZnO and (0 0 4) of ZB-ZnO structure were observed in X-ray diffraction patterns. The surface morphology was observed using atomic force microscope (AFM) at RT in air. The PL was measured with conventional far-field PL spectroscope and near-field PL spectroscope at RT and 77 K. The experimental setup is represented in Fig. 1. A continuous wave He-Cd laser (λ = 325 nm) was used for exciting ZnO nanocrystallites. Far-field PL spectra were measured through a cooled charge coupled device with a monochromator. The signal of near-field PL was collected through the fiber probe. For the effective detection of near-field PL, the fiber probe was controlled in close proximity to the sample surface (~10 nm) by shear force feedback technique. The fiber probe was fabricated using an UV fiber constituted of pure silica core and fluorine-doped cladding [5]. The tip of fiber was sharpened by employing the pulling/etching technique. Then the cone angle and the apex diameter of the fiber tip was 60° and <10 nm. The sharpened tip was coated with 500 nm thick Al film by an evaporator. The Al film on the top of the core was removed by using a focused ion beam to fabricate an aperture with the diameter as small as 80 nm.

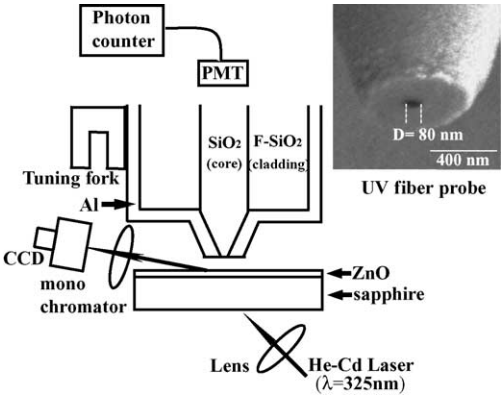

Fig. 1. Experimental setup for measurement of far- and near-field photoluminescence. The aperture diameter of used fiber probe is 80 nm.

3. Results and discussion

Fig. 2a shows the surface of the oxidized film observed by AFM. Columnar and hexagonal crystallites with the size of 30–50 nm are clearly observed. Considering the crystallographic structures, it can be suggested that the hexagonal phase and the columnar phase represent typically c-axis oriented W structure and c-axis oriented ZB structure, respectively. This suggestion is proved from the θ–2θ XRD patterns measured on the film. As shown in Fig. 2b, the two dominant diffraction peaks from the (0 0 0 2) plane of

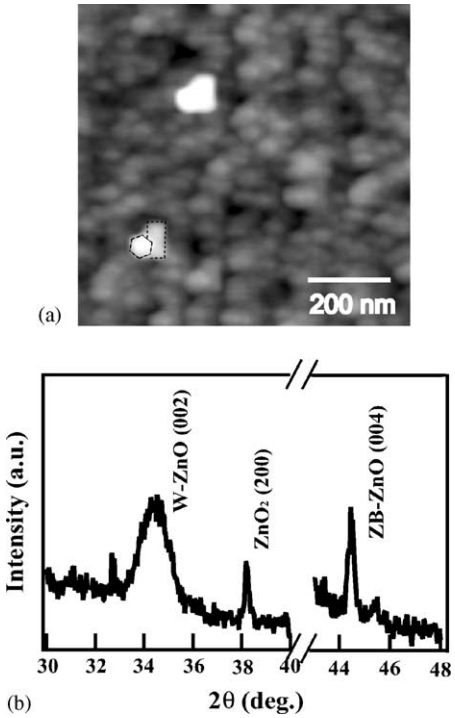

Fig. 2. (a) AFM image of the surface and (b) θ–2θ XRD patterns for ZnO film obtained by thermal oxidation of ZnS film deposited with the thickness of 3 nm on a sapphire (0 0 0 1) substrate.

W structure and the (0 0 4) plane of ZB structure are observed, which indicates that the oxidized film is made up of ZnO nanocrystallites with W and ZB structures.

Fig. 3a and b shows the far-field PL spectra measured at RT and 77 K, respectively. One emission peak with its energy of 3.17 eV ($\lambda = 390$ nm) is observed at RT, while two peaks with peak energies of 3.22 eV ($\lambda = 384$ nm) and 3.12 eV ($\lambda = 397$ nm) are obtained at 77 K due to the suppression of spectral broadening resulted from diminished phonon scattering effect. The emission energy difference of the two peaks is 0.10 eV, which is very close to the calculated difference in energy gap between ZB and W–ZnO structures (0.08 eV) [6]. Consistent with the surface morphology of the ZnO film showing hexagonal and columnar crystallites, the emission energy difference shows that the two emission peaks are attributed to W and ZB-ZnO structure. The emission with higher energy is assigned to W structure and that with lower energy to ZB structure.

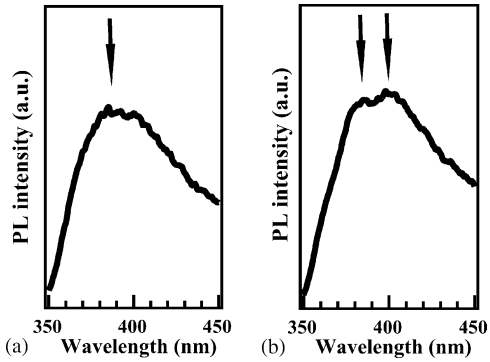

Fig. 3. Far-field PL spectra measured at (a) room temperature and (b) 77 K for ZnO film obtained by thermal oxidation of ZnS film with the thickness of 3 nm grown on a sapphire (0 0 0 1) substrate.

To exclude the spectral broadening appeared in far-field PL spectroscope due to size fluctuation of nanocrystallites, PL measurement was performed at RT using near-field PL spectroscope with high spatially and spectrally resolution. It has been reported the spatial and spectral resolution of the used near-field optical microscope at room temperature [3]. The spatial resolution of the near-field optical microscope was estimated from a monochromatic near-field PL image measured for ZnO nanocrystallites with the grain size in the range of 30–160 nm. The diameter of apertured UV fiber probe was 80 nm, which was the same probe as used in this study. The cross sectional profile of spots in the near-field PL image was comparable to the grain size of ZnO nanocrystallites. In addition, the spatial resolution of the near-field PL spectroscope was sufficient to resolve the single ZnO nanocrystallite with the size of 55 nm [4]. This indicates that our near-field PL spectroscope system has considerable spatial variation reflecting the local crystallite structure with the size of 30–50 nm. Accordingly, as known from the crystallite size shown in Fig. 2, the PL signal from a single columnar and a single hexagonal crystallite can be detected through the aperture with the diameter of 80 nm. Fig. 4 shows the near-field PL spectrum measured at RT. The two peaks were observed obviously by fitting the PL spectrum even at RT. The peak energies were 3.22 eV ($\lambda = 384$ nm) and 3.12 eV ($\lambda = 397$ nm), which are well in accordance with those measured by far-field PL spectroscope at 77 K. Thus it is concluded that the two emission peaks originates from W

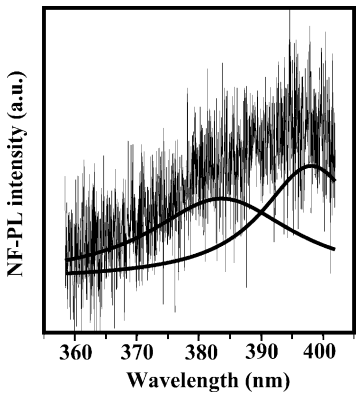

Fig. 4. Near-field PL spectrum measured at room temperature for ZnO film obtained by thermal oxidation of ZnS film with the thickness of 3 nm grown on a sapphire (0 0 0 1) substrate.

and ZB nanocrystallites shown as columnar and hexagonal phase, respectively. The observation of the two peaks at RT is based on the high spatial and spectral resolution, the most important feature of near-field PL spectroscope [7]. In addition, the intensity of emission peak of ZB structure with lower energy is stronger than that of W structure with higher emission energy, which is not observed in far-field PL spectrum. The excitonic effect in W-ZnO is quenched by piezoelectric field effect resulted from residual strain, while the $\langle 0\,0\,1 \rangle$ direction in ZB structure are free from the piezoelectric field. It has also been reported that the near-field PL spectroscope used in this study showed the difference in the near-field PL intensity between the ZnO nanocrystallites with different orientations [3]. Because the exciton density depends on the crystal orientation in ZnO [8], the difference in the emission intensity means the difference of exciton density. Thus the two emission peaks in Fig. 4 suggests that the emission stimulated by excitons in ZB structure may be stronger than that in W structure. This phenomenon could be observed by near-field PL spectrum. Because a single ZB and a single W crystallites were measured in near-field PL spectrum, the quenched excitonic effect of W crystallite could be clearly detected and thus the PL intensity of excitonic emission from ZB crystallite was observed stronger than that from W crystallite. To our knowledge, this is the first report on the comparison of the feature of excitonic emission between W and ZB-ZnO structures.

4. Conclusions

The characteristic difference of 0.10 eV in optical bandgap of zinc-blend and wurtzite ZnO structures was observed at room temperature by near-field PL spectroscope. The quenched excitonic effect of wurtzite crystallite could be detected obviously and thus the PL intensity of excitonic emission from zinc-blend crystallite was stronger than that from wurtzite crystallite, which indicates that ZnO film with zinc-blend structure offers the possibility of realizing more effective UV light emitting devices. In addition, the successful growth of ZB-ZnO nanocrystallite, in the metastable form, will be very useful information when nanophotonic devices integrated with ZnO nanocrystallines or ZnO nanostructures are fabricated on sapphire substrate.

References

[1] Z.K. Tang, G.K.L. Wong, P. Yu, M. Kawasaki, A. Ohtomo, H. Koinuma, Y. Segawa, Appl. Phys. Lett. 72 (1998) 3270.
[2] D.M. Bagnall, Y.F. Chen, Z. Zhu, T. Yao, M.Y. Shen, T. Goto, Appl. Phys. Lett. 73 (1998) 1038.
[3] T. Yatsui, T. Shimizu, Y. Yamamoto, M. Kourogi, M. Ohtsu, G.H. Lee, Appl. Phys. Lett. 79 (2001) 2369.
[4] T. Yatsui, T. Shimizu, Y. Yamamoto, M. Kourogi, M. Ohtsu, G.H. Lee, Appl. Phys. Lett. 80 (2002) 1444.
[5] S. Mononobe, T. Saiki, T. Suzuki, S. Koshihara, M. Ohtsu, Opt. Commun. 146 (1998) 45.
[6] C. Yeh, S. Wei, A. Zunger, Phys. Rev. B 50 (1994) 2715.
[7] M. Ohtsu (Ed.), Near-field Nano/Atom Optics and Technology, Springer, Tokyo, 1999, Chapter 3.
[8] S. Bloom, I. Ortenburger, Phys. Status Solidi B 57 (1973) 561.

Room-temperature synthesis of ultraviolet-emitting nanocrystalline GaN films using photochemical vapor deposition

Shunsuke Yamazaki
Interdisciplinary Graduate School of Science and Engineering, Tokyo Institute of Technology, 4259 Nagatsuta, Midori-ku, Yokohama, Kanagawa, 226-8502 Japan

Takashi Yatsui[a)]
Solution-Oriented Research for Science and Technology (SORST), Japan Science and Technology Agency, 687-1 Tsuruma, Machida, Tokyo, 194-0004 Japan

Motoichi Ohtsu[a)]
School of Engineering, The University of Tokyo, 7-3-1 Hongo, Bunkyo-ku, Tokyo 113–8656, Japan and SORST, Japan Science and Technology Agency, 687–1 Tsuruma, Machida, Tokyo, 194–0004 Japan

Taw-Won Kim
Kanagawa Academy of Science and Technology (KAST), 3-2-1 Sakado, Takatsu-ku, Kawasaki, Kanagawa, 213-0012 Japan

Hiroshi Fujioka
Institute of Industrial Science, The University of Tokyo, 4-6-1 Komaba, Meguro-ku, Tokyo, 153–8505 Japan and KAST, 3-2-1 Sakado, Takatsu-ku, Kawasaki, Kanagawa, 213-0012 Japan

(Received 6 April 2004; accepted 17 August 2004)

We fabricated UV-emitting nanocrystalline gallium nitride (GaN) films at room temperature using photochemical vapor deposition (PCVD). For the samples synthesized at room temperature with V/III ratios exceeding 5.0×10^4, strong photoluminescence peaks at 3.365 and 3.310 eV, which can be ascribed to transitions in a mixed phase of cubic and hexagonal GaN, were observed at 5 K. A UV emission spectrum with a full width at half-maximum of 100 meV was observed, even at room temperature. In addition, x-ray photoelectron spectroscopy measurement revealed that the film deposited by PCVD at room temperature was well nitridized. © *2004 American Institute of Physics*. [DOI: 10.1063/1.1806271]

For future optical transmission systems with high data transmission rates and capacity, we have proposed nanometer-scale photonic devices (i.e., nanophotonic devices).[1] These devices consist of nanometer-scale dots and wires, and an optical near-field is used as the signal carrier. As a representative device, a nanophotonic switch can be realized by controlling the dipole forbidden optical energy transfer among resonant energy states in nanometer-scale quantum dots via an optical near field.[1]

GaN is a promising material for use in nanophotonic switches at room temperature, due to its large exciton binding energy (26 meV). Recently, many different techniques have been used to fabricate high-quality GaN films, such as molecular-beam epitaxy,[2,3] metalorganic chemical vapor deposition (MOCVD),[4,5] and pulsed-laser deposition.[6,7] Furthermore, stimulated emission has been demonstrated in single-crystal GaN nanowires.[8]

The application of single GaN nanocrystallites in a nanophotonic switch requires lateral integration with nanometer-scale resolution. To meet this requirement, we proposed and demonstrated near-field optical chemical vapor deposition (NFO-CVD).[9,10] Using the photochemical reaction between the reactant molecules and the optical near field generated at the tip of an optical fiber probe, NFO-CVD is applicable to various materials, including metals, semiconductors, and insulators, while precisely controlling their size and position. To apply NFO-CVD in fabricating GaN nanocrystallites, it is necessary to reduce the thermal drift of the substrate and probe to deposit smaller nanocrystallites. Although photo-CVD (PCVD) growth is a technique that can reduce the growth temperature[11,12] by yielding the reactive radicals Ga and N via photolysis of their precursors, and the photolytic synthesis of GaN has been demonstrated at 500 °C, its detailed optical properties remain unclear.[11,12]

In this letter, we report on the dependence of photoluminescence (PL) spectra on the V/III ratio of nanocrystalline GaN films deposited at room temperature using PCVD. The growth chamber was evacuated to a base pressure of 10^{-7} Torr. GaN samples 100 nm thick were grown on a sapphire (0001) substrate at room temperature. We used trimethylgallium (TMG) and semiconductor grade (99.999%) NH_3 as the III and V sources, respectively. H_2 was used as the carrier gas for the TMG. The partial pressure of NH_3 was fixed at 500 Torr, so that the V/III ratio (γ) was varied by changing the partial pressure of TMG. Since gas-phase TMG and NH_3 have strong photoabsorption at $\lambda<270$ nm (Ref. 13) and $\lambda<220$ nm,[14] respectively, we used a frequency-quintupled Q-switched Nd:YAG laser ($\lambda=213$ nm) as the light source for the photodissociation of the precursors. The PL spectra of the samples were examined using a continuous wave He-Cd laser ($\lambda=325$ nm). To check the atomic composition of the sample, x-ray photoelectron spectroscopy (XPS; PHI 5400 MC equipped with a monochromatic Al $K\alpha$ radiation of $h\nu=1446.9$ eV) was used after removing a surface layer of the sample.

[a)]Author to whom correspondence should be addressed; electronic mail: yatsui@ohtsu.jst.go.jp

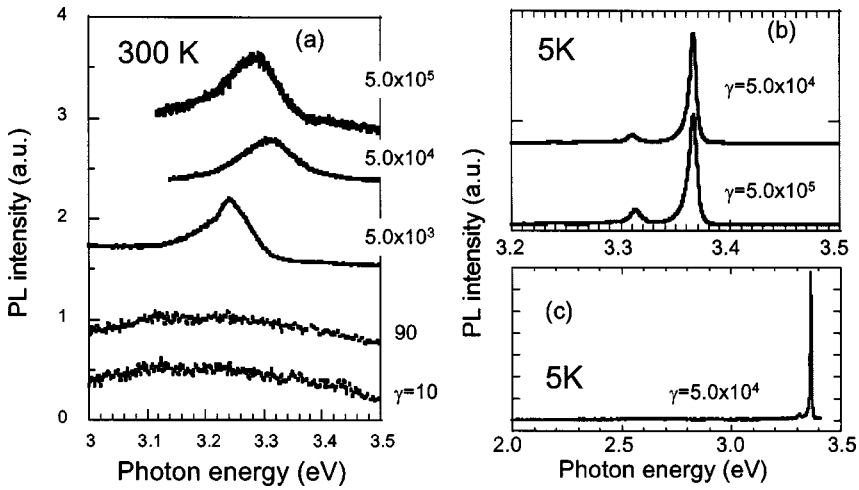

FIG. 1. PL spectra as a function of the V/III ratio (γ) measured at (a) 300 and (b) and (c) 5 K.

Figure 1(a) shows the room-temperature (300 K) PL spectra for samples fabricated in the range of $10 \leqslant \gamma \leqslant 5 \times 10^5$. A broad peak with a full width at half-maximum (FWHM) of 0.5 eV is observed around 3.1eV for the samples deposited with $\gamma \leqslant 90$. These peaks correspond to the oxygen defect-related emission of hexagonal GaN.[11] In contrast, a sharp peak (FWHM of 100 meV) from 3.26 to 3.32 eV is observed for the samples with $\gamma > = 5.0 \times 10^3$ [Fig. 1(a)]. The low-temperature (5 K) PL spectra of the samples with $\gamma = 5 \times 10^4$ and 5×10^5 are shown in Fig. 1(b). Yellow luminescence was undetectable in either sample [see Fig. 1(c)]. Both samples show two dominant PL peaks at 3.366 (I_3) and 3.310 eV (I_4). These peaks have been reported in a mixed cubic and hexagonal GaN structure in regions close to the substrate.[15,16]

Further experiments on the temperature-dependent evolution of the PL spectra of the deposited film confirmed the origin of the PL peaks. Figure 2(a) shows typical PL spectra of a film deposited with $\gamma = 5 \times 10^5$ measured over the temperature range from 5 to 300 K. At 5 K, a strong, sharp peak (I_3) is observed at 3.361 eV, accompanied by a broad peak around 3.310 eV (I_4). These values are consistent with those reported by Mah *et al.*,[16] who proposed a model to explain the emission mechanism for peaks I_3 and I_4; that is, these peaks arise from the quantum confinement of carriers in cubic inclusions within the hexagonal material, analogous to a type-I quantum well. They attributed I_3 and I_4 to the transition from the confined state in the cubic phase, and to the transition involving an electron in the hexagonal phase that escaped from the confined state in the cubic phase to the shallow acceptor level in the cubic phase, respectively. Although further analysis is required to confirm the microstructure of the sample, their results might explain both of the peaks observed in our case. Peak I_3 shifted with temperature, following Varshni's equation, which defines the temperature dependence of the bandgap.[17] Moreover, the narrow linewidths of 6.5 meV and the temperature behavior both indicate an excitonic nature. The height of peak I_3 decreased drastically with increasing temperature, and it almost disappeared at temperatures above 70 K. By contrast, a new peak

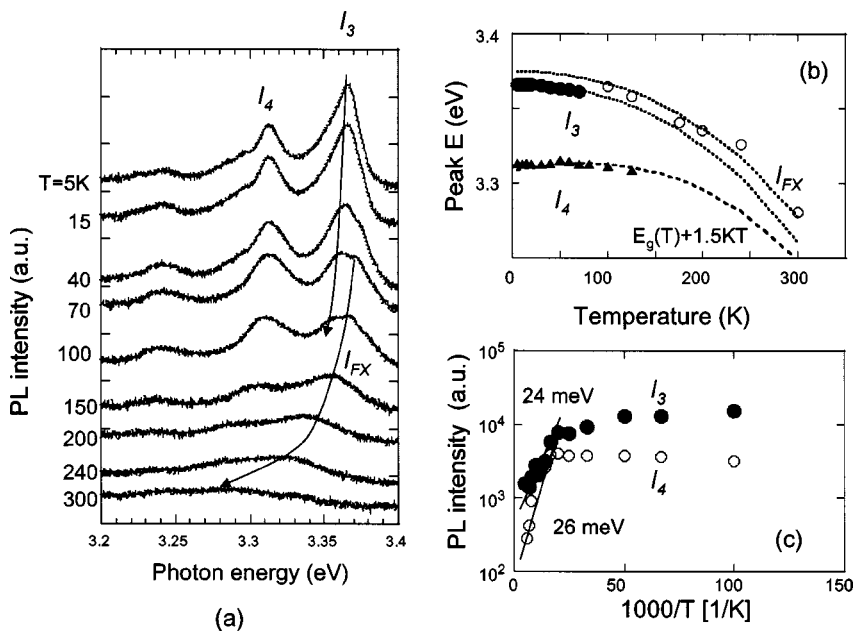

FIG. 2. (a) Temperature dependence of the PL spectra for the sample with $\gamma = 5 \times 10^5$. (b) Temperature dependence of the peak position for the prominent emission. (c) Temperature dependence of the integrated intensities of I_3 and I_4.

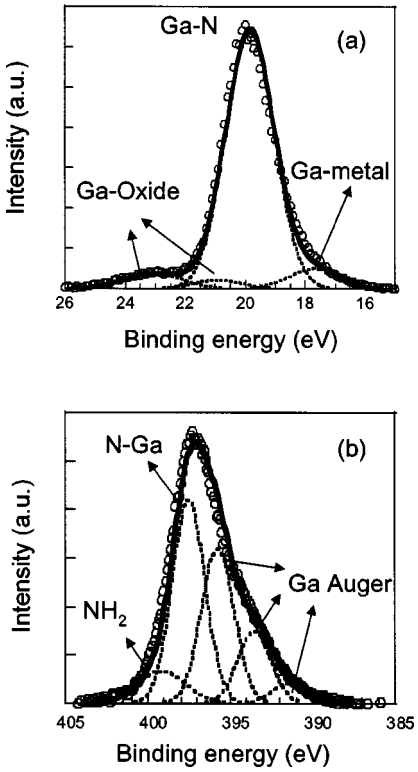

FIG. 3. XPS spectra of (a) Ga 3*d* and (b) N 1*s* for an as-grown GaN film with $\gamma=5\times10^5$. The XPS signals are plotted as open circles. The summed spectra of the decomposed components are superimposed on the measured spectra using solid lines.

(labeled I_{FX}) emerged instead of I_3 at above 70 K, and it was even observed at room temperature. This behavior presumably resulted from the decomposition of localized excitons in the cubic-phase quantum well to free excitons, due to the increased thermal energy. Peak I_4 observed at 3.310 eV did not follow Varshni's equation, since it shifted towards the line of peak I_3 with increasing temperature [see Fig. 2(b)]. This can be ascribed to two possible transitions. One is the well-known donor–acceptor pair transition; however, this possibility is ruled out by the different peak positions,[18] and because the small activation energy of 26 meV for I_4 [see Fig. 2(c)] is clearly distinct from the typical value for a DAP of about 200 meV.[19] The other is the free-to-bound transition characterized by the equation $E_g(T)+nKT$. We determined $n=1.5$ empirically [see Fig. 2(b)], which is in good agreement with the value of MOCVD-grown $(11\bar{2}0)$ GaN.[20] Furthermore, the height of peak I_4 increased with temperature at the expense of peak I_3 [see Fig. 2(c)], implying that energy was transferred from peak I_3 to I_4. These results imply that I_4 is a recombination of a free electron in the hexagonal phase, which escaped from a confined state in the cubic phase with sufficient thermal energy for release, with a hole bound on an acceptor center in the cubic phase. Detailed evaluations of the distribution of the hexagonal or cubic phase and their size are currently underway using high-resolution transmission electron microscope images and the corresponding selected-area electron diffraction patterns, which correspond to a mixture of hexagonal and cubic phase; the results will be published separately.

XPS analysis was used to check the atomic composition ratio of gallium and nitrogen.[21] Figure 3 shows Ga 3*d* (a) and N 1*s* (b) spectra measured for the sample with $\gamma=5.0\times10^5$. As shown in Fig. 3(a), the Ga 3*d* spectrum is decomposed into four components at 17.6, 19.8, 20.9, and 23.1 eV, which can be ascribed to metallic Ga, GaN, oxide, and oxide, respectively.[21,22] The N 1*s* spectrum [see Fig. 3(b)] is decomposed into five components at 391.5, 393.5, 395.8, 397.5, and 399.2 eV. The first three components correspond to the Auger lines of Ga,[22] and the last two can be ascribed to the nitride and NH_2, respectively.[21] The NH_2 species are reported to be formed on a GaN surface via the interaction between the surface and NH_3 gas.[23] The atomic composition ratio of the nitrized gallium was determined using the relative sensitivity factor (Ga 3*d*:0.43 and N 1*s*:0.499): gallium, 54.5%; nitrogen, 45.5%. This implies that the deposited film was well nitridized by the PCVD due to the large V/III ratio, even at room temperature.

In conclusion, UV-emitting nanocrystalline GaN films were fabricated using PCVD at room temperature. For the samples synthesized at large V/III ratios ($\geqslant5.0\times10^4$), a strong UV emission spectrum was observed, even at room temperature. Since the technique of depositing GaN presented here is performed at room temperature, this method is applicable to NFO-CVD, which could be used to fabricate size- and position-controlled nanometer-scale optoelectronic devices.

[1] M. Ohtsu, K. Kobayashi, T. Kawazoe, S. Sangu, and T. Yatsui, IEEE J. Sel. Top. Quantum Electron. **8**, 839 (2002).
[2] C. Wetzel, D. Volm, B. K. Meyer, K. Pressel, S. Nilsson, E. N. Mokhov, and P. G. Baranov, Appl. Phys. Lett. **65**, 1033 (1994).
[3] P. Waltereit, O. Brandt, A. Trampert, H. T. Grahn, J. Menniger, M. Ramsteiner, M. Reiche, and K. H. Ploog, Nature (London) **406**, 865 (2000).
[4] H. Amano, M. Kito, K. Hiramatsu, and I. Akasaki, Jpn. J. Appl. Phys., Part 2 **28**, L2112 (1989).
[5] S. Nakamura, T. Mukai, and M. Senoh, Appl. Phys. Lett. **64**, 1687 (1994).
[6] R. F. Xiao, X. W. Sun, Z. F. Li, N. Cue, H. S. Kwok, Q. Z. Liu, and S. S. Lau, J. Vac. Sci. Technol. A **15**, 2207 (1997).
[7] J. Ohta, H. Fujioka, and M. Oshima, Appl. Phys. Lett. **83**, 3060 (2003).
[8] J. C. Johnson, H. J. Choi, K. P. Knutsen, R. D. Schaller, P. Yang, and R. J. Saykally, Nat. Mater. **1**, 106 (2002).
[9] Y. Yamamoto, M. Kourogi, M. Ohtsu, V. Polonski, and G. H. Lee, Appl. Phys. Lett. **76**, 2173 (2000).
[10] T. Yatsui, T. Kawazoe, M. Ueda, Y. Yamamoto, M. Kourogi, and M. Ohtsu, Appl. Phys. Lett. **81**, 3651 (2002).
[11] S. S. Lee, S. M. Park, and P. J. Chong, J. Mater. Chem. **3**, 347 (1993).
[12] B. Zhou, X. Li, T. L. Tansley, and K. S.A. Butcher, J. Cryst. Growth **160**, 201 (1996).
[13] H. Okabe, M. K. Emadi-Babaki, and V. R. McCrary, J. Appl. Phys. **69**, 1730 (1991).
[14] K. Watanabe, J. Chem. Phys. **22**, 1564 (1954).
[15] C. Wetzel, S. Fischer, J. Krüger, E. E. Haller, R. J. Molnar, T. D. Moustakas, E. N. Mokhov, and P. G. Baranov, Appl. Phys. Lett. **68**, 2556 (1996).
[16] K. W. Mah, J.-P Mosnier, E. McGlynn, M. O. Henry, D. O'Mahony, and J. G. Lunney, Appl. Phys. Lett. **80**, 3301 (2002).
[17] Y. P. Varshni, Physica (Amsterdam) **34**, 149 (1967).
[18] J. Wu, H. Yaguchi, K. Okabe, R. Ito, and Y. Shiraki, Appl. Phys. Lett. **71**, 2067 (1997).
[19] S. Fischer, C. Wetzel, E. E. Haller, and B. K. Meyer, Appl. Phys. Lett. **67**, 1298 (1995).
[20] Z. Chen, D. Lu, X. Liu, X. Wang, P. Han, D. Wang, H. Yuan, Z. Wang, G. Li, and Z. Fang, J. Appl. Phys. **93**, 316 (2003).
[21] D. Li, M. Sumiya, S. Fuke, D. Yang, D. Que, Y. Suzuki, and Y. Fukuda, J. Appl. Phys. **90**, 4219 (2001).
[22] C. D. Wagner, W. M. Briggs, L. E. Davis, J. F. Moulder, and G. E. Muilenberg, *Handbook of x-ray photoelectron spectroscopy* (Perkin-Elmer, Eden Pairie, MN, 1979).
[23] S. W. King, E. P. Carlson, R. J. Terrien, J. A. Christman, R. J. Nemanich, and R. F. Davis, J. Appl. Phys. **86**, 5584 (1999).

Erratum: "Room-temperature synthesis of ultraviolet-emitting nanocrystalline GaN films using photochemical vapor deposition" [Appl. Phys. Lett. 85, 3059 (2004)]

Shunsuke Yamazaki
Interdisciplinary Graduate School of Science and Engineering, Tokyo Institute of Technology, 4259 Nagatsuta, Midori-ku, Yokohama, Kanagawa, 226-8502 Japan

Takashi Yatsui[a)]
Solution-Oriented Research for Science and Technology (SORST), Japan Science and Technology Agency, 687-1 Tsuruma, Machida, Tokyo, 194-0004 Japan

Motoichi Ohtsu
School of Engineering, The University of Tokyo, 7-3-1 Hongo, Bunkyo-ku, Tokyo 113-8656, Japan and SORST, Japan Science and Technology Agency, 687-1 Tsuruma, Machida, Tokyo, 194-0004 Japan

Tae-Won Kim
Kanagawa Academy of Science and Technology (KAST), 3-2-1, Sakado, Takatsu-ku, Kawasaki, Kanagawa, 213-0012 Japan

Hiroshi Fujioka
Department of Applied Chemistry, The University of Tokyo, 7-3-1 Hongo, Bunkyo-ku, Tokyo 113-8656 Japan and KAST, 3-2-1, Sakado, Takatsu-ku, Kawasaki, Kanagawa, 213-0012 Japan

(Received 22 October 2004; accepted 22 October 2004)

[DOI: 10.1063/1.1831540]

Tae-Won Kim's name was misspelled in the author listing. The correct byline is shown above.

[a)]Author to whom correspondence should be addressed; electronic mail: yatsui@ohtsu.jst.go.jp

Observation of cold atom output from an evanescent-light funnel

Akifumi Takamizawa,[a] Haruhiko Ito, Shungo Yamada, and Motoichi Ohtsu
Interdisciplinary Graduate School of Science and Engineering, Tokyo Institute of Technology, 4259 Nagatsuta-cho, Midori-ku, Yokohama 226-8502, Japan

(Received 9 March 2004; accepted 28 June 2004)

We report the demonstration of an atom funnel composed of evanescent light. The flux intensity of cold Rb atoms output from a 240 μm exit hole was 7×10^7 atom/cm^2 s at a blue detuning of 1.2 GHz. Sisyphus cooling doubled the output efficiency. The estimated flux intensity was 10^{12} atom/cm^2 s when the exit-hole diameter was 110 μm. © *2004 American Institute of Physics*. [DOI: 10.1063/1.1786362]

Nanophotonic integrated circuits using optical near fields[1] are devices that are expected to advance optical technology and communication significantly in the next generation. An optical nanoswitch, which is one element of such circuits, is made by placing coherently controllable quantum dots in an orderly manner[2–4]. The switch regulates on–off signals via the interaction between localized photons and excitons induced in the quantum dots.[1,5] In order to work such a nanoswitch, we must arrange quantum dots of specific sizes in specific positions precisely. However, it is difficult to fabricate a nanoswitch using conventional methods, such as the self-organized growth technique.[6] To this end, chemical vapor deposition using near-field light has been developed, and several nanometric structures have been produced.[1,7–9]

Atom-by-atom deposition is the ultimate method for fabricating such quantum dots. We have proposed two atom-optical techniques based on mechanical interactions between atoms and near-field light: Atom deflection[10] and single-atom trapping.[11] Since near-field light is not affected by the diffraction limit, it is localized within a nanometer region. We now consider how to control individual atoms selectively using resonant forces from near-field light and how to apply this to optical atom-by-atom deposition.

Dense, cold atoms moving at very slow speeds are required for efficient interaction with nanometric near-field light. To generate such atoms, we have proposed an atom funnel that uses blue-detuned evanescent light.[12] The funnel collects atoms cooled with a magnetooptical trap (MOT) and outputs them as an atomic beam with a high flux intensity. In this letter, we report the observation of cold Rb atoms exiting the funnel.

Figure 1 shows the funneling of cold atoms schematically. First, total-internal reflection of a blue-detuned hollow light beam shone upward is used to excite evanescent light on the surface of the inner wall of the funnel optics, which are oriented vertically. Then, the cold atoms generated by the MOT are released, and they fall in response to gravity. Finally, a pumping light beam that induces Sisyphus cooling is shone downward. When the cold atoms approach the inner wall, they are reflected by the repulsive dipole force from the evanescent light[13] and simultaneously lose their kinetic energy because of the Sisyphus cooling.[14,15] By repeating the inelastic reflection, the cold atoms fall to the bottom and exit via a small hole. The output atoms are confined inside the hollow light beam by the repulsive dipole force and are guided through the beam. Consequently, a cold atomic beam can be generated by multiloading cold atoms from the MOT.

We demonstrated an evanescent-light funnel for Rb atoms. Figure 2 shows the experimental configuration with a double MOT. The funnel optics consisted of three plates of quartz glass measuring 15 mm on each side and 3 mm thick. The refractive index, n, was 1.45 for the resonant wavelength $\lambda=780$ nm. A triangular hole with 320 μm sides was made in the ground-flat bottom and served as an exit hole, with an effective diameter of $2R=240$ μm. The upper MOT was used to generate cold Rb atoms at a vacuum pressure of 10^{-9} Torr, while the lower MOT was used to detect outputted atoms 25 cm below the exit hole at a background pressure of 10^{-11} Torr. Each MOT was composed of three orthogonal pairs of counterpropagating σ^+-σ^- light beams, repumping light beams, and a pair of anti-Helmholtz coils.

By operating the upper MOT for 2 s using polarization gradient cooling,[16] we generated a cold ^{87}Rb atom ensemble of $N_{\rm in}=3\times10^6$ with a distribution diameter of $2\sigma=2$ mm and a mean temperature of $T=9$ μK, where the center was $H=5$ mm above the exit hole. A Ti:Al_2O_3 laser beam with a power of 110 mW and a waist of 4 mm illuminated the lower part of the funnel optics at an incident angle of $\theta=55°$ to the inner surface and induced the evanescent light. Here, we used a Gaussian beam instead of a hollow beam. A pumping light beam with an intensity of 7 μW/cm^2 was overlapped to transfer ^{87}Rb atoms in the $5S_{1/2}$, $F=2$ higher hyperfine ground state into the $5S_{1/2}$, $F=1$ lower ground state, where the frequency was red-detuned by 10 MHz with respect to the $5S_{1/2}$, $F=2-5P_{3/2}$, $F=2$ transition. It was introduced along a thalweg of the funnel optics, such that it did

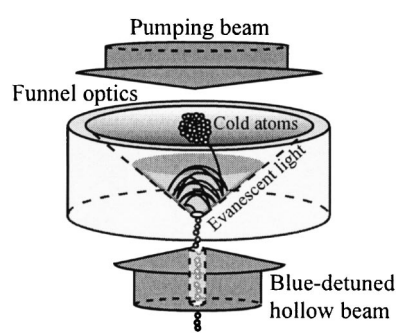

FIG. 1. Funneling cold atoms using repulsive evanescent light excited in funnel optics by total internal reflection of a blue-detuned hollow light beam. Cold atoms released from an MOT are reflected again with Sisyphus cooling and are output from a small exit hole at the bottom.

[a]Electronic mail: akifumi.takamizawa@physik.uni-muenchen.de

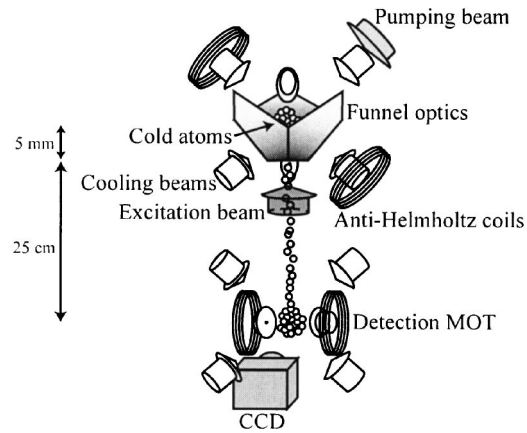

FIG. 2. Experimental configuration using double MOTs to observe atoms output from the evanescent-light funnel. Each MOT consists of 3D cooling beams and anti-Helmholtz coils. The upper MOT is used to generate cold atoms inside the funnel optics, while the lower MOT with the CCD is used to detect the output atoms. An additional pumping light beam induces Sisyphus cooling. The funnel optics with a 240 μm exit hole is composed of three glass plates.

not affect the output atoms. The funneling time, τ, was 1 s. We repeated the generation and funneling process 50 times and stored the output atoms in the lower MOT with a capture efficiency of 0.6 and a trapping time of 270 s.[17] The number of trapped atoms was estimated from the intensity of the resonant fluorescence measured using a charge-coupled device (CCD) camera.

Due to the Sisyphus cooling induced by evanescent light, which occurs in Λ-type three-level atoms, such as Rb, on applying a pumping light,[14,15] the atoms accelerated by gravity were recooled and collected at the bottom. In order to estimate the net number of funneled atoms, we subtracted the number obtained without the pumping light beam from that obtained with the pumping light, since some atoms (0.5% of N_{in}) passed through the exit hole without reflection. Figure 3 plots the result as a function of the frequency detuning δ measured with respect to the $5S_{1/2}$, $F=1-5P_{3/2}$, $F=0$ transition. The number of funneled atoms was maximal at $\delta/2\pi = +1.2$ GHz and accounted for 50% of the total number of output atoms. As shown in Fig. 3, the spectrum shows the dispersion character of the dipole force in relation to the atomic resonance frequency.[18]

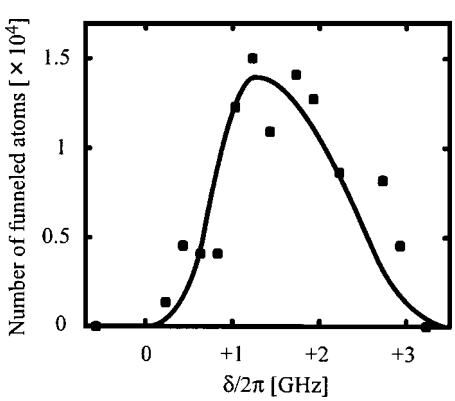

FIG. 3. Net number of funneled ^{87}Rb atoms plotted as a function of the frequency detuning δ with respect to the $5S_{1/2}$, $F=1-5P_{3/2}$, $F=0$ transition, where the number of incident atoms is 3×10^6 and the excitation light power is 110 mW. We subtract the number obtained without the pumping light beam from that obtained with it.

The number N_{out}^0 of atoms output without reflection can be approximated by[19]

$$N_{\mathrm{out}}^0 \simeq N_{\mathrm{in}}\left[1-\exp\left(-\frac{R^2}{\sigma^2+\dfrac{4k_BTH}{mg}}\right)\right], \tag{1}$$

where k_{B}, m, and g are the Boltzmann constant, atomic mass, and gravitational acceleration, respectively. Here, the number of output atoms decreases during the flight to the detection region due to scattering caused by the evanescent-light excitation beam propagating upward. In order to consider this loss, the number of funneled atoms is calibrated by comparing the number N_{out}^0 estimated using Eq. (1) with the number obtained experimentally with the excitation beam only. Under detuning at +1.2 GHz, where the total number N_{out} of output atoms is $2N_{\mathrm{out}}^0$, the flux intensity is obtained as

$$F=\frac{N_{\mathrm{out}}}{\pi R^2\tau}, \tag{2}$$

and is estimated to be 7×10^7 atom/cm^2 s under the experimental conditions. If a hollow light beam is used as the excitation beam, output atoms are guided through the hollow region without loss, maintaining the flux intensity.

In Sisyphus cooling, when a ^{87}Rb atom transfers from the $F=1$ lower ground state with a large light shift to the $F=2$ higher ground state with a small light shift, it loses kinetic energy. The pumping light returns it to the lower ground state, so that the energy-loss process is repeated. At the same time, since the reflection potential in the lower ground state is higher than that in the higher ground state, the reflection efficiency increases on applying the pumping light. Therefore, the number of atoms output from the funnel increases due to the two effects. Under our experimental conditions, however, if Sisyphus cooling did not occur, the number of funneled atoms was estimated to be 1/8 the number that occurred with Sisyphus cooling. Consequently, Sisyphus cooling contributes principally to the evanescent-light funnel.

The flux intensity depends markedly on the size of the exit hole. As the exit hole becomes smaller, the flux intensity increases. Indeed, we require a flux intensity of 10^{12} atom/cm^2 s for the precise control of atoms using 10 nm near-field light, which is comparable to the de Broglie wavelength. Let us estimate the flux intensity as a function of the hole diameter, $2R$, and the light power, P. The reflection efficiency inside the funnel, and the output efficiency, depend on the mean atomic kinetic energy, K. Assuming that Sisyphus cooling necessarily occurs during reflection, the energy variance ΔK per bounce in the direction perpendicular to the inner-wall surface is given by[14]

$$\Delta K = 1-\frac{2}{3}\frac{\delta_{\mathrm{hfs}}}{\delta+\delta_{\mathrm{hfs}}}, \tag{3}$$

where δ_{hfs} is the hyperfine splitting (=6.8 GHz for ^{87}Rb). Averaging over the atomic incident angle between 0 and $\pi/2$, we get the three-dimensional (3D) variance $\Delta K_{3\mathrm{D}} = (1/3)+(2/3)\Delta K$. Then, the reflection efficiency η_{ref}^i in the ith bounce is approximated by

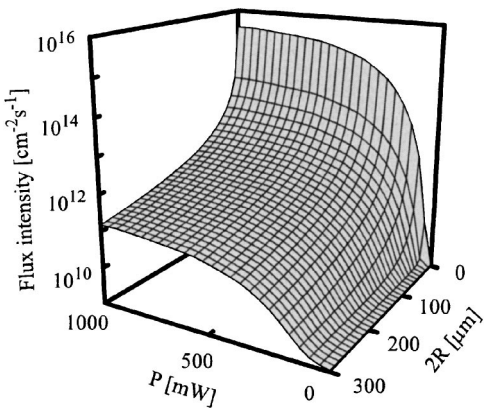

FIG. 4. Flux intensity of output ^{87}Rb atoms calculated as a function of the light power, P, and the exit-hole diameter, $2R$, where $\delta/2\pi=+1.2$ GHz and $N_{\mathrm{in}}=10^8$. The estimated flux intensity is 10^{12} atom/cm^2 s for $2R=110$ μm and $P=1$ W.

$$\eta_{\mathrm{ref}}^{i} \simeq \min\left[(\Delta K_{3\mathrm{D}})^{-(i-1)}\frac{P}{P_0}\epsilon, 1\right], \tag{4}$$

and the output efficiency η_{out}^{i} after the ith bounce is given by

$$\eta_{\mathrm{out}}^{i} \simeq \min\left[(\Delta K_{3\mathrm{D}})^{-2i}\frac{N_{\mathrm{out}}^{0}}{N_{\mathrm{in}}}, 1\right], \tag{5}$$

where P_0(=110 mW) is the light power in the experiment and $\min[\alpha,\beta]$ is a function that returns the lesser of α and β. The constant ϵ equals η_{ref}^{1} with $P=P_0$. Consequently, the total output efficiency, $\eta_{\mathrm{out}}^{\mathrm{total}}=N_{\mathrm{out}}/N_{\mathrm{in}}$, is written as

$$\eta_{\mathrm{out}}^{\mathrm{total}} = \eta_{\mathrm{out}}^{0} + \sum_{i}\prod_{j=1}^{i}\eta_{\mathrm{ref}}^{j}(1-\eta_{\mathrm{out}}^{j-1})\eta_{\mathrm{out}}^{i}. \tag{6}$$

Substituting $N_{\mathrm{out}}=\eta_{\mathrm{out}}^{\mathrm{total}}N_{\mathrm{in}}$ into Eq. (2), we calculate the flux intensity. Figure 4 shows the result for $\delta/2\pi=+1.2$ GHz and $N_{\mathrm{in}}=10^8$. Here, we take the upperlimit of i as $\tau/\Delta t=67$, where $\Delta t=15$ ms is the bounce period.[13] Under the experimental conditions, $\eta_{\mathrm{out}}^{\mathrm{total}}$ is 0.01 and ϵ is 0.12. Using these values, we obtain a flux intensity of 10^{12} atom/cm^2 s for $2R=110$ μm and $P=1$ W.

Monte Carlo simulations indicate that the mean temperature of atoms output from the evanescent-light funnel is 20 μK.[20] By contrast, the decay length of the evanescent light is $\xi=\lambda/2\pi\sqrt{n^2\sin^2\theta-1}=190$ nm, which equals the allowed minimum radius of the exit hole. An atomic funnel with such a small hole can be made by etching a silicon-on-insulator substrate using photolithography.[21] Since the small exit is clearly fixed, we can direct a cold atomic beam through the hole toward a given position precisely, unlike other schemes using propagating light.[22–24]

In conclusion, we demonstrated an atom funnel that uses evanescent light. Sisyphus cooling increases the output of cold atoms. The cold atomic beam generated by the funnel will be used for atom manipulation using near-field light.

[1] M. Ohtsu, K. Kobayashi, T. Kawazoe, S. Sangu, and T. Yatsui, IEEE J. Sel. Top. Quantum Electron. **8**, 839 (2002).
[2] N. H. Bonadeo, J. Erland, D. Gammon, D. Park, D. S. Katzer, and D. G. Steel, Science **282**, 1473 (1998).
[3] T. H. Stievater, X. Li, D. G. Steel, D. Gammon, D. S. Katzer, D. Park, C. Piermarocchi, and L. J. Sham, Phys. Rev. Lett. **87**, 133603 (2001).
[4] H. Kamada, H. Gotoh, J. Temmyo, T. Takagahara, and H. Ando, Phys. Rev. Lett. **87**, 246401 (2001).
[5] T. Kawazoe, K. Kobayashi, S. Sangu, and M. Ohtsu, Appl. Phys. Lett. **82**, 2957 (2003).
[6] D. Leonard, M. Krishnamurthy, C. M. Reaves, S. P. Denbaars, and P. M. Petroff, Appl. Phys. Lett. **63**, 3203 (1993).
[7] V. Polonski, Y. Yamamoto, M. Kourogi, H. Fukuda, and M. Ohtsu, J. Microsc. **194**, 545 (1999).
[8] Y. Yamamoto, V. Polonski, G. H. Lee, M. Kourogi, and M. Ohtsu, Appl. Phys. Lett. **76**, 2173 (2000).
[9] T. Yatsui, T. Kawazoe, M. Ueda, Y. Yamamoto, M. Kourogi, and M. Ohtsu, Appl. Phys. Lett. **81**, 3651 (2002).
[10] K. Totsuka, H. Ito, K. Suzuki, K. Yamamoto, and M. Ohtsu, Appl. Phys. Lett. **82**, 1616 (2003).
[11] H. Ito and M. Ohtsu, *Near-Field Nano/Atom Optics and Technology*, edited by M. Ohtsu (Springer, Tokyo, 1998), Chap. 11.
[12] H. Ito, K. Sakaki, W. Jhe, and M. Ohtsu, Phys. Rev. A **56**, 712 (1997).
[13] A. Takamizawa, H. Ito, and M. Ohtsu, Jpn. J. Appl. Phys., Part 1 **41**, 6215 (2002).
[14] J. Söding, R. Grimm, and Y. B. Ovchinnikov, Opt. Commun. **119**, 652 (1995).
[15] Y. B. Ovchinnikov, I. Manek, and R. Grimm, Phys. Rev. Lett. **79**, 2225 (1997).
[16] J. Dalibard and C. Cohen-Tannoudji, J. Opt. Soc. Am. B **6**, 2023 (1989).
[17] A. Takamizawa, H. Ito, S. Yamada, and M. Ohtsu, Jpn. J. Appl. Phys., Part 1 **42**, 3658 (2003).
[18] J. P. Dowling and J. Gea-Banacloche, *Advances in Atomic, Molecular, and Optical Physics*, edited by B. Bederson, and H. Walther (Academic, San Diego, 1996), Vol. 37, p. 1.
[19] D. S. Weiss, E. Riis, Y. Shevy, P. J. Ungar, and S. Chu, J. Opt. Soc. Am. B **6**, 2072 (1989).
[20] A. Takamizawa, H. Ito, and M. Ohtsu, Tech. Dig. I-512, 4th Pacific Rim Conference on Lasers and Electro-Optics, TuH2-1 (2001).
[21] T. Yatsui, M. Kourogi, K. Tsutsui, M. Ohtsu, and J. Takahashi, Opt. Lett. **25**, 1279 (2000).
[22] K. Dieckmann, R. J. C. Spreeuw, M. Weidemüller, and J. T. M. Walraven, Phys. Rev. A **58**, 3891 (1998).
[23] S. Weyers, E. Aucouturier, C. Valentin, and N. Dimarcq, Opt. Commun. **143**, 30 (1997).
[24] Z. T. Lu, K. L. Corwin, M. J. Renn, M. H. Anderson, E. A. Cornell, and C. E. Wieman, Phys. Rev. Lett. **77**, 3331 (1996).

Evaluation of the discrete energy levels of individual ZnO nanorod single-quantum-well structures using near-field ultraviolet photoluminescence spectroscopy

T. Yatsui[a)]
Solution-Oriented Research for Science and Technology (SORST), Japan Science and Technology Agency, Machida, Tokyo 194-0004, Japan

J. Lim and M. Ohtsu[b)]
Interdisciplinary Graduate School of Science and Engineering, Tokyo Institute of Technology, Yokohama, Kanagawa 226-8502, Japan

S. J. An and G.-C. Yi
National CRI Center for Semiconductor Nanorods and Department of Materials Science and Engineering, Pohang University of Science and Technology (POSTECH), San 31 Hyoja-dong, Pohang, Gyeongbuk 790-784, Korea

(Received 13 February 2004; accepted 2 June 2004)

Spatially and spectrally resolved photoluminescence imaging of individual ZnO/ZnMgO nanorod single-quantum-well structures (SQWs) with a spatial resolution of 55 nm was performed using the optical near-field technique with a metallized UV fiber probe. Using excitation power density-dependent photoluminescence spectra of a ZnO/ZnMgO SQW nanorod, we observed the discrete energy levels in a ZnO quantum-well layer. © *2004 American Institute of Physics*.
[DOI: 10.1063/1.1776338]

For future optical transmission systems with high data transmission rates and capacity, we have proposed nanometer-scale photonic devices (i.e., nanophotonic devices) and a method of integrating them.[1] These devices consist of nanometer-scale dots, and an optical near field is used as the signal carrier. As a representative device, a nanophotonic switch can be realized by controlling the dipole forbidden optical energy transfer among resonant energy level in nanometer-scale quantum dots via an optical near field.[2] It is made of sub-100-nm scale dots and wires, and their size and position on the substrate must be controlled with nanometer-scale accuracy. A nanometer-scale ZnO dot is a promising material for realizing these devices at room temperature, due to its large excition binding energy (60 meV).[3,4] Furthermore, the recent demonstration of semiconductor nanorod quantum-well structure enables us to fabricate nanometer-scale electronic and photonic devices on single nanorods.[5–8] Recently, ZnO/ZnMgO nanorod multiple-quantum-well structures (MQWs) were fabricated and the quantum confinement effect of the MQWs was successfully observed.[8] In addition, further improvement in the fabrication of nanorod heterostructures has resulted in the observation of significant photoluminescence (PL) intensity, even from nanorod single-quantum-well structures (SQWs).[9]

To confirm the promising optical properties of individual ZnO/ZnMgO SQWs for realizing nanophotonic devices, we measured the PL spectra using a low temperature near-field optical microscope (NOM). Using a metallized UV fiber probe, the spatial distribution of PL intensity and sharp PL spectra of individual ZnO well layers were observed.

ZnO/$Zn_{1-x}Mg_xO$ SQWs were fabricated on the ends of ZnO nanorods with a mean diameter of 40 nm using catalyst-free metalorganic vapor phase epitaxy.[8,10] The nanorods were grown on Al_2O_3(0001) substrate. The average concentration of Mg (x) in the $Zn_{1-x}Mg_xO$ layers used in this study was determined to be $x=0.2$ using energy dispersive x-ray spectroscopy in a transmission electron microscopy chamber. The ZnO well layer thickness (L_w) investigated in this study was 2.5 nm, while the thicknesses of the $Zn_{0.8}Mg_{0.2}O$ bottom and top barrier layers in the SQWs were fixed at 60 and 18 nm, respectively (Fig. 1 shows a schematic diagram of the SQWs).

Figure 2(a) shows far-field PL spectra taken at 15 K at various excitation power densities. A strong, sharp peak (I_2)

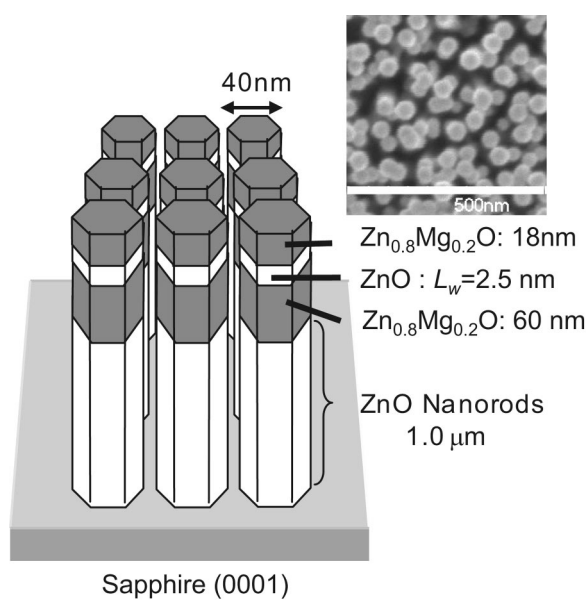

FIG. 1. Schematic of ZnO/ZnMgO SQWs on the ends of ZnO nanorods. The inset shows an overview of the ZnMgO/ZnO nanorod SQWs.

[a)]Electronic mail: yatsui@ohtsu.jst.go.jp
[b)]Also with: SORST, Japan Science and Technology Agency, 687-1 Tsuruma, Machida, Tokyo 194-0004, Japan.

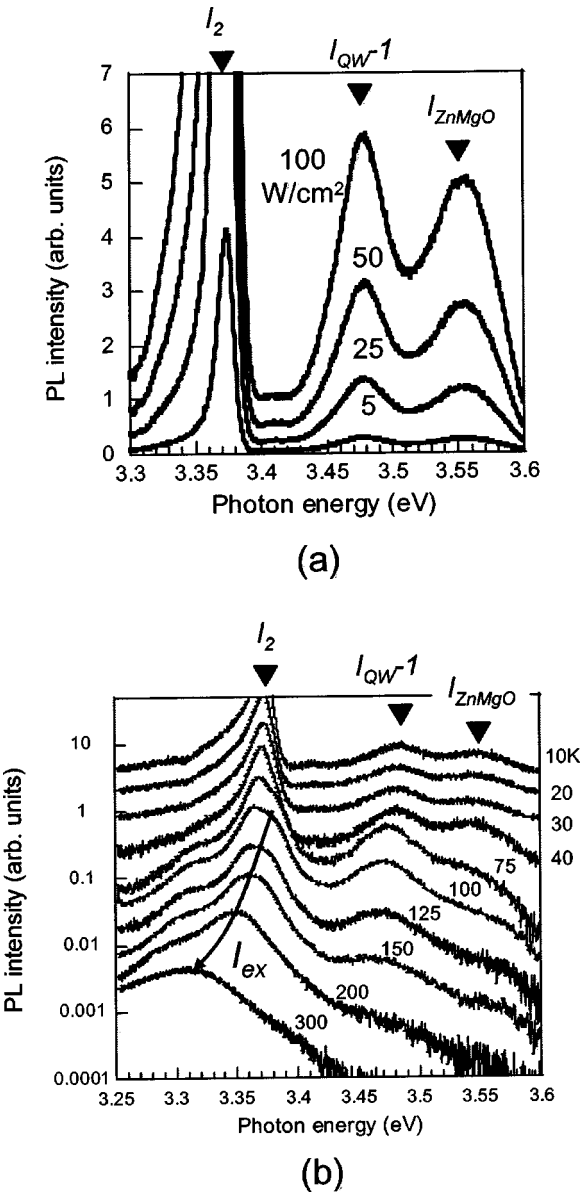

FIG. 2. (a) Power- (at 15 K) and (b) temperature-dependence of the far-field PL spectra of ZnO/ZnMgO nanorod SQWs.

was observed at 3.371 eV, while broad peaks ($I_{QW}-1$ and I_{ZnMgO}) appeared at 3.480 and 3.555 eV. The number of peaks and their positions did not change up to 100 W/cm^2. Further experiments on the temperature-dependent evolution of the PL spectra in ZnO/$Zn_{0.8}Mg_{0.2}O$ nanorod SQWs confirmed the origin of the PL peaks. Figure 2(b) shows typical PL spectra of ZnO/$Zn_{0.8}Mg_{0.2}O$ nanorod SQWs measured over a temperature range from 10 to 293 K. At 10 K, a strong, sharp peak (I_2) was observed at 3.371 eV, while broad peaks appeared at 3.485 eV ($I_{QW}-1$) and 3.555 eV (I_{ZnMgO}). As the temperature increased, the intensities of the I_2 and I_{ZnMgO} peaks decreased drastically, and they almost disappeared at temperatures above 100 K, while the I_{ex} and $I_{QW}-1$ peaks increased relative to I_2 and I_{ZnMgO}. This behavior presumably results from the decomposition of bound excitons to free excitions owing to the increased thermal energy, and supports the argument described above, that PL I_{ex} and $I_{QW}-1$ peaks correspond to a free exciton peaks, and I_2 and I_{ZnMgO} are the well-known neutral-donor bound exciton peak emitted from ZnO nanorod stems and

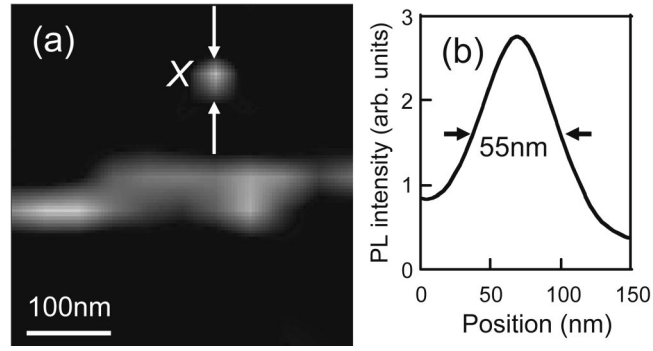

FIG. 3. Monochromatic PL image of ZnO/ZnMgO nanorod SQWs obtained at a photon energy of 3.483 eV. (b) Cross-sectional PL profile through spot *X*.

$Zn_{0.8}Mg_{0.2}O$ barrier layers, respectively. Furthermore, the $I_{QW}-1$ peak quenched rather slowly in comparison with the rapid quenching behavior of I_2. Slow thermal quenching is characteristic of quantum structures, supporting our postulate that I_{QW}-1 results from the quantum confinement effect. The experimental I_{QW}-1 peak energy was consistent with the theoretical value in a one-dimensional square potential well, in which $0.28m_0$ and $1.8m_0$ are the effective masses of electron and hole in ZnO, respectively, at a ratio of conduction and valance band offsets ($\Delta E_c/\Delta E_v$) of 9, and a band gap offset (ΔE_g) of 250 meV.

To examine the optical properties of individual ZnO/ZnMgO nanorod SQWs, we performed spatially and spectrally resolved PL spectroscopy using a low-temperature NOM system in illumination-collection mode.[11] A sharpened UV fiber probe with a 50-nm-thick aluminum film was used for the scanning. He–CD laser light ($\lambda = 325$ nm) was used to excite the ZnO/ZnMgO SQW through the UV fiber probe. The PL signal was collected with the same fiber probe as used for excitation, and detected using a cooled charge coupled device through a monochromator. The fiber probe was kept in close proximity to the sample surface (~10 nm) using the shear-force feedback technique.

Figure 3(a) shows the spatially and spectrally resolved PL image at 3.483 eV. Considering the rod diameter (40 nm), the bright spot labeled *X* [see Fig. 3(a)], the full width at half maximum of which was as small as 55 nm [see Fig. 3(b)], originated from one SQW nanorod. The spatial resolution, which almost equals the ZnO nanorod diameter, indicates that carrier tunneling between the nanorods can be neglected. Since the deep potential depth between the vacuum and the barrier layer is as much as 4 eV,[12] the carriers generated in the barrier layer in one nanorod are confined to the same nanorod through which the PL signal is collected. Furthermore, high spatial resolution imaging can be realized by enhancing the spatial resolution due to the plasmon resonance at the metallized sharpened tip.[13] Since the sharpened UV probe is entirely coated with a thin metal film, light propagates inside the fiber core and is efficiently converted into the surface plasmon mode at the metallic tip, just as with a Kretschmann configuration.[14] Such plasmon excitation effectively excites the carriers in the barrier layer and scatters the evanescent field of the ZnO quantum-well layer.

The five solid curves in Fig. 4(a) show the near-field PL spectra and their power dependence as determined by fixing the fiber probe at position *X* in Fig. 3(a). In the weak exci-

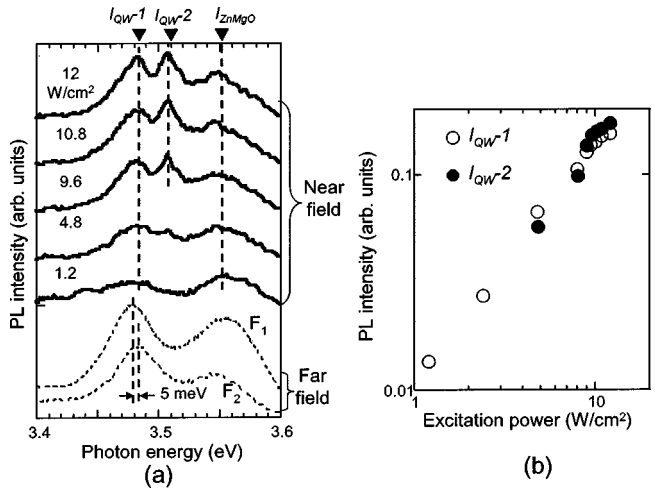

FIG. 4. (a) Solid curves show the near-field PL spectra of ZnO/ZnMgO nanorod SQWs at excitation densities ranging from 1.2 to 12 W/cm^2. The dashed curves (F_1 and F_2) show the far-field PL spectra. All the spectra were obtained at 15 K. (b) The excitation power dependence of the PL intensity at 3.483 (open circles) and 3.508 (closed circles) eV.

tation condition, a single PL peak is observed at 3.483 eV ($I_{QW}-1$). At excitation power densities exceeding 5 W/cm^2, another peak appears and grows at an energy of 3.508 eV ($I_{QW}-2$), which is 25 meV higher than $I_{QW}-1$. To confirm the origin of these emission lines, we plot the integrated PL intensity for the emission lines of both $I_{QW}-1$ and $I_{QW}-2$ in Fig. 4(b). The PL intensity of $I_{QW}-1$, indicated by the open circles, increases almost linearly up to 9 W/cm^2 and gradually saturates. This strongly implies that the $I_{QW}-1$ emission line originates from the recombination of the ground state, and the saturation suggests band-filling. As shown in the far-field spectra in Fig. 4(a) [see dashed curves F_1 and F_2], the energy difference at different positions was as small as 5 meV. Therefore, the large difference (25 meV) between $I_{QW}-1$ and $I_{QW}-2$ is not due to fluctuations in the ZnO well width. Furthermore, changing the temperature drastically alters the emission energy, as shown in Fig. 2(b); thermal heating due to the illumination light is absent. At a power density of around 6 W/cm^2, the PL line of $I_{QW}-2$ indicated by the closed circles appears. From this threshold-like PL behavior as a function of excitation power density, the PL line of $I_{QW}-2$ is associated with the emission of the first excited state. Considering the composition and size of the SQWs, the energy separation between $I_{QW}-1$ and $I_{QW}-2$ (25 meV) is in agreement with the prediction of the theoretical value of the energy difference ($\Delta E = E_{h2} - E_{h1} = 21$ meV) between the first excited state of the hole (E_{h2}) and the ground state of the hole (E_{h1}). In this calculation, we used the following parameters: 0.28 m_0 and 1.8 m_0 for the effective masses of the electron and hole, respectively, and a band gap offset (ΔE_g) of 250 meV. This is the first detection of the excited state in ZnO quantum structures, although it has previously been observed in high-quality ZnO bulk crystals.[15]

In conclusion, we investigated the power-dependent features of individual ZnO/ZnMgO nanorod SQWs. Using a thin aluminum-coated UV fiber probe, we observed band-filing in the ground state and the resultant first excited state of a hole in ZnO/ZnMgO SQWs. This successful detection is attributed to the high spatial resolution (55 nm) of NOM and the high detection sensitivity utilizing plasmon resonance at the tip of the metallized UV fiber probe. The results shown here provide one criterion for realizing nanophotonic devices, such as the switching devices confirmed by the authors in CuCl quantum cubes.[2]

Research by S.J.A. and G.C.Y. was supported by Korea Research Foundation Grant No. KRF-2002-041-C00098.

[1] M. Ohtsu, K. Kobayashi, T. Kawazoe, S. Sangu, and T. Yatsui, IEEE J. Sel. Top. Quantum Electron. **8**, 839 (2002).
[2] T. Kawazoe, K. Kobayashi, S. Sangu, and M. Ohtsu, Appl. Phys. Lett. **82**, 2957 (2003).
[3] A. Ohtomo, K. Tamura, M. Kawasaki, T. Makino, Y. Segawa, Z. K. Tang, G. K. L. Wong, Y. Matsumoto, and H. Koinuma, Appl. Phys. Lett. **77**, 2204 (2000).
[4] M. H. Huang, S. Mao, H. Feick, H. Yan, Y. Wu, H. Kind, E. Weber, R. Russo, and P. Yang, Science **292**, 1897 (2001).
[5] Y. Wu, R. Fan, and P. Yang, Nano Lett. **2**, 83 (2002).
[6] M. T. Björk, B. J. Ohlsson, C. Thelander, A. I. Persson, K. Deppert, L. R. Wallenberg, and L. Samuelson, Appl. Phys. Lett. **81**, 4458 (2002).
[7] M. S. Gudiksen, L. J. Lauhon, J. Wang, D. C. Smith, and C. M. Lieber, Nature (London) **415**, 617 (2002).
[8] W. I. Park, G.-C. Yi, M. Kim, and S. J. Pennycook, Adv. Mater. (Weinheim, Ger.) **15**, 526 (2003).
[9] W. I. Park, S. J. An, G.-C. Yi, S. Hong, T. Joo, and H. M. Cheong, Appl. Phys. Lett. (in press).
[10] W. I. Park, D. H. Kim, S.-W. Jung, and G.-C. Yi, Appl. Phys. Lett. **80**, 4232 (2002).
[11] T. Saiki and K. Matsuda, Appl. Phys. Lett. **74**, 2773 (1999).
[12] M. W. Wang, J. O. McCaldin, J. F. Swenberg, T. C. McGill, and R. J. Hauenstein, Appl. Phys. Lett. **66**, 1974 (1995).
[13] T. Yatsui, K. Itsumi, M. Kourogi, and M. Ohtsu, Appl. Phys. Lett. **80**, 2257 (2002).
[14] *Surface Plasmons*, edited by H. Raether (Springer, Berlin, 1988).
[15] D. C. Reynolds, D. C. Look, B. Jogai, C. W. Litton, G. Cantwell, and W. C. Harsch, Phys. Rev. B **60**, 2340 (1999).

[II] PRESENTATIONS

IN INTERNATIONAL CONFERENCES

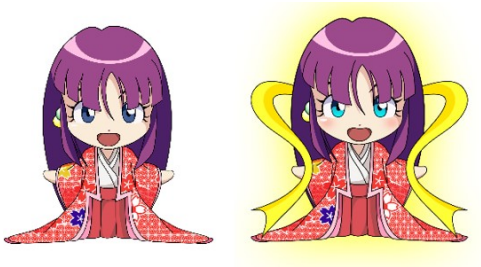

Nonadiabatic photochemical reaction and application to photolithography

Hiroki Yonemitsu[1], Tadashi Kawazoe[2], and Motoichi Ohtsu[1, 2]

[1]Department of Electronics Engineering, University of Tokyo, Bunkyo-ku, Tokyo, 113-8656, Japan. [2]Japan Science and Technology Agency, Machida, Tokyo 194-0004, Japan.

Spatially localized nature of the optical near field (ONF) is applicable to novel nanofabrication. For example, we have found the nonadiabatic photochemical reaction (NPR) of organic molecules by nonresonant ONF with photon energy lower than the dissociation energy of molecule [1]. For the optical far field, only the electrons in the molecule respond to the electric field with the same phase and intensity. Therefore, the photon energy of light must resonate to the reacting molecules in order to excite the molecules from the electronic ground state to an excited electronic state for photochemical reaction. The Franck-Condon principle supports this photochemical reaction. However, the ONF with a steeply spatial gradient of optical intensity can excite the molecule under nonresonant condition. Since the intensity in a molecule is not uniform for an ONF, and the electrons feel non-uniform field intensity, the molecular orbital changes and molecules are polarized. Thus the molecular vibration modes are excited. Our proposed NPR [1] is the multiple-step molecular activating via such vibration modes. We can explain NPR quantitatively using the exciton-phonon polariton (EPP) model. In EPP model, the ONF, *i.e.*, electromagnetic field in a nano-system, is described as quasiparticle, which is an exciton polariton trailing the phonon (lattice vibration) generated by the steep spatial gradient of its optical field, as shown in Fig.1.

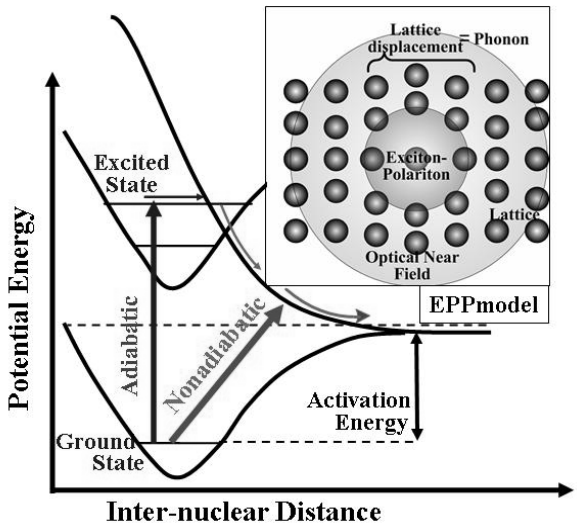

Fig.1.Schematic drawings of potential curves of an electron in molecular orbital and the exciton phonon polariton (EPP).

Here, we explain EPP model and demonstrated a novel nano-photolithography using NPR. In the experiment, we used the UV-photoresist and electron-beam (EB) photoresist. As a result of the irradiation of ONF, the UV-photoresist was exposed, while th used red-light source which has no ability to expose the UV-photoresist. In the same way, while the EB photoresist is insensitive to far-field light, it was exposed. Finally, we succeeded in the patterning of 50-nm width using the spatial locality of ONF and NPR. We call this technique "*nonadiabatic photolithography*". NPR phenomenon is physically interest and the nonadiabatic photolithography is promising as the next generation photolithography overcoming the diffraction limit of light.

A part of this work was supported by "Nanotechnology Support Project" of the Ministry of Education, Culture, Sports, Science and Technology (MEXT), Japan.

Keyword: Nonadiabatic Photochemical Reaction, Photolithography, Nanophotolithography, Nanofabrication,

[1] T.kawazoe, et al., Proceeding of Spie, **5339**, p.624, (2004).; APL, **79**, p.1184, (2001).; J. Chem. Phys., **122**, 024715, (2005).

Demonstration of Nanophotonic Devices using Near-Field Optically Coupled Quantum Dots

Tadashi Kawazoe[1], Kiyoshi Kobayashi[2], Kouichi Akahane[3], Naokatsu Yamamoto[3], Naoki Ohtani[3], and Motoichi Ohtsu[1,4]

[1] Japan Science and Technology Agency, Machida, Tokyo 194-0004, Japan. [2] Department of Physics, Tokyo Institute of Technology, Meguro-ku, Tokyo 152-8551, Japan. [3] National Institute of Information and Communications Technology, Koganei, Tokyo 184-8795, Japan. [4] Department of Electronics Engineering, University of Tokyo, Bunkyo-ku, Tokyo, 113-8656, Japan.

An optical near-field generated on a nanometric element, is free from the diffraction of light and enables the operation and integration of nanometric optical devices. By using the localized optical near-field as the signal carrier, which is transmitted from one nanometric element to another, a nanoscale photonic device can be realized. The primary advantage of nanophotonics is the capacity to achieve novel functions that are based on local electromagnetic interactions, while realizing nanometer-sized photonic devices. Based on this idea, we observed an optically forbidden energy transfer between cubic CuCl quantum dots (QDs) [1] and proposed several nanometric optical devices: a nanometric AND-gate [1], a nanometric XOR-logic gate [2], and an optical nanofountain (*i.e.*, a nanometric optical condenser) [1]. So far, we have demonstrated operation of them.

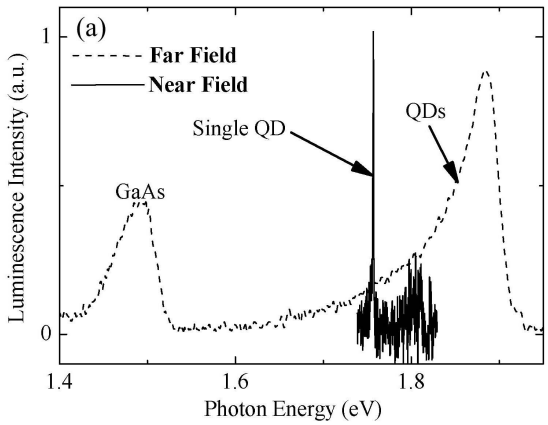

Fig.1.Near- and Far field Luminescence of $In_{0.5}Al_{0.5}As$ QDs.

Here, we demonstrate nanometric devices using CuCl QDs. CuCl QDs are unsuitable for the actual integration owing to their size and position inhomogeneity and chemical instability. For the III-V semiconductor, we can obtain size- and position- controlled quantum dots using molecular beam epitaxial growth (MBE). Toward their actual integration in nanophotonic modules, we prepare the InAlAs quantum dots using MBE and discuss a NOT-gate using InAlAs quantum dots. In the III-V semiconductors, InAlAs is suitable for our purpose; realization of nanophotonic integrated device. Because its bandgap can be widely controlled from 0.3 eV to 2.2 eV, the strong confined system (such as CuCl quantum dots in NaCl) is possible. Finally, we obtained luminescence from a single $In_{0.5}Al_{0.5}As$ quantum dot at around 1.8 eV, using a near-field spectrometer, for the first time (Fig.1). The experimental results have shown physically interest; the luminescence intensity from single QD depends on the distance between the probe and the QD. We also discuss the high expectation of InAlAs quantum dots acting as the nanophotonic device.

Keyword: Nanophotonic device, Near-field luminescence, single quantum dot

[1] T.kawazoe, et al., Phys. Rev. Lett. **88**, 067404 (2002).; Appl. Phys. Lett., **82**, 2957 (2003).; Appl. Phys. Lett., **86**, 103102, (2005).

[2] S. Sangu, et.al, Phys. Rev. B, **69**, 115334, (2004).

Fabrication of nanophotonic devices and their integration by optical near-field

Takashi Yatsui[1], Motoichi Ohtsu[1,2]
[1]*SORST, JST;* [2]*Univerisity of Tokyo, Japan*
abstract presenting; yatsui@ohtsu.jst.go.jp,

Abstract To realize the nanophotonic device required by future systems, we demonstrated the feasibility of nanometer-scale optical chemical vapor deposition using optical near-field techniques. Furthermore, the possibilities of self-assembling integration using optical near-field were also presented.

Optical transmission systems require increased integration of photonic switching devices. To support this increase, it is estimated that the size of photonic matrix switching devices should be reduced to less than 100 nm by the year 2015. To realize this, we have proposed nanometer-scale photonic devices and their integration [i.e., nanophotonic integrated circuits (ICs)] [1]. These devices consist of nanometer-scale dots, and an optical near field is used as the signal carrier (see Fig. 1). As a representative device, a nanophotonic switch can be realized by controlling the dipole forbidden optical energy transfer among resonant energy states in nanometer-scale quantum dots via an optical near field [2].

In order to realize the nanophotonic switch, we proposed and demonstrated near-field optical chemical vapor deposition (NFO-CVD), which enables the fabrication of nanometer-scale structures, while precisely controlling their size and position [3-5]. In this process, resonant photons excite metal-organic molecules from the ground state to the excited electronic state and the excited molecules relax to the dissociation channel [6]. Then the dissociated metal atoms adsorb to the substrate. Thus, NFO-CVD is applicable to various materials, including metals, semiconductors, and insulators [see Figs. 2(a), (b), and (c)]. We also fabricated UV-emitting ZnO dots by oxidizing Zn immediately after deposition to confirm that the deposited dots are Zn [see Fig. 2(d)] [5].

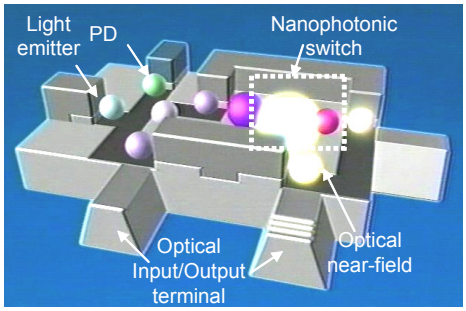

Fig. 1 Nanophotonic switch

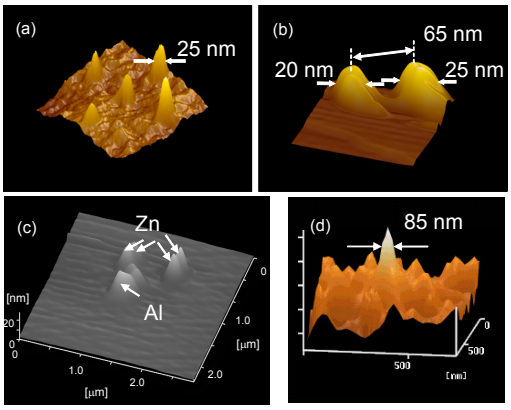

Fig. 2 Shear-force images of deposited Al dots (a), Zn dots (b), and Zn and Al dots (c). (e) Photoluminescence image of single deposited ZnO dot.

In order to realize further controllability in size, we studied dependence of nanoparticle formation on photon energy used for the NFO-CVD. As the light source for the photodissociation of diethylzinc (DEZn), a He-Cd laser [photon energy E_p = 3.81 eV] was used. This is a resonant light because its photon energy exceeds the band edge energy of DEZn. Figure 3(a) shows topographical image of Zn deposited on a (0001) sapphire substrate by NFO-CVD.

To control the size distribution, we introduced Ar^+ (E_p = 2.54 eV) or He-Ne (E_p = 1.96 eV) lasers, in addition to the He-Cd laser. Their photon energies are lower than the absorption band edge energy of DEZn, i.e., they are nonresonant light sources for the dissociation of DEZn. Figures 3(b) and 3(c) show topographical images of Zn deposited by NFO-CVD with irradiation at E_p = 3.81 and 2.54 eV and at E_p = 3.81 and 1.96 eV, respectively. The respective FWHMs were 60, 30, and 15 nm [see Fig. 3(d)]; i.e., a lower photon energy gave rise to smaller particles.

The dependency of fabricated size on the photon energy is due to plasmon resonance of optical absorption in a metal nanoparticle [7-9], which strongly depends on particle size. This can

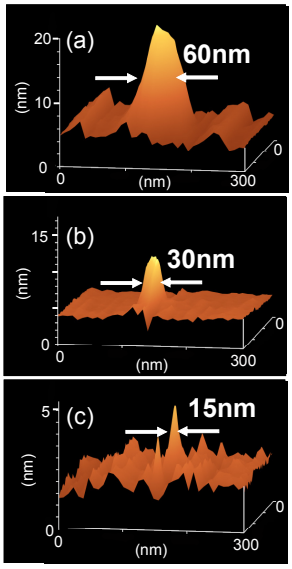

Fig. 3 Bird's-eye views of shear-force topographical images of Zn deposited by NFO-CVD with (a) E_p = 3.81 eV, (b) E_p = 3.81 and 2.54 eV, and (c) E_p = 3.81 and 1.96 eV, respectively.

induce the desorption of the deposited metal nanoparticles [10]. As the deposition of metal nanoparticles proceeds in the presence of light, the growth of the particles is affected by a trade off between deposition and desorption, which determines their size, and depends on the photon energy.

These results suggest that the additional light controls the size of the dots and reduces the size fluctuation, i.e., size regulation is realized. Furthermore, the position can be controlled accurately by controlling the position of the fiber probe used to generate the optical near field. The experimental results and the suggested mechanisms described above show the potential advantages of this technique in improving the regulation of size and position of deposited nanodots. Furthermore, since our deposition method is based on a photodissociation reaction, it could be widely used for nanofabrication of the other material for example GaN, GaAs, and so on.

For realization of mass-production of nanometric structures, we also demonstrated possibilities of applying such a near-field desorption to other deposition technique, which does not use fiber probe. We performed metal-nanoparticles deposition over the pre-formed grooves on the glass substrate by the sputtering uneder the illumination [see Fig. 3(a)]. Since the optical near-field is enhanced at the edge of the groove, it can induce the desorption of the deposited metal nanoparticles when they reach at their resonant size for optical absorption. By illuminating 2.33-eV light during the

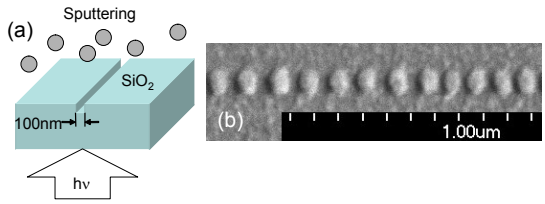

Fig. 3 (a) Fabrication process of metal dots-chain by the spattering using near-field desorption technique. (b) Al dots-chain with 2.33-eV light illumination.

depostion of Al film, we successefully fabricated 80-nm Al dots chain with 40-nm separation as long as 20 μm [see Fig. 3(b)]

In order to realize a far/near -field conversion device coupling nanophotonic ICs with external conventional diffraction-limited photonic devices, we will also discuss possibilities of applying such a structure to a nano-dot coupler, in which energy transfer relies on near-field coupling between plasmon-polariton modes of neighboring particles [11].

References

1) M. Ohtsu, K. Kobayashi, T. Kawazoe, S. Sangu, and T. Yatsui, IEEE J. Sel. Top. Quantum Electron. IEEE J. Selected Topics in Quantum Electron., **8**, 839 (2002).
2) T. Kawazoe, K. Kobayashi, S. Sangu, and M. Ohtsu, Appl. Phys. Lett., **82**, 2957 (2003).
3) Y. Yamamoto, M. Kourogi, M. Ohtsu, V. Polonski, and G. H. Lee, Appl. Phys. Lett., **76**, 2173 (2000).
4) Y. Yamamoto, M. Kourogi, M. Ohtsu, and T. Kawazoe, IEICE Trans. Electron., **E85-C**, 2081 (2002).
5) T. Yatsui, T. Kawazoe, M. Ueda, Y. Yamamoto, M. Kourogi, and M. Ohtsu, Appl. Phys. Lett.,.**81**, 3651 (2002).
6) R. L. Jackson, J. Chem. Phys., **96**, 5938 (1992).
7) G. T. Boyd, Th. Rasing, J. R. R. Leite, and Y. R. Shen, Phys. Rev. B, **30**, 519 (1984).
8) H. Kuwata, H. Tamaru, K. Esumi, and K. Miyano, Appl. Phys. Lett. **83**, 4625 (2003).
9) R. G. Yarovaya, I. N. Shklyarevsklii, and A. F. A. El-Shazly, Sov. Phys. JETP, **38**, 331 (1974).
10) K. F. MacDonald, V. A. Fedotov, S. Pochon, K. J. Ross, G. C. Stevens, N. I. Zheludev, W. S. Brocklesby, and V. I. Emel'yanov, Appl. Phys. Lett. **80**, 1643 (2002).
11) W. Nomura, T. Yatsui, and M. Ohtsu, Appl. Phys. Lett., **88**, 181108 (2005).

Proceedings of 2005 5th IEEE Conference on Nanotechnology
Nagoya, Japan, July 2005

Evaluating the quantum confinement effect of isolated ZnO nanorod single-quantum-well structures using near-field ultraviolet photoluminescence spectroscopy

T. Yatsui,[1] T. Kawazoe,[1] M. Ohtsu,[1,2] S. J. An,[3] J. Yoo,[3] and G.-C. Yi[3]

[1]SORST, Japan Science and Technology Agency, Machida, Tokyo, Japan 194-0004
[2]School of Engineering, The University of Tokyo, Bunkyo-ku, Tokyo, Japan 113-8656
[3]National CRI Center for Semiconductor Nanorods and Department of Materials Science and Engineering, Pohang University of Science and Technology (POSTECH) Gyeongbuk 790-784, Korea

***Abstract* — Using low-temperature near-field spectroscopy of isolated ZnO nanorod single-quantum-well structures (SQWs), the dependence of the quantum confinement effect of the photoluminescence peak on the well width was observed. Furthermore, the homogeneous linewidth of the isolated ZnO SQWs was determined as small as 3 meV.**

***Index Terms* — Nanophotonics, ZnO, single-quantum-well, nanorod, optical near-field.**

I. Introduction

Future optical transmission systems will require nanophotonic integrated circuits [1] composed of nanometer-scale dots to increase data transmission rates and capacity. ZnO nanocrystallite is a promising material for realizing room-temperature nanophotonic devices, owing to its large exciton binding energy [2]. Furthermore, the recent demonstration of a semiconductor nanorod quantum-well structure enabled us to fabricate nanometer-scale electronic and photonic devices on single nanorods [3-5]. Recently, ZnO/ZnMgO nanorod multiple-quantum-well structures (MQWs) were fabricated and the quantum confinement effect was observed successfully [6]. Further improvement in the fabrication of nanorod heterostructures has resulted in the observation of significant PL intensity, even from ZnO/ZnMgO nanorod single-quantum-well structures (SQWs) [7]. To confirm the promising optical properties of individual ZnO SQWs for realizing nanophotonic devices, we measured the photoluminescence (PL) spectra from isolated ZnO SQWs for the first time using a low-temperature near-field optical microscope (NOM).

II. ZnO/ZnMgO SQW nanorods

ZnO/ZnMgO SQWs were fabricated on the ends of ZnO nanorods with a mean diameter of 40 nm using catalyst-free metalorganic vapor phase epitaxy [8]. The average concentration of Mg in the ZnMgO layers used in this study was determined to be 20 at. %. The ZnO well layer thickness, L_w, investigated in this study were 2.5, 3.75, and 5.0 nm, while the thicknesses of the ZnMgO bottom and top barrier layers in the SQWs were fixed at 60 and 18 nm, respectively. After growing ZnO nanorod SQWs on sapphire (0001) substrate, they were dispersed on the substrate to be isolated.

III. Near-field spectroscopy

To confirm the promising optical properties of individual ZnO SQWs, we used collection-mode NOM at 15K, using a He-Cd laser (λ=325 nm) for the excitation, and a UV fiber probe with an aperture diameter of 30 nm [Fig. 1].

In the near-field spectra, the emission peaks around 3.365 and 3.552 eV originate from the neutral-donor bound exciton (DOX) in the ZnO stem, and the free exciton in the ZnMgO layers, respectively, which

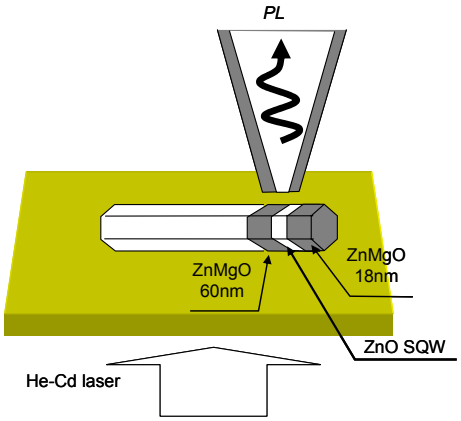

Fig. 1 Schematic of near-field spectroscopy of isolated ZnO SQWs on the ends of ZnO nanorod.

correspond to the peaks in the far-field spectra [dashed curves in Fig. 2(a)]. At the well layer, however, the emission from DOX was suppressed, while blue-shifted PL emission peaks emerged at I^{QW}_1: 3.499 (L_w = 2.5 nm), I^{QW}_2: 3.444 (L_w = 3.75 nm), and I^{QW}_3: 3.410 eV (L_w = 5.0 nm). Their peak positions were consistent with the theoretical prediction (3.488, 3.430, and 3.410 eV) using the finite square-well potential of the quantum confinement effect in the ZnO well layer for L_w = 2.5, 3.75, and 5.0 nm, respectively, we concluded that peak I^{QW}_1-I^{QW}_3 originated from the ZnO SQWs. The theoretical calculation used $0.28m_0$ and $1.8m_0$ as the effective masses of an electron and hole in ZnO, respectively, at a ratio of conduction and valance band offsets (ΔE_c /ΔE_v) of 9, and a band gap offset (ΔE_g) of 250 meV [7]. The spatial distribution of the optical near-field intensity for ZnO SQWs of L_w = 3.75 nm [Figs. 2(b) and 2(c)] supported the postulate that the blue-shifted emission peaks were confined to the end of the ZnO stem. Furthermore, the spectral widths (3 meV) of the ZnO SQWs for L_w = 2.5 nm and L_w = 3.75 nm were much narrower than those of the far-field spectra (40 meV).

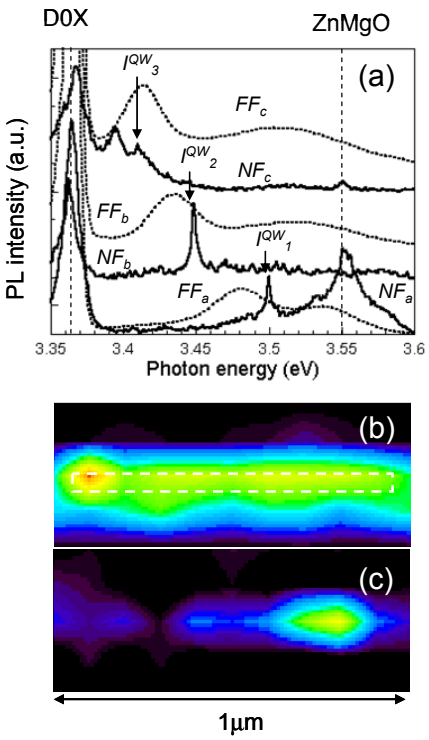

Fig. 2. (a) Size-dependent PL spectra of isolated ZnO nanorod SQWs with L_W = 2.5 nm (FF_a, NF_a), 3.75 nm (FF_b, NF_b), and 5.0 nm (FF_c, NF_c), obtained at 15 K. *FF*: far-field spectrum of vertically aligned ZnO nanorod SQWs. *NF*: near-field PL spectrum of the isolated ZnO SQWs obtained at the well layer. The near-field intensity distributions of the isolated ZnO SQWs (L_w = 3.75 nm) obtained at (b) 3.365 and (c) 3.444 eV, respectively

To estimate the linewidth of the isolated ZnO SQWs, we observed power-dependent PL spectra of L_w = 3.75 nm [Fig. 3(a)] at excitation densities ranging from 0.6 to 4.8 W/cm^2. The shape of each spectrum was reproduced by the Lorentzian function indicated by the solid line. As shown in Figs. 3(b) and 3(c), the integrated PL intensity (I_{PL}) increased linearly, while the homogeneous width (Δ) remained constant around 3 meV. These results indicate that the emission line at 3.444 eV was the emission from a single-exciton state in ZnO SQWs, and that the linewidth of the PL spectra is governed by the homogeneous broadening that is the result of the internal electric field effect in ZnO [9] or a large stem width (40 nm).

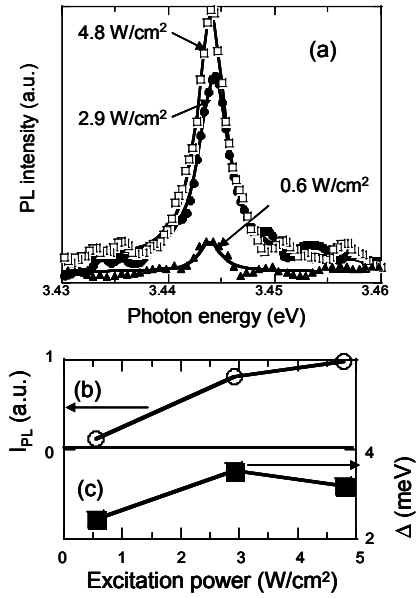

Fig. 3. (a) Low-temperature (15 K) near-field PL spectrum of the isolated ZnO SQWs (L_W=3.75 nm) at excitation densities ranging from 0.6 to 4.8 W/cm^2. Power dependence of the (b) integrated PL intensity (I_{PL}) and (c) linewidth (Δ).

IV. Conclusions

The results shown here provide criteria for realizing nanophotonic devices using a two-level system. As a representative device, a nanophotonic switch can be realized by controlling the dipole forbidden optical energy transfer among resonant energy levels in nanometer-scale QD via an optical near field [10]. By considering the amount of the energy shift of the single exciton state in ZnO nanocrystallites owing to the quantum confinement effect at room temperature, it is estimated that the size

accuracy in ZnO nanocrystallites must be as low as ±10% in order to realize efficient near-field energy transfer among the resonant energy state in a nanophotonic switch composed of 5-, 7-, and 10-nm QDs [10]. Therefore, the success of near-field PL and absorption measurement of isolated SQWs described above is a promising step toward designing a nanophotonic switch and related devices.

REFERENCES

[1] M. Ohtsu, K. Kobayashi, T. Kawazoe, S. Sangu, and T. Yatsui, "Nanophotonics: design, fabrication, and operation of nanometric devices using optical near fields," IEEE Journal of Selected Topics in Quantum Electronics 8, 2002, pp.839-862.

[2] A. Ohtomo, K. Tamura, M. Kawasaki, T. Makino, Y. Segawa, Z. K. Tang, G. K. L. Wong, Y. Matsumoto, and H. Koinuma, "Room-temperature stimulated emission of excitons in ZnO/(Mg, Zn)O superlattices," Appl. Phys. Lett. 77, 2000, pp. 2204-2206.

[3] Y. Wu, R. Fan, and P. Yang, "Block-by-block growth of single crystalline Si/SiGe superlattice nanowires," Nano Lett. 2, 2002, pp.83-86.

[4] M. T. Björk, B. J. Ohlsson, C. Thelander, A. I. Persson, K. Deppert, L. R. Wallenberg, and L. Samuelson, "Nanowire resonant tunneling diodes," Appl. Phys. Lett. 81, 2003, pp. 4458-4460.

[5] M. S. Gudiksen, L. J. Lauhon, J. Wang, D. C. Smith, and C. M. Lieber, "Growth of nanowire superlattice structures for nanoscale photonics and electronics." Nature 415, 2002, pp.617-620.

[6] W. I. Park, G.-C. Yi, M. Y. Kim, and S. J. Pennycook, "Quantum confinement observed in ZnO/ZnMgO nanorod heterostructures," Adv. Mater. 15, 2003, 526-529.

[7] W. I. Park, S. J. An, J. L. Yang, G.-C. Yi, S. Hong, T. Joo, and M. Kim, "Photoluminescent properties of $ZnO/Zn_{0.8}Mg_{0.2}O$ nanorod single-quantum-well structures," J. Phys. Chem. B 108, 2004, pp.15457-15460.

[8] W. I. Park, D. H. Kim, S.-W. Jung, and G.-C. Yi, "Metalorganic vapor-phase epitaxial growth of vertically well-aligned ZnO nanorods," Appl. Phys. Lett. 80, 2002, pp.4232-4234.

[9] T. Makino, A. Ohtomo, C. H. Chia, Y. Segawa, H. Koinuma, and, M. Kawasaki, "Internal electric field effect on luminescence properties of ZnO/(Mg,Zn)O quantum wells," Physica E 21, 2004, 671-675.

[10] T. Kawazoe, K. Kobayashi, S. Sangu, and M. Ohtsu, "Demonstration of a nanophotonic switching operation by optical near-field energy transfer," Appl. Phys. Lett. 82, 2003, pp.2957-2959.

Proceedings of 2005 5th IEEE Conference on Nanotechnology
Nagoya, Japan, July 2005

Demonstration of a Nanophotonic NOT-Gate using Near-Field Optically Coupled Quantum Dots

Tadashi Kawazoe[1], Kiyoshi Kobayashi[2], Kouichi Akahane[3], Naokatsu Yamamoto[3], Naoki Ohtani[3], and Motoichi Ohtsu[1,4]

[1]Japan Science and Technology Agency, Machida, Tokyo 194-0004, Japan.
[2]Department of Physics, Tokyo Institute of Technology, Meguro-ku, Tokyo 152-8551, Japan.
[3]National Institute of Information and Communications Technology, Koganei, Tokyo 184-8795, Japan.
[4]Department of Electronics Engineering, University of Tokyo, Bunkyo-ku, Tokyo 113-8656, Japan.

***Abstract* — We demonstrate, for the first time, operation of a nanometric optical NOT-gate using CuCl quantum dots coupled by an optical near-field interaction. The device size was smaller than 20nm and its operation energy was much lower than that of a conventional photonic device. Toward an actual nanophotonic device, we discuss the possibility of coupled InAlAs quantum dots. Double-layer InAlAs quantum dots was prepared using MBE. On the near-field luminescence spectroscopy, a luminescence peak from a single InAlAs quantum dots was observed for the first time. We show that the sample has great potential for a nanophotonic device.**

***Index Terms* — Nanometric optical control, nanophotonic devices, optical near field, quantum dots, near-field spectroscopy.**

I. Introduction

Optical data transmission systems require increased integration of photonic devices for higher data transmission rates. It is estimated that the size of photonic switching devices should be reduced to a sub-wavelength scale, since in the near future it will be necessary to integrate more than 10,000×10,000 input and output channels on a module. As conventional photonic devices, *e.g.*, diode lasers and optical waveguides, have to confine light waves within their cavities and core layers, respectively, their minimum sizes are limited by the diffraction of light. Therefore, they cannot meet the size requirement, which is beyond this diffraction limit. It can be readily understood that a novel optical nanotechnology, *i.e.*, nanophotonics, is required in order to go beyond the diffraction limit [1].

An optical near-field generated on a nanometric element, is free from the diffraction of light and enables the operation and integration of nanometric optical devices. By using the localized optical near-field as the signal carrier, which is transmitted from one nanometric element to another, a nanoscale photonic device beyond the diffraction limit can be realized. The primary advantage of nanophotonics is the capacity to achieve novel functions that are based on local electromagnetic interactions, while realizing nanometer-sized photonic devices. Based on this idea, we observed an optically forbidden energy transfer between neighboring cubic CuCl QDs via an optical near-field [2] and proposed several nanometric optical devices: a nanometric AND-gate (*i.e.*, a nanophotonic switch) [3], a surface plasmon-polariton condenser [4], a nanometric XOR-logic gate [5], and an optical nanofountain (*i.e.*, a nanometric optical condenser) [6]. So far, we have demonstrated operation of the AND gate, surface plasmon-polariton condenser and optical nanofountain [3, 4, 6]. Here, we propose a nanometric NOT-gate using CuCl quantum dots embedded in a NaCl matrix, and demonstrate its operation. CuCl quantum dots are unsuitable for the actual integration owing to their size and position inhomogeneity and chemical instability, but they are suitable for verifying the operation principle. For the III-V semiconductor, we can obtain size- and position-controlled quantum dots using molecular beam epitaxial growth (MBE). Toward their actual integration in nanophotonic modules, we prepare the InAlAs quantum dots using MBE and discuss a NOT-gate using InAlAs quantum dots. Finally, we obtained luminescence from a single InAlAs quantum dot at around 1.8 eV using a near-field spectrometer, for the first time. The experimental results give rise to high expectation of InAlAs quantum dots acting as the nanophotonic device.

II. Nanophotonic NOT-gate

Figure 1 shows a schematic explanation of the proposed nanophotonic NOT-gate. In a cubic quantum dot, the carriers are quantized and their discrete energy levels are given by the quantum numbers (n_x, n_y, n_z)[2]. Assuming two cubic quantum dots with side lengths $\sqrt{2}L$ (QD_{IN}), and $L+\alpha$ (QD_{OUT}), respectively, the quantized energy levels (2,1,1) in QD_{IN} and (1,1,1) in QD_{OUT} are not resonant with

each other, but are nearly resonant. Here, α is the extra size required to detune their energy levels. QD_{IN} is used as the input terminal of the gate. Optical power is supplied to QD_{OUT}, which acts as the output terminal. Without the input signal, the energy from the optical power supply is emitted from QD_{OUT} directly, generating output (Fig. 1(a) In=0 & Out=1). Conversely, by applying the input signal, the energy level (2,1,1) in QD_{IN} shifts owing to the band renormalization or the DC-Shark effect, by which it becomes resonant to (1,1,1) in QD_{IN}. Therefore, the energy from the optical power supply in QD_{IN} is transferred to QD_{OUT} by an optical near-field interaction [2], which suppresses output signal generation (Fig. 1(b) In=1 & Out=0). As a result, an output signal with temporal behavior that is inverted from that of the input signal is obtained. These operations correspond to a NOT-gate.

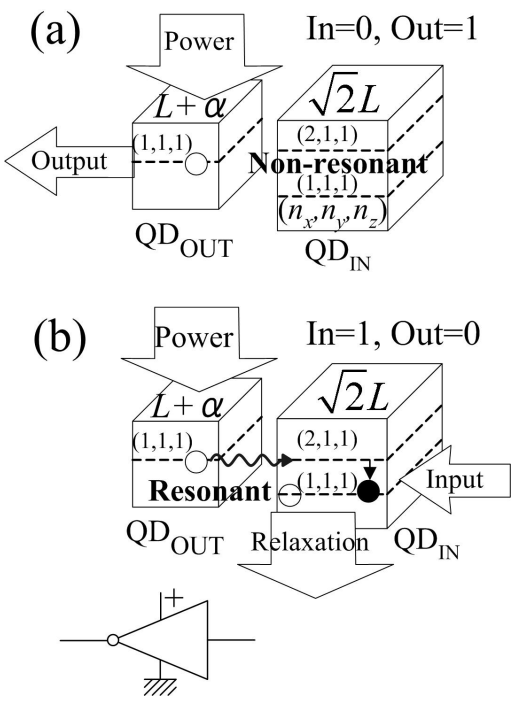

Fig. 1. Schematic explanation of the operation of a nanophotonic NOT-gate using cubic quantum dots. QD_{IN} acts as the input terminal. QD_{OUT} acts as the output and power supply terminals.

III. NOT-GATE OPERATION USING CUCL QUANTUM DOTS

We used CuCl QDs embedded in a NaCl matrix to verify NOT-gate operation, as CuCl QDs offer discrete energy levels similar to the exciton described in Fig. 1 [7]. In the experiment, the second harmonic generation (SHG) of CW Ti:sapphire laser ($h\nu$ = 3.2704 eV) and the SHG of a mode-locked Ti:sapphire laser ($h\nu$ = 3.2195 eV) were used as the optical power supply and input signal pulse, respectively. The respective power densities of the optical power supply and input signal were 1 and 2 W/cm^2 at the sample surface. The sample temperature was controlled at 15 K. Figure 2(a) shows the spatial distribution of the optical near-field output-signal intensity without an input signal, *i.e.*, with the optical power supply only. Figure 2(b) shows the distribution with an input signal pulse. These images were acquired using near-field optical spectrometry in the area of the sample. The insets in Fig. 2 are schematic drawings of the existing QD pair for NOT-gate operation, which were confirmed from the luminescence spectra. The sizes of the two QDs, estimated from the wavelengths of their luminescence, were 5.0 and 6.3 nm, which satisfy the NOT-gate operation condition, as shown in Fig. 1. We measured the NOT-gated signal at the center of the circles in Fig. 2, from which the size of this device was estimated to be 20 nm.

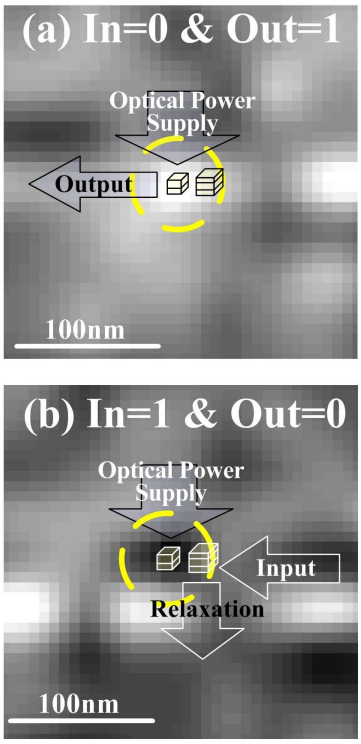

Fig. 2. Spatial distribution of the output signal from a nanophotonic NOT-gate measured using a near-field microscope at Input=0 (a) and Input =1 (b).

The dynamic behavior of the NOT-gate was evaluated using the time correlation single photon counting method. The repetition rate and pulse duration of the laser were 80 MHz and 2 ps, respectively. The time resolution of the experiment was 15 ps. Figure 3 shows the temporal

evolution of the output signal. The horizontal broken line shows the output signal level without an input signal pulse. The output signal rises synchronously within a time period shorter than the time resolution (the high, short pulses synchronous with the input signal pulses arise from leakage of the pump pulse to the detection instruments, and are artifacts), and it decreases to a level lower than the level indicated by the broken line. The fall time of the output signal is about 100 ps, which corresponds to the energy transfer time between QDs. This output signal recovers to the level of the broken line within 10 ns, which is close to the exciton lifetime in CuCl QDs. This means that this NOT-gate can operate at a 100-MHz repetition frequency. The advantages of this nanophotonic NOT-gate are its small size and low power consumption. We estimated that the switching energy of this device was about 5 orders of magnitude smaller than the conventional electronic gate.

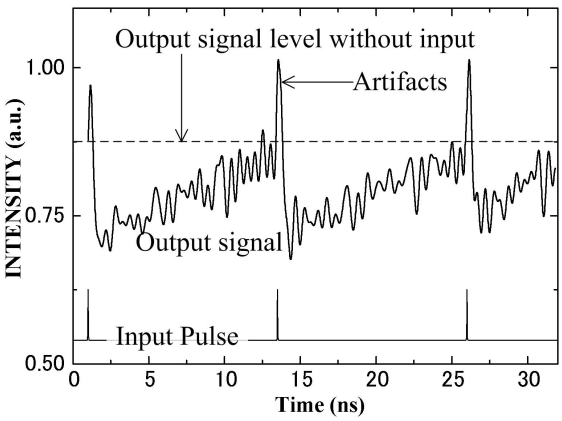

Fig. 3. Temporal evolution of the output (upper) and input pulse (lower) signals from the nanophotonic NOT gate circled in Fig. 2.

IV. Nanophotonic device using InAlAs qunatum dots

CuCl quantum dots embedded in NaCl have the potential to be an optical near-field coupled system because the possibility of other energy transfer, such as carrier tunneling and Coulomb coupling, can be neglected. However, CuCl is not suitable for an actual device owing to its chemical instability and the controllability of dot size and position. Therefore, we have attempted to construct nanophotonic devices using other materials [8, 9]. The III-V compound semiconductor is one of the promising materials for an actual nanophotonic device. In the III-V semiconductors, InAlAs is suitable for our purpose: realization of a nanophotonic integrated device. As its bandgap can be controlled widely from 0.3 eV to 2.2 eV, a strong confined system (such as CuCl quantum dots in NaCl) is possible. For the first step, we selected X=0.5 as the composition ratio of $In_XAl_{1-X}As$ quantum dots to make the bandgap energy exceed 1.6 eV, where general photodetectors have high sensitivity.

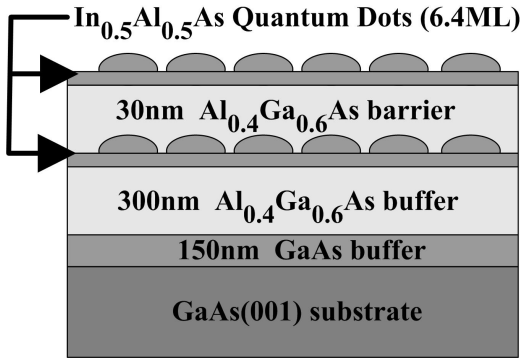

Fig. 4. Sample structures fabricated using MBE in S-K mode growth. The mean size of the double layer $In_{0.5}Al_{0.5}As$ quantum dots was 5 nm high and 25 nm in diameter.

Figure 4 shows sample structures fabricated using MBE in S-K mode growth [10, 11]. The mean $In_{0.5}Al_{0.5}As$ quantum dots were 5 nm high and 25 nm in diameter. For nanophotonic device operation, double quantum dots layers were grown. Using this fabrication method, the quantum dots can be aligned vertically. Therefore, we can easily obtain the quantum dots pair acting as a NOT-gate. To investigate the suitability of the fabricated sample as a nanophotonic device, we measured the far- and near-field luminescence spectra. In Fig.5 (a), the broken curve shows the far-field luminescence spectrum at 12 K. The luminescence peak at 1.5 eV comes from the GaAs buffer layer and the luminescence around 1.8 eV comes from the $In_{0.5}Al_{0.5}As$ quantum dots. The far-field luminescence from the quantum dots is broadened owing to the size inhomogeneity. The solid curve shows the typical near-field luminescence spectrum at 11 K. For the near-field spectroscopy, we used a HeNe laser ($h\nu$ = 1.958 eV) and obtained the luminescence spectrum form a single quantum dot. Its luminescence linewidth was free from size inhomogeneity and was much narrower. The luminescence from a single quantum dot appeared at 1.7569 eV. The spectral linewidth (FWHM) was less than 500 μeV, which was limited by the spectral resolution of the spectrometer used. This is the first observation of such narrow luminescence from a single InAlAs quantum dot and this narrowness of luminescence indicates that the sample was of high quality.

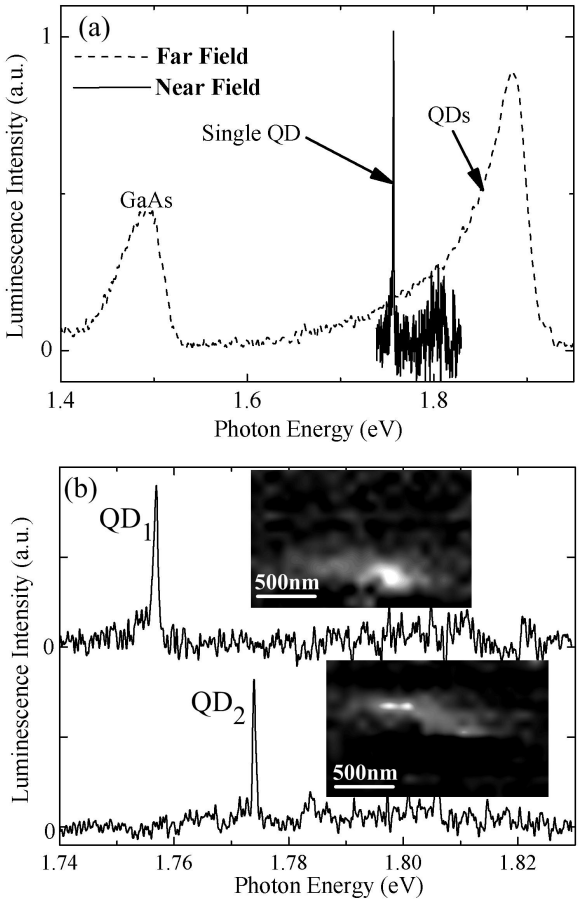

Fig. 5. (a) Far-field (broken curve) and near-field (solid curve) luminescence spectra of the fabricated sample (InAlAs quantum dots). (b) Near-field luminescence spectra from different quantum dots at different positions. The Insets show the luminescence intensity distributions on the sample surface measured using the scanning near-field spectrometer.

Figure 5 (b) shows the near-field luminescence spectra at the different positions on the sample surface. The insets show the intensity distributions of the respective luminescence peaks QD_1 and QD_2. As their photon energies and intensity distributions differ, the luminescence peaks QD_1 and QD_2 come from different quantum dots. In this way, we confirmed the existences of several quantum dots within an area of 1 μm^2. The density of the quantum dots measured using atomic force microscopy exceeded 1000 /μm^2. We postulate that there are two reasons for the low quantum-dot density measured using near-field spectrometry. 1: Energy-selective excitation. The photon energy of the laser used was lower than the bandgap of the barrier layer. Therefore, when the linewidths of the discrete energy sublevels in a quantum dots are narrow, the number of quantum dots decreased due to the energy-selective excitation. 2: Energy transfer to the surface quantum-dot layer and non-radiative energy dissipation. The luminescence efficiency of the quantum dots without cap layer is very low owing to the non-radiative recombination pass [12]. When vertical energy transfer from quantum dots with a cap layer to quantum dots without a cap layer occurs, most of the quantum dots dissipate the excitation energy non-radiatively. These two reasons support the postulate that the sample acts as the desired nanophotonic device, because reason 1 means sample quality is high and the energy transfer in reason 2 is necessary for operation of the nanophotonic device.

V. Conclusion

We demonstrated operation of a nanometric optical NOT-gate with a device size of 20 nm using two cubic CuCl quantum dots. This device utilizes the resonant optical near-field energy transfer and the small energy shift owning to the band renormalization or DC-Shark effect of quantum dots. For an actual nanophotonic integrated device, we fabricated the double layer InAlAs quantum dots and observed the luminescence of a single quantum dot for the first time. Finally, we described the potential of InAlAs quantum dots as a nanophotonic device.

References

[1] M. Ohtsu, K. Kobayashi, T. Kawazoe, S. Sangu, and T. Yatsui, IEEE J. Sel. Top. Quant. Electron **8**, 839 (2002).
[2] T. Kawazoe, K. Kobayashi, J. Lim, Y. Narita, and M. Ohtsu, Phys. Rev. Lett. **88**, 067404 (2002).
[3] T. Kawazoe, K. Kobayashi, S. Sangu, and M. Ohtsu, Appl. Phys. Lett., **82**, 2957 (2003).
[4] W. Nomura, T. Yatsui, and M. Ohtsu, submitted to Appl. Phys. Lett.
[5] S. Sangu, K. Kobayashi, A. Shojiguchi, and M. Ohtsu, Phys. Rev. B, **69**, 115334.
[6] T. Kawazoe, K. Kobayashi, and M. Ohtsu, to be published Appl. Phys. Lett., **86**, (2005).
[7] N. Sakakura and Y. Masumoto, Phys. Rev. B **56**, 4051 (1997).
[8] T. Yatsui, M. Ueda, Y. Yamamoto, T. Kawazoe, M. Kourogi, and M. Ohtsu, Appl. Phys. Lett. **81**. 3651 (2002).
[9] T. Kawazoe, K. Kobayashi, S. Takubo, and M. Ohtsu, J. Chem. Phys. **122** 024715 (2005).
[10] L. Goldstein, F. Glas, J. Y. Marzin, M. N. Charasse, and G. Le Roux, Appl. Phys. Lett. **47**. 1099 (1985).
[11] K. Akahane, N. Yamamoto and N. Ohtani, Physica E **21** 295 (2004).
[12] H. Saito, K. Nishi and S. Sugou, Applied Physics Letters **73** 2742 (1998).

Proceedings of 2005 5th IEEE Conference on Nanotechnology
Nagoya, Japan, July 2005

Nanofabrication using Nonadiabatic Near-Field Photolithography

Hiroki Yonemitsu[1], Tadashi Kawazoe[2], and Motoichi Ohtsu[1, 2]
[1]Department of Electronics Engineering, University of Tokyo, Bunkyo-ku, Tokyo 113-8656, Japan
[2]Japan Science and Technology Agency, Machida, Tokyo 194-0004, Japan

Abstract: **This paper presents a novel photolithography method based on a nonadiabatic photochemical process, which is photo-activation via the molecular vibration energy level using an optical near field, to exceed light diffraction limits. We used this process to expose UV-photoresist, which does not react to visible light, using a 672-nm light source. Using independent coherence and polarization, which are intrinsic features of optical near-fields, we succeeded in forming T-, L-, and ring-shaped two-dimensional arrays. Finally, we found that even an electron-beam resist, which is completely photo-insensitive, could be exposed using this method, and we obtained a fine structure 50 nm wide.**

Index Terms: **Fabrication, nanotechnology, nonadiabatic photochemical reaction, photolithography, nanophotolithography**

I. INTRODUCTION

Novel methods of nano-fabrication are required for mass production of photonic and electronic devices. Fabrication that uses nano-imprint lithography, near-field phase mask lithography, and evanescent near-field optical lithography (ENFOL) [1] is less expensive and has a higher throughput than that using electron or ion beams, X-rays, or deep UV lithography. ENFOL is especially useful because it allows for the use of conventional photolithographic components and systems.

Spatial locality of an optical near field can be used in novel fabrication. For example, we found that in near-field optical chemical vapor deposition (NFO-CVD), metal organic molecules can be photodissociated even by an optical near field with a lower photon-energy than the dissociation energy of a molecule [2]. This unique photodissociation is due to a nonadiabatic photochemical process based on an exciton-phonon polariton model [3, 4]. According to this model, the nonadiabatic photochemical process is a universal phenomenon applicable to many other photochemical processes, including photoresist exposure.

Following from this model, we proposed a novel method of photolithography that uses a nonadiabatic photochemical process, *i.e.*, nonadiabatic near-field photolithography. Using this method, UV-photoresist, which is suitable for nano-lithography, can be exposed using inexpensive visible light sources and equipment without using expensive UV light sources.

The wave properties of light can cause problems for nanometric photolithography, including not only the diffraction limit, but also coherency and polarization dependence. In photolithography of high-density nanometric arrays, the optical coherent length is longer than the separation between adjacent corrugations, even when an Hg lamp is used, and there is not enough photoresist absorption to suppress fringe interference of scattered light due to the narrow separation. The transmission intensity of light passing through a photo-mask strongly depends on its polarization, so the design of photo-mask structures must include such effects. Since the optical near field in nonadiabatic near-field photolithography has no wave properties, these problems are easily solved.

In this study, we attempted nano-photolithography using visible 672- and 532-nm lasers for the UV photoresist; this paper illustrates the exposure time dependence of exposure depth. We were able to fabricate T-, L-, and ring-shaped arrays using nonadiabatic near-field photolithography. We were also able to demonstrate, for the first time, nonadiabatic near-field photolithography using a photo-insensitive electron-beam resist.

II. NONADIABATIC PHOTOLITHOGRAPHY USING UV PHOTORESIST

Figure 1 (a) shows a schematic configuration of the photo-mask used and the Si-substrate on which the photoresist (OFPR-800 or TDMR-AR87: Tokyo-Ohka Kogyo Co.) was spin-coated. These were used in contact mode, and we kept the gap between the photo-mask and photoresist as narrow as possible. Figures 1 (b)-(d) show atomic force microscopy (AFM) images of the photoresist surface after exposure and development. Figure 1 (b) shows that the nonadiabatic photochemical process created a corrugated pattern on the photoresist although photoresist OFPR-800 does not react to propagating 672-nm light. The corrugated pattern was 30 nm deep and 150 nm wide, much smaller than the wavelength of the light source.

To decrease exposure time, we used other light sources and photoresists, keeping in mind the material properties of the nonadiabatic photochemical process and its strong

dependence on photon energy [3, 4]. Figure 1 (c) illustrates our use of photoresist TDMR-AR87 with the g-line of a Hg lamp as the light source. The corrugated pattern on the photoresist caused by the nonadiabatic photochemical process was obtained with a 60-s exposure, although TDMR-AR87 does not react to the g-line. Figure 1 (d) shows that a similar pattern was obtained with exposure times as short as 3 s.

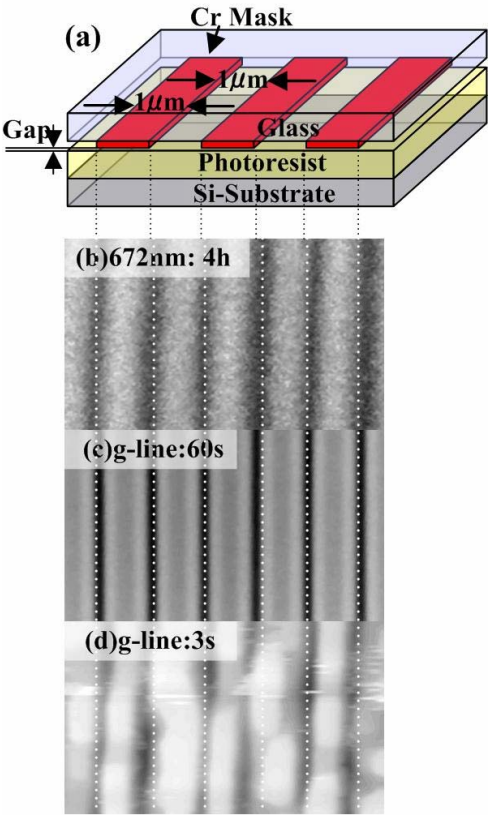

Figure 1. (a) A schematic of the photo-mask and the Si-substrate spin-coated with photoresist (OFPR-800 or TDMR-AR87) during the exposure process; (b) Atomic force microscopy images of photoresist OFPR-800 developed after a 4-h exposure to a 672-nm laser; (c) Atomic force microscopy images of photoresist TDMR-AR87 exposed to the g-line of a Hg lamp for 30 s; and (d) Atomic force microscopy images of photoresist TDMR-AR87 exposed to the g-line of a Hg lamp for 3 sec.

Grooves on the photoresist appeared along the edges of the Cr mask pattern. In this region, a steeply spatial gradient of optical energy indicates the existence of an optical near field. Therefore, these results of exposure indicate that the nonadiabatic process originates from an optical near-field effect [3,4].

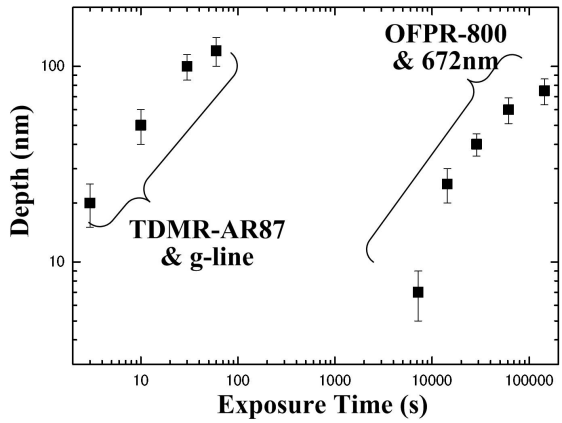

Figure 2. Depth of the developed grooves versus exposure time.

Figure 2 shows the exposure time dependency of groove depth in the corrugated pattern for two sets of light source and photoresist. The optical power densities of the exposure lights were 30 mW/cm^2 for the g-line light and 1 W/cm^2 for the 672-nm laser; both dependencies saturated at a depth of about 100 nm. These results support the hypothesis that the nonadiabatic process originates from an optical near-field effect, since the optical near field is localized at the edge of the Cr mask. The exposure rate in the first set of TDMR-AR87 and a g-line light source was more than 10^4 times higher than for the OFPR-800 with a 672-nm laser. This increase in exposure rate drastically decreased the exposure time, making it sufficiently short for mass production.

III. Formation of T-, L-, and Ring- Arrays

In demonstrations of conventional nano-photolithography reported by other researchers, the photomask with the lines and spaces structure are popularly used, because the problems come from the interference fringes and the negative effect of light polarization can be reduced by selecting the polarization. For more general patterns such as T-, L-, and ring-shaped arrays, however, it is impossible to reduce the problem, even if polarization is controlled. Figure 3 shows AFM photoresist images after development. We used photo-masks with T-, L-, and solid-circle Cr mask-arrays (see Figs. 3 (a), (b), and (c), respectively). At exposure, we used linear polarized light with the Hg g-line (λ=435nm) and TDMR-AR87 i-line (λ=365nm) photoresist. We were able to reproduce the formation of arrays with the expected shapes. For comparison, we exposed the photoresist using the i-line of a Hg lamp, which is used for

conventional photolithography. We did not obtain the expected shape, but only a pattern exposed by fringe light interference. Since the TDMR-AR87 photoresist has a low absorbance, there was a strong interference effect. This successful development of arrays with complex structures means that nonadiabatic near-field photolithography can have practical uses.

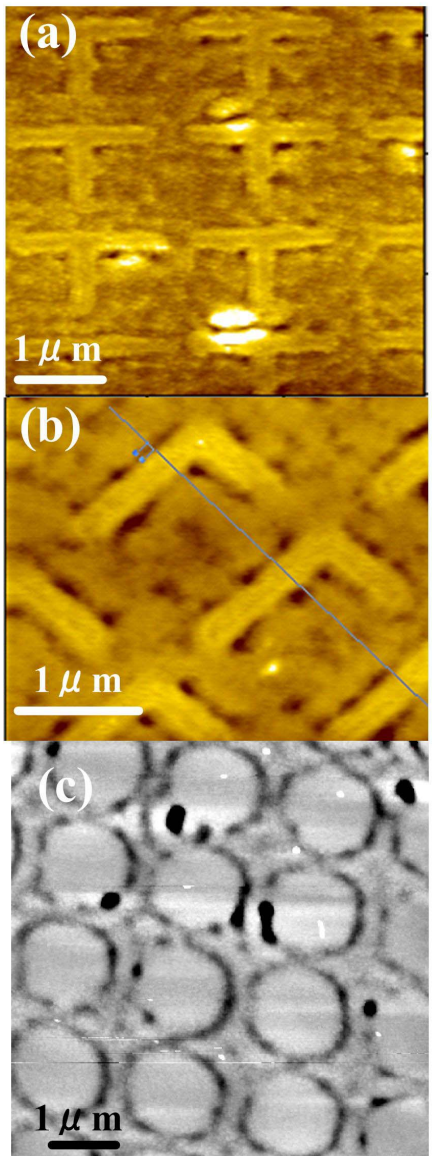

Figure 3. Atomic force microscopy images after development of photoresist TDMR-AR87 exposed to the g-line: (a) T-shaped array, (b) L-shaped array, and (c) solid circle-shaped array.

III. Using Electron Beam Resist

Since this novel process results from the excitation of molecular vibration modes, the nonadiabatic photochemical process using an optical near field can induce a photochemical reaction even in photo-insensitive organic molecules; electron beam resist is one example.

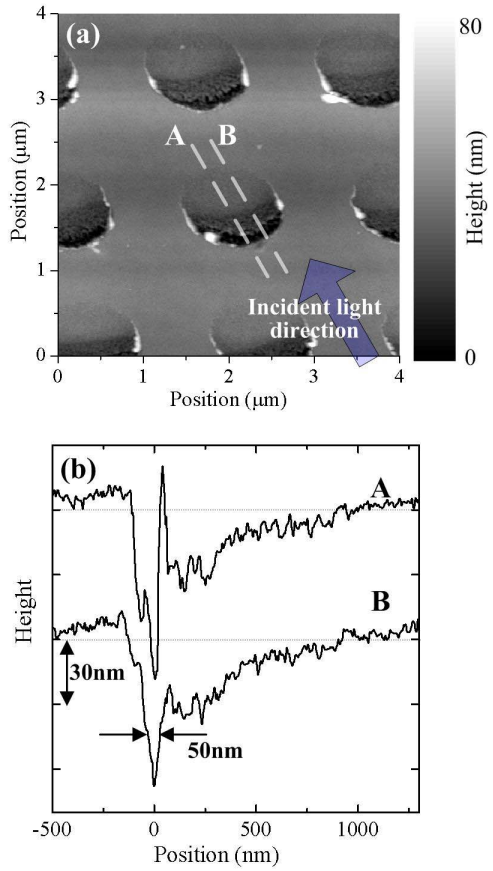

Figure 4. (a) Atomic force microscopy images after developing electron beam resist exposed using a 355-nm laser. (b) Cross-sectional profiles of the developed pattern along broken lines A and B in Fig. 4 (a).

Figure 4 shows atomic force microscope images of the electron beam resist (ZEP520: ZEON) surfaces after exposure and development using nonadiabatic near-field photolithography. The exposure light source was the third harmonic generation of a Q-switched Nd:YAG laser with a repetition rate of 20 Hz and a typical pulse width of 10 ns. The exposure light power density was 20 mW/cm^2 and the exposure duration was 5 minutes. The resist thickness was less than 80 nm, and the electron beam resist was prebaked at 180°C for 2 min. We used a photo-mask with a two-dimensional array pattern of 1 μm diameter Cr-disks (the disks were 100 nm thick and separated by 2 μm). The

incident angle of the exposure light was 70°, as shown in Fig. 5.

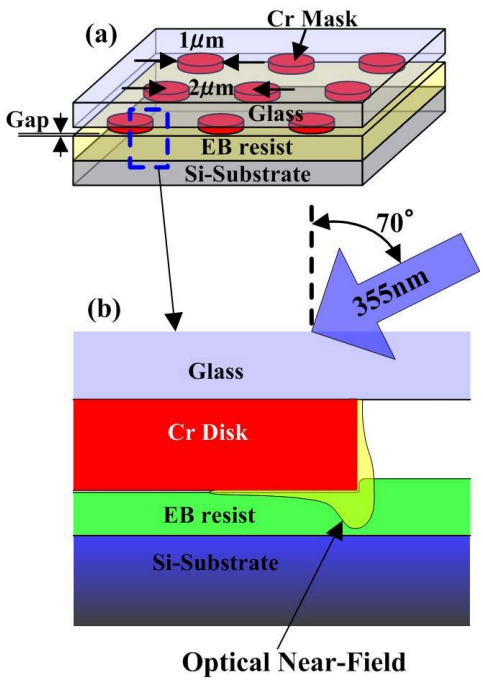

Figure 5. (a) Schematic configuration of the photo-mask used and the Si-substrate spin-coated with electron beam resist (ZEP520) during the exposure process. (b) Magnified schematic drawing of the contact region. The optical near field is eliminated, as shown in the drawing, due to the low incident angle of the exposure light.

In Fig. 4 (a), the arrow indicates the direction of the incident light. After development, we obtained fabricated two-dimensional arrays on the photoresist. The nonadiabatic photochemical process exposed even the electron-beam resist. The photoresist was not exposed by direct photo-irradiation, and the fabricated structure, which had a diameter of 1 μm, was asymmetrical because the light incident angle was 70° (see Fig. 5). Therefore, this result strongly supports the hypothesis that exposure of electron beam resists is due to the nonadiabatic photochemical process; the optical near-field distribution was not cylindrically symmetrical due to the large incident angle of light, as shown in Fig. 5 (b). Figure 4 (b) shows cross-sectional profiles of the patterns developed across broken lines A and B in Fig. 4 (a). The pit width was 50 nm, which is much smaller than the wavelength of the incident lights. The pit depth was 70 nm, deep enough to reach the Si substrate. The structure fabricated on the electron beam resist had a keen edge, providing a higher fabrication resolution, compared with fabricated structures using a photoresist (see Figs. 1 and 3). The great advantages of this keen edge are due to the properties of the electron beam resist, including a greater uniformity and smoother surface.

IV. Conclusion

Using nonadiabatic near-field photolithography, we succeeded in exposing UV photoresist using a visible light source, while the photoresist is inactive to visible light. Optical near-field features enable fabrication of nanometric two-dimensional arrays with complex shapes. Experimental results support the hypothesis that nonadiabatic photolithography is suitable for developing actual electronic and photonic devices.

Finally, we succeeded in exposing the electron beam resist using nonadiabatic photolithography. Since the properties of the electron beam resist make it suitable for developing fine structures, we obtained nanometric structures: keen-edged nano-pits 50 nm wide and 70 nm deep.

This work was supported by “Nanotechnology Support Project” of the Ministry of Education, Culture, Sports, Science and Technology (MEXT), Japan.

References

[1] M. M. Alkaisi, R. J. Blaikie, S. J. McNab, R. Cheung, and D. R. S. Cumming, “Sub-diffraction-limited pattering using Evanescent near field optical lithography”, Appl. Phys. Lett. **75**, 3560-3562 (1999).

[2] T. Kawazoe, Y. Yamamoto, and M. Ohtsu, “Fabrication of nanometric Zn dots by nonresonant near-field optical chemical-vapor deposition”, Appl. Phys. Lett., **79**, 1184-1186 (2001).

[3] T. Kawazoe, K. Kobayashi, S. Takubo, and M. Ohtsu, “Nonadiabatic photodissociation process using an optical near field”, J. Chem. Phys. **122** 024715-1-5 (2005).

[4] T. Kawazoe and M. Ohtsu, “Adiabatic and nonadiabatic nanofabrication by localized optical near fields”, J. J. Dubowski, D. B. Geohegan, and F. Träger, eds., Proc. SPIE **5339**, 619-630 (2004).

Hierarchical Optical Memory System Using Near- and Far-field Accesses

Makoto Naruse
National Institute of Information and Communications Technology, 4-2-1 Nukui-kita, Koganei, Tokyo 184-8795, Japan

Takashi Yatsui
Japan Science and Technology Agency, 687-1 Tsuruma, Machida, Tokyo 194-0004, Japan

Wataru Nomura and Motoichi Ohtsu
University of Tokyo, 7-3-1 Hongo, Bunkyo-ku, Tokyo 184-8795, Japan

Abstract: We propose a hierarchical optical memory system in which near-fields and far-fields read detailed dipole distributions and features within a region-of-interest, respectively. With hierarchical coding, near- and far-field accesses are associated with different hierarchical information.

OCIS codes: (210.0210) Optical data storage; (210.4680) Optical memories; (070.6020) Signal processing

1. Introduction

Ultrahigh-capacity optical data storage is an important technology. Various methods to increase the storage density have been pursued, such as shortening the operating wavelength [1]. With such methods, the storage density is still bound by the diffraction limit of light. One technique to overcome this limitation, which we make use of in our proposed system, is optical near-fields [2]. These high-density optical memories, however, need certain seeking or scanning mechanisms, which might be a problem, for instance, when searching terabyte- or petabyte-scale memories.

In dealing with this problem, we first note that information has hierarchy in terms of its meaning or quality, such as "*abstract*" and "*detailed*" information, "*low*" and "*high*" resolution information, and so forth. Similarly, as discussed below, we can find physical hierarchy in the different modes of light propagation. For example, in a near-field, a spatial distribution of the dipole moments is obtained, whereas in a far-field, the macroscopic features of the dipole moments are obtained. We associate these hierarchies in the system demonstrated in this paper, that is, a hierarchical optical memory system having both near- and far-field readout functions with a simple digital coding scheme. As schematically shown in Fig. 1, in the far-field mode, low-density, rough information is read-out, whereas in the near-field mode, high-density, detailed information is read-out.

2. Logical model of hierarchical coding

The two-layer hierarchical memory in this paper is explained using the notations *far-code* and *near-code*. The *far-code* depends on the array of bits distributed within a certain area and is determined logically to be either ZERO or ONE. Each *far-code* is comprised of multiple smaller-scale elements, whose existence is determined by the *near-code*. To obtain such information hierarchically, we introduce the following simple logical model.

Consider an (N+1)-bit digital code, where N is an even number. Now, let the *far-code* be defined depending on the number of ONEs (or ZEROs) contained in the (N+1)-bit digital code:

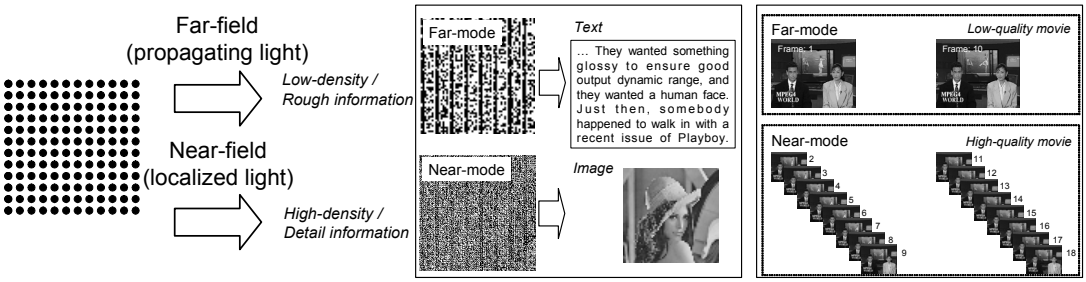

Fig. 1 Hierarchical optical memory using near- and far-field accesses.

$$far-code = \begin{cases} 1 & \text{If the number of ONEs} \geq \text{N/2} \\ 0 & \text{otherwise} \end{cases} \tag{1}$$

The (N+1) digits provide a total of 2^{N+1} possible different permutations, or codes. Here, we note that half of them, namely 2^N permutations, have less than N/2+1 ONEs among the (N+1) digits (i.e., *far-code* = 1), and the other half, also 2^N permutations, have more than N/2+1 ZEROs (i.e., *far-code* = 0). In other words, 2^N different codes could be assigned to two (N+1)-bit digital sequences so that their corresponding *far-codes* are ZERO and ONE, respectively. We call this (N+1)-bit code a *near-code*.

In Fig. 2, example *near-codes* are listed when N = 8. The correspondence between 2^N original codes and the (N+1)-bit *near-codes* is arbitrary. Therefore, we need a table-lookup when decoding an (N+1)-bit *near-code* to the original code. The example *near-codes* shown in Fig. 2(a) are listed in ascending order, but other lookup-tables or mappings are also possible.

Fig. 2(b) schematically demonstrates example codes in which a 9-bit *near-code* is represented in a 3 × 3 array of circles, where black and white mean ONE and ZERO, respectively. Here, (1) if the number of ONEs in the *near-code* is larger than five, then the *far-code* is ONE; and (2) if the number of ONEs in the *near-code* is four or less, then the *far-code* is ZERO.

Suppose, for example, that the *far-code* stores text data and the *near-code* stores 256-level (8-bit) image data. Consider a situation where the *far-code* should represent an ASCII code for "A", whose binary sequence is "0100001". Here, we assume that the gray levels of the first two pixels, which will be coded in the *near-code*, are the same value. (Here, they are at a level of "92".) However, the first two *far-codes* are different (ZERO followed by ONE). Referring to the rule shown in Fig. 2(a), and noticing that the first *far-code* is ZERO and the *near-code* should represent "92", the first *near-code* should be "001101010". In the same way, the second *near-code* is "110001011", so that it represents the level "92", while its corresponding *far-code* is ONE.

3. Physical model of the near- and far-codes

The *far-code* is determined based on the rule given by eq. (1), which depends on the number of ONEs coded in the *near-code*. Here, we employ a simple physical model where the *near-code* is represented by an array of dipole moments. As schematically shown in Fig. 3(a), dipole moments are distributed in an *xy* plane, where an (N+1)-bit code is assigned in an equally spaced grid. The electrical field at position $\boldsymbol{r}$ in Fig. 3(a) is given by

$$E(\boldsymbol{r}) = \sum_{i,j} E_{i,j} e^{-i\omega t + ik|\boldsymbol{r}-\boldsymbol{s}_{i,j}|} \frac{1}{|\boldsymbol{r}-\boldsymbol{s}_{i,j}|} \tag{2}$$

where ω is the operating frequency, k is the wave number, and $\boldsymbol{s}_{i,j}$ represents the position of a dipole specified by indexes i and j [3]. The existence of the dipole at the position $\boldsymbol{s}_{i,j}$ is given by the *near-code* as

$$E_{i,j} = \begin{cases} 0 & \text{nearcode}(i,j) = 0 \\ E_0 & \text{nearcode}(i,j) = 1 \end{cases} \tag{3}$$

Suppose that the pitch of adjacent dipoles is given by b. Here, if we assume that b<<1<<r, then eq. (2) is simplified

(a)

Given 8-bit code	***Near-code*** (***far-code* = 0**)	***Near-code*** (***far-code* = 1**)
0	000000000 (0)	000011111(31)
1	000000001 (1)	000101111(47)
2	000000010 (2)	000110111(55)
⋮	⋮	⋮
92	001101010 (106)	110001011(395)
93	001101100 (108)	110001101(397)
94	001110000 (112)	110001110(398)
⋮	⋮	⋮
253	111001000 (456)	111111101(509)
254	111010000 (464)	111111110(510)
255	111100000 (480)	111111111(511)

(b)

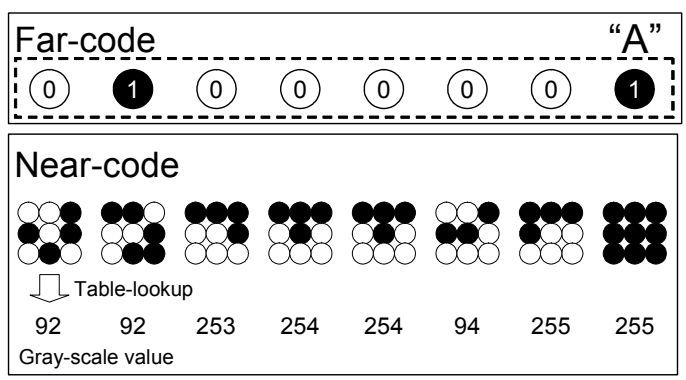

Fig. 2 Example of logical model for the *near-code* and *far-code*. Here, the original 8-bit information is coded differently in *near-code* depending on its corresponding *far-code* which is either ZERO or ONE.

to

$$E(\mathbf{r}) = E_0 \frac{e^{-i\omega t + ikr}}{r} \sum_{i,j} \text{nearcode}(i, j) \tag{4}$$

which means that the electrical field intensity at position ***r*** is proportional to the number of ONEs given by the *near-code* in that area.

4. Experiment and Simulation

For the experiment, an array of particles was made, in which 100-nm-diameter Au particles were distributed over a SiO_2 substrate. Each group of 3 × 3 Au particles with 300-nm pitch represented a *near-code*, and adjacent *near-codes* were located with 2-μm spacing. An SEM picture is shown in Fig. 3(b-1). These particles were fabricated by using electron-beam (EB) lithography using a Cr buffer layer (a liftoff technique), which allowed Au formation on the SiO_2 substrate with features having a diameter down to 35 nm, as shown in Fig. 3(b-2). Although final experimental results are still pending, basic simulations were performed assuming ideal isotropic metal particles to see how the scattering light varies depending on the number of particles for the *far-code* using a Finite Difference Time Domain simulator (Fujitsu Inc. Poynting). Fig. 3(c) shows calculated scattering cross sections as a function of the number of particles. The assignment of particle(s) in the grid is also shown. A linear correspondence to the number of particles was observed.

5. Summary

In summary, we propose a hierarchical optical memory system in which near-fields are used to read detailed dipole distributions, whereas far-fields are used to detect features within a region-of-interest. An experimental device and simulations were also shown. With hierarchical coding, near- and far-field accesses are associated with different hierarchical information, which should help overcome problems involved in searching huge memory spaces. General design of the logical model and applications will also be pursued as well as physical implementations.

References
[1] For example, http://www.blu-ray.com/
[2] M. Ohtsu, K. Kobayashi, T. Kawazoe, S. Sangu, and T. Yatsui, "Nanophotonics: design, fabrication, and operation of nanometric devices using optical near fields," IEEE J. Select. Topics Quantum Electron. **8**, 839-862 (2002).
[3] M. Ohtsu and K. Kobayashi, *Optical Near Fields* (Springer, 2004), Chap. 4.

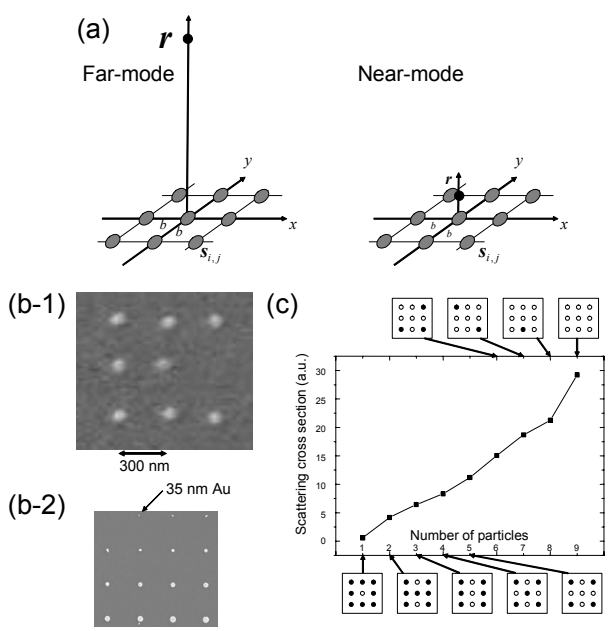

Fig. 3 (a) Physical model. (b) Au particle arrays for the experiment. (c) Simulation of the *far-code*.

Nanophotonic Memory-Based Computation Using Optical Near-Field Interactions

Makoto Naruse
National Institute of Information and Communications Technology, 4-2-1 Nukui-kita, Koganei, Tokyo 184-8795, Japan

Tadashi Kawazoe
Japan Science and Technology Agency, 687-1 Tsuruma, Machida, Tokyo 194-0004, Japan

Suguru Sangu
Ricoh Co. Ltd., 16-1 Shinei-cho, Tsuzuki-ku, Yokohama, Kanagawa 224-0035, Japan

Kiyoshi Kobayashi
Tokyo Institute of Technology, 2-12-1 Ookayama, Meguro-ku, Tokyo 152-8551, Japan

Motoichi Ohtsu
University of Tokyo, 7-3-1 Hongo, Bunkyo-ku, Tokyo 184-8795, Japan

Abstract: We propose and demonstrate a memory-based computation architecture combining data summation and broadcast mechanisms using optical near-field interactions between quantum dots, which will allow high-density integration beyond the diffraction-limit of light.

OCIS codes: (070.6020) Signal processing; (270.0270) Quantum optics; (200.4650) Optical interconnects

Optical technologies are expected to provide novel solutions to accommodate the continuously growing volume of data traffic in communication systems, for example, by further enhancing the overall system performance by performing certain functional behavior in the optical domain. In this regard, all-optical signal processing technologies have been intensively investigated, and the application of intrinsic optical characteristics, such as the high degree of parallelism, in computing systems has been studied since the 1970s [1, 2]. However, many technological difficulties remain to be overcome; one problem is the low level of hardware integration due to the diffraction limit of light, which is much larger than the gate width achievable in VLSI circuits. This results in relatively bulky hardware configurations. Nanophotonics, on the other hand, is free from the diffraction limit since it is based on local interactions between nanometric particles, such as quantum dots (QDs), via optical near fields [3]. In this paper, using such local optical interactions, we propose a nanophotonic computing architecture based on table-lookup operations, as schematically shown in Fig. 1. The essential basic functions, data summation [4] and broadcast mechanisms, are implemented using near-field interactions, which enable ultra-high density and low power dissipation compared to electronic content addressable memory (CAM) chips or conventional optical implementations.

First, we begin by relating the table lookup problem to an inner product operation. The inner product of two N-bit vectors $\boldsymbol{S} \bullet \boldsymbol{D} = \sum_{i=1}^{N} s_i \bullet d_i$, where $\boldsymbol{S} = (s_1, \cdots, s_N)$ represents input data and $\boldsymbol{D} = (d_1, \cdots, d_N)$ represents reference data, will provide a maximum value when the input perfectly matches the reference data by assuming an appropriate data

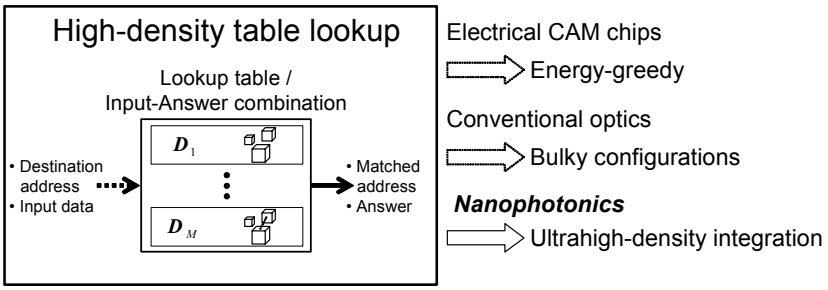

Fig. 1 Table-lookup operations and examples of their implementation.

representation [4]. Also, multiple inner products are equivalent to a matrix-vector multiplication, which can represent a wide range of parallel computations [2]. Furthermore, arbitrary combinational logic can be reformulated as a table lookup operation; the computation is equivalent to table lookup where all possible "input-answer" combinations are pre-recorded.

In the inner product operation, the multiplication of two bits, namely $x_i = s_i \bullet d_i$, based on local optical near-field interactions can be achieved by a combination of three quantum dots [5, 6]. Two additional basic functionalities are important for this architecture. One is a data gathering, or summation, mechanism for similarity evaluation, denoted by Σx_i, where all data bits should be taken into account (Fig. 2(a)) [4]. The other is a broadcast architecture where input data is uniformly distributed to multiple table entries (Fig. 2(b)). Optics is in fact well suited to such broadcast purposes, as in the form of imaging optics [1, 2] or optical waveguide couplers, thanks to its wave propagation nature. However, its integration density is physically limited by the diffraction limit of light, which leads to bulky system configurations. In nanophotonics, on the other hand, the near-field interaction happens only locally. In other words, "functionally global" behavior is required even though the principle of optical near-field interactions is inherently "physically local".

We utilize a uni-directional energy transfer via near-field interactions to implement such global behavior. For summation, by using a configuration where surrounding excitations are transferred towards a quantum dot QD_C located at the center (Fig. 2(c)) based on a so-called nanophotonic fountain [7]. As a fundamental case, we assume two quantum dots QD_A and QD_B, as shown in Fig. 2(d). The ratio of the sizes of QD_A and QD_B is $1:\sqrt{2}$. There is a resonant quantized energy sublevel between those two dots, which are coupled by an optical near-field interaction. Since the intra-sublevel relaxation via exciton-phonon coupling is fast, the population is quickly transferred to the lower (1,1,1)-level in QD_B. Therefore, the exciton population in the (1,1,1)-level in QD_A is transferred to the (2,1,1)-level in QD_B [5]. Similar energy transfers may take place among the resonant energy levels in the dots surrounding QD_C so that energy flow can occur, which provides a global sum of the excitons. It should be noted that this interaction is forbidden for far-field light; this plays a critical role in the internal operation of nanophotonic devices.

Here, we also note that the input energy level for the QDs, that is, the (1,1,1)-level, can also couple to the far-field excitation (Fig. 2(e)). We utilized this fact for data broadcasting, which is explained as follows. Suppose that arrays of nanophotonic circuit blocks are distributed within an area whose size is comparable to the wavelength, as shown in Fig. 2(f). Here, for broadcasting, multiple input QDs simultaneously accept identical input data carried by a diffraction-limited beam of focused far-field light by tuning the optical frequency so that the light is coupled to dipole-allowed energy sublevels. One of the design restrictions is that energy sublevels for input channels do not overlap with those for outputs. Also, if there are QDs internally used for near-field coupling, dipole-allowed energy sublevels for those QDs cannot be used for input channels since the inputs are provided by far-field light, which may lead to misbehavior of internal near-field interactions if resonant levels exist.

A proof-of-principle experiment was performed to verify the nanoscale summation and broadcast mechanisms using CuCl quantum dots in an NaCl matrix, which has also been employed for demonstrating nanophotonic switches [5]. We selected a quantum dot arrangement where small QDs (QD_1 to QD_3) surrounded a "large" QD (QD_C), as schematically shown in Fig. 2(c). Here, we irradiated three light beams with different wavelengths, 325 nm, 376 nm, and 381.3 nm; these beams respectively excite the quantum dots QD_1 to QD_3 having diameters of 1 nm, 3.1 nm, and 4.1 nm, respectively. The excited excitons are transferred nonradiatively to QD_C, which then relaxes and

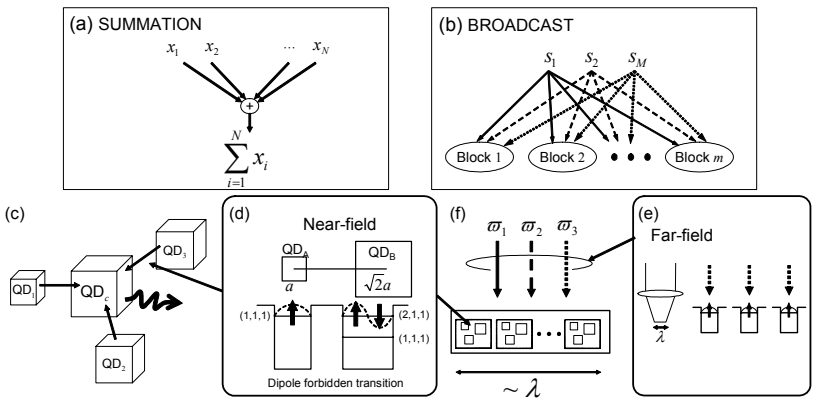

Fig. 2 Data summation and broadcast mechanism for the memory-based architecture.

radiates light, which is observed by a near-field fiber probe. Notice the output signal intensity at a photon energy level of 3.225 eV in Fig. 3(a), which corresponds to a wavelength of 384 nm, or a QD_C size of 5.9 nm. The intensity varies approximately as 1:2:3 depending on the number of excited QDs in the vicinity. The spatial intensity distribution was measured by scanning the fiber probe, as shown in Fig. 3(b), where the energy is converged at the center. Hence, this architecture works as a summation mechanism based on exciton energy transfer via optical near-field interactions. Such a quantum-dot-based data gathering mechanism is also extremely energy-efficient compared to other optical methods such as focusing lenses or optical couplers. For example, the transmittance between two materials with refractive indexes n_1 and n_2 is given by $4n_1n_2/(n_1+n_2)^2$; this gives a 4% loss if n_1 and n_2 are 1 and 1.5, respectively. The transmittance of an N-channel guided wave coupler from the input to the output is 1/N if the coupling loss at each coupler is 3 dB. In nanophotonic summation, the loss is attributed to the dissipation between energy sublevels, which is significantly smaller. Incidentally, it is energy- and space-efficient compared to electrical CAM VLSI chips.

To verify the broadcasting method using multiple 3-dot nanophotonic switches (2-input AND gates), we irradiated two input light beams (IN1 and IN2) via far-field light. When both inputs exist, an output signal is obtained through optical near-field interactions from the positions where the switches exist, as described above. In the experiment, IN1 and IN2 were assigned to 325 nm and 384.7 nm, respectively: They were irradiated over the entire sample (global irradiation). The spatial intensity distribution of the output, at 382.6 nm, was measured by scanning a near-field fiber probe within an area of 1 μm × 1 μm, as shown in Fig. 3. In Fig. 3(c), only IN1 was applied to the sample, whereas in Fig. 3(d) both inputs, IN1 and IN2, were applied. Here, note the regions marked by ■, ●, and ◆. In those regions, the output signal levels were respectively low and high in Fig. 3(c) and (d), which indicates that multiple AND gates were integrated at densities beyond the diffraction limit of light while input data was globally irradiated, that is to say, using broadcast interconnects, by far-field light.

In summary, an architecture for nanophotonic computing is proposed based on table lookup using near-field interactions between quantum dots (QDs). Its basic functions, data summation and broadcast mechanisms, are discussed and their proof-of-principle experiments are demonstrated using CuCl QDs. Owing to its ultrahigh spatial density and low power dissipation, a massive array of such functional components will be useful in applications such as massive table lookup operations in networking and information processing systems.

References

[1] J. W. Goodman, A. R. Dias, and L. M. Woody, "Fully parallel, high-speed incoherent optical method for performing discrete Fourier transforms," Opt Lett. **2**, 1-3 (1978).
[2] P. S. Guilfoyle and D. S. McCallum, "High-speed low-energy digital optical processors," Opt. Eng. **35**, 436-442 (1996).
[3] M. Ohtsu, K. Kobayashi, T. Kawazoe, S. Sangu, and T. Yatsui, "Nanophotonics: design, fabrication, and operation of nanometric devices using optical near fields," IEEE J. Select. Topics Quantum Electron. **8**, 839-862 (2002).
[4] M. Naruse, T. Miyazaki, F. Kubota, T. Kawazoe, K. Kobayashi, S. Sangu, and M. Ohtsu, "Nanometric summation architecture using optical near-field interaction between quantum dots," Opt. Lett. **30**, 201-203 (2005).
[5] T. Kawazoe, K. Kobayashi, S. Sangu, and M. Ohtsu, "Demonstration of a nanophotonic switching operation by optical near-field energy transfer," Appl. Phys. Lett., **82**, 2957-2959 (2003).
[6] S. Sangu, K. Kobayashi, A. Shojiguchi, and M. Ohtsu, "Logic and functional operations using a near-field optically coupled quantum-dot system," Phys. Rev. B **69**, 115334-1-13 (2004).
[7] T. Kawazoe, K. Kobayashi, and M. Ohtsu, "The optical nano-fountain: a biomimetic device that concentrates optical energy in a nanometric region," Appl. Phys. Lett. **85**, in press.

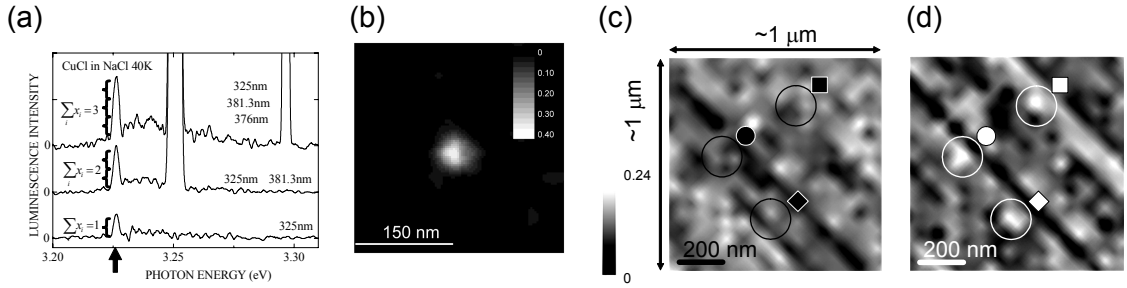

Fig. 3 (a, b) Nanophotonic summation. (c, d) Broadcast example. Spatial intensity distribution of the output (382.6 nm) of AND gates. (c) Output level: low (1 AND 0 = 0), and (d) output level: high (1 AND 1 = 1).

A Nanophotonic NOT-Gate using Near-Field Optically Coupled Quantum Dots

Tadashi Kawazoe
SORST, Japan Science and Technology Agency, Tenkoh building 17-4F, 687-1 Tsuruma, Machida, Tokyo 194-0004, Japan.
Tel:+81-42-788-6039, fax:+81-42-788-6031, e-mail: kawazoe@ohtsu.jst.go.jp

Kiyoshi Kobayashi
Department of Physics, Tokyo Institute of Technology, 2-12-1 Ookayama, Meguro-ku, Tokyo 152-8551, Japan.

Motoichi Ohtsu
Department of Electronics Engineering, University of Tokyo, 7-3-1 Hongo, Bunkyo-ku, Tokyo 113-8656, Japan.

Abstract: We demonstrate, for the first time, operation of a nanometric (20 nm) optical NOT-gate using quantum dots coupled by an optical near-field interaction. We propose that the complete set of logic gates can be realized.

OCIS codes: (230.1150) All-optical device; (999.9999) Nanometric Optical Control; (999.9999) Nanophotonic devices

An optical near-field enables the miniaturization of photonic devices beyond the diffraction limit of light [1]. Recently, we observed an optically forbidden energy transfer between neighboring cubic CuCl QDs via an optical near-field [2], and demonstrated nanometric optical switching (*i.e.*, a nanophotonic AND-gate) by controlling this energy transfer [3].

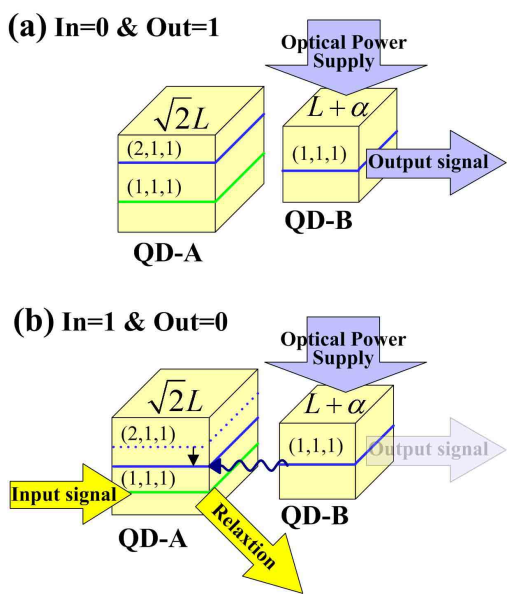

Fig.1. Schematic explanation of the operation of a nanophotonic NOT-gate using cubic quantum dots. QD-A acts as the input terminal. QD-B acts as the output and power supply terminals.

Here, we propose that a NOT-gate can also be realized based on the energy transfer between QDs via the optical near-field interaction. Figure 1 shows a schematic explanation of the proposed nanophotonic NOT-gate. Assuming two cubic QDs with side lengths $\sqrt{2}L$ (QD-A), and $L+\alpha$ (QD-B), respectively, the quantized energy levels (2,1,1) in QD-A and (1,1,1) in QD-B are not resonant with each other, but are nearly resonant. Here, α is the extra size required to detune their energy levels, and (n_x, n_y, n_z) refers to the quantum numbers for the sublevels in the cubic QDs. QD-A is used as the input terminal of the gate. Optical power is supplied to QD-B, which acts as the output terminal. Without the input signal, the energy from the optical power supply is emitted from QD-B directly, by which output is generated (Fig. 1(a) In=0 & Out=1). Conversely, by applying the input signal, the energy level (2,1,1) in QD-A shifts owing to the band renormalization or DC-Shark effect, by which it becomes resonant to (1,1,1) in QD-B. Therefore, the energy from the optical power supply in QD-B is transferred to QD-A

by an optical near-field interaction [1], which suppresses output signal generation (Fig. 1(b) In=1 & Out=0). As a result, an output signal whose temporal behavior is inverted from that of the input signal is obtained. These operations correspond to a NOT-gate.

We used CuCl QDs embedded in a NaCl matrix to verify NOT-gate operation, as CuCl QDs offer discrete energy levels similar to the exciton described in Fig. 1 [4]. Figure 2(a) shows the spatial distribution of the optical near-field output signal intensity without an input signal, *i.e.*, with only the optical power supply (λ=379 nm cw-laser). Figure 2(b) shows the distribution with an input signal pulse (λ=385 nm mode-locked laser). These images were acquired using near-field optical spectrometry in the area of the sample. The insets in Fig. 2 are schematic drawings of the existing QD pair for NOT-gate operation, which were confirmed from the luminescence spectra. The sizes of the two QDs, estimated from the wavelengths of their luminescence, were 5.0 and 6.3 nm, which satisfy the NOT-gate operation condition, as shown in Fig. 1. We measured the NOT-gated signal at the center of the circles in Fig. 2, from which the size of this device was estimated to be 20 nm.

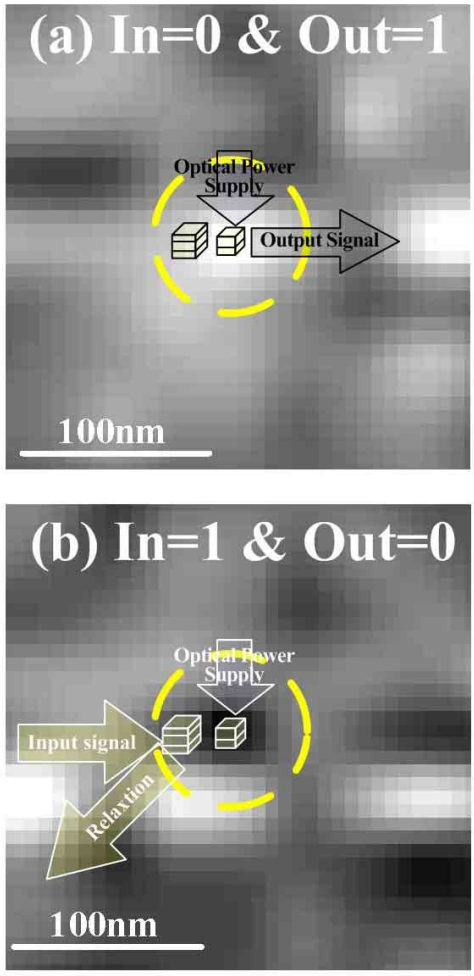

Fig.2. Spatial distribution of the output signal from a nanophotonic NOT-gate measured using a near-field microscope at Input=0 (a) and Input =1 (b).

The dynamic behavior of the NOT-gate was evaluated using the time correlation single photon counting method. For the input signal pulse, the 385-nm second harmonic generation (SHG) of a mode-locked Ti-sapphire laser was used. The repetition rate and pulse duration of the laser were 80 MHz and 2 ps, respectively. The time resolution of the experiment was 15 ps. Figure 3 shows the temporal evolution of the output signal. The horizontal broken line shows the output signal level without an input signal pulse. The output signal rises synchronously within a time period shorter than the time resolution (the high, short pulses synchronous with the input signal pulses are owing to leakage of the pump pulse to the detection instruments, and are artifacts), and it decreases to a level lower than the level indicated by the broken line. The fall time of the output signal is about 100 ps, which corresponds to the

energy transfer time between QDs. This output signal recovers to the level of the broken line within 10 ns, which is close to the exciton lifetime in CuCl QDs. This means that this NOT-gate can operate at a 100-MHz repetition frequency.

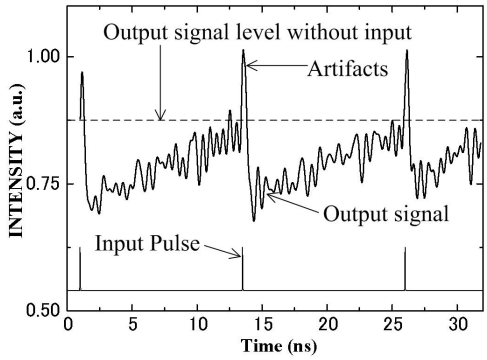

Fig.3. Temporal evolution of the output (upper) and input pulse (lower) signals from the nanophotonic NOT gate circled in Fig. 2.

Additional functional nanophotonic logic gates (*e.g.*, NAND-, NOR-, and OR-gates) can be realized by combining this NOT-gate with the nanophotonic AND-gate [3], allowing realization of the complete set of nanophotonic logic devices. Using these nanophotonic logic gates, novel data processing systems, such as a photon computer, may be developed in the future.

References

1. M. Ohtsu, K. Kobayashi, T. Kawazoe, S. Sangu, and T. Yatsui, "Nanophotonics: design, fabrication, and operation of nanometric devices using optical near fields," IEEE J. Sel. Top. Quant. Electron, 8 839-862 (2002).
2. T. Kawazoe, K. Kobayashi, J. Lim, Y. Narita and M. Ohtsu, "Direct Observation of Optically Forbidden Energy Transfer between CuCl Quantum Cubes via Near-Field Optical Spectroscopy," Phys. Rev. Lett. 88, 6, 067404-1-4 (2002).
3. T. Kawazoe, K. Kobayashi, S. Sangu, and M. Ohtsu, "Demonstration of a nanophotonic switching operation by optical near-field energy transfer," Appl. Phys. Lett., 82 No.18 2957-2959(2003).
4. N. Sakakura and Y. Masumoto, "Persistent spectral-hole-burning spectroscopy of CuCl quantum cubes," Phys. Rev. B 56, 4051-4055 (1997).

Optical Interconnects using Optical Far- and Near-field Interactions for High-density Data Broadcasting

Makoto Naruse and Fumito Kubota
National Institute of Information and Communications Technology, 4-2-1 Nukui-kita, Koganei, Tokyo 184-8795, Japan

Tadashi Kawazoe
Japan Science and Technology Agency, 687-1 Tsuruma, Machida, Tokyo 194-0004, Japan

Suguru Sangu
Ricoh Co. Ltd., 16-1 Shinei-cho, Tsuzuki-ku, Yokohama, Kanagawa 224-0035, Japan

Kiyoshi Kobayashi
Tokyo Institute of Technology, 2-12-1 Ookayama, Meguro-ku, Tokyo 152-8551, Japan

Motoichi Ohtsu
University of Tokyo, 7-3-1 Hongo, Bunkyo-ku, Tokyo 184-8795, Japan

Abstract: Ultrahigh-density data-broadcasting optical interconnects are proposed and experimentally demonstrated using optical near-field interactions between quantum dots, which are forbidden for far-field light, allowing sub-wavelength device functions and far-field excitation for global interconnects.

OCIS codes: (200.4650) Optical interconnects, (270.0270) Quantum optics, (070.6020) Signal processing

Optical interconnects have been thoroughly investigated to overcome the limitation of their electrical counterparts [1, 2]. Nanophotonics requires yet another type of interconnect since it is based on local electromagnetic interactions between a few nanometer-size particles, such as quantum dots (QDs), via optical near fields, which in turn allows device integration at densities beyond the diffraction limit [3]. As interconnects for such high-density devices, near- and far-field converters based on, for example, plasmon waveguides have been studied [4, 5]. In this paper, we propose another interconnection method based on both far- and near-field interactions for data broadcasting; the method is schematically shown in Fig. 1 (a) and (b). Broadcast interconnects is an important subset for applications such as matrix vector multiplication [6], broadcast-and-select architectures [7], and so forth.

In nanophotonics, uni-directional energy transfer is possible between neighboring QDs via optical near-field interactions, as schematically shown in Fig. 1(c); such energy transfer is forbidden for far-field light [3, 8, 9]. This unique feature enables nonlinear functions such as optical switching [10] and data summation [11], as well as extremely high integration density. From the view point of interconnects, however, it invokes a stringent requirement for individual addressability since the devices are arrayed on the sub-wavelength scale. However, data broadcasting allows another interconnection scheme. Suppose that arrays of nanophotonic circuit blocks, such as the

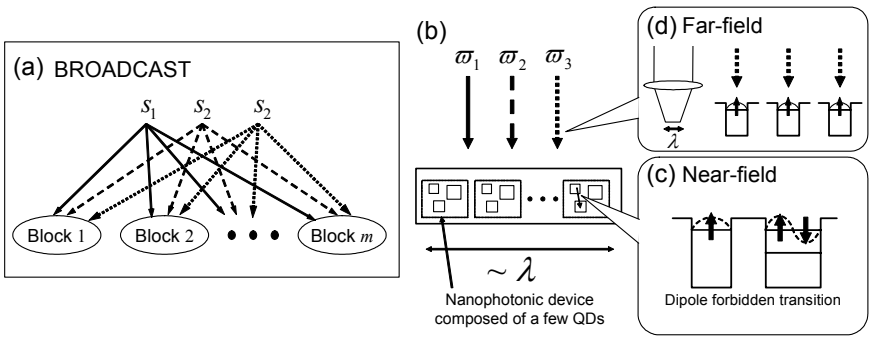

Fig. 1 (a) Broadcast-type interconnects and (b) their nanophotonics implementation. (c) Near-field interaction between quantum dots for internal functions. (d) Far-field excitation for identical data input (broadcast) to nanophotonic devices within a diffraction-limit-sized area.

nanophotonic switches described later, are distributed within an area whose size is comparable to the wavelength, as shown in Fig. 1(d). Here, for broadcasting, multiple nanophotonic input QDs simultaneously accept identical input data carried by diffraction-limited far-field light by tuning the optical frequency so that the light is coupled to dipole-allowed energy sublevels, as describe below. In a frequency multiplexing sense, this interconnection method is similar to multi-wavelength chip-scale interconnects [12]. However, known methods require a physical space comparable to the number of diffraction-limited input channels due to wavelength demultiplexing, whereas in our proposed scheme, the device arrays are integrated on the sub-wavelength scale, and multiple frequencies are multiplexed in the far-field light supplied to the device.

Here we explain the near- and far-field coupling mentioned above based on a model assuming CuCl QDs, which are later employed in experiments; these QDs are also used to demonstrate the principles of nanophotonic switching [6] and summation [7]. The potential barrier of CuCl QDs in a NaCl crystal can be regarded as infinitely high, and the energy eigenvalues for the quantized Z_3 exciton energy level (n_x,n_y,n_z) in a CuCl QD with side of length L are given by

$$E_{(n_x,n_y,n_z)} = E_B + \frac{\hbar^2\pi^2}{2M(L-a_B)^2}(n_x^2+n_y^2+n_z^2) \tag{1}$$

where E_B is the bulk energy of the Z_3 exciton, M is the translational mass of the exciton, a_B is its Bohr radius, n_x, n_y, and n_z are quantum numbers (n_x, n_y, n_z=1,2,3,…), and a=L-a_B corresponds to an effective side length found after considering the dead layer correction. The exciton energy levels with even quantum numbers are dipole-forbidden states [13]. The optical near-field interaction, however, is allowed for such energy levels. According to (1) there exists a resonance between the quantized exciton energy sublevel of quantum number (1,1,1) for the QD with effective side length a and that of quantum number (2,1,1) for the QD with effective side length $\sqrt{2}a$. (For simplicity, we refer to the QDs with effective side lengths a and $\sqrt{2}a$ as "QD a" and "QD $\sqrt{2}a$", respectively.) Therefore, energy transfer between QD a and QD $\sqrt{2}a$ occurs, which is forbidden for far-field light; this plays a critical role in the internal operation of nanophotonic devices.

Here, we notice that the input energy level for the QDs, that is, the (1,1,1)-level, can also couple to the far-field excitation. We utilized this fact for data broadcasting. One of the design restrictions is that energy-sublevels for input channels do not overlap with those for outputs. Also, if there are QDs internally used for near-field coupling, dipole-allowed energy sublevels for those QDs cannot be used for input channels since the inputs are provided by far-field light, which may lead to misbehavior of internal near-field interactions if resonant levels exist. Therefore, frequency partitioning among the input, internal, and output channels is important; this is schematically shown in Fig. 2(a).

Fig. 2(b) shows a diagram for illustrating frequency partitioning, where the horizontal axis shows QD size and the vertical axis shows energy sublevels. The 3-digit sets in the diagram are the principle quantum numbers of the QDs. As an example, we used a nanophotonic switch (2-input AND gate) composed of three QDs with a size ratio of $1:\sqrt{2}:2$. The details of the switching principle are shown in reference [10]. The two input channels are assigned to QD a and QD 2a, and the output appears from QD $\sqrt{2}a$. Here, multiple input dots QD a and QD $2a$ can accept identical input data via far-field light for broadcasting purposes. Also, adding more optical switches means adding different size dots so that the corresponding far-field resonant frequencies do not overlap with the other channels. For instance by multiplying the scale of the QDs by a natural number, such as $2\sqrt{2}a$, $4a$, and $4\sqrt{2}a$, the number of

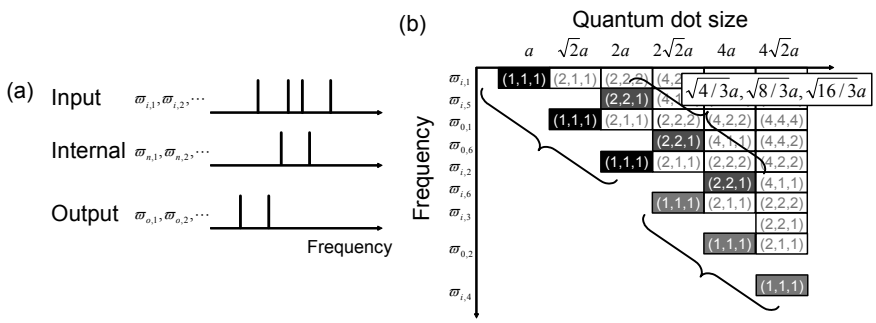

Fig. 2 (a) Frequency partitioning for external and internal nanophotonic operations. (b) Frequency-diagram for multiple implementations of 3-dot nanophotonic switches.

channels increases. More dense integration is also possible by appropriately configuring the size of the QDs. As an example, consider a QD whose size is $\sqrt{4/3}a$. The (1,1,1)-level in this QD $\sqrt{4/3}a$ can couple to the far-field excitation. It should be noted that this particular energy level is equal to the (2,2,1)-level in QD 2*a*, which is an already-used input channel; however, the far-field excitation cannot couple to QD 2*a* since the (2,2,1)-level in QD 2*a* is a dipole-forbidden energy sub-level. Therefore, a QD trio composed of $\sqrt{4/3}a$, $\sqrt{8/3}a$, and $\sqrt{16/3}a$ can make up another optical switch, while not interfering with other channels even though all of the input light is irradiated in the same area whose size is determined by the diffraction limit of light. The size of these QDs should be approximately an integer multiple of half the lattice constant.

To verify the broadcasting method, we performed the following experiments using CuCl QDs which were inhomogeneously distributed in a NaCl matrix at a temperature of 22 K. To operate a 3-dot nanophotonic switch (2-input AND gate) in the device, we irradiated at most two input light beams (IN1 and IN2) via far-field light. When both inputs exist, an output signal is obtained through optical near-field interactions from the positions where the switches exist, as described above. In the experiment, IN1 and IN2 were assigned to 325 nm and 384.7 nm, respectively: They were irradiated over the entire sample (global irradiation). The spatial intensity distribution of the output, at 382.6 nm, was measured by scanning a near-field fiber probe within an area of 1 μm × 1 μm, as shown in Fig. 3. In Fig. 3(a), only IN1 was applied to the sample, whereas in Fig. 3(b) both inputs were irradiated. Here, note the regions marked by ■, ●, and ◆. In those regions, the output signal levels were respectively low and high in Fig. 3(a) and (b), which indicates that multiple AND gates were integrated at densities beyond the diffraction limit of light while input data was globally irradiated, that is to say, using broadcast interconnects, by far-field light.

In summary, broadcast interconnects for nanophotonic devices are proposed and experimentally demonstrated using far- and near-field interactions. Combining this broadcasting mechanism with switching [10] and summation [11] will allow the development of nano-scale integration of optical parallel processing devices, which have conventionally resulted in bulky systems.

Reference

[1] D. A. B. Miller, "Rationale and Challenges for Optical Interconnects to Electronic Chips," Proc. IEEE, **88**, 728-749 (2000).
[2] N. McArdle, M. Naruse, H. Toyoda, Y. Kobayashi, and M. Ishikawa, "Reconfigurable Optical Interconnections for Parallel Computing," Proc. IEEE **88**, 829-837 (2000).
[3] M. Ohtsu, K. Kobayashi, T. Kawazoe, S. Sangu, and T. Yatsui, "Nanophotonics: design, fabrication, and operation of nanometric devices using optical near fields," IEEE J. Select. Topics Quantum Electron. **8**, 839-862 (2002).
[4] T. Yatsui, M. Kourogi, and M. Ohtsu, "Plasmon waveguide for optical far/near-field conversion," Appl. Phys. Lett. **79**, 4583-4585 (2001).
[5] J. Takahara, Y. Suguru, T. Hiroaki, A. Morimoto, and T. Kobayashi, "Guiding of a one-dimensional optical beam with nanometer diameter," Opt. Lett. **22**, 475-477 (1997).
[6] P. S. Guilfoyle and D. S. McCallum, "High-speed low-energy digital optical processors," Opt. Eng. **35**, 436-442 (1996).
[7] B. Li, Y.Qin, X. Cao, and K. M. Sivalingam, "Photonic packet switching: Architecture and performance," Optical Networks Magazine **2**, 27-39 (2001).
[8] K. Kobayashi and M. Ohtsu, "Quantum theoretical approach to a near-field optical system," J. Microsc. **194**, 249-254 (1999).
[9] T. Kawazoe, K. Kobayashi, J. Lim, Y. Narita, and M. Ohtsu, "Direct Observation of Optically Forbidden Energy Transfer between CuCl Quantum Cubes via Near-Field Optical Spectroscopy", Phys. Rev. Lett. **88**, 067404-1-4 (2002).
[10] T. Kawazoe, K. Kobayashi, S. Sangu, and M. Ohtsu, "Demonstration of a nanophotonic switching operation by optical near-field energy transfer," Appl. Phys. Lett. **82**, 2957-2959 (2003).
[11] M. Naruse, T. Miyazaki, F. Kubota, T. Kawazoe, K. Kobayashi, S. Sangu, and M. Ohtsu, "Nanometric summation architecture using optical near-field interaction between quantum dots," Opt. Lett., in press.
[12] E. A. De Souza, M. C. Nuss, W. H. Knox, and D. A. B. Miller, "Wavelength-division multiplexing with femtosecond pulses," Opt. Lett. **20**, 1166-1168 (1995).
[13] Z. K. Tang, A. Yanase, T. Yasui, Y. Segawa, and K. Cho, "Optical selection rule and oscillator strength of confined exciton system in CuCl thin films," Phys. Rev. Lett. **71**, 1431-1434 (1993).

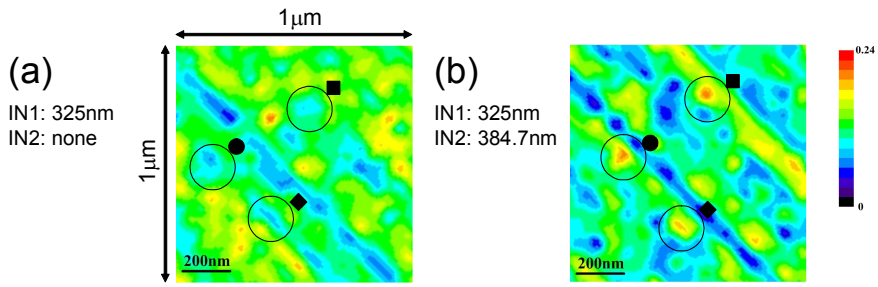

Fig. 3 Experimental results. Spatial intensity distribution of the output (382.6nm) of AND gates. (a) Output level: low (1 AND 0 = 0), and (b) output level: high (1 AND 1 = 1)

Evaluating the quantum confinement effect of isolated ZnO nanorod single-quantum-well structures using near-field ultraviolet photoluminescence spectroscopy

T. Yatsui,[*] J. Lim,[†] T. Kawazoe,[*] and M. Ohtsu,[*,†,‡]
[*] *SORST, Japan Science and Technology Agency*
687-1 Tsuruma, Machida, Tokyo, Japan 194-0004
+81 42-788-6040, +81 42-788-6031, yatsui@ohtsu.jst.go.jp
[†] *Interdisciplinary Graduate School of Science and Engineering, Tokyo Institute of Technology*
4259 Nagatsuta, Midori-ku, Yokohama, Japan 226-8502
+81 45-924-5476, +81 45-924-5599
[‡] *Faculty of Engineering, The University of Tokyo, , Bunkyo-ku, Tokyo, Japan 113-8656*
+81 3-5841-1189, +81 3-5841-1140

S. J. An, J. Yoo, and G.-C. Yi
National CRI Center for Semiconductor Nanorods and Department of Materials Science and Engineering,
Pohang University of Science and Technology (POSTECH)
San 31 Hyoja-dong, Pohang, Gyeongbuk 790-784, Korea
+82 54-279-2155, +82 54-279-8635

Abstract: Using low-temperature near-field spectroscopy of ZnO nanorod single-quantum-well structures, the dependence of the quantum confinement effect of the photoluminescence peak on the well width was observed and the homogeneous linewidth was determined as 3 meV.

OCIS codes: (300.6540) Spectroscopy, ultraviolet, (310.6860) Thin films, optical properties

Future optical transmission systems will require nanophotonic integrated circuits [1] composed of nanometer-scale dots to increase data transmission rates and capacity. ZnO nanocrystallite is a promising material for realizing room-temperature nanophotonic devices, owing to its large exciton binding energy [2]. Furthermore, the recent demonstration of a semiconductor nanorod quantum-well structure enabled us to fabricate nanometer-scale electronic and photonic devices on single nanorods [3-5]. Recently, ZnO/ZnMgO nanorod multiple-quantum-well structures (MQWs) were fabricated and the quantum confinement effect was observed successfully [6]. Further improvement in the fabrication of nanorod heterostructures has resulted in the observation of significant PL intensity, even from ZnO/ZnMgO nanorod single-quantum-well structures (SQWs) [7]. To confirm the promising optical properties of individual ZnO SQWs for realizing nanophotonic devices, we measured the photoluminescence (PL) spectra from isolated ZnO SQWs for the first time using a low-temperature near-field optical microscope (NOM).

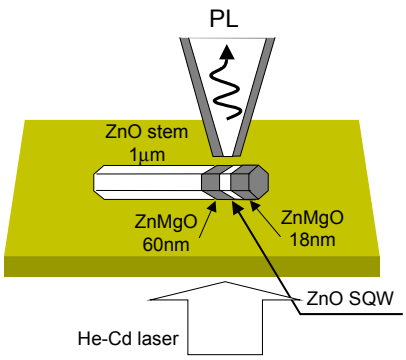

Fig. 1 Schematic of near-field spectroscopy of isolated ZnO SQWs on the ends of ZnO nanorod.

ZnO/ZnMgO SQWs were fabricated on the ends of ZnO nanorods with a mean diameter of 40 nm using catalyst-free metalorganic vapor phase epitaxy [8]. The average concentration of Mg in the ZnMgO layers used in this study was determined to be 20 at. %. The ZnO well layer thickness, L_w, investigated in this study were 2.5, 3.75, and 5.0 nm, while the thicknesses of the ZnMgO bottom and top barrier layers in the SQWs were fixed at 60 and 18 nm, respectively. After growing ZnO nanorod SQWs on sapphire (0001) substrate, they were dispersed on the substrate to be isolated. To confirm the promising optical properties of individual ZnO SQWs, we used collection-mode NOM at 15K, using a He-Cd laser (λ=325 nm) for the excitation, and a UV fiber probe with an aperture diameter of 30 nm [Fig. 1].

In the near-field spectra, the emission peaks around 3.365 and 3.352 eV originate from the neutral-donor bound exciton (DOX) in the ZnO stem, and the free exciton in the ZnMgO layers, respectively, which correspond to the peaks in the far-field spectra [dashed curves in Fig. 2(a)]. At the well layer, however, the emission from DOX was suppressed, while blue-shifted PL emission peaks emerged at 3.499 (L_w = 2.5 nm), 3.444 (L_w = 3.75 nm), and 3.410 eV (L_w = 5.0 nm). The amount of the blue shift was consistent with the theoretical prediction using the finite square-well potential of the quantum confinement effect in the ZnO well layer. The spatial distribution of the optical near-field intensity for ZnO SQWs of L_w = 3.75 nm [Figs. 2(b) and 2(c)] supported the postulate that the blue-shifted emission peaks were confined to the end of the ZnO stem. Furthermore, the spectral widths (3 meV) of the ZnO SQWs for L_w = 2.5 nm and L_w = 3.75 nm were much narrower than those of the far-field spectra (40 meV).

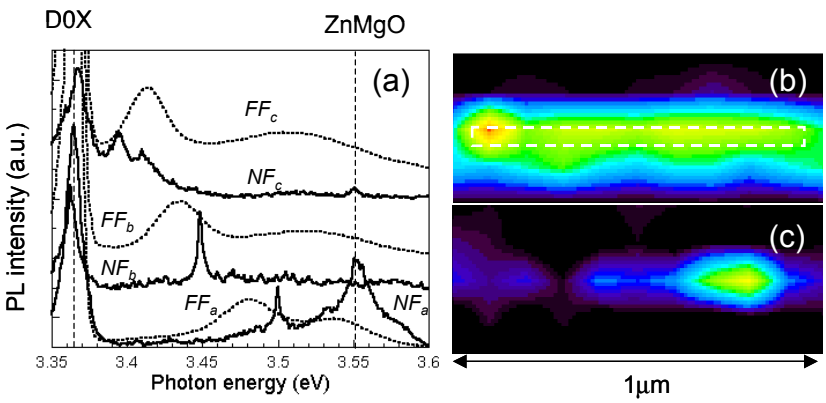

Fig. 2. (a) Size-dependent PL spectra of isolated ZnO nanorod SQWs with L_W = 2.5 nm (FF_a, NF_a), 3.75 nm (FF_b, NF_b), and 5.0 nm (FF_c, NF_c), obtained at 15 K. *FF*: far-field spectrum of vertically aligned ZnO nanorod SQWs. *NF*: near-field PL spectrum of the isolated ZnO SQWs obtained at the well layer. The near-field intensity distributions of the isolated ZnO SQWs (L_w = 3.75 nm) obtained at (b) 3.365 and (c) 3.444 eV, respectively.

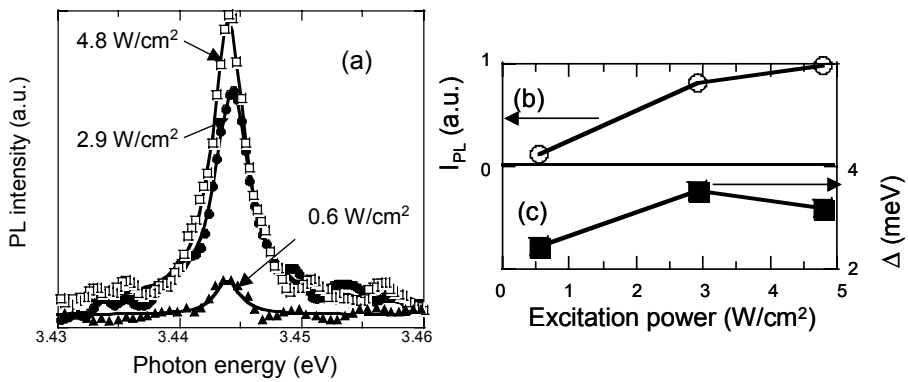

Fig. 3. (a) Low-temperature (15 K) near-field PL spectrum of the isolated ZnO SQWs (L_W=3.75 nm) at excitation densities ranging from 0.6 to 4.8 W/cm^2. Power dependence of the (b) integrated PL intensity (I_{PL}) and (c) linewidth (Δ).

To estimate the linewidth of the isolated ZnO SQWs, we observed power-dependent PL spectra of L_w = 3.75 nm [Fig. 3(a)] at excitation densities ranging from 0.6 to 4.8 W/cm^2. The shape of each spectrum was reproduced by the Lorentzian function indicated by the solid line. As shown in Figs. 3(b) and 3(c), the integrated PL intensity (I_{PL}) increased linearly, while the homogeneous width (Δ) remained constant around 3 meV. These results indicate that the emission line at 3.444 eV was the emission from a single-exciton state in ZnO SQWs, and that the linewidth of the PL spectra is governed by the homogeneous broadening that is the result of the internal electric field effect in ZnO [9] or a large stem width (40 nm).

The results shown here provide criteria for designing nanophotonic devices, such as the switching devices confirmed by the authors in CuCl quantum cubes by controlling the dipole forbidden optical energy transfer among resonant energy states in quantum dots [10].

References

1. M. Ohtsu, K. Kobayashi, T. Kawazoe, S. Sangu, and T. Yatsui, "Nanophotonics: design, fabrication, and operation of nanometric devices using optical near fields," IEEE Journal of Selected Topics in Quantum Electronics **8**, 839-862 (2002).
2. A. Ohtomo, K. Tamura, M. Kawasaki, T. Makino, Y. Segawa, Z. K. Tang, G. K. L. Wong, Y. Matsumoto, and H. Koinuma, "Room-temperature stimulated emission of excitons in ZnO/(Mg, Zn)O superlattices," Appl. Phys. Lett. **77**, 2204-2206 (2000).
3. Y. Wu, R. Fan, and P. Yang, "Block-by-block growth of single crystalline Si/SiGe superlattice nanowires," Nano Lett. **2**, 83-86 (2002).
4. M. T. Björk, B. J. Ohlsson, C. Thelander, A. I. Persson, K. Deppert, L. R. Wallenberg, and L. Samuelson, "Nanowire resonant tunneling diodes," Appl. Phys. Lett. **81**, 4458-4460 (2003).
5. M. S. Gudiksen, L. J. Lauhon, J. Wang, D. C. Smith, and C. M. Lieber, "Growth of nanowire superlattice structures for nanoscale photonics and electronics." Nature **415**, 617-620 (2002).
6. W. I. Park, G.-C. Yi, M. Y. Kim, and S. J. Pennycook, "Quantum confinement observed in ZnO/ZnMgO nanorod heterostructures," Adv. Mater. **15**, 526-529 (2003).
7. W. I. Park, S. J. An, J. L. Yang, G.-C. Yi, S. Hong, T. Joo, and M. Kim, "Photoluminescent properties of ZnO/$Zn_{0.8}Mg_{0.2}O$ nanorod single-quantum-well structures," J. Phys. Chem. B **108**, 15457-15460 (2004).
8. W. I. Park, D. H. Kim, S.-W. Jung, and G.-C. Yi, "Metalorganic vapor-phase epitaxial growth of vertically well-aligned ZnO nanorods," Appl. Phys. Lett. **80**, 4232-4234 (2002).
9. T. Makino, A. Ohtomo, C. H. Chia, Y. Segawa, H. Koinuma, and, M. Kawasaki, "Internal electric field effect on luminescence properties of ZnO/(Mg,Zn)O quantum wells," Physica E **21**, 671-675 (2004).
10. T. Kawazoe, K. Kobayashi, S. Sangu, and M. Ohtsu, "Demonstration of a nanophotonic switching operation by optical near-field energy transfer," Appl. Phys. Lett. **82**, 2957-2959 (2003).

Size-, position-, and separation-controlled one-dimensional alignment of nanoprticles using an optical near field

T. Yatsui,[*] W. Nomura,[‡] and M. Ohtsu,[*,‡]
[*] *SORST, Japan Science and Technology Agency*
687-1 Tsuruma, Machida, Tokyo, Japan 194-0004
+81 42-788-6040, +81 42-788-6031, yatsui@ohtsu.jst.go.jp
[‡] *Faculty of Engineering, the University of Tokyo, Tokyo, Japan*
+81 3-5841-1189, +81 3-5841-1140

Abstract: Colloidal gold nanoparticles were aligned with the desired position and separation on the edge of a Si wedge by controlling the particle-substrate and particle-particle interactions using an optical near field.

OCIS codes: (240.6670) Surface photochemistry, (230.3120) Integrated optics devices

For future optical transmission and signal-processing systems with high data-transmission rates and capacity, we have proposed nanometer-sized photonic integrated circuits (*i.e.*, nanophotonics ICs) [1]. As a representative device, the operation of a nanophotonic switch was demonstrated by controlling the dipole forbidden optical energy transfer among resonant energy states in CuCl quantum cubes via an optical near field [2]. Coupling these nanophotonic ICs with external conventional diffraction-limited photonic devices requires a nanometer-sized optical waveguide for far-/near-field conversion. To realize this, it has been suggested that electromagnetic energy can be guided along a nano-dot coupler, which is an array of closely spaced metallic nanoparticles [3]. Energy transfer in the nano-dot coupler relies on dipole-dipole coupling between neighboring nanoparticles. To realize a nano-dot coupler consisting of 50-nm gold nanoparticles with 50-nm separation, the dispersion of their separation has to be as small as 10 nm to maintain an efficiency higher than 50% that of the perfectly ordered array [3].

Promising components for integrating these nanometer-sized photonic devices include chemically synthesized nanocrystals, because they have uniform size, controlled shape, a defined chemical composition, and tunable surface chemical functionality. However, position- and size-controlled deposition methods have not yet been developed. As several methods have been developed to prepare nanometer-sized templates reproducibly, it is expected that the self-assembly of colloidal nanostructures into a lithographically patterned substrate will enable precise control at all scales. Capillary forces play an important role, because colloidal nanostructures are synthesized in solution. Recently, the successful integration of polymer and silica spheres [4] into templates by controlling the capillary force using appropriate template structures has been reported, although their size and separation are typically uniform.

To control position and separation very accurately, preliminary deposition was performed on a patterned Si substrate, in which an array of 10-μm holes in 100-nm-thick SiO_2 was fabricated using photolithography [Fig. 1(a)]. Subsequently, s suspension of latex beads was dropped onto the Si substrate while it was spun at 3,000 revolutions per minute. As shown in Fig. 1(b), the suspension flow split into two branches at the SiO_2 rim of a hole. Scanning

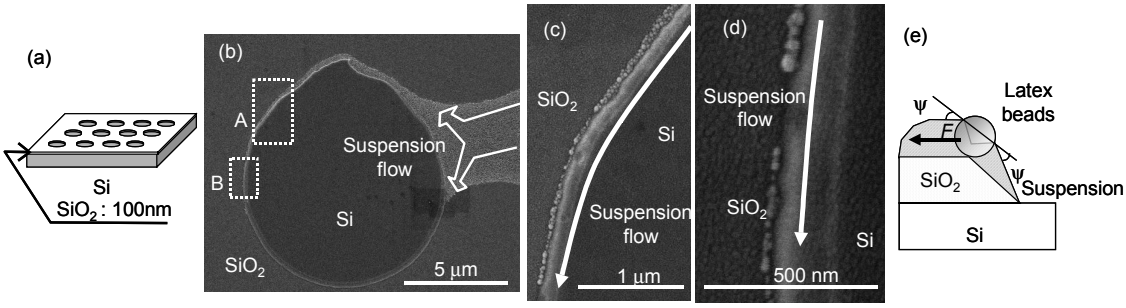

Fig. 1 (a) Schematic of a lithographically patterned Si substrate. (b) SEM image of latex beads dispersed on a lithographically patterned Si substrate rotated at 3,000 rpm. Higher-magnification SEM images of white squares A (c) and B (d) in (b). (e) Schematic of the particle-assembly process driven by the capillary force and suspension flow.

electron microscope (SEM) images [Figs. 1(c) and (d)] show a chain of colloidal beads aligned at the Si/SiO_2 interface. Note that the number of rows of latex beads decreased as the flow advanced [Figs. 1(c) and 1(d)] and only the smallest beads, which were 20 nm in diameter, reached the front of the suspension flow [Fig. 1(d)]. Assuming the same particle-suspension contact angle [denoted ψ in Fig. 1(e)] for various particle diameters, the flow speed of the larger latex beads had greater deceleration, as the magnitude of the force pushing the particles on the SiO_2 [denoted F in Fig. 1(e)] owing to evaporation of the solvent is proportional to the particle diameter [4]. In other wards, size selection was realized.

Based on the results of preliminary deposition, we tried assembling metallic nanoparticles, which can be used to construct nano-dot couplers [3]. In this trial, we investigated the assembly of colloidal gold nanoparticles with a mean diameter of 20 nm dispersed in citrate solution at 0.001%. The nanoparticles were prepared by the citric acid reduction of gold ions and terminated by a carboxyl group with a negative charge. Therefore, aggregation could not use the same deposition process as used for the latex beads. To control separation and positioning, we examined the aggregation of colloidal gold nanoparticles under illumination, because the colloidal gold nanoparticles have strong optical absorption. Strong absorption should desorb the carboxyl group from the colloidal gold nanoparticles and result in their aggregation. As frontal illumination through the suspension pushes the aggregated nanoparticles outside the beam spot [Fig. 2(a)], the suspension was illuminated through a glass substrate [Fig. 2(b)] to realize selective aggregation of the gold nanoparticles at the desired position.

Next, we used a Si wedge as the substrate [Fig. 2(c)], because this is a suitable structure for a far-/near-field conversion device [5]. Colloidal gold nanoparticles were deposited around the edge of the wedge after evaporating the suspension without illumination [Figs. 3(a) and 3(b)] because the suspension at the edge of the wedge is thinner than that on the Si(111) slant owing to its low capillarity, which causes the convective transport of particles toward the edge [6]. Further selective alignment along the edge of the Si wedge was realized by illumination through the substrate. Figures 3(c) and 3(d) show the colloidal gold nanoparticles deposited with illumination with 690-nm light (25 mW/mm^2) for 60 seconds. Since the optical near-field energy is enhanced at the edge owing to the high refractive index of Si [see Fig. 2(b)], selective aggregation along the edge with higher density is seen in these figures. This is the result of the desorption of the carboxyl group by the absorption of light by the colloidal gold nanoparticles.

Note that the colloidal gold nanoparticles were closely aggregated and aligned linearly to form an array when the polarization was perpendicular to the edge axis [Fig. 3(c)], while they were aligned with a separation of several tens of nanometers with parallel polarization [Fig. 3(d)]. Since the optical near-field energy is higher with parallel polarization than with perpendicular polarization, greater aggregation was expected with parallel polarization.

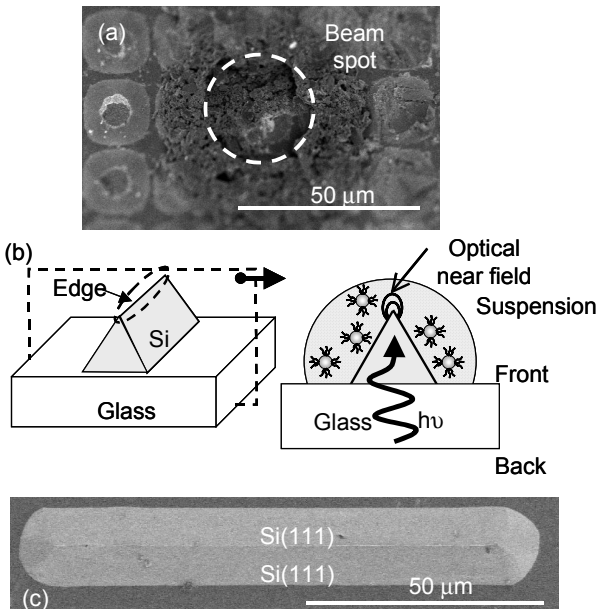

Fig. 2 (a) Aggregated colloidal gold nanoparticles with frontal illumination with 690-nm light (25 mW/mm^2) for 60 seconds. (b) Schematic of the experimental setup. (c) SEM image of the fabricated Si wedge structure.

Unexpectedly, the parallel polarization resulted in weaker aggregation. We believe that this incongruity originated from differences in the charge distribution induced inside the gold nanoparticles. Based on the polarization-dependence of the aggregation, it is reasonable to consider the aggregation along the edge with perpendicular polarization as owing to partially adsorbed carboxyl groups [Fig. 3(e)], while the disaggregation with the parallel polarization resulted from the repulsive force induced by the carboxyl groups partially attached to the colloidal gold nanoparticles [Fig. 3(f)].

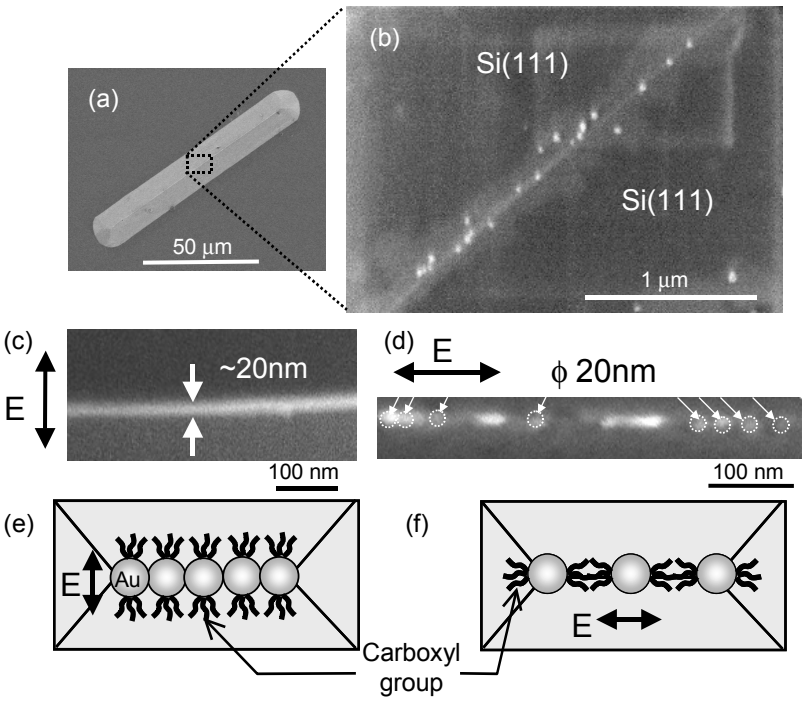

Fig. 3 (a) Overview of the Si wedge structure. (b) SEM image of colloidal gold nanoparticles deposited on the edge of the Si wedge structure without illumination. SEM images of colloidal gold nanoparticles on the Si wedge structure under illumination with polarization perpendicular (c) and parallel (d) to the edge. White arrows indicate gold nanoparticles aligned along the edge. Schematic diagrams of colloidal gold nanoparticles aggregated along the edge of the Si wedge with polarization perpendicular (e) and parallel (f) to the edge.

The experimental results and suggested mechanisms described here show the potential advantages of this technique for improving the regulation of the separation and positioning of nanoparticles, and possible application to realize a nano-dot coupler for far-/near-field conversion.

References

1. M. Ohtsu, K. Kobayashi, T. Kawazoe, S. Sangu, and T. Yatsui, "Nanophotonics: design, fabrication, and operation of nanometric devices using optical near fields," IEEE Journal of Selected Topics in Quantum Electronics **8**, 839-862 (2002).
2. T. Kawazoe, K. Kobayashi, S. Sangu, and M. Ohtsu, "Demonstration of a nanophotonic switching operation by optical near-field energy transfer," Appl. Phys. Lett. **82**, 2957-2959 (2003).
3. S. A. Maier, P. G. Kik, H. A. Atwater, S. Meltzer, E. Harel, B. E. Koel, and A. G. Requicha, "Local detection of electromagnetic energy transport below the diffraction limit in metal nanoparticle plasmon waveguides," Nature Materials **2**, 229-232 (2003).
4. Y. Cui, M. T. Björk, J. A. Liddle, C. Sönnichsen, B. Boussert, and A. P. Alivisatos, "Integration of colloidal nanocrystals into lithographically patterned devices," Nano Lett. **4**, 1093-1098 (2004).
5. T. Yatsui, M. Kourogi, and M. Ohtsu, "Plasmon waveguide for optical far/near-field conversion," Appl. Phys. Lett. **79**, 4583-4585 (2001).
6. N. D. Denkov, O. D. Velev, P. A. Kralchevsky, I. B. Ivanov, H. Yoshimura, L. Nagayama, "Two-dimensional crystallization," Nature **361**, 26 (1993).

E11.8

Room-temperature synthesis of ultraviolet-emitting nanocrystalline GaN films using photochemical vapor deposition. Takashi Yatsui[1], Syunsuke Yamazaki[2], Takashi Nagira[2], Motoichi Ohtsu[3,1,2], Tae-Won Kim[4] and Hiroshi Fujioka[3,4]; [1]SORST, JST, Machida, Tokyo, Japan; [2]Interdisciplinary Graduate School of Science and Engineering, Tokyo Institute of Technology, Yokohama, Kanagawa, Japan; [3]Faculty of Engineering, the University of Tokyo, Bunkyo-ku, Tokyo, Japan; [4]Kanagawa Academy of Science and Technolog, Kawasaki, Kanagawa, Japan.

GaN is a promising material for use in nano-scale photonic switches at room temperature (RT). Recently, many different techniques have been used to fabricate high-quality GaN films, such as MBE and MOCVD. Although high-quality GaN has been fabricated at high temperatures above 1300 K, such high temperatures can be detrimental to synthesis of GaN on more temperature-sensitive substrates due to the intense reactivity between NH_3 and the substrate. Hence, the development of low-temperature synthesis of high-quality GaN would allow us not only to fabricate abrupt heterointerfaces between GaN and the substrate but also to reduce the defects due to the difference in the thermal expansion coefficients. Photo-CVD (PCVD) growth is a technique that can reduce the growth temperature by yielding the reactive radicals Ga and N via photolysis of their precursors. Although, the photolytic synthesis of GaN has been demonstrated at 800 K, its detailed optical properties remain unclear. We report here on the dependence of PL spectra on the V/III ratio of nanocrystalline GaN films deposited at RT using PCVD. GaN samples (100-nm thickness) were grown on a sapphire (0001) substrate at RT. We used TMG and semiconductor grade NH_3 as the III and V sources, respectively. $H_2$was used as the carrier gas for the TMG. The partial pressure of NH_3 was fixed at 500 Torr, so the V/III ratio (g) was varied by changing the partial pressure of TMG. We used a frequency-quintupled Q-switched Nd:YAG laser (λ = 213 nm) as the light source for the photodissociation. The PL spectra of the samples were examined using a CW He-Cd laser (λ = 325nm). To check the atomic composition of the sample, X-ray photoelectron spectroscopy (XPS) was used after removing a surface layer of the sample. The RT PL spectra for samples fabricated in the range of $10 \leq g \leq 90$ show a broad peak with a full width at half maximum (FWHM) of 0.5 eV. It is observed around 3.1 eV for the samples deposited with $g \leq 90$, corresponding to the oxygen defect-related emission of hexagonal GaN. In contrast, a sharp peak (FWHM of 100 meV) from 3.26 to 3.32 eV is observed for the samples with $g \leq 5000$. Furthermore, the low temperature (5 K) PL spectra of the samples with g = 50000 and 500000 show two dominant PL peaks at 3.366 and 3.310 eV, which can be ascribed to transitions from the quantum confinement of carriers in cubic inclusions within the hexagonal material. XPS analysis was used to check the atomic composition ratio of gallium and nitrogen. The atomic composition ratio of the nitrized gallium was determined using the relative sensitivity factor: gallium, 54.5%; nitrogen, 45.5%. This implies that the deposited film was well nitridized by the PCVD due to the large V/III ratio, even at RT.

4:15 PM O3.4

Evaluation of the Fine Structures of Isolated ZnO Nanorod Single-Quantum-Well Structures using Near-Field Ultraviolet Photoluminescence Spectroscopy.

Takashi Yatsui[1], Jungshik Lim[2], Tadashi Kawazoe[1], Motoichi Ohtsu[1,2,3], Sung Jin An[4] and Gyu-Chul Yi[4]; [1]SORST, JST, Machida, Tokyo, Japan; [2]Interdisciplinary Graduate School of Science and Engineering, Tokyo Institute of Technology, Yokohama, Kanagawa, Japan; [3]Faculty of Engineering, the University of Tokyo, Bunkyo-ku, Tokyo, Japan; [4]Department of Materials Science and Engineering, POSTECH, Pohang, Kyungbuk, South Korea.

A nanometer-scale ZnO dot is a promising material for realizing nanometer-scale photonic devices at room temperature, due to its large exciton binding energy. Furthermore, recent demonstration of semiconductor nanorod quantum-well structure enables us to fabricate nanometer-scale electronic and photonic devices on single nanorods. Recently, ZnO/ZnMgO nanorod multiple-quantum-well structures (MQWs) were fabricated and the quantum confinement effect of the MQWs was successfully observed. In addition, further improvement in the fabrication of nanorod heterostructures has resulted in the observation of significant PL intensity, even from nanorod single-quantum-well structures (SQWs). To confirm the promising optical properties of individual ZnO/ZnMgO SQWs for realizing nanometer-scale photonic devices, we measured the PL spectrum using a low temperature (15K) near-field optical microscope. In this measurement, we found fine structures of PL spectra from isolated ZnO SQWs. ZnO/ZnMgO SQWs were fabricated on the ends of ZnO nanorods with a mean diameter of 40 nm using catalyst-free metalorganic vapor phase epitaxy. The average concentration of Mg in the ZnMgO layers used in this study was determined to be 0.2. The ZnO well layer thickness L investigated in this study were 2.5, 3.8, and 5.0 nm, while the thicknesses of the ZnMgO bottom and top barrier layers in the SQWs were fixed at 60 and 18 nm, respectively. After the growth of ZnO/ZnMgO nanorod SQWs on sapphire (0001) substrate, they were dispersed on the substrate to be isolated. A 325-nm light source was used to excite the ZnO/ZnMgO nanorod SQWs. We used UV fiber probe with an aperture diameter of 30 nm. In the near-field spectra obtained at the ZnO nanorod, the single emission peak was observed at 3.365 eV, which correspond to the neutral-donor bound exciton (DOX). However, at the well layer, the emission from DOX was suppressed, while blue-shifted PL emission peak was emerged at 3.393 (L = 2.5 nm), 3.447 (L = 3.8 nm), and 3.499 eV (L = 5.0 nm). The value of the blue shift was consistent with the theoretical prediction using finite square-well potential of the quantum confinement effect in the ZnO well layer. Their spectral width (3 meV) were much narrower than those of far-field spectra (40 meV). The far-field PL spectra measure an ensemble of SQW with size fluctuations, which resulted in inhomogeneously broadened spectral features. However, since the near-field measurement restricts the isolated SQWs, it had made it possible to observe discrete energy levels. The results shown here provide criteria for realizing nano-scale photonic devices, such as the switching devices confirmed by the authors in CuCl quantum cubes.

Anti-parallel coupling of Quantum Dots with an Optical Near-Field Interaction

Tadashi Kawazoe[1,*], Kiyoshi Kobayashi[2], and Motoichi Ohtsu[1, 3]

1) SORST, Japan Science and Technology Agency, Tenkoh building 17-4F, 687-1 Tsuruma, Machida, Tokyo 194-0004, Japan.Tel:+81-42-788-6039, Fax:+81-42-788-6031, e-mail: kawazoe@ohtsu.jst.go.jp
2) Interdisciplinary Graduate School of Science and Engineering, Tokyo Institute of Technology, 4259 Nagatsuta, Midori-ku, Yokohama 226-8502, Japan.
3) Department of Electronics Engineering,University of Tokyo7-3-1 Hongo, Bunkyo-ku, Tokyo 113-8656, Japan.

We report the direct observation of optically forbidden energy transfer between cubic CuCl quantum dots via an optical near-field interaction using time-resolved near-field photo-luminescence (PL) spectroscopy.

Figures 1 shows the spatial distribution of the luminescence intensity from the 4.6-nm QC at 15 K with the 325-nm CW probe light and the 385-nm 10-ps pump pulse. The excitation intensity of pump and probe laser was 1 W/cm^2 and 100nJ/cm^2·pulse. The photon energy of the pump pulse tuned to the (1,1,1) exciton energy level in the 6.3-nm QC. The inset shows the energy transfer between the QCs [1] when the pump pulse excites the 6.3-nm QC. In this case, because the exciton energy in the 4.6-nm QC cannot be transferred to the (1,1,1) exciton energy level in the 6.3-nm QC due to the state filling effect, the exciton energy flows back and forth between the (1,1,1) exciton energy level in the 4.6-nm QC and (2,1,1) exciton energy level in the 6.3-nm QC, and some excitons recombine in the 4.6-nm QC. Therefore, the PL signal from the 4.6-nm QC was detected as a hot region in Fig. 1. We measured the temporal evolution of this PL signal. The energy transfer time between QCs is observed as the signal rise time. As a result of the experiments for the several QC pairs, we found the decay time (*i.e.*, the exciton lifetime) of the PL signal depend on the signal rise time, as shown in Fig.2. The exciton lifetime increased as the energy transfer time fell, which strongly supports the notion that near-field coupling has anti-parallel dipole features. Namely, a quantum-dots pair coupled by an optical near field has a long exciton lifetime and optically forbidden features due to its anti-parallel electric dipole pair.

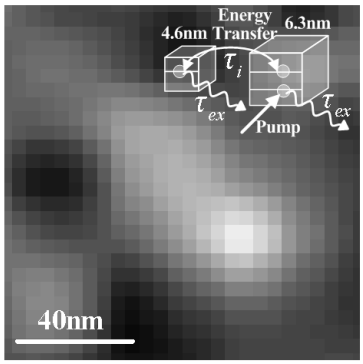

Fig.1

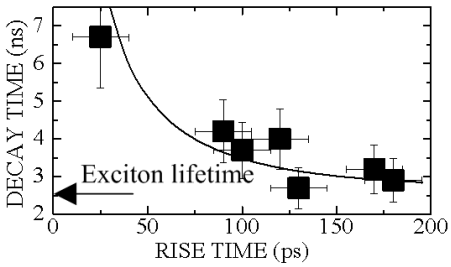

Fig.2

These features are of interest physically and are applicable to photonic devices, such as optical nanometric sources, long phosphorescence devices, and optical battery cells.

[1] T. Kawazoe, K. Kobayashi, J. Lim, Y. Narita, and M. Ohtsu, Phys. Rev. Lett. **88**, pp.067404 (2002).

12-C-1

Fabrication of a Near-Field Optical Probe by Electroless Plating under Ultrasonic Irradiation

Yuichi Saito, Shuji Mononobe[*,**], Ikuhiro Kato, Motoichi Ohtsu[*,***], Hideo Honma
Graduate School of Eng., Kanto Gakuin University, Yokohama-shi 236-8501, Japan
[*]*Kanagawa Academy of Science and Technology, KSP East 408, 3-2-1 Sakado, Takatsu, Kawasaki 213-0012, Japan, Fax: +81-44-819-2072, E-mail:mononobe@net.ksp.or.jp*
[**]*PRESTO, Japan Science and Technology Agency, Kawasaki 213-0012, Japan*
[***]*Department of Electronics Engineering, University of Tokyo, Tokyo 113-8656, Japan*

Scanning near field optical microscopy (SNOM) employing a fiber probe has been widely applied for nanometric optical imaging, spectroscopic investigation, and molecular sensing. [1,2] To fabricate the probe, tapering an optcal fiber, metallizing, and making an aperture is known as an effective method. For the aperture formation, the metallized probes have to be compounded against a close substrate under shear-force feedback control. However, it is difficult to mass-produce the probes by this method. To fabricate SNOM probes, we propose a new method based on electroless plating under ultrasonic irradiation. [3] We successfully fabricated the SNOM probe with high reproducibility. Fig.1 shows scanning electron micrograph of magnified top regions of the fabricated probe. The white line indicates the cross sectional profiles of the tapered fiber. The nickel film thickness gradually decreases toward the apex. The nickel thickness of the tip region is less than 40nm and the foot region is more than 200nm. The metallized probe with a nanometric tip is very effective for high resolution SNOM/shear-force microscopy.

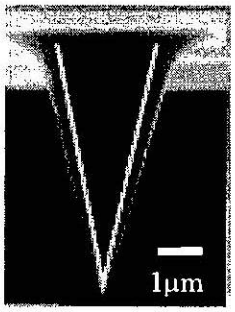

Fig.1 Scanning electron micrograph of the fabricated probes by electroless plating.

References

[1] *Near Field Optics*, eds. D.W.Pohl and D. Courjon (Kluwer, Dordrecht, 1993), NATO ASI Series E, Vol. 242.

[2] S. Mononobe 'Probe fabrication' in *Near-Field Nano/Atom Optics and Technology* (Springer, Tokyo, 1998).

[3] S.Mononobe, Y.Saito, M.Ohtsu, and H.Honma, *Jpn. J.Appl. Phys.* 43, Part 1, No. 5B, 2862-2863 (2004).

12-C-2

Surface Activation Based on Oxygen-Reactive Sputtering of Palladium to Plate Near-Firld Optical Fiber Probes

Shuji Mononobe[*,**], Ikuhiro Kato[***], Hideo Honma[***], Motoichi Ohtsu[**,****]

[*]*PRESTO, Japan Science and Technology Agency, Kawasaki 213-0012, Japan*

[**]*Kanagawa Acad. of Sci. and Technol., KSP East 408, 3-2-1 Sakado, Takatsu, Kawasaki 213-0012, Japan; Phone +81-44-819-2075; Fax +81-44-819-2072; E-mail mononobe@net.ksp.or.jp*

[***]*Graduate School of Eng., Kanto Gakuin University, Yokohama-shi 236-8501, Japan*

[****]*Department of Electronics Engineering, University of Tokyo, Tokyo 113-8656, Japan*

We have proposed a method based on size dependent electroless plating [1] to fabricate a probes with a nanometric aperture for near-field optical microscopy. This method involves tapering a silica fiber, surface activation, and electroless nickel plating. To perform the surface activation, we previously dipped the tapered probe in two aqueous solutions of $SnCl_2$ and $PdCl_2$. However, the aperture size of the plated probe was seriously affected by temporal degradations of Sn salt and its solution. To avoid this problem, one has to develop an alternative process for surface activation. In this paper, we present a new activation technique based on palladium sputtering in order to improve the reproducibility of the plating method.

We performed the plating method involving palladium sputtering using a double clad fiber [2]. First, the fibers were tapered by dipping in a buffered HF with a volume ration of 40%NH_4F:50%HF:H_2O=10:1:1. Next, palladium nuclei were generated on the tapered probes by reactive O_2/Ar plasma sputtering of palladium. The mixed ratio of O_2 is around 1%. The probe with palladium nuclei was coated with nickel except for the apex region by dipping in a plating solution including 0.01mol/L-Ni^{2+} and 0.03mg/L-Pb^{2+}. The temperature was 60°C. At a plating time of 5min, we obtained a near-field probe with an aperture diameter of 40nm. The present method is much higher reproducible than that based on $SnCl_2$ and $PdCl_2$ solutions. In the case of using pure argon gas for sputtering process, cracks were generated in the plated nickel film. We consider that the reactive oxygen in the sputtering plays a significant role of controlling the catalytic power of generated Pd nuclei.

References

[1] S. Mononobe, Y. Saito, M. Ohtsu, and H. Honma, *Jpn. J. Appl. Phys.* **43**, Part 1 (5B), p. 2862 (2004).

[2] S. Mononobe and M. Ohtsu, *IEEE Photonics Technol. Lett.* **10** (1), p. 99 (1998).

Nanophotonics: Optical near field phenomena and applications to devices, fabrication, and systems

Motoichi OHTSU
Department of Electronics Engineering, School of Engineering, The University of Tokyo
7-3-1 Hongo, Bunkyo-ku, Tokyo 113-8656, Japan
E-mail: ohtsu@ee.t.u-tokyo.ac.jp URL: http://www.nanophotonics.info/

As an introduction to the symposium, this talk presents the definition, true nature, and technical progress of nanophotonics[1-4]. Nanophotonics, proposed by M. Ohtsu in 1993, is defined as a novel technology that utilizes local electromagnetic interactions between a few nanometer-sized elements and optical near fields. Since optical near fields are free from the diffraction limit of light due to its size-dependent localization and size-dependent resonance features, nanophotonics enables fabrication, operation, and integration of nanometric devices (Fig.1).

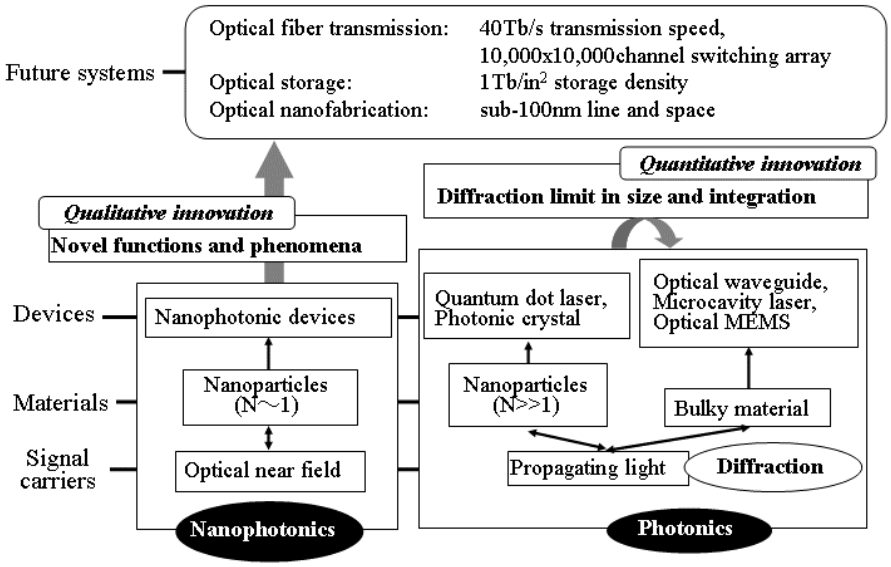

Fig. 1 Concepts of nanophotonics.

It should be noted that nanophotonics is not only to realize nanometer-sized optical technology (*quantitative innovation*). True nature of nanophotonics is to realize "novel functions and phenomena, which are not possible as long as propagating lights are used (*quantitative innovation*)". These novel functions and phenomena are possible by noting that the nanometric system (composed of nanometer-sized elements and optical near fields) is buried in a macroscopic heat bath. Energy non-conservation can be observed in the nanometric system due to energy exchange between the two systems. Higher order effects, e.g., magnetic dipole or electric quardrupole transitions are not neglected due to localized nature of optical near fields. Further, nonadiabatic processes, deviating from the Franck-Condon's principle, are also possible.

Recent technical progress of devices, fabrications, and systems to be presented are; (1) two

types of nanophotonic devices, i.e., phonon-coupled devices (optical switch, AND gate, NOT gate, content addressable memory, D/A converter, etc.) and propagating light-coupled devices (buffer memory, super-radiant optical pulse generator, etc.), (2) interface devices connecting macroscopic and nanophotonic devices, i.e., metallic nano-dot array, (3) nanophotonic fabrication, i.e., size- and position-controlled photochemical vapor deposition including nonadiabatic process, desorption and self-organization based on sized-dependent resonance, application of nonadiabatic process to photo-lithography, and (4) nanophotonic systems, i.e., optical routers in fiber communication, optical memory, optical data processing, etc.

References

1) M. Ohtsu, *Near-Field Nano/Atom Optics and Technology*, Springer, Berlin, 1998.

2) M. Ohtsu, et al., "Nanophotonics: Design, Fabrication, and Operation of Nanometric Devices Using Optical Near Fields", IEEE J. Selected Topics in Quantum Electron., vol.8, no.4 (2002), pp.839-862.

3) M. Ohtsu (ed.), *Progress in Nano-Electro-Optics, I – III*, Springer, Berlin, 2002-2004.

4) M. Ohtsu and K. Kobayashi, *Optical Near Fields*, Springer, Berlin, 2003.

Motoichi OHTSU received the B.E., M. E., and Dr. E. degrees in electronics engineering from the Tokyo Institute of Technology, in 1973, 1975, and 1978, respectively. In 1978, he was appointed a Research Associate, and in 1982, he became an Associate professor at the Tokyo Institute of Technology. From 198 to 1987, while on leave from the Tokyo Institute of Technology, he joined the Crawford Hill Laboratory, AT&T Bell Laboratories. In 1991, he became a Professor at the Tokyo Institute of Technology. In 2004, he moved to the University of Tokyo. Since 1993, he has been concurrently the leader of the "Photon Control" project of the Kanagawa Academy of Science and Technology. Since 1998, he has been concurrently the leader of the "Localized Photon" project of ERATO. Since 2002, He is a leader of the national project on "Ultrahigh density optical storage" sponsored by METI. He has written over 320 papers and received 87 patents. He is the author and co-author of 39 books. In 2000, he was the President of the IEEE/LEOS Japan Chapter. From 2000, he is an executive director of the Japan Society of Applied Physics. In 2001, he served as a Technical Program Co-chair for the 4th CLEO/PR01. He has been a tutorial lecturer o the SPIE and the OSA. He is a member of several boards of the MEXT, METI, and so on.

Prof. Ohtsu is a Fellow of the OSA, a senior member of IEEE, and member of several academic societies. He has been awarded ten prizes from academic institutions, including the I. Koga Gold Medal of URSI in 1984, the Japan IBM Science Award in 1988, two awards from the JSAP in 1982 and 1990, and the Inoue Science Foundation Award in 1999.

Abs. 57, 206th Meeting, © 2004 The Electrochemical Society, Inc.

Electroless Nickel Plating under Ultrasonic Irradiation And Its Application to a Scanning Near-Field Optical Microscopy Probe

Yuichi SAITO, Shuji MONONOBE*, Ikuhiro KATO, Motoichi OHTSU**, Hideo HONMA

Honma Lab., School of Engineering, Kanto Gakuin University, Mutsuurahigashi, Kanazawa-ku, Yokohama 236-8501, Japan

* Kunitake "Organization and Function" Research Area, PRESTO, Japan Science and Technology Agency / Kanagawa Academy of Science and Technology, KSP East 408, 3-2-1 Sakado, Takatsu-ku, Kawasaki 213-0012, Japan

** School of Electronics Engineering, University of Tokyo, 7-3-1 Hongo, Bunkyo-ku, Tokyo 113-8656, Japan

Recently, a scanning near-field optical microscope (SNOM) employing shear-force feedback technique, which provides simultaneous topographic and SNOM imaging, has been widely applied nanometric optical imaging and local spectroscopy. To develop a high resolution SNOM / shear-force microscopy, we have proposed a new type of probe tip having a metal film those thickness gradually decreases to a few tens of nanometers toward the apex. [1] To realize such probes, we have developed a method based on electroless nickel plating under ultrasonic irradiation. In this paper, we present a plating method of fabricating a SNOM probe with a nickel film those thickness gradually decreases to a few tens of nanometers toward the apex.

Figure 1(a) shows schematic design of the probe. Here, the body and portions with fiber diameters of more than the optical wavelength have fairly thick thicknesses in comparison to the skin depth. θ is the cone angle of the tapered fiber. **Figure 1(b)** represents the magnified apex region of the probe. The term of d_s and t_s are defined as the fiber diameter and radial thickness in the same cross-section, respectively. And, t_a is the thickness of metal covering the apex.

The method involves tapering an optical fiber and electroless nickel plating with ultrasonic agitation. Firstly, a GeO_2-doped fiber with a core diameter of 2μm and an index difference of 2% was etched in buffered HF. The obtained probe has a conical tapered core protruding from the flat clad end with a diameter of 25μm. The cone angle of θ=20° and the apex diameter less than 10nm. Next, we plated the tapered probe under 1MHz ultrasonic irradiation by plating unit as shown in Fig. 1(c). Here, since the transducers radiates directional ultrasonic waves, the ultrasonic energy is strongly confined within the region indicated by the dotted rectangular. The total area of transducers and total electric input power were and 126mm × 110mm and 300W, respectively. The distance h between the transducers and probe tip is 220 mm.

Figures 2(a) and **2(b)** show scanning electron micrographs of the magnified top regions of the nickel-coated probes under ultrasonic irradiation and without additional agitation, respectively. Here, the white lines represent the cross-sectional profiles of the tapered fibers with a cone angle of 20°. In **(a)**, the radial thickness of the nickel film increases from an estimated value of t_a=20nm toward the foot of the protruded core and converses to 400nm. In **(b)**, the probe tip is entirely coated with nickel. These results indicate the size-dependence effect of electroless nickel plating is caused by ultrasonic agitation. This probe with a small tip diameter and metal film is effective in high resolution SNOM / shear-force microscopy.

In summary, we found that size-dependence effect of electroless nickel plating is induced by ultrasonic irradiation. By applying this plating to a tapered fiber, we succeeded in fabricating a nickel-coated SNOM probe those nickel thickness decreases from 400nm to 40nm toward the apex.

Reference

[1] S. Mononobe, Y. Saito, M. Ohtsu, and H. Honma, *Jpn. J. Appl. Phys.* 43, Part 1, No. 5B, (2004).

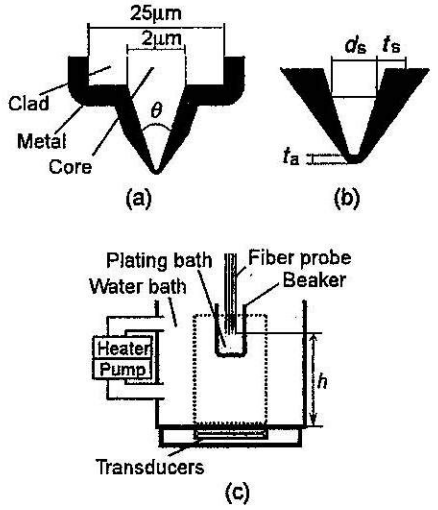

Fig. 1. (a) Schematic design of the near-field optical fiber probe having a metal film whose thickness gradually decreases toward the apex. (b) Schematic explanation of electroless plating unit with an ultrasonic generator.

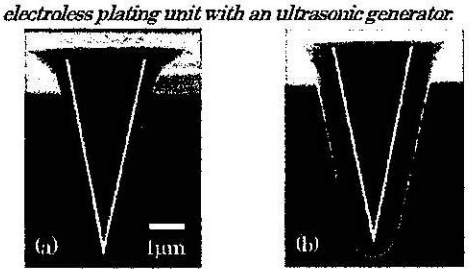

Fig. 2 SEM images of magnified top regions of the fabricated probes by electroless plating (a) under 1MHz-ultrasonic irradiation and (b) without additional agitation.

Fabrication of a SNOM probe using electroless nickel plating with ultrasonic irradiation

Yuichi Saito, Shuji Mononobe**,***, Motoichi Ohtsu**, Hideo Honma*
Graduate School of Engineering, Kanto Gakuin University
*Faculty of Eng., Kanto Gakuin Univ.,
1-50-1 Mutsuurahigashi, Yokohama 236-8501, Japan
e-mail:honma@kanto-gakuin.ac.jp
*** PRESTO, Japan Sci. & Technol. Agency, **Kanagawa Acad. of Sci. & Technol.
KSP East 408, 3-2-1, Sakado, Takatsu, Kawasaki 213-0012 Japan

Scanning near field optical microscopy (SNOM) employing a probe is widely applied for nanometric optical imaging, spectroscopic investigation, molecular sensing, and so on. To fabricate high resolution probes, tapering an optical fiber, metallizing, and protruding its apex from metal film has been used as an effective method. However, it is difficult to mass-produce SNOM probes by this methods due to the low reproducibility of the protruding. To mass-produce SNOM probes, we recently proposed a new method based on electroless plating under ultrasonic irradiation. This method involves four wet processes: etching, surface sensitization, palladium nucleation, and electroless plating with ultrasonic agitation. We successfully fabricated nickel coated probes using a 1MHz-ultrasonic generator. Fig. 1(a) and 1(b) show scanning electron micrographs of magnified top regions of the fabricated probe and entirely coated probe plated without ultrasonic agitation, respectively.

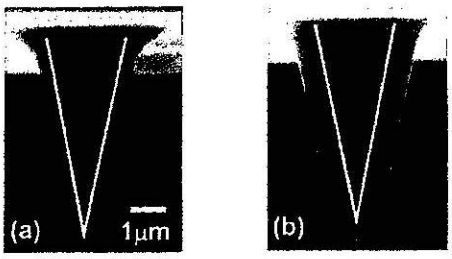

Fig.1 Scanning electron micrographs of magnified top views of the fabricated probes by electroless plating (a) under 1MHz-ultrasonic irradiation and (b) without additional agitation. The white curves represent the cross-sectional profile of tapered fiber, respectively. In (a), the electric power into ultrasonic generator is 300W.

Fabrication of a Near-Field Optical Fiber Probe Based on Size-Dependent Electroless Nickel Plating

Shuji Mononobe,
Kunitake "Organization and Function" Research Area, PRESTO, Japan Science and Technology Agency/ Kanagawa Academy of Science and Technology, KSP East 408, 3-2-1 Sakado, Takatsu-Ku, Kawasaki-Shi 213-0012, Japan.
Ikuhiro Kato, Yuichi Saito, and Hideo Honma,
Faculty of Engineering, Kanto Gakuin University, Mutsuurahigashi, Yokohama-Shi 236-8501, Japan.
Motoichi Ohtsu,
Department of Electronics Engineering, School of Engineering, The University of Tokyo, 7-3-1 Hongo, Bunkyo-Ku, Tokyo 113-8656, Japan.

Recently, a scanning near-field optical microscope (SNOM) employing shear-force feedback technique, which provides simultaneous topographic and SNOM imaging, has been widely applied to super-resolution imaging and local spectroscopy. To develop a high resolution SNOM/shear-force microscope, we have proposed a novel metallized fiber probe with a tiny tip as shown in Fig. 1(a), where the metal coating thickness gradually decreases to a few tens of nanometers toward the apex. To realize such probes, we have developed a method based on size-dependent electroless nickel plating.[1] In this paper, we present a plating method of fabricating a SNOM probe with a nickel film whose thickness gradually decreases to toward the apex.

The method involves tapering an optical fiber and electroless nickel plating with ultrasonic agitation. First, a GeO_2–doped fiber with a core diameter of 2 μm and an index difference of 2% was etched in buffered HF. The obtained probe has a conical tapered core protruding from the flat clad end with a diameter of 25 μm. The cone angle of θ=20°, and the apex diameter less than 10 nm. Next, we plated a set of four tapered fibers under 1MHz ultrasonic irradiation. Figure 1(b) schematically shows the lateral positions of the 4 probes in the plating bath. Figure 1(c) shows a set of scanning electron micrographs (SEM) of the four probes, where the dotted lines represent the cross-sectional profiles of the tapered fibers with a cone angle of 20°. The nickel thicknesses covering the apexes of the fiber were estimated to be less than 20 nm. To evaluate the decreasing thickness profiles, we estimated the radial thickness for a cross-sectional fiber diameter of 200 nm. The average and deviation of the 4 probes take values of 17 nm and 90 nm, respectively. This result indicates that the probe was fabricated with high reproducibility.

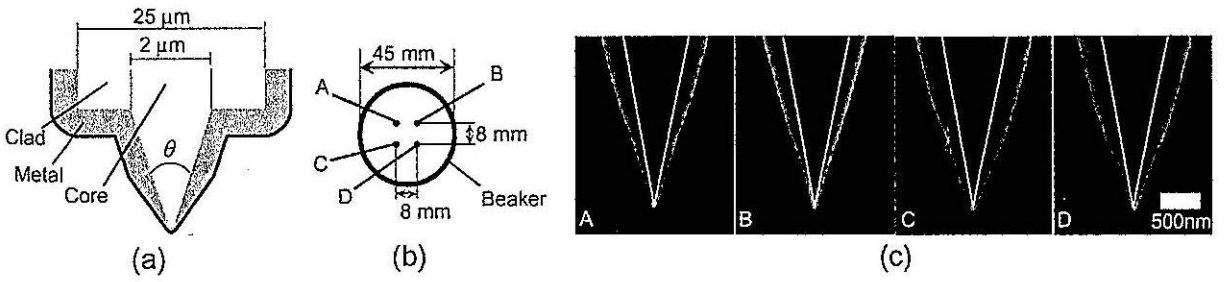

Figure 1: (a) Schematic illustration of a fiber probe with a metal film whose thickness gradually decreases toward the apex. (b) Schematic top view of the nickel plating bath and four probes immersed in it. Here, A–D show lateral positions of the probes. (c) SEM images of the top regions of probes A–D.

References

[1] S. Mononobe, Y. Saito, M. Ohtsu, and H. Honma, *Jpn. J.Appl. Phys.* 43, Part 1, No. 5B, (2004).

Quasi-Particle Model for Optical Near-Field Interaction with Single Atom, Molecule and Nanomaterials

K. Kobayashi (1) and M. Ohtsu (2), (3)
(1) Department of Physics, Tokyo Institute of Technology, Tokyo 152-8551, Japan
(2) SORST, Japan Science and Technology Agency, Tokyo 194-0004, Japan
(3) Department of Electronics Engineering, University of Tokyo, Tokyo 133-8656, Japan

Light-matter interaction on a nanometer scale is one of the key issues in nano-optics, and is great importance for the advancement of nanotechnology using optical near fields, as well as for deep understanding of physics behind the phenomena. We have proposed a model based on a quasi-particle that is exchanged in a relevant system such as a probe tip-single atom/molecule system, or a few-quantum-dot (QD) system [1,2]. The induced interaction in the relevant system as an isolated system, which we call the optical near-field interaction, can be expressed in terms of the Yukawa function, after renormalizing the effects from the irrelevant system [1,2]. The effective mass appearing in the Yukawa function shows the finiteness of the interaction range, which reflects the size or discrete energy levels of the system. In this paper, we discuss the applicability and issues of the model.

Finiteness and steepness of the optical near-field interactions provide unique phenomena and dynamics inherent in the optical near field. For example, individual excitation of a quantum dot produces the nearest-neighbor couplings in a few-QD-system that are not allowed by global excitation due to the usual propagating far field [3]. In addition, a dipole-ordered state as a quasi-steady state can be predicted for a special case in such a system [4]. Using this kind of dynamics, we have theoretically and experimentally studied nanophotonic devices such as a switch, logic gates, and so on [3-5], and obtained reasonable agreements between theoretical and experimental results.

However, there exists a recent experimental result on molecular dissociation and nanofabrication [6] that cannot be explained by the above model. It indicates that a vapor molecule of diethylzinc (DEZn) can be dissociated by an incident photon with less energy than the dissociation energy of DEZn only if an optical near field is used. We try to extend the above model, including an ionic or vibrational excitation, and discuss the key issues to be solved in the future.

References

[1] K. Kobayashi and M. Ohtsu, *J. Microsc.* **194**, 249 (1999).
[2] K. Kobayashi, S. Sangu, H. Ito, and M. Ohtsu, *Phys. Rev.* A **63**, 013806 (2001).
[3] S. Sangu, K. Kobayashi, A. Shojiguchi, and M. Ohtsu, *Phys. Rev.* B **69**, 115334 (2004).
[4] A. Shojiguchi, K. Kobayashi, S. Sangu, K. Kitahara, and M. Ohtsu, *J. Phys. Soc. Jpn.* **72**, 2984 (2003).
[5] M. Ohtsu, K. Kobayashi, T. Kawazoe, S. Sangu, and T. Yatsui, *IEEE J. Sel. Top. Quantum Electron.* **8**, 839 (2002).
[6] T. Kawazoe, K. Kobayashi, S. Takubo, and M. Ohtsu, submitted to *J. Chem. Phys.*

Optical near-field-assisted dry etching of silica in a sulfur hexafluoride atmosphere

V. Polonski, B. Martin, R. Netterfield
Commonwealth Scientific & Industrial Research Organisation (CSIRO) Division of Industrial Physics
Bradfield Road, Lindfield (Sydney) NSW 2070 Australia

T. Yatsui, T. Kawazoe
Japan Science and Technology Agency (JST) Exploratory Research for Advanced Technology
687-1 Tsuruma, Machida, Tokyo 194-0004 Japan

M. Ohtsu
Department of Electronics Engineering, University of Tokyo
7-3-1 Hongo, Bunkyo-ku, Tokyo 113-8656 Japan

The domain of nanofabrication has recently seen the addition of a number of optical near-field based techniques [1-6]. They appear to not only offer the integrity and reproducibility required by numerous emerging science applications, but also the additional functionality inherent to nanophotonic solutions. We report on one such process, namely optical near-field assisted dry etching of a planar aperture array. Its counterintuitive operation (using far less energy than the energy threshold required in traditional approaches) may prove to be one of the future disruptive technologies. At the very least it promises to free certain industrial processes from the use of toxic components and equipment with a high cost of ownership.

A 1.5 μm silica layer on a Si substrate was spun with photoresist, subjected to an interferometric lithography step, exposed and developed. The resulting periodic pattern of islands in photoresist was then coated with 20 nm of gold. A lift off step, followed by ultrasonic cleaning, left apertures in the gold with typical dimensions of between 100 nm and 250 nm. The wafer was placed inside a reaction chamber in 40 mTorr of sulfur hexafluoride gas (a common plasma-assisted dry etchant for SiO_2), flushed at 10 sccm. The substrate was then illuminated from the Si side by 1539 nm, 10 mW/mm^2 light for 10 minutes. The back-illumination was possible because the substrates are transparent at this wavelength. On irradiation by such light an optical near-field is generated close to the boundary of the aperture. After exposure the gold layer was removed and etched features were examined using an AFM. Etched features of planar shape, coinciding with former aperture locations, could readily be distinguished by the AFM. Step heights of 0.5 nm were observed. No etching was observed in areas that were not illuminated by the infrared light, unambiguously pointing to a sub-threshold optical effect as the key factor in the observed etching.

This process can be attributed to the exponentially decaying evanescent fields and coating material influences. Under these conditions, etching can be triggered by a non-adiabatic photochemical reaction [7] that provided sufficient energy to sustain the dry etch process, even with low power incident infrared light. The photon energy of 1.5 μm is lower than that of the absorption edge of SF_6. The extremely short diffusion length of electrons in gold results in a concentration of electrons at the edge of the aperture, inducing a steep gradient in the electric field which can dissociate SF_6 even using nonresonant light.

References

[1] I. Smolyaninov, D. Mazzoni and C. Davis, *Appl. Phys. Lett.*, **67**, 3859 (1995)
[2] V.V. Polonski, Y. Yamamoto, M. Kourogi, H. Fukuda, and M. Ohtsu, *J. Microsc* **194**, 545 (1999)
[3] Y.Yamamoto, M.Kourogi, M.Ohtsu, V.Polonski, G.H.Lee, *Appl. Phys. Lett.*, **76**, 2173 (2000)
[4] H. Diesinger, A. Bsiesy and R. Hérino, *J. Appl. Phys.*, **90**, 4862 (2001)
[5] T. Kawazoe, Y. Yamamoto and M. Ohtsu, *Appl. Phys. Lett.*, **79**, 1184 (2001)
[6] G. Wysocki, J.Heitz, and D. Bäuerle, *Appl. Phys. Lett.*, **84**, 2025 (2004)
[7] T. Kawazoe & M. Ohtsu, *Proc.SPIE – Int. Soc. Opt.Eng.*, **5339**, 619 (2004)

Nanometric Summation Architecture Using Optical Near-field Coupling Between Quantum Dots

Makoto Naruse (1), Tadashi Kawazoe (2), Suguru Sangu (3),
Kiyoshi Kobayashi (4), Tetsuya Miyazaki (1), Fumito Kubota (1), and Motoichi Ohtsu (2)(5)
1: National Institute of Information and Communications Technology,
4-2-1 Nukui-kita, Koganei, Tokyo 184-8795, Japan, E-mail: naruse@nict.go.jp
2: Japan Science and Technology Agency 3: Ricoh Co., Ltd
4: Tokyo Institute of Technology 5: University of Tokyo

Abstract *A nano-scale data summation architecture is proposed and experimentally demonstrated using exciton energy transfer between quantum dots based on local electromagnetic interaction via optical near-fields. It will enable high-density, low-power content addressable memory architecture.*

Introduction

To benefit from the transparency of optical communication, considerable efforts are being made, for example, in all-optical packet switching [1]. Optical implementation of table lookup has also been studied using, for instance, optical waveguides [2]. One serious problem with these approaches, however, is the level of integration achievable, which is essentially constrained by the diffraction limit of light.

Nanophotonics, on the other hand, is not restricted by the diffraction limit since it is based on local electromagnetic interactions between a few nanometric elements individually excited by optical near fields [3]. Here we propose and experimentally demonstrate a data summation mechanism based on nanophotonics, which, for instance, forms the basis for table lookup or content addressable memory (CAM) [4], as schematically shown in Fig. 1(a).

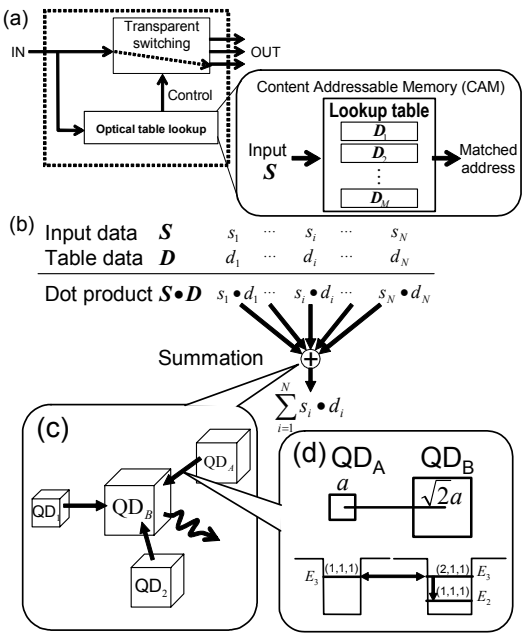

Fig. 1 (a) Table lookup or content addressable memory (CAM) for optical switching. (b) Inner product operation as a data matching application. (c) Summation mechanism in quantum dots. (d) Inter-dot interaction via an optical near field.

Nanometric content addressable memory

We can relate the CAM architecture to an inner product operation. We assume an N-bit input signal $\boldsymbol{S}=(s_1,...,s_N)$ and reference data $\boldsymbol{D}=(d_1,...,d_N)$. Here the inner product $\boldsymbol{S}\cdot\boldsymbol{D}=\Sigma s_i\cdot d_i$ will provide a maximum value when the input perfectly matches the reference data. The multiplication of two bits, namely $x_i=s_i\cdot d_i$, has already been demonstrated by a combination of three quantum dots (QDs) [5]. Therefore, the key operation remaining in order to achieve an optical CAM is the summation, Σx_i, where all data bits x_i (i=1,...,N) should be taken into account; this is schematically shown in Fig. 1(b). The existing ways of realizing such a data gathering scheme include focusing lenses, optical waveguide couplers, and so forth; however, such methods impose yet another barrier to integration and miniaturization. In nanophotonics, on the other hand, optical energy is attracted to a certain quantum dot by optical near-field couplings between quantum dots, as described later. The exclusiveness of the matching operations should be noted. The inner product $\boldsymbol{S}\cdot\boldsymbol{D}$ is, in fact, not enough to determine the correct matching of input $\boldsymbol{S}$ and reference $\boldsymbol{D}$; the inner product of the inverted input signal and reference data is also required. Inversion is, however, a difficult function to implement optically. One possible option is to properly design the modulation format [6], for instance by representing a logical level by two digits, such as by Logic 1="10" and Logic 0="01". Then, an N-bit logical input is physically represented by 2N bits, which makes the inner product equivalent to the matching operation. For the purpose of implementing longest prefix matching, which is important for packet data transfer [7], a "don't care" status is also required and it can be coded by "11" in this scheme.

Nanometric summation mechanism

The nanometric summation architecture is based on inter-dot interaction via an optical near field, as schematically shown in Fig. 1(c) where excitations are transferred towards a certain quantum dot (at the centre). As a fundamental case, we assume two quantum dots QD_A and QD_B, as shown in Fig. 1(d).

The ratio of the sizes of QD_A and QD_B is $1:\sqrt{2}$. Between those two dots, there are resonant energy levels that are coupled by an optical near-field interaction [5,8,9]. Therefore, the exciton population is transferred to QD_B [8,9]. It should be noted that this interaction is forbidden for far-field light. Since the sublevel relaxation via exciton-phonon coupling is fast, the population is quickly transferred to the lower level in QD_B, which constitutes a uni-directional signal flow. Similar energy transfers may take place in the dots surrounding QD_B among the resonant energy-levels so that energy flow can occur. One could worry that if the lower energy level of QD_B is occupied, another exciton cannot be transferred due to the Pauli exclusion principle. Here, thanks again to the nature of the optical near-field interaction, the exciton population goes back and forth between QD_A and QD_B, which is called nutation [9,10]. Therefore, we can effectively regard this state as the exciton remaining waiting until QD_B becomes empty.

Numerical calculations were performed based on quantum master equations in a density matrix formalism. First, we considered an initial condition where there are two excitons, one in QD_A and one in QD_B (two-exciton system). The solid and dotted curves in Fig. 2 respectively show the time evolution of the exciton population of the lower level of QD_B and the other states where an exciton remains in QD_A. Nutation is observed, as indicated by the dotted curve. We then compared the population to a one-exciton system. The dashed line in Fig. 2 shows the population of the lower level of QD_B with the initial condition of one exciton in QD_A. Physically the "output" signal is related to the integration of the population in the lower level of QD_B. By numerically integrating the population between 0 and 5 ns, we can see that the ratio of the output signals between the two- and one-exciton systems is 1.86:1, which reflects the number of initial excitons, or the summation mechanism.

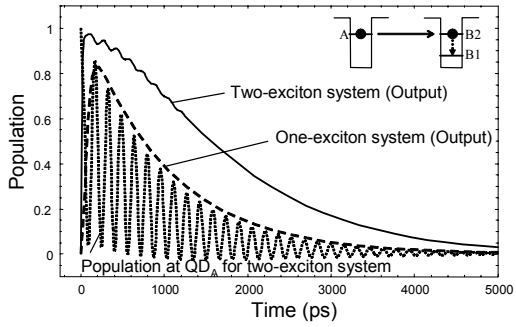

Fig. 2 Population comparison between one- and two-exciton systems.

Experiment

A proof-of-principle experiment was performed to verify the nano-scale summation using CuCl quantum dots in a NaCl matrix. We choose a quantum dot arrangement where "small" QDs surrounded a "large" QD, as schematically shown in Fig. 3(a). Here, we irradiate at most three light beams with different wavelength, 325 nm, 376 nm, and 381.3 nm, which respectively excite QDs having a size of 1 nm, 3.1 nm, and 4.1 nm. The excited excitons are transferred to the bigger QD, and its radiation is observed by a near-field fibre probe. Notice the output signal intensity at a photon energy level of 3.225 eV in Fig 3(b), which corresponds to a wavelength of 384.8 nm or a QD size of 5.9 nm. The intensity varies approximately as 1:2:3 depending on the number of excited QDs in the vicinity, as observed in Fig. 3(b). The spatial intensity distribution was measured by scanning the fibre probe, as shown in Fig. 3(c), where the energy is converged to the centre. Hence, the architecture works as a summation mechanism based on exciton energy transfer via optical near-field interactions.

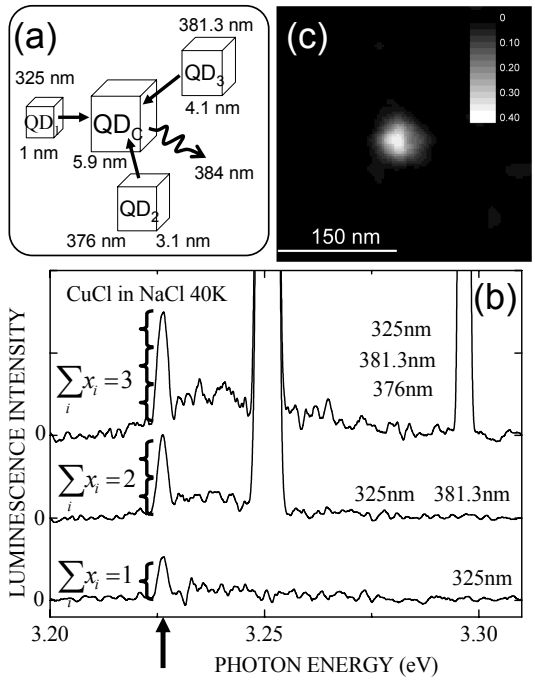

Fig. 3 Nanometric summation: experimental results.

Conclusions

To achieve highly dense optical table lookup, an architecture for data summation is presented using near-field coupling between quantum dots, and its principle is experimentally demonstrated.

References

1 M. J. O'Mahony, et al., IEEE Commun. Mag. **39**, 128 (2001).
2. P. C. Teh, et al., JLT **19**, 1352 (2001).
3. M. Ohtsu, et al., JSTQE **8**, 839 (2002).
4. H. Liu, IEEE Micro **22**, 58 (2002).
5. T. Kawazoe, et al., APL **82**, 2957 (2003).
6. M. Naruse, et al., OL **29**, 608 (2004).
7. K. Kitayama, et al., JLT **21**, 2753 (2003).
8. T. Kawazoe, et al., PRL **88**, 067404-1 (2002).
9. S. Sangu, et al., PR B **69**, 115334 (2004).
10. S. Sangu, et al., JAP **93**, 2937 (2003).

[III] REVIEW PAPERS

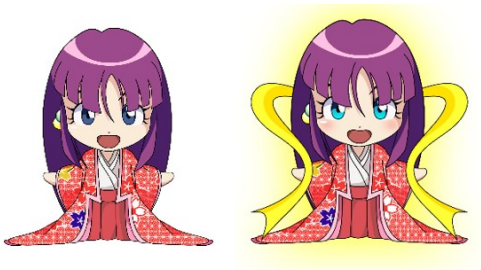

[解説]

光の回折限界を超える ナノフォトニクスとその材料

東京大学大学院　大津 元一[*1]／独立行政法人 科学技術振興機構　八井　崇[*2]、川添　忠[*3]

光の回折限界を超えて新機能と現象を実現する日本発の革新技術、ナノフォトニクスが急進展している。本稿では加工、デバイス、システムを広くカバーするこの技術に用いられるいくつかの材料について概説する。

ナノフォトニクスとは

将来の高度情報・高度福祉社会を支えるために光デバイス、光加工の微小化、高密度化が要求され、光システムには新規機能が要求されている。しかし従来の光技術は光波の回折のために、回折限界という基本的限界を超えた微小化は不可能、また物質の微視的励起による新規機能は不可能という問題を抱えている。量子ドットレーザーやフォトニック結晶と呼ばれる技術ではナノテクノロジーによりデバイス用材料を微小化しているのみであり、通常の伝搬光を使っているのでこの問題を解決できない。

回折限界を超え、問題の解決のために日本で生まれた革新技術がナノフォトニクスであり、物質とともに光を微小化して使う。すなわち、ナノ寸法物質表面にエネルギー局在した微小な近接場光を発生させ、これを用いて加工、デバイス、システムを実現する技術である。近接場光とは何か、さらにナノフォトニクスによる加工の概略については本誌の連載[1]を参照されたい。なお、ナノフォトニクスの本質は回折限界を超えたナノ寸法を実現するという量的変革にあるのではなく、従来の光技術で使われていた伝搬光を利用していたのでは不可能な新機能と現象を実現するという質的変革にあり、将来の光科学技術の騎手と考えられている。

ここでは、ナノフォトニクスのための材料に関する現状を概説したい。

ナノフォトニクス用材料に要求されること

ナノフォトニクスによる新規の光デバイス、すなわちナノフォトニックデバイスは数個の量子ドットによって構成される[2)3)]。一例として、図1に3個の量子ドットで構成される光スイッチのオフ状態とオン状態を示す。この3個の量子ドットはそれぞれ互いに共鳴する光励起準位を持ち、入力信号は近接場光によって共鳴レベル間を移動する。スイッチ動作はこのエネルギー移動の量を制御することで実現される。

このような動作原理を持つナノフォトニックデバイスの材料に求められる特徴は、量子サイズ効果の発現する微小寸法の微粒子が、その位置と寸法を誤差1nm以内で基板上に制御性よく形成できることである。さらに次の特徴が要求される。

①ナノ寸法の量子ドットを高密度に作製できるこ

*1おおつ　もといち：工学系研究科　教授
〒113-8656　東京都文京区本郷7-3-1
☎03-5841-1189
*2やつい　たかし、*3かわぞえ　ただし：
SORSTナノフォトニクスチーム　研究員
〒194-0004　東京都町田市鶴間687-1 第17天幸ビル
☎042-788-6030

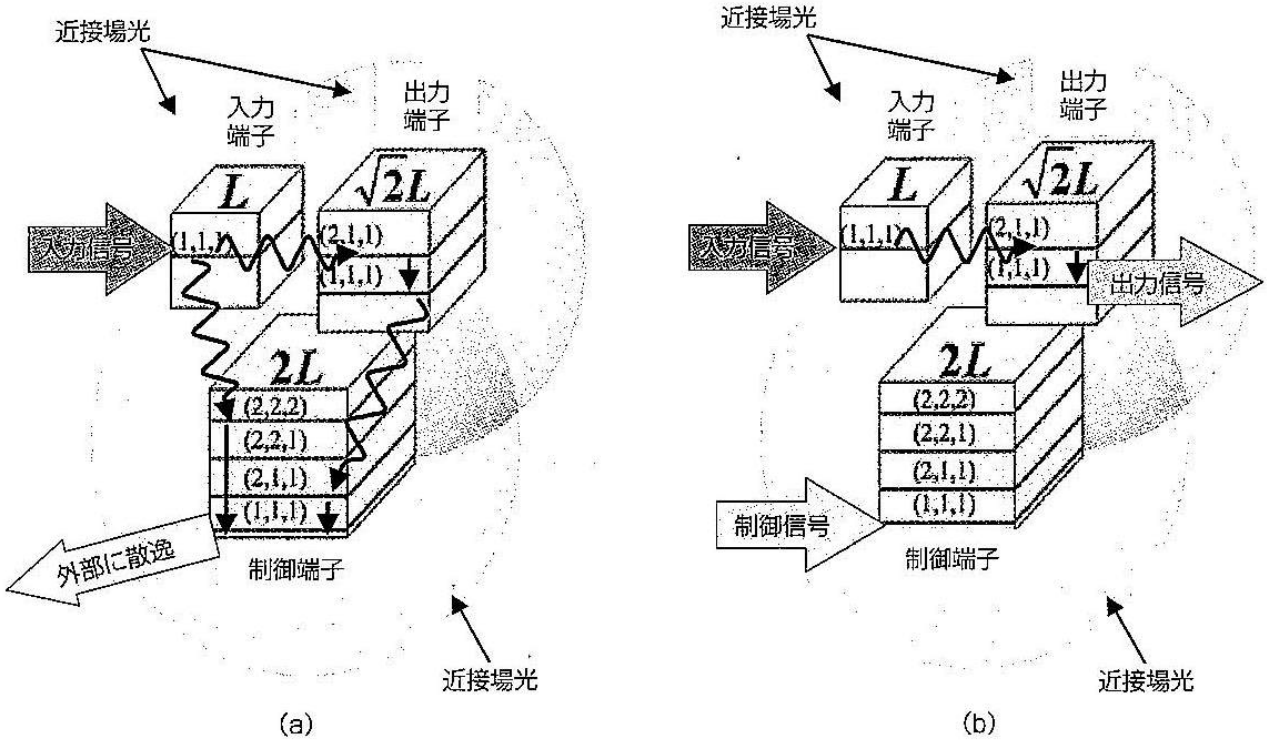

図1 光スイッチの構造。(a)オフ状態、(b)オン状態

と。

②上記、量子ドットが光励起状態(励起子ポラリトン・プラズモンポラリトンなど)にない場合、孤立した状態であること。

③材料の混合比や寸法によって高励起準位のエネルギーを広く制御できること。

④室温においても光素励起が安定に存在し、よりエネルギーの高い励起準位と縮退がないこと。

①の条件は量子ドットが近接場光で結合できることに対応し、②の条件を満たさない場合は光なしに量子ドットが結合していることを意味し、入力信号の伝送が起きず、入力信号は単に結合した量子ドットの結合準位を励起するだけとなり、デバイスとして動作しなくなる。また、③および④は室温で動作することや、光通信帯域を含む波長で動作するための条件である。

ナノフォトニクス用材料

上記の特徴を満たす材料としてGaN、ZnOなどの化合物半導体の量子ドット、さらには金属ナノ微粒子が採用されている。

1．GaN

青色発光ダイオードとして注目を集めているGaNは励起子の結合エネルギーが大きく、p型の作製が早くから実現していたことから[4]、発光素子として広く実用化に至っている。ナノフォトニックデバイス作製のためには単原子層で精密に制御する必要がありMBE(Molecular Beam Epitaxy)法により良質のGaN結晶が得られるようになってきた。GaNのバンドギャップ3.4eVに対し6.4eVのバンドギャップをもつAlNを障壁層に選ぶことにより、上記条件①から④を満たす材料として使用可能である。作製されたGaN量子ドット間でのエネルギー移動も確認されている[5]。

なお、MBE法では基板温度を1000℃以上にする必要があり、これによる基板の劣化や、GaN膜内部での転移の増加などが問題となる。この問題を解決する手法として、光化学気相堆積法(光CVD法)が開発された。この手法では、窒素源となるアンモニアなどの分解に必要な熱エネルギーを光により与えることが可能となるため、室温での堆積が可能であり強い紫外発光が報告されている[6]。さらには、パターニング基板を用いることで、ナ

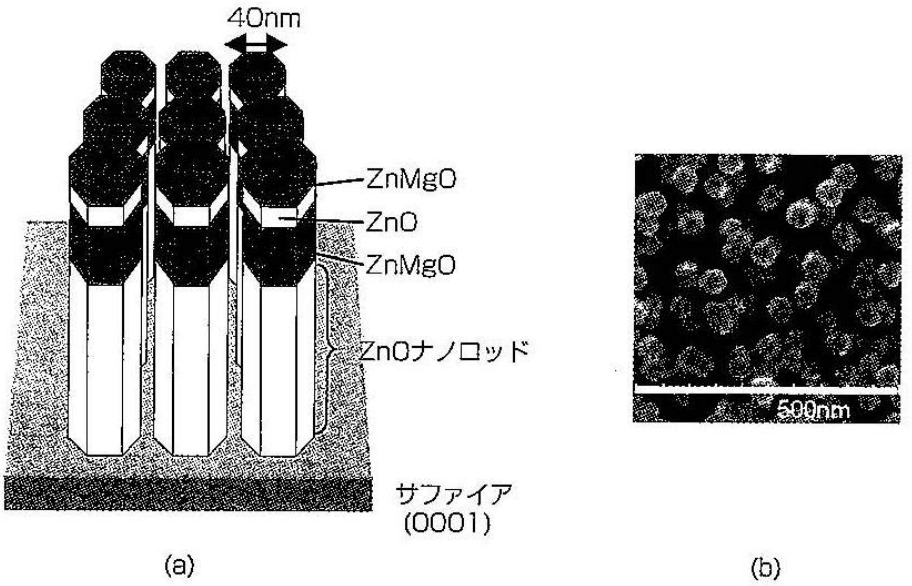

図2　先端にZnO単一量子井戸構造を有するZnOナノロッド。(a)構造、(b)電子顕微鏡像

ノ寸法での位置および寸法が制御された選択成長も実現している[7]。

2．ZnO

液晶ディスプレイ用の透明電極として注目されているZnOは、発光材料としても大気中および室温中で化学的・熱的に安定な性質を示し、励起子結合エネルギーもGaNの2倍以上と大きいことから、室温で動作する紫外光源として期待されている。さらに近年、p型半導体の作製も報告されたことから[8]、GaNを凌駕する紫外発光材料として期待されている。特に各種の半導体微結晶の中で最も発光効率が高い形状としてナノロッド形状が古くから研究されている。その作製には金属触媒を用いたVLS(Vapor-Liquid-Solid)法が用いられており、ナノロッド内部にひずみの全く存在しない単結晶として成長するため、低閾値のレーザとしても注目されている[9]。さらに近年、金属触媒を全く用いない成長法がZnOにおいて報告された[10]。

これにより、金属不純物の影響もなくなり、ZnOナノロッド先端に形成された量子井戸構造(図2)から室温においても量子サイズ効果が得られるなど良質な発光特性が報告され[11]、室温で動作するナノフォトニックデバイス[12]を実現する材料として期待される。

3．金属ナノ微粒子

金属ナノ微粒子内部の電子と結合した光は、光の閉じ込めが非常に強いために、回折限界を超えたナノ寸法光導波路として期待されている。その一例として、ナノドットカプラーがある。これは、金属ナノ微粒子を等間隔に配列させたものであるが、この構造において微粒子間を近接場光により

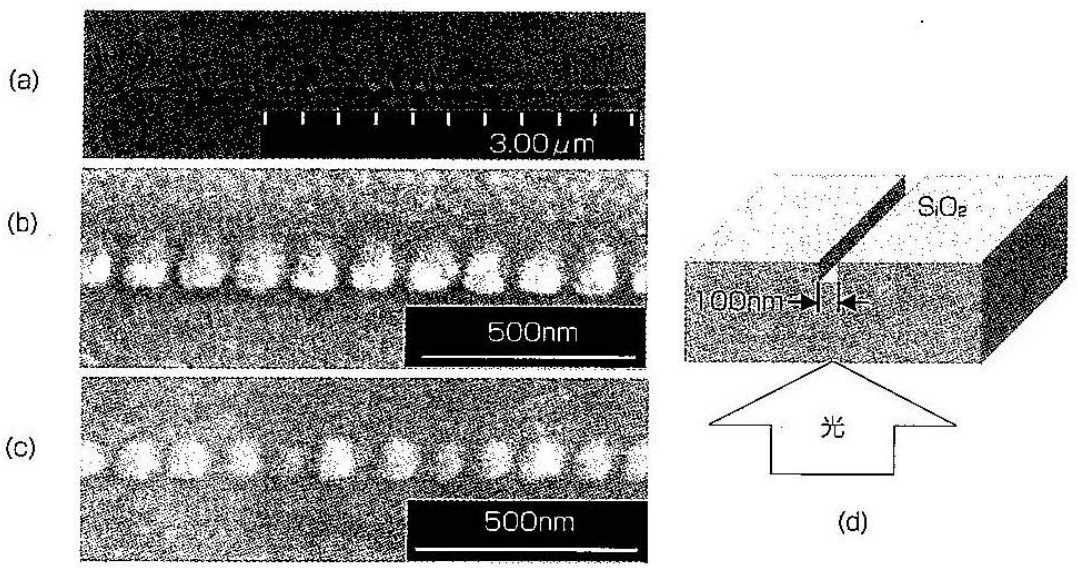

図3
物質寸法に依存する光脱離法により作製された金属ナノ微粒子の列の電子顕微鏡像。(a)Au、(b)Al、(c)Pt、(d)は作製法

エネルギーが伝搬される様子が観測されている[13]。ナノドットカプラーの作製に電子ビーム描画装置を使う場合、作製に時間がかかるうえに、微小化にも限界がある。この問題を解決する手法として、物質寸法に依存する光脱離法が開発された[14]。これにより、形成されるパターンの寸法が発生する近接場光の光子エネルギーの値によって決定され、大面積に渡り一括で微粒子列を作製することが可能となる。

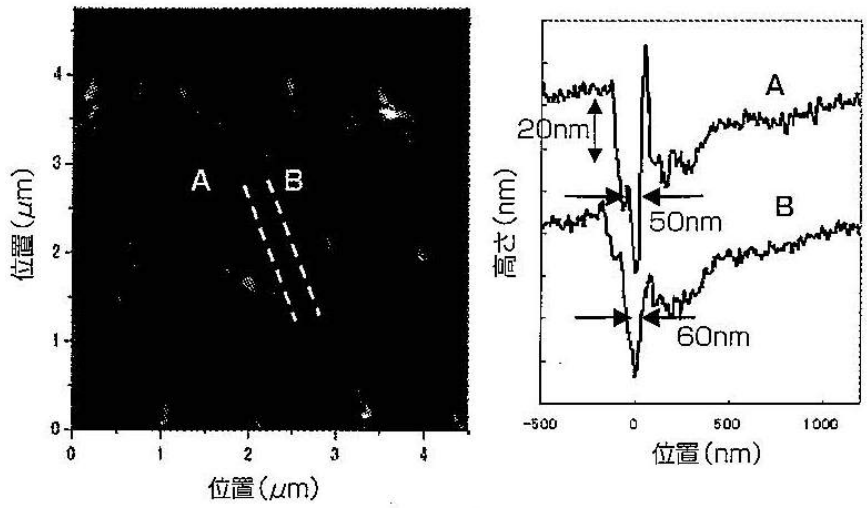

図4　電子ビーム描画用のレジストが近接場光に感光し、作製されたパターンの原子間力顕微鏡像とその断面

図3は以上の手法により作製された、Au、Al、Pt微粒子の一次元配列結果である[15]。これらの構造は、ナノ寸法の溝を有する基板を用いて、スパッタリング中にレーザ照射を行うことで作製されるが、溝に沿って発生した近接場光により、直径100nm以下の半球状の微粒子が制御性よく一列に形成されていることが分かる。

今後の展開

本稿で取り上げたGaN、ZnOなどの化合物半導体の他に、InAlAsなどの材料などの有望な材料が採用されつつあるが、これらについてはスペースの都合上省略した。また、ナノフォトニクスによる光リソグラフィが開発され、数十nmの寸法のパターンの一括加工が実現しているが、そこでは近接場光の局在性がフォトレジストに対し特異な光化学反応を起こしている。我々が非断熱光化学反応過程[16]と呼ぶこの現象を利用することで、紫外光にしか感度を持たないフォトレジストを可視光源で感光したり、通常は光に全く感度を持たない電子ビーム描画用のレジストを感光させることが可能である（図4）[17]。

この例は、従来の光加工には使われていなかった光学的に不活性な材料がナノフォトニクスでは使用可能となることを意味しており、今後はさらに新しい材料の開発が待望される。

参考文献

1）大津元一、工業材料、52、2005年6月号掲載
2）T. Kawazoe, K. Kobayashi, S. Sangu, and M. Ohtsu, Appl. Phys. Lett., **82**, 2957(2003).
3）T. Kawazoe, K. Kobayashi, J. Lim, Y. Narita, and M. Ohtsu, Phys. Rev. Lett. **88**, 067404(2002)
4）H. Amano, M. Kito, K. Hiramatsu, I. Akasaki: Jpn. J. Appl. Phys., **28**, L2112(1989)
5）A. Neogi, B. P. Gorman, H. Morkoç, T. Kawazoe and M. Ohtsu, Appl. Phys. Lett., **86**, 043103(2005)
6）S. Yamazaki, T. Yatsui, M. Ohtsu, T.W. Kim, H. Fujioka: Appl. Phys. Lett., **85**, 3059(2004)
7）柳楽 崇，八井 崇、大津元一、応用物理学会秋季講演会予稿集、第3分冊、1535(2004)
8）A. Tsukazaki, A. Ohtomo, T. Onuma, M. Ohtani, T. Makino, M. Sumiya, K. Ohtani, S. F. Chichibu, S. Fuke, Y. Segawa, H. Ohno, H. Koinuma, M. Kawasaki: Nature Materials, **4**, 42 (2005).
9）M. H. Huang, S. Mao, H. Feick, H. Yan, Y. Wu, H. Kind, E. Weber, R. Russo, P. Yang: Science, **292**, 1897(2001)
10）W. I. Park, G.-C. Yi, M. Y. Kim, S. J. Pennycook: Adv. Mater., **15**, 526(2003)
11）T. Yatsui, J. Lim, M. Ohtsu, S. J. An, G.-C. Yi: Appl. Phys. Lett., 85, 727(2004)
12）T. Kawazoe, K. Kobayashi, and M. Ohtsu: Appl. Phys. Lett., **86**, 103102(2005)
13）W. Nomura, T. Yatsui, M. Ohtsu: Appl. Phys. Lett., **86**, May 2 issue(2005)
14）T. Yatsui, S. Takubo, J. Lim, W. Nomura, M. Kourogi, M. Ohtsu: Appl. Phys. Lett., **83**, 1716(2003)
15）野村 航、八井 崇、大津元一、応用物理学会春期講演会予稿集，第3分冊、1167(2005)
16）川添忠、小林潔、米満広樹、大津元一、応用物理学会春季講演会予稿集、第2分冊、823(2005)
17）米満広樹、川添忠、小林潔、大津元一、応用物理学会秋季講演会予稿集、第3分冊、823(2005)

新連載

❶ ナノフォトニック加工

ナノフォトニクスとは：そのニーズとシーズ

大津 元一*
東京大学大学院

まえがきと連載の趣旨

新規の高機能デバイスを作製するために、微細加工技術の性能向上に対する要求が高まっている。とくに、近年のナノテクノロジーの進歩を支えるために、ナノメートルの加工精度が要求されている。本連載では、この要求を満たす新しい光加工技術について解説することを目的としている。表には次回以降の記事の内容を列挙する。

工業材料には、多岐にわたり基板の損傷や汚染のない「ソフトでクリーンな」加工法を用いることが有利である。荷電粒子ビーム(電子、イオンなど)を用いた加工法が実用化されているが、それと比して光を用いる加工法は「ソフトでクリーンな」点で優位にある。光リソグラフィがその代表例であり、図1はその技術ロードマップである。ところで、光の波は空間的に広がろうとする性質(これは回折と呼ばれている)があるので、それを凸レンズで集光しても光のスポット径は波長以下の寸法にはならない。そのために光リソグラフィでの加工可能な寸法の限界は光波長程度であり、この限界は回折限界と呼ばれている。

図1では、光源をより短波長化することにより、回折限界の枠組みの中で加工寸法の微小化を図っている。ただし、短波長の光源は大型、高価格、真空中での使用などの実用上の致命的な問題があ

*おおつ もといち：工学系研究科 教授
(財)科学技術振興機構 SORST ナノフォトニクスチーム リーダー
〒113-8656 東京都文京区本郷7-3-1
☎03-5841-1189 E-mail：ohtsu@ee.t.u-tokyo.ac.jp

表 次回以降の記事の内容

第2回	寸法精度の高いナノ光加工。とくに近接場光CVD、寸法依存共鳴脱離など。
第3回	自己組織的作製手法。とくにファイバプローブとフォトマスクが不要な方法、微粒子列配列など。
第4回	非断熱光化学反応を用いた光加工。とくにその原理、可視光を用いた近接場光CVD。
第5回	非断熱光化学反応を用いた光加工の実際。とくに可視光を用いた近接場光CVDと近接場光リソグラフィの実際など。
第6回	国内外の動向、デバイスとシステムへの応用例、市場規模予測など。

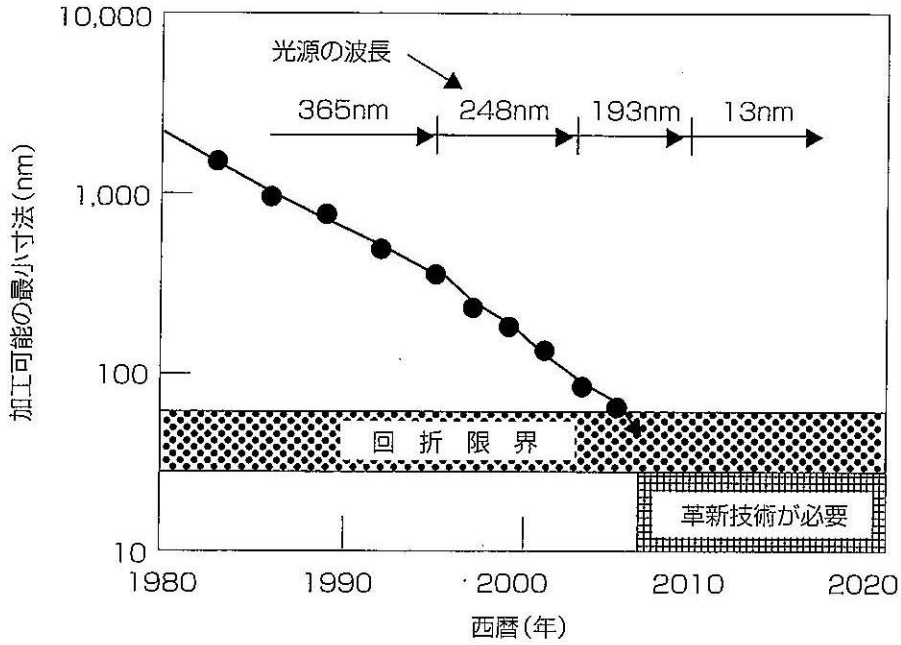

図1
光リソグラフィの技術ロードマップ

るので、今後の微細加工の進歩のためには、これらを解決するための革新技術が必要である。すなわち、回折限界を超えて加工寸法の微小化、加工精度の高精度化を実現するための「量的変革」が待望されている。

この量的変革は、近接場光(次節で説明)と呼ばれる光の小さな粒によって実現される[1]。本シリーズの趣旨の一つは、この具体例について紹介することである。近接場光を使った光技術はナノフォトニクスと呼ばれている(1993年に大津が命名)が[2),3)]、その定義は「近接場光により媒介されるナノ物質間の局所相互作用にもとづく加工、デバイス動作、システム構築の技術」である。

本連載では、とくに加工について解説する。このようなナノフォトニクスを加工へ応用する技術は、本連載のタイトルにあるように「ナノフォトニック加工」と呼ばれている。

さて、ナノフォトニクスではすでに上記の量的変革を実現したが、ナノフォトニクスの本質はこの量的変革ではなく、「伝搬光では実現し得ない機能、現象を引き出して使うこと、これにより光技術の『質的変革』を実現すること」である。本連載のもう一つの趣旨は(これが主であるが)、このような「質的変革」の具体例を紹介することである。たとえば、

(1)紫外線にのみ反応するフォトレジストや有機金属分子が赤色、緑色などの近接場光に反応し、微細なパターンが形成される。

(2)自己組織的に形成される微細パターンの寸法と位置の精度が著しく向上する。

などである。

近接場光とは

近接場光とは、物質表面近傍の、光の波長に比べ充分近い位置に発生する電磁場である[4)]。ここでは物質の寸法が波長に比べずっと小さい場合を考える。近接場光は(a)非伝搬(物質表面に局在している)、(b)エネルギーは物質表面から遠ざかるにつれ減少(その減少の度合いを表す「しみ出し長」は物質の寸法程度)、という2つの際立った性質を持つ。

図2は近接場光の発生の様子を示している。すなわち、電気的に中性な半径rの物質(球A)に光が入射したとき、その中の多数の原子に時間的に振動する電気双極子モーメント誘起され、その電気双極子モーメントから電磁場が発生する。この電磁場を表す電気力線は近隣の電気双極子モーメントどうしを結び、その一部は球Aの外にしみ出し

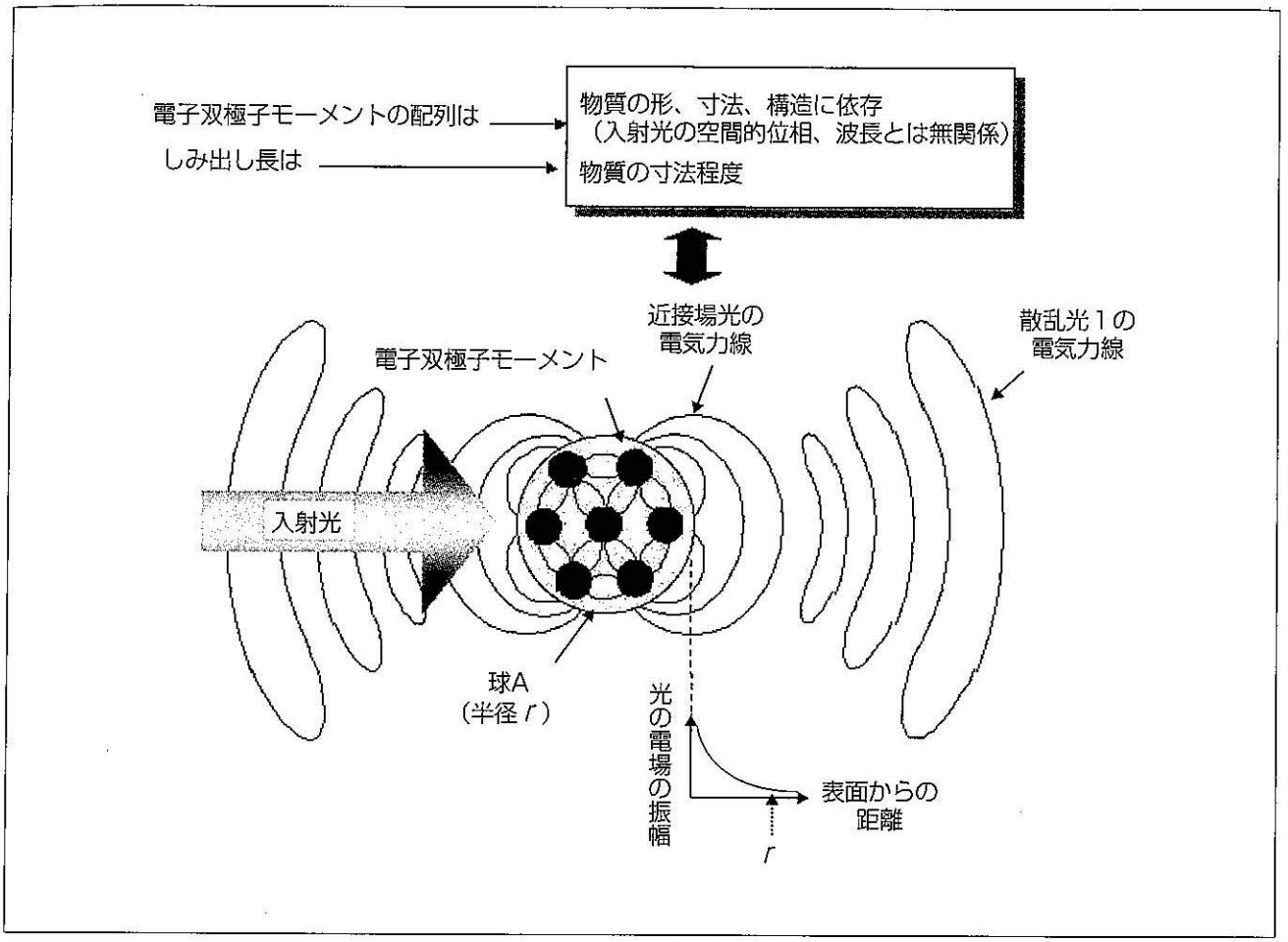

図2　近接場光の発生の様子

ている。このしみ出した電気力線が表す光が近接場光である。

この電気力線は、電気双極子モーメントから発して電気双極子モーメントに終端しているので、非伝搬であることを表している(性質(a)に対応)。その外側にある閉曲線状の電気力線は、遠方へと回折しながら伝搬する光を表すが、これは従来の光技術で使われている光である(散乱光1と呼ぶ)。半径rが入射光の波長に比べずっと小さい場合、発生する多数の電気双極子モーメントの配列の仕方は、入射光の空間的位相、波長とは無関係となり、球Aの形、寸法、構造に依存するので、近接場光のしみ出し長は球Aの半径r程度となる(性質(b)に対応)。

近接場光は非伝搬なので、近接場光の発生(図2)のみの考察では不充分で、検出についての考察が必須である。検出するためには、**図3**のように近接場光の中に第二の球Bを置くことによって近接場光を乱す。乱された近接場光は、散乱光(散乱光2と呼ぶ)となって遠くに伝搬するので、光検出器を用いれば散乱光2のパワーを測定できる。これが近接場光の検出過程である。

図3のように近接場光に起因する電気力線が2つの球を結びつけているということは、近接場光が2つの球により多重散乱されることを意味している。いいかえると、近接場光のエネルギーが2つの球の間を移動している。このように、近接場光の検出の過程で発生するエネルギー移動を積極的に利用すると、球Aを用いて球Bを加工することができる。すなわち、一方の球が他方の球の構造、形状を変化させる。

ナノフォトニクスで本質的なことは、前節の「質的変革」を実現することである。これは(1)近接場光のエネルギーが光の波長よりもずっと小さ

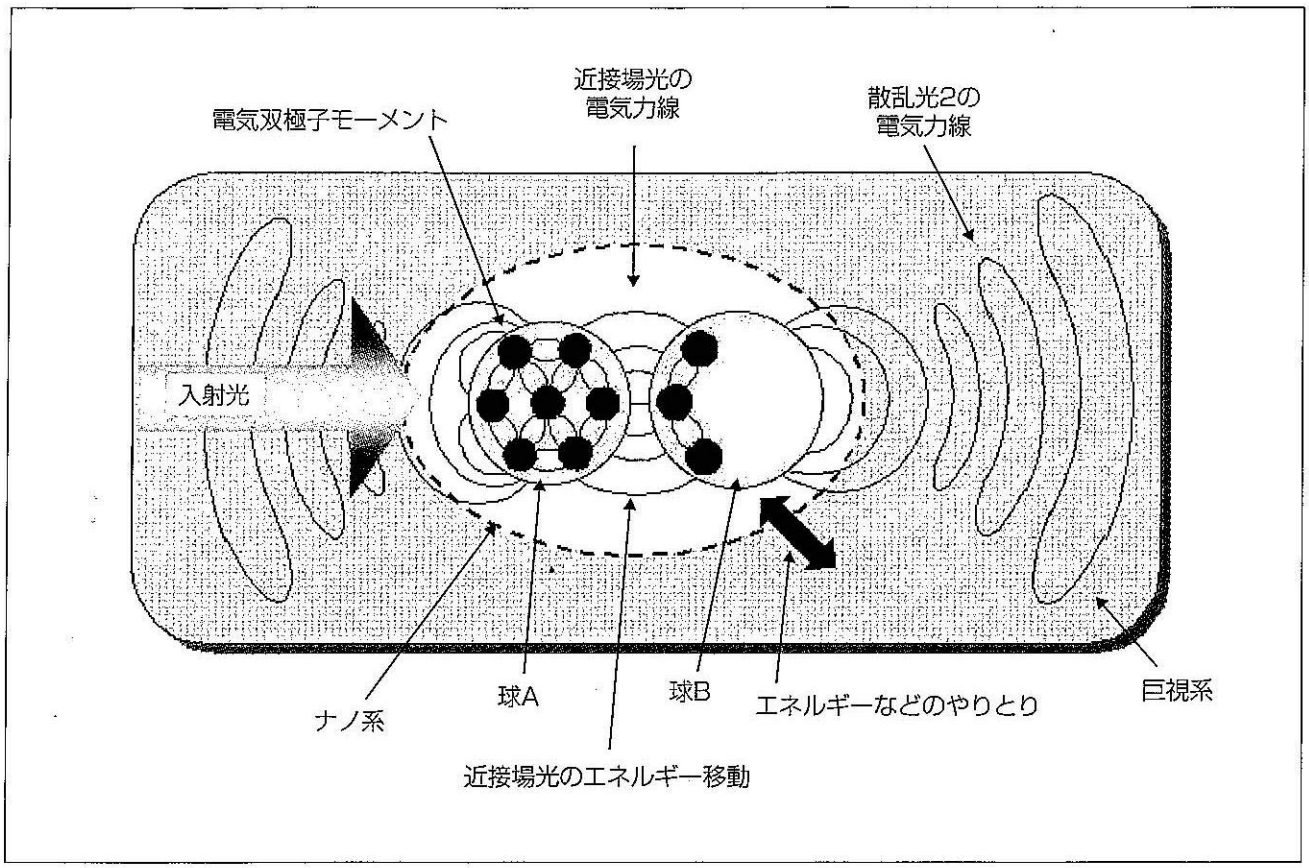

図3　近接場光の測定の様子(破線の楕円はナノ系と巨視系との間の境界を示す)

い寸法の空間に局在していること、(2)図3に示すように近接場光、微粒子からなるナノ寸法の系が熱浴(入射光、散乱光、基板などからなる巨視的寸法の系)の中に埋もれており、両系の間でエネルギーなどのやりとりがあること、などに起因する。

なお、これらの考え方は、互いに共通する内容を別の表現で述べているにすぎない。これらを統一的に記述するには、波動光学の枠組みでは不充分で、とくに、微小物質との電磁気学的相互作用を取り入れ、さらに、巨視系の中に埋もれたナノ系としての振る舞いを記述するために量子論が必要となる[4]。

加工の実際と次回以降のトピックス

次回以降に紹介する加工の具体例として、削る技術としてのリソグラフィのみでなく、積む技術としての化学気相堆積(CVD)などの例を示す。

なお、原理確認のためにはファイバプローブを用いて、その先端に近接場光を発生させ、一筆書きの加工法をとる場合もあるが、実際には一括加工のためのフォトマスクを使用し、さらには、フォトマスクさえも不要な方法など、実用的な方法が提案されている。本連載では、これらについてもふれる。

これらのトピックスが、本誌読者諸氏にとって工業材料開発の一助になれば幸いである。

参考文献

1)大津元一：ポピュラーサイエンス239、光の小さな粒、裳華房(2001)
2)大津元一：ナノ・フォトニクス、米田出版(1999)
3)大津元一監修：ナノフォトニクスへの挑戦、米田出版(2003)
4)大津元一、小林潔：近接場光の基礎、オーム社(2003)

特集　いろいろつかえるソノケミストリー(2)

超音波照射下無電解めっきによる近接場光学顕微鏡プローブの作製

Fabrication of a near-field optical probe based on electroless plating under ultrasonic irradiation

物部　秀二　科学技術技術振興機構　さきがけ　国武「組織化と機能」領域
Shuji MONONOBE
齋藤　裕一　関東学院大学　表面工学研究所
Yuichi SAITO
本間　英夫　関東学院大学　工学部
Hideo HONMA
大津　元一　神奈川科学技術アカデミー（KAST）　光科学重点研究室
Motoichi OHTSU

問合せ/モノノベ　シュウジ　〒213-0012川崎市高津区坂戸3-2-1 KSP東棟409 神奈川科学技術アカデミー
TEL 044-819-2075　FAX 044-819-2072　E-mail mononobe@net.ksp.or.jp

キーワード：メガヘルツ超音波，無電解めっき，光ファイバー，エッチング，近接場光学

[Abstract] We describe a method to fabricate a near-field optical probe with a nickel film whose thickness gradually decreases to a few tens of nanometers toward the apex. This method consists of etching an optical fiber and electroless nickel plating with ultrasonic agitation. Using 1 MHz ceramic transducers, we have reproducibly fabricated the probe with a tip diameter of less than 40 nm. This reproducibility is high compared to those for Langevin-type transducers.

1　はじめに

電気めっきによって金属が堆積をする場合，めっき開始後，反応部位近傍において金属イオンの濃度低下が生じるため，電気エネルギーの増加に対して堆積速度はある値まで増加後，飽和あるいは低下する現象がしばしば見られる．溶液の攪拌はめっき反応種を反応部位へ供給し，反応部位から反応生成物や老廃物を拡散させるため，この電気めっき浴に不活性ガスバブリング等で攪拌を加えれば，飽和領域において堆積速度を増加させることが可能である．しかし，水素発生を伴う自己触媒型の無電解ニッケルめっきにおいては，反応部位への原子状水素の吸着によって堆積速度が増大し，また，反応部位の近傍溶存水素飽和層は触媒能を保持する働きをするため，めっき溶の攪拌や被めっき物の揺動はニッケル堆積速度の低下をもたらす．一方，この無電解ニッケルめっきは，あるサイズ以上でのみめっきが行われる特異なサイズ依存性を示す．このサイズ依存性と臨界サイズをサブミクロンからナノメートルの範囲で制御することができれば，無電解めっきを近接場光学顕微鏡[1]（光を情報媒体とする走査型プローブ顕微鏡）の心臓デバイスであるナノ開口プローブ[2),3)]の作製に応用できる．本稿では，近接場光学プローブの作製のため，開発を行っている超音波照射を用いたサイズ依存無電解めっき[4),5)]について述べる．次節では，これにより作製される伝播光遮断型プローブとめっき法について述べ，第3節でメガヘルツPZT振動子とランジュバン型振動子を用いた結果について議論し，第4節でまとめる．

2　伝播光遮断型プローブティップと超音波照射を用いた無電解めっき作製法

近接場光学顕微鏡の分解能は主として先端径と試料―プローブ間距離によって決定され，伝播光成分や観測点以外からの近接場光の低フーリエ周波数成分や散乱光はノイズとなる．我々は伝播光を遮断し，かつ，試料プローブ間距離制御に用いるShear―Force顕微鏡を高分

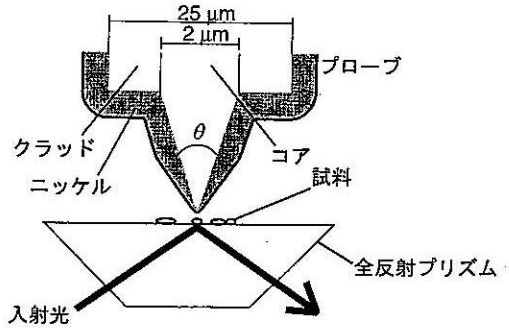

図 1　先端に向かって徐々に金属膜厚が減少する伝播光遮断型プローブティップと集光方式近接場光学顕微鏡

解能化するため，従来の開口型プローブに代えて，先端に向かって膜厚が徐々に減少する伝播光遮断型プローブティップ（図 1 上部）を提唱している．図 1 のように，このプローブを用いて，試料上の近接場光を散乱検出する集光方式近接場光学顕微鏡を構成すると，テーパー化されたプローブの先端部分の極薄金属膜は近接場光を検出する散乱体として働き，サブミクロン以上の膜厚の金属ブロックは部分は伝播光ノイズを遮断する．

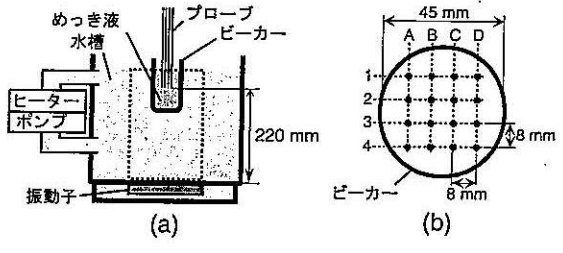

図 2　(a) 超音波照射を用いる無電解めっき装置　(b)16 本の光ファイバーのビーカー内浸漬位置

このプローブを実現するための無電解めっき法は (1) 光ファイバーの化学エッチング，(2) 感受性化と触媒化，(3) 超音波照射下無電解めっきからなる．まず，クラッド径 125μm，コア径 2μm，比屈折率差 2%の分散補償光ファイバーを緩衝フッ化水素溶液に浸漬し，コア先鋭角 20°，クラッド径 25μm のテーパー化光ファイバーを作製した[3]．次に，このテーパー化ファイバーを $SnCl_2$ と $PdCl_2$ の 2 つの溶液に次々に浸漬し，Sn-Pd 混合触媒を付与した．最後に，周波数 1MHz の振動子を用いた超音波照射めっき装置と，100kHz 振動子のめっき装置を用いて，それぞれ 16 本のテーパー化光ファイバーの無電解ニッケルを行った．2 つのビーカーは，表 1 に示される同組成のめっき液が使用された．めっき浴への浸漬時間は共に 15 分間であり，めっき浴温度は，1MHz の場合が 60 ℃，100kHz ランジュバン型で 55 ℃であった．図 2(a)(b) はそれぞれ超音波めっき装置の概略図と，16 本の光ファイバーのビーカー内浸漬位置を表す模式図である．図 (b) で，A1 から D4 の 16 個の点は超音波めっき装置内のファイバーの位置を示す．また，超音波照射は光ファイバーをめっき浴に浸漬後，5 秒後からめっき終了時まで連続的に行われた．図 3(a)(b) はそれぞれ，水槽底部に位置する 1MHz 圧電セラミックス薄膜型（本多電子,W−357HP）とランジュバン型（本多電子，W-100HF MKII）の振動子ユニットの模式図である．W−357HP の振動板 4 枚分の総面積 126mm×110mm に対して入力できる最大電力は 600W であり，W-100HF MKII のランジュバン型振動子 10 個への最大入力電力は 300W である．

表 1　無電解ニッケルめっき浴組成

$NiSO_4 \cdot 6H_2O$	0.1 mol·dm^{-3}
CH_3COONH_4	0.4 mol·dm^{-3}
$NaPH_2O_2 \cdot H_2O$	0.2 mol·dm^{-3}
pH	5.0

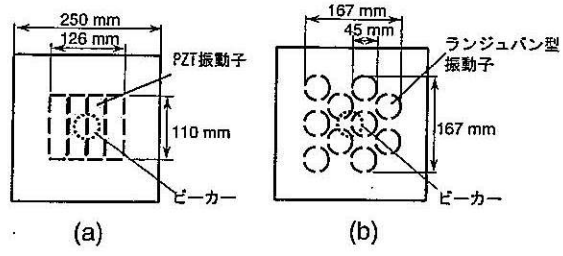

図 3　(a)1MHz 圧電セラミックス薄膜型と (b)100kHz ランジュバン型の振動子ユニット

3　結果および考察

超音波照射を行わず無電解めっきを行った場合，テーパー先端までニッケル膜で覆われたのに対し，図 4 に示す A1 から D4 は周波数 1MHz，入力電力 300W で PZT セラミック振動子を駆動し，ニッケルめっきを行った 16 本のプローブの先端付近の電子顕微鏡写真である．図中の白線は，テーパー化された光ファイバーコ

アの断面形状を表す．ニッケルで覆われたプローブの先端径はいずれも 40nm 以下であり，先端を覆う金属膜厚は 20nm 以下と推定される．また，ニッケル膜がの膜厚が先端部に向かって 200nm から徐々に薄くなる伝播光遮断型プローブの構造を持ち，それが高い再現性を持って作製されていることが分かる．特に中心部分に配置された B2，B3，C2，C3 はニッケル膜形状が非常によく一致しており，中心部領域にプローブを集中配置することによりより再現性が向上させることができると考えられる．

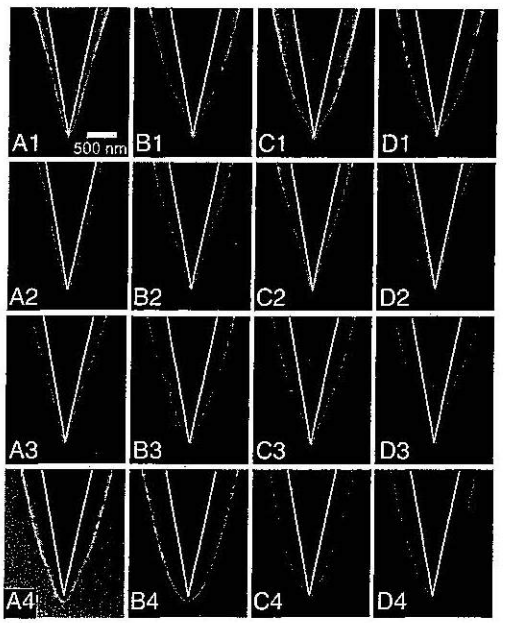

図 4　1MHz 超音波照射下で作製された 16 本のニッケルコートプローブの電子顕微鏡写真

図 5 は周波数 100kHz のランジュバン型振動子を用いて超音波攪拌を行った場合のニッケルコートプローブの電子顕微鏡像である．ランジュバン型振動子 10 個への総入力電力は 300W である．C3 にはファイバー先端がニッケル膜から突出したプローブが見られるものの，ビーカー中心部に配置された他の 3 つのプローブの先端は 100nm 以上の厚さのニッケルにより覆われており，図 4 のものに比べてニッケル膜形状のばらつきも大きい．以上の結果から，形状再現性に優れたプローブ作製のためには，100kHz ランジュバン型よりも 1MHz セラミック型振動子がはるかに効果的であることが分かる．また，市販の 45kHz ランジュバン型超音波洗浄器を用いてめっきを行った例でも，100kHz の

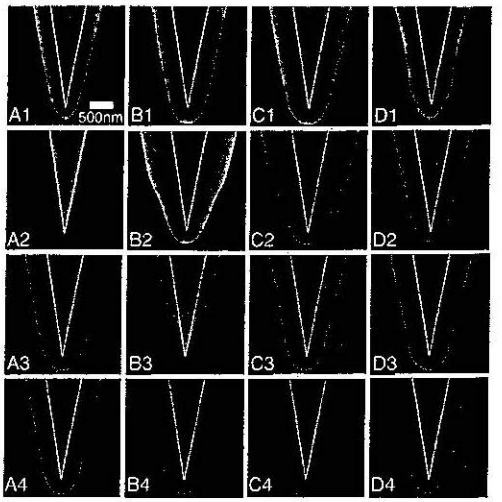

図 5　100kHz ランジュバン型振動子を用いて作製された 16 本のプローブの電子顕微鏡写真

結果と同様に，いくつかの例でサイズ効果が見られたものの再現性に乏しい結果が得られたことから，再現性の高さは周波数よりもむしろ振動子タイプによって決まると考えらる．ＰＺＴセラミック薄膜型振動子が指向性のよい超音波を発生し，図 2(a) の点線で囲まれた部分に超音波エネルギーが効率よくに閉じ込められるため，プローブ作製に効果的な均一性に優れためっき液攪拌が実現できた．

めっき抑制化学種である溶存酸素のめっき液への混入は ppm オーダーでも，サイズ依存性に影響を及ぼす．上記の実験では，めっき前に窒素ガスバブリングにより溶存酸素をパージしているが，時間と共に徐々に溶存酸素が増加する．超音波による攪拌はそれを促進し，また，無攪拌時には水素膜で保護されていためっき部位への溶存酸素の吸着を顕著に増大させるだろう．実際，超音波照射下のめっきプローブで，ニッケル膜のグレインが微細化し，またサブミクロン領域でサイズ効果を生むような堆積速度の変化が生じていることは，溶存水素保護膜を通り抜けた酸素が吸着し，水素が比較的効率よく拡散する先端部でめっきを抑制することを予想させる．すなわち，上記の超音波攪拌の結果は，水素保護層の拡散と溶存酸素の吸着の両方を促進させた複合的なものであると考えられる．大気中めっきで溶存酸素の連続パージを行うため，窒素ガスバブリングと超音波攪拌を併用しながら行った例では，グレインの微細化が生じず，ミクロンレベルのサイズ依存性が生じる一方で，最先端部で

は堆積速度の増加が確認された．今後，直径 40nm 以下の小さなティップを形成するためには，物理的攪拌に加えて，溶存酸素のような抑制種の添加とその濃度制御がより効果的であると考えられる．

4　まとめ

近接場光学顕微鏡用プローブを作製するため開発した，メガヘルツ超音波攪拌を用いる無電解ニッケルめっき法について概説した．この手法により，先端径 40nm 以下でテーパー化プローブの先端に向かってニッケル膜厚が減少する構造を持つ伝播光遮断型プローブを作製することに成功した．今後，ナノオーダーのめっき制御を目指して，溶存気体制御下で超音波攪拌とめっき抑制化学種添加を組み合わせるなどの複合技術により，膜厚減少部位での膜厚プロファイルの制御精度をサブミクロンからサブサブミクロンに向上させることを目指す．

[参考文献]

1) ナノ光工学ハンドブック，大津元一，河田聡，堀裕和 編，(朝倉書店, 2002)．
2) S. Mononobe, In: *Progress in Nano-Electro Optics* Ⅲ, M. Ohtsu it ed., (Springer-Verlag, Berlin, 2005), Chap. 1.
3) 物部秀二，博士学位論文，(東京工業大学，1999), http://www.kast.or.jp/Mononobe.pdf.
4) S. Mononobe, Y. Saito, M. Ohtsu, H. Honma, *Jpn. J. Appl. Phys.*, **43** (5B), 2862–2863 (2004).
5) T. Kobayashi, J. Ishibashi, S. Mononobe, M. Ohtsu, H. Honma, *J. Electrochem. Soc.*, **147**(3), 1046–1049 (2000).

解説

ナノ物質間の近接場光相互作用の研究と展開

科学技術振興機構 SORST　川添　忠
東京工業大学大学院理工学研究科　小林　潔
東京大学大学院工学系研究科，科学技術振興機構 SORST　大津元一

§1　はじめに

1959年，R. P. ファインマンは世に先駆け「ナノスケール領域には研究すべき多くの余地がある.」と言う趣旨の講演を米国物理学会で行いナノスケールの物理の重要性を提唱した[1]．最近では，ナノテクノロジーという言葉が一般化し，ナノスケールの様々な研究が行われ，「ナノテクにより」と形容されるような製品を目にすることも少なくない．これらの多くはナノスケールの領域に現れる物理現象を利用している．物質のサイズを電子のコヒーレンス長より小さくしていくと物質中に局在した電子のエネルギーは離散化し，バルク結晶の物性とは異なる特異な特性，たとえば，負性抵抗[2]，量子トンネル効果[3]，非線形性の増大などが現れる．このようなナノ構造の光物性研究を基に光エレクトロニクス分野たとえば，光スイッチ・レーザーをはじめとする光学非線形デバイス[4]などの研究が進展している．また，何らかの相互作用で結合した複数個のナノ構造が示す特性は単独で存在する場合に比べ，より興味深く，応用にも適した特性を持つことがある．多くのナノ構造を周期的に並べることによって作られる超格子やフォトニック結晶，あるいは，結合した少数個のナノ構造を利用したクーロンブロッケード単電子トランジスタ[5]などがその例である．このように，物質をナノ寸法化することの恩恵は計り知れない．それらは既に光の波長と比べ遥かに小さい．しかしながら主要な相互作用の媒介となる光の波長はナノ寸法と言うには大き過ぎ，従来の光技術では回折限界のため，波長程度あるいはそれを物質の屈折率で割った程度の大きさの系の制御しかできない．われわれは世界に先駆けて近接場光による光のナノ寸法化に取り組んできた．そして，最近の研究によって，光のナノ寸法化は物質のナノ寸法化に劣らない恩恵をもたらすと思われる興味深い結果を得ている．本稿では，光の波長に比べ十分に小さい領域に隣接した少数個のナノ物質が光電磁場を介してどのように相互作用(近接場光相互作用)するか[6~9]，またそれに伴って生じるナノ物質間のエネルギー移動について論じ，関連する実験結果を紹介する．最後に，近接場光を応用する技術，ナノフォトニクスを利用したナノ寸法光デバイス(ナノフォトニックデバイス)[6]について簡単に紹介する．

まず，ナノ微粒子間に働く“光”を介した相互作用を考える．電気双極子相互作用が電気的に中性なナノ微粒子間に働く相互作用の中で最も大きいことから，ここでは，電気双極子相互作用のみを仮定する．第1図に光の波長より十分に小さい2つの中性なナノ微粒子を示す．これらは，外部から光(時間依存性 $e^{-i\omega t}$ は省略する)を照射されている，あるいは自ら発光しているとする．微粒子間の中心距離 r が微粒子のサイズに比べ十分に大きい場合，第1図(a)に示すように，ナノ微粒子間に働く相互作用はそれぞれの位置を微粒子の中心位置で代表し，それぞれの電気双極子モーメント $\boldsymbol{p}_1$ と $\boldsymbol{p}_2$ を用いて，相互作用ポテンシャルエネルギーを

$$U=\frac{(\boldsymbol{p}_1\cdot\boldsymbol{p}_2)r^2-3(\boldsymbol{p}_1\cdot\boldsymbol{r})(\boldsymbol{p}_2\cdot\boldsymbol{r})}{r^5} \qquad (1)$$

と表わすことができる．一方，微粒子間の距離が微粒子サイズと同程度に小さくなった場合，第1

図(b)に示すように，もはや微粒子位置をその中心位置で代表できない．つまり，電気双極子モーメントを微粒子中の場所に依存する $\boldsymbol{P}_1(r_j)$, $\boldsymbol{P}_2(r_j)$ としなければならない．それに伴い相互作用ポテンシャルエネルギーはそれぞれの微小空間の相互作用を足し合わせたものにする必要があり，(1)式を用いるような相互作用の表現では見通しが悪くなる．言い換えれば，光と近接したナノ物質の相互作用を考える場合，通常は無視される電気4重極相互作用や磁気双極子相互作用も無視できなくなるということである．この理由をもう少し議論しよう．光の周波数 ω は約10^{15} Hz と大変高いため，光と物質の相互作用では，主に物質中の電子が光の振動電場により摂動を受ける．物質中の束縛電子がこの摂動により遷移する場合を考えると，光と電子の相互作用ハミルトニアン H' は

$$H' = -\frac{e}{mc}\sum_i \boldsymbol{A}(r_i, t)\cdot \boldsymbol{p}_i \qquad (2)$$

によって与えられる．ここで，$\boldsymbol{A}$ はベクトルポテンシャル，$\boldsymbol{p}_i$ は電子の運動量である．このような摂動により電子が状態 $|\Psi_m\rangle$ から $|\Psi_n\rangle$ に遷移する確率 P_{nm} は

$$P_{nm} = \frac{4\pi}{(\hbar\omega)^2}\frac{e}{m}I(\omega)\,d\omega \times f_m\left|\langle\Psi_n|\sum_i p_{iz}\exp(ikx)|\Psi_m\rangle\right|^2 \qquad (3)$$

で与えられる．ここでは簡単のため x 方向に伝搬する光により z 方向に電子が分極する場合を考えている．また I は電子の密度である．絶対値の中に着目し，級数展開をすると

$$e^{ikx}p_z = -i\hbar\frac{\partial}{\partial z} + \frac{\hbar k}{2}\left(x\frac{\partial}{\partial z} - z\frac{\partial}{\partial x}\right) + \frac{\hbar k}{2}\left(x\frac{\partial}{\partial z} + z\frac{\partial}{\partial x}\right) + \cdots\cdots \qquad (4)$$

となる．第1項目は電気双極子遷移に，第2，第3項目はそれぞれ，磁気双極子遷移，電気4重極遷移に相当する部分である．真空中を伝搬する光の波数が $k = 2\pi/\lambda$ であること，電子の広がりが原子サイズもしくはナノ微粒子サイズであることを考慮すると，電気双極子遷移成分の大きさに比べ，磁気双極子・電気4重極遷移の大きさが無視できるほど小さいことがわかる．このため，通常，

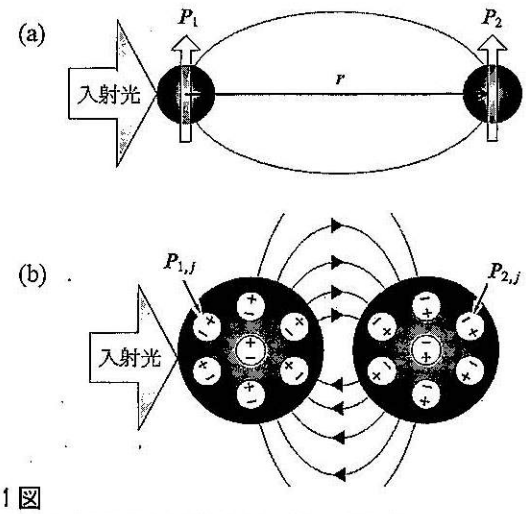

第1図
電磁相互作用で結合する二つのナノ物質．
(a) 二つのナノ物質が光の波長より離れている場合．
(b) ナノ物質の寸法程度に近接している場合．

光と物質の相互作用を考えるとき，電気双極子遷移に起因する光学定数のみを考慮する立場で考えることが多い．ここでもう一度，第1図(b)を見てもらいたい．図中にはすべての電気力線を記しているわけではないが，電気力線の一部は一方のナノ微粒子を出発し，他方のナノ微粒子を通過し，元の位置に戻る輪を作っていることがわかる．これは局在した光の成分を表わしておりその波数はナノ微粒子間の距離の逆数程度になり，第1図(b)の場合おおよそナノ微粒子サイズの逆数程度の大きさを持つ波数の光が存在することになる．すなわち，(4)式において真空中を伝搬する光とマクロな物質の相互作用では無視できた磁気双極子遷移，電気4重極遷移に相当する項が，近接するナノ物質の場合，電気双極子遷移の項と同程度の大きさを持つ．また(4)式の級数展開の高次の項に関しても同様に電気双極子相互作用と同程度の大きさを持ちえる．加えて，われわれが通常扱うナノ微粒子は真空中に浮かんでいるわけではない．第2図に示すように相互作用をするナノ微粒子の周辺にはナノ微粒子を固定する基板や母結晶が存在する．このようなナノ微粒子周辺の環境がナノ微粒子間の相互作用に影響を与えるため，(1)式に代表されるような点双極子近似や長波長近似など通常の手法を直接適用することはできない．以上に述べた理由から，ナノ微粒子を用

いた実験結果を厳密に議論することは難しく，新しい物理現象の発見や予測のために，より直感的に，ナノ物質間に働く相互作用を理解し，それを用いて算出した物理量が実験結果と容易に比較できることが望まれる．われわれは第1図(b)や第2図に描かれているナノ微粒子に張り付いて伝搬しない光の成分を近接場光と定義し，この近接場光を介した相互作用を湯川関数で表わされる“有効相互作用”の方法によって取り扱うことを提案している．

§2　有効相互作用

簡単のために第2図に示すように(a)母結晶中に二つのナノ微粒子(微粒子S，微粒子P)が近接して存在する場合，あるいは，(b)基板上に存在する場合を考える．図中の微粒子Sは外部からの光により励起され(外部からの光は微粒子Sを励起後，取り除く)，それによって生じる近接場光

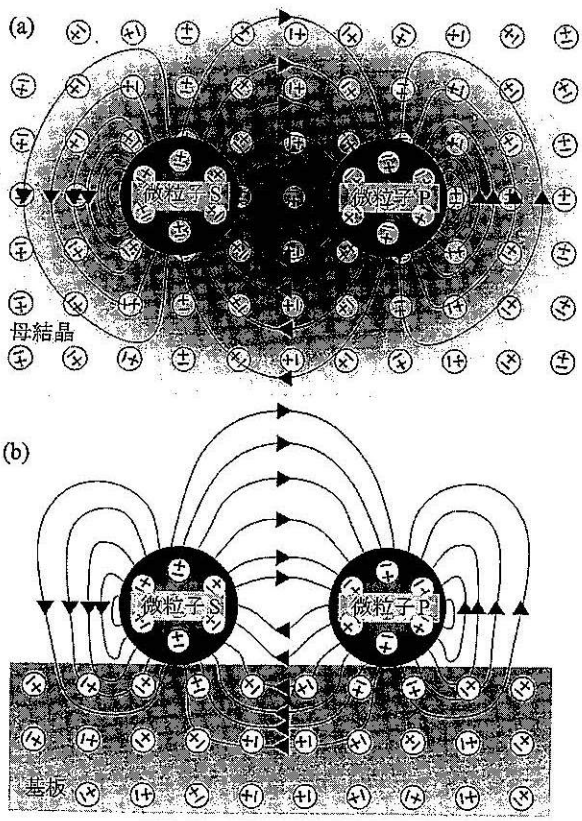

第2図
電磁相互作用により結合するナノ物質と周囲の環境．(a) 母結晶中，(b) 基板上．

により微粒子Pと電磁相互作用している．微粒子間に働く相互作用を厳密に取り扱うためには，環境としての母結晶や基板の振舞いも同時に取り込まなければならない．また，このような系を観測する場合，検出器までを系に含める必要がある．しかし，興味があるのは微粒子間に働く相互作用であるから，環境の影響を取り込んで二つの微粒子間の相互作用として表現することを試みる．

二つの微粒子SとPが独立に存在するときのエネルギー固有状態ベクトルを $|S\rangle, |P\rangle$ と表わす．さらにそれぞれの基底状態および励起状態を添字g, eを用いて表わし，それぞれ $|S_g\rangle, |S_e\rangle$，および $|P_g\rangle, |P_e\rangle$ と書く．この系で取り扱いたいのは微粒子S, Pが相互作用により，励起をお互いに受け渡しあう状態である．すなわち，二つの微粒子が取り得る状態は $|S_e\rangle, |P_g\rangle$ または $|S_g\rangle, |P_e\rangle$ である．二つの微粒子以外の空間は微粒子が生成する近接場光や散乱光の場に関係しているので物質励起と電磁場の混成状態である励起子ポラリトンとして記述し，$|m; k, \Omega(k)\rangle$ と表わす．ここで，$m, k, \Omega(k)$ はそれぞれポラリトンの個数，波数，角周波数である．二つの状態 $|\phi_1\rangle = |S_e\rangle|P_g\rangle|0; k, \Omega(k)\rangle$ および $|\phi_2\rangle = |S_g\rangle|P_e\rangle|0; k, \Omega(k)\rangle$ の二つの状態で構成されるP空間($=\{|\phi_1\rangle, |\phi_2\rangle\}$)に関する有効相互作用を求める．励起子ポラリトンの真空状態 $|0; k, \Omega(k)\rangle$ を取り入れることによって，われわれの興味のないQ空間(P空間の補空間)の影響は取り入れるが，その自由度は消去し，興味の対象である系があたかも周囲から独立しているかのように取り扱うわけである．すなわち，二つの微粒子と環境(母結晶や基板)の各要素間に働いていた相互作用を考える代わりに，二つの微粒子のみが存在しその要素間に環境の影響を含んだ有効相互作用が働くと見なせるように矛盾のない表現を求めようというわけである．微粒子S, Pと電磁場との相互作用ハミルトニアンは(2)式をPower-Zienau-Woolley変換することにより

$$\hat{V} = -\{\hat{p}_S \cdot \hat{D}(r_S) + \hat{p}_P \cdot \hat{D}(r_P)\} \qquad (5)$$

となる．このハミルトニアンの利点は横波光子だけを媒介することによりリタデーションを正確に記述し，しかも静的クーロン相互作用を含まない

で見やすい形に表わせることである．(5)式中の添字のP, Sは微粒子P, Sを表わし，$\hat{p}$は微粒子に誘起される電気双極子，rは微粒子の位置，$\hat{D}(r)$は電束密度を表わす．$\hat{D}(r)$は光子の生成消滅演算子$\hat{a}_\lambda^\dagger(k)$, $\hat{a}_\lambda(k)$を用いて(λは入射光の偏光状態を表わす添字)

$$\hat{D}(r)=\sum_k\sum_{\lambda=1}^{2}\left(\frac{2\pi\hbar\omega_k}{V}\right)^{1/2}e_\lambda(k)\times\{\hat{a}_\lambda(k)e^{ik\cdot r}-\hat{a}_\lambda^\dagger(k)e^{-ik\cdot r}\}\qquad(6)$$

と表わすことができる．ここで，k, ω_k, V, $e_\lambda(k)$はそれぞれ，光子の波数ベクトル，光子の角周波数，今考えている電磁場の存在する空間の体積，光子の偏光方向を表わす単位ベクトルである．(6)式を励起子ポラリトンの生成消滅演算子$\hat{\xi}^\dagger(k)$, $\hat{\xi}(k)$で書き換えた後，(5)式に代入すると

$$\hat{V}=-i\left(\frac{2\pi\hbar}{V}\right)^{1/2}\sum_{\alpha=\mathrm{S}}^{\mathrm{P}}(\hat{B}(r_\alpha)+\hat{B}^\dagger(r_\alpha))\times\sum_k(K_\alpha(k)\hat{\xi}(k)-K_\alpha^*(k)\hat{\xi}^\dagger(k))\qquad(7)$$

となる．ただし，

$$K_\alpha(k)=\sum_{\lambda=1}^{2}(p_\alpha\cdot e_\lambda(k))f(k)e^{ik\cdot r_\alpha}=\sum_{j=1}^{3}\sum_{\lambda=1}^{2}p_{\alpha j}(e_j\cdot e_\lambda(k))f(k)e^{ik\cdot r_\alpha}\qquad(8)$$

$$f(k)=\frac{ck}{\sqrt{\Omega(k)}}\sqrt{\frac{\Omega^2(k)-\Omega^2}{2\Omega^2(k)-(ck)^2-\Omega^2}}\qquad(9)$$

であり，$p_{\alpha j}$, e_jはそれぞれ，微粒子に誘起される電気双極子p_αのx, y, z軸方向成分，x, y, z方向の単位ベクトルである．また，電気双極子演算子$\hat{p}_\alpha$に含まれる生成消滅演算子を$\hat{B}^\dagger$, $\hat{B}$とし，$K_\alpha(k)$, $K_\alpha^*(k)$は二つの微粒子と励起子ポラリトンで表わされる環境との結合の強さを表わす係数とその複素共役，cは真空中の光速，$\hbar\Omega(k)$は励起子ポラリトンのエネルギー固有値，$\hbar\Omega$は環境を構成する物質中の電子のエネルギー固有値である．

ここで(7)式の$\hat{V}$に対し，射影演算子の手法を用いると環境の影響を取り込んだ任意のP空間での有効相互作用演算子$\hat{V}_{\mathrm{eff}}$は

$$\hat{V}_{\mathrm{eff}}=(P\hat{f}^\dagger\hat{f}P)^{-1/2}(P\hat{f}^\dagger\hat{V}\hat{f}P)(P\hat{f}^\dagger\hat{f}P)^{-1/2}\qquad(10)$$

となる．ここでPは射影演算子で，今仮定したP空間を構成する状態ベクトル$|\phi_1\rangle$, $|\phi_2\rangle$を用いると

$$P=|\phi_1\rangle\langle\phi_1|+|\phi_2\rangle\langle\phi_2|\qquad(11)$$

により定義される．演算子$\hat{f}$はP空間と相互作用$\hat{V}$により結ばれる補空間Q($Q=1-P$)に関する演算子で，

$$\hat{f}=[1-(E_j-\hat{H}_0)^{-1}Q\hat{V}]^{-1}\qquad(12)$$

と書け，ゼロとならない最低次は

$$\hat{f}=(E_P{}^0-E_Q{}^0)^{-1}Q\hat{V}P\qquad(13)$$

となる．$\hat{H}_0$は系が孤立しているときのハミルトニアン，$\hat{V}$は相互作用ハミルトニアンであり，E_jは$\hat{H}=\hat{H}_0+\hat{V}$のエネルギー固有値，$E_P{}^0$および$E_Q{}^0$は$\hat{H}_0$の固有関数$|\phi_j\rangle$を使って$\hat{H}_0P|\phi_j\rangle=E_P{}^0P|\phi_j\rangle$, $\hat{H}_0Q|\phi_j\rangle=E_Q{}^0Q|\phi_j\rangle$となる固有値である．(10)式で表わされる相互作用の大きさは始状態を$|\phi_1\rangle=|S_e\rangle|P_g\rangle|0;k,\Omega(k)\rangle$, 終状態を$|\phi_2\rangle=|S_g\rangle|P_e\rangle|0;k,\Omega(k)\rangle$として，

$$V_{\mathrm{eff}}(ps)=\langle\phi_2|\hat{V}_{\mathrm{eff}}|\phi_1\rangle\qquad(14)$$

となる．ここで，(13)式を(14)式に代入すると

$$\begin{aligned}V_{\mathrm{eff}}(ps)&=\langle\phi_2|[P\hat{V}Q(E_P{}^0-E_Q{}^0)^{-1}\hat{V}P+P\hat{V}(E_P{}^0-E_Q{}^0)^{-1}Q\hat{V}P]|\phi_1\rangle\\&=2\langle\phi_2|[P\hat{V}Q(E_P{}^0-E_Q{}^0)^{-1}\hat{V}P]|\phi_1\rangle\\&=2\langle\phi_2|[P\hat{V}Q|m\rangle\langle m|Q(E_P{}^0-E_Q{}^0)^{-1}\hat{V}P]\times|\phi_1\rangle\end{aligned}\qquad(15)$$

となる．(15)式第3行目の行列要素のうち$\langle m|Q(E_P{}^0-E_Q{}^0)^{-1}\hat{V}P|\phi_1\rangle$はP空間の初期状態$|\phi_1\rangle$からQ空間の中間状態$|m\rangle$への仮想遷移が起きること，また$\langle\phi_2|P\hat{V}Q|m\rangle$は続いてその中間状態$|m\rangle$からP空間の終状態$|\phi_2\rangle$への仮想遷移が起きることを表わしている．また，Q空間の中間状態$|m\rangle$のうち，微粒子を取り巻く環境に関しては運動量$\hbar k$を持つ励起子ポラリトンが1個存在する状態$|1;k,\Omega(k)\rangle$のみが，0でないV_{eff}を与えることに着目すると

$$V_{\mathrm{eff}}(ps)=-\frac{4\pi}{(2\pi)^3}\int d^3k\left[\frac{K_p(k)K_s^*(k)}{\Omega(k)-\Omega_0(s)}+\frac{K_s(k)K_p^*(k)}{\Omega(k)-\Omega_0(p)}\right]\qquad(16)$$

となる．以下の解析解を得るためには必ずしも必要ではないが，計算を簡略化するために((23)-(26)式参照)，(16)式に以下の3つの付加条件を課す．

① 二つの微粒子のエネルギー固有値をそれぞれ

$\hbar\Omega_0(p)$, $\hbar\Omega_0(s)$と表わし，それぞれ幅a_p, a_sの無限井戸型ポテンシャル中の電子のエネルギー固有値で最小の値に対応すると考える．

$$\hbar\Omega_0(p)=\frac{3\hbar^2}{2m_{ep}}\left(\frac{\pi}{a_p}\right)^2 \tag{17}$$

$$\hbar\Omega_0(s)=\frac{3\hbar^2}{2m_{es}}\left(\frac{\pi}{a_s}\right)^2 \tag{18}$$

である．ここで，m_{ep}, m_{es}はそれぞれ微粒子P，微粒子Sのポテンシャル内に束縛された電子の有効質量である．

② $\Omega(k)$の値のk依存性は励起子ポラリトンの分散関係に対応するが，これをkの二次関数で近似し

$$\hbar\Omega(k)=\hbar\Omega+\frac{(\hbar k)^2}{2m_p} \tag{19}$$

とする．ここでm_pは励起子ポラリトンの有効質量である．

③ (9)式の$f(k)$はほぼ定数と見なせるのでK_p, K_sを表わす(8)式中の$e^{ik\cdot r_\alpha}$の項以外は定数とする．

以上の①～③を用いて(16)式を積分すると

$$V_{\mathrm{eff}}(ps)\propto\frac{\exp\left(-\dfrac{\pi\mu_p r}{a_p}\right)}{r}+\frac{\exp\left(\dfrac{i\pi\mu_s r}{a_s}\right)}{r} \tag{20}$$

となる．ここで，

$$r=|r_p-r_s|,\quad \mu_p=\frac{\sqrt{3}\,m_p}{m_{ep}},\quad \mu_s=\frac{\sqrt{3}\,m_s}{m_{es}}$$

であり，近接領域において(20)式の第1項が支配的となり，近接領域での有効相互作用が湯川関数によって表わせることがわかった．なお，第2項は指数の中に虚数を含み，伝搬していく光の成分(伝搬光)に対応する．(20)式の近接場光の成分だけを取り出すと近接した二つのナノ微粒子に働く電磁相互作用(以下では近接場光相互作用と呼ぶ)は

$$V_{\mathrm{eff}}(ps)=A\frac{\exp(-\mu r)}{r} \tag{21}$$

のように単純化でき，(20)式中のAやμを実験結果あるいは微粒子を構成する材料の物性値，母結晶や基板材料の物性値から求めることによって，相互作用の大きさを簡単にそして，直感的に求めることができる．このように近接した微粒子間の電磁相互作用が(20)式の湯川関数で表わされたということはその相互作用は有効質量μを持つポラリトンの交換によって起きていること意味する．また，(21)式を級数展開するとわかるように，

$$V_{\mathrm{eff}}(ps)=\sum_{j=1}^{\infty}a_j r^{-j}$$

の形になっており，電気多重極相互作用や磁気双極子相互作用など高次の電磁相互作用を取り込んでいることがわかる．複雑なナノ微粒子間の相互作用を(21)式のように単純化できることは，特に実験に際しては，実験結果の解釈や結果の予測[10]，またナノ微粒子をナノフォトニックデバイス[11,12]などに応用する場合大変有用である．これは，物質中の電子や正孔，励起子の振舞いを記述する際，それらの運動エネルギーの分散を有効質量によって扱うことが，厳密さにはかけるが有効であるのと同じである．

§3 量子ドット間のエネルギー移動の観測

次に近接場光相互作用を介したナノ物質間の励起エネルギー移動の観測に触れておこう．以前より近接場光相互作用が関与していると思われるエネルギー移動の研究が行われてきた．たとえば，光合成バクテリアにおけるLH1やLH2と呼ばれる光捕獲アンテナ中の分子間のエネルギー移動は点双極子相互作用では説明がつかず，近接した多重極間相互作用を用いて説明されている[13]．量子ドット間のエネルギー移動に関してはBawendiらによってCdSe量子ドット間の静的双極子相互作用によるエネルギー移動が論じられている[14]．最近ではわれわれの研究[10]が種になり，Klimovらのグループから制御されたサイズを持つ量子ドット間のエネルギー移動の研究が報告されている[15]．近接場光相互作用によるエネルギー移動を観測するためには，隣接する量子ドット間隔が光の波長と比べ十分に小さいが，量子ドット中に存在する電子の波動関数の広がりによって近接した量子ドットが結合状態を形成しない必要がある．以下では近接場分光法を用いたエネルギー移動観測に関するわれわれの実験結果を紹介する．

われわれがエネルギー移動の観測に用いた試料

はNaCl結晶中に成長させた立方体形状のCuCl量子ドットである[16]．このCuCl量子ドットは1辺約2 nm–10 nmの大きさを持ち，量子ドット密度はCuClの濃度によって制御可能であり，典型的な量子ドット間平均距離は10 nm–30 nmである．また，CuClのバンドギャップ3.4 eVに対しNaClは7.3 eV以上のバンドギャップを持ち，CuCl量子ドット中の電子はほぼ無限井戸に閉じ込められた状態と見なしてよい．これらの特性からNaCl結晶中のCuCl量子ドットは量子ドット間に起きる近接場光相互作用を介したエネルギー移動の観測に適している．CuCl量子ドットではバンド端吸収はZ_3励起子によって形成される．そしてCuCl量子ドットの形状が立方体である場合，1辺Lの量子箱に閉じ込められたZ_3励起子は，

$$E_{n_x,n_y,n_z}=E_B+\frac{\hbar^2\pi^2}{2M(L-a_B)^2}(n_x^2+n_y^2+n_z^2) \tag{22}$$

で示されるような離散的なエネルギー準位をもつ．ここでE_Bはバルク結晶におけるZ_3励起子のエネルギー，Mは励起子の有効質量，n_x, n_y, n_z (=1, 2, 3, …)は主量子数である．また，a_Bは励起子のボーア半径であり，CuClのZ_3励起子では，0.68 nmである．量子ドットのサイズから励起子のボーア半径を引いたサイズ$L_{eff}=L-a_B$は有効サイズと呼ばれる．さて，**第3図**(a)に示すように同じサイズの量子ドットが隣接している場合を考えると，量子ドット中の励起子のエネルギー準位は共鳴する．もし一方の量子ドットに励起子を生成したとすると(21)式で与えた近接場光相互作用により，二つの量子ドットは相互作用し，その相互作用の大きさに相当するラビ周波数で二つの量子ドットの間に章動が起こる．この周期は量子ドットのサイズを1辺5 nmとし，間隔が10 nmである場合，およそ100 psとなる[10,17]．これは5 nmのCuCl量子ドット中の励起子寿命約2 nsに比べ十分に短く観測可能である．しかしながら，この状態は単に近接場光相互作用によって結合した二つの量子ドットが作る結合準位を励起しただけであり，緩和過程を経て初めて量子ドット間のエネルギー移動が起こる．

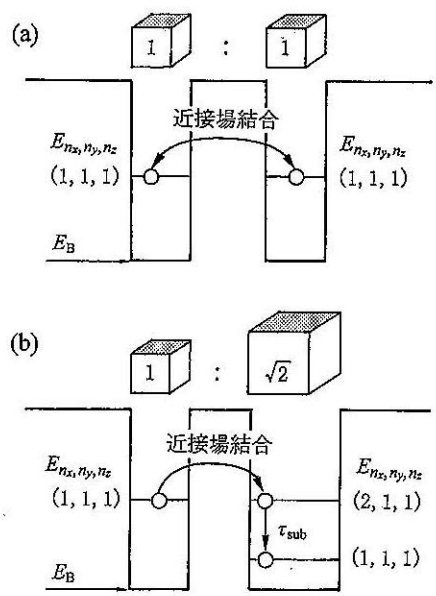

第3図
近接場光相互作用により，結合した二つの立方体形状をした量子ドット．
(a) 二つの量子ドット寸法が同じ場合．
(b) 寸法比が$1:\sqrt{2}$の場合．

次に第3図(b)に示すように量子ドットの有効サイズ比が$1:\sqrt{2}$の場合を考える．この場合，量子ドットaの励起子基底準位$E_{1,1,1}$と量子ドットbの励起子第一励起励起子準位である$E_{2,1,1}$が共鳴する．この場合，量子ドットaに励起子を生成すると励起エネルギーのほとんどは近接場光相互作用によって量子ドットbに移動し，再び量子ドットaに戻る確率は小さい．なぜなら，量子ドットbの励起準位に移動した励起子は量子ドットaに戻る前に10 ps以下の時定数を持つサブレベル間緩和[18]によって，量子ドットbの$E_{1,1,1}$準位に緩和するからである．そして，量子ドットbの$E_{1,1,1}$と共鳴する準位が量子ドットaには存在しないため，量子ドットbに移動した励起子はそのまま量子ドットb中で再結合発光し消滅する．このように量子ドットaに与えたエネルギーは量子ドットbに移動し緩和することにより小さい量子ドットから大きい量子ドットにエネルギー移動が起こる．このような励起エネルギー移動は光合成バクテリアにおける光捕獲アンテナに含まれる分子B800からB850そしてB875へと小さい分子から大きい分子へ励起エネルギーが移動するのと同じ形態である．ここで，立方体形状の量子ドットでは$E_{2,1,1}$準位は光学(電気双極子)禁制であることに注目して欲しい．すなわち，ここ

で説明したエネルギー移動は通常の光を介した発光–再吸収の過程では起こらない，近接場光相互作用によって初めて生じる物理現象である．

実際に実験で使用したCuCl量子ドットは，厚さ約100 μmのNaCl結晶中に成長させたものであり，吸収スペクトルから求めた平均サイズは立方体形状1辺4.3 nmであった．励起子のサブレベルを分離し，解析を容易にするため15 Kにて測定を行った．励起光源にはHe-Cdレーザー(λ=325 nm)を用いた．第4図(a)に用いた試料の発光スペクトルを示す．この発光スペクトルは非常に多数のCuCl量子ドットの発光によるものであり，そのスペクトル幅は量子ドットのサイズ不均一性に起因して広がっている．エネルギー移動の検証実験のためには高い空間分解能が必要である．われわれはこの試料の背面から励起を行い，近接場分光顕微鏡によって試料の発光スペクトルの分布を観測した．プローブは第4図(b)挿入図の電子顕微鏡像に示すような光ファイバーをエッチングによって先鋭化させ，表面に金属コートを施したプローブを用いた．プローブ先端には50 nm程度の開口を作製しており，この開口サイズが空間分解能を与える．第4図(b)に典型的な近接場分光顕微鏡によるスペクトル観測結果を示す．空間分解能が上がることによりスペクトル中に含まれるCuCl量子ドットの個数が減少する．実験に用いた試料では非常に高密度(0.1 mol～1 mol%)に量子ドットが分散されているが，開口50 nmのプローブを用いることで数個～20個程度の量子ドットからの発光を反映したスペクトルが観測できる．このスペクトルは(22)式で表わされる$E_{1,1,1}$の準位からの発光に対応し，各量子ドットのサイズによって発光波長が異なる．たとえば，第4図(b)中A, Bのピークはそれぞれ4.6 nm, 6.3 nmのCuCl量子ドットからの発光に対応する．またこのサイズの量子ドットは近接場光を介した共鳴エネルギー移動が観測される条件を満たし，有効サイズ比はほぼ$1:\sqrt{2}$である．すなわち，4.6 nmのCuCl量子ドットの励起子基底準位$E_{1,1,1}$

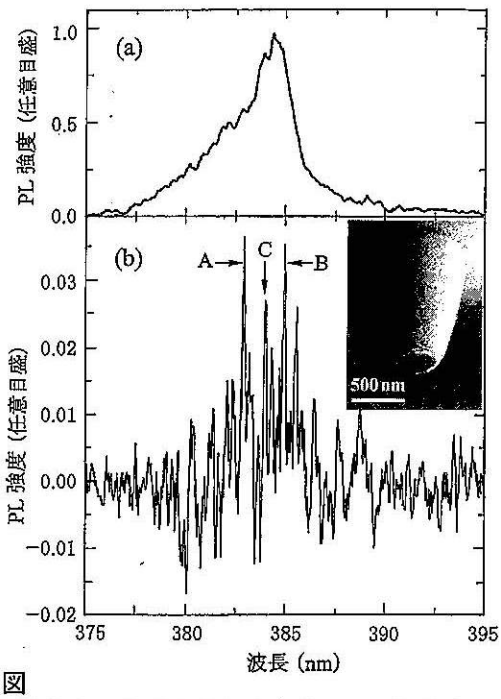

第4図
NaCl結晶中に成長させた立方体CuCl量子ドットの発光スペクトル．
(a) 伝搬光による測定．
(b) 近接場光分光顕微鏡による測定；A, B, Cのピークは：4.6 nm, 6.3 nm, 5.3 nmの寸法を持つ量子ドットからの発光，挿入図は光ファイバーを先鋭化し金属コートを施して作製したプローブのSEM像．

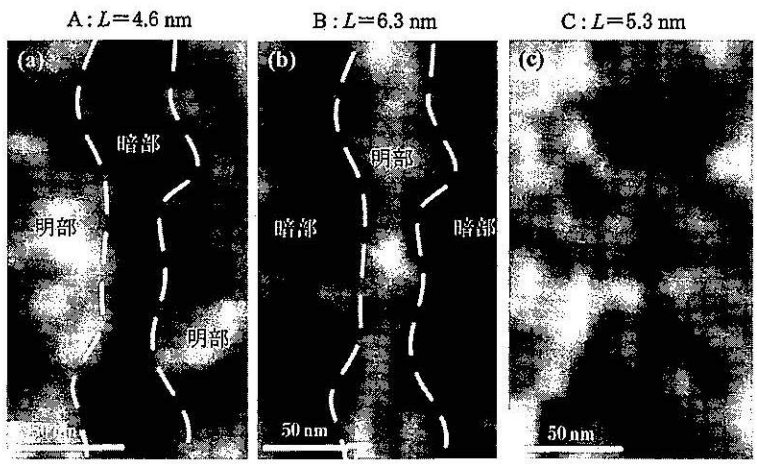

第5図
CuCl量子ドット試料の近接場顕微鏡による発光強度分布．
(a) 寸法4.6 nmの量子ドットの発光(第4図(b)のピークA)の強度分布．
(b) 寸法6.3 nmの量子ドットの発光(第4図(b)のピークB)の強度分布．
(c) 寸法5.3 nmの量子ドットの発光(第4図(b)のピークC)の強度分布．

と 6.3 nm の量子ドットの励起子励起準位 $E_{2,1,1}$ は共鳴している．

第 5 図(a)，(b)に A，B 各々の発光ピークの空間強度分布を測定した結果を示す．図中破線で分けられた領域に注目すると発光強度分布が反転しているように見える．実験に使用した試料の量子ドットの平均サイズが 4.3 nm であるので，4.6 nm のサイズの量子ドットは 6.3 nm の量子ドットに比べ圧倒的に多数存在する．偶然，近接領域に 6.3 nm の量子ドットが存在する 4.6 nm の量子ドットは発光できずにエネルギーを 6.3 nm の量子ドットへ受け渡す結果，暗い領域ができ，その領域では 6.3 nm の量子ドット発光が強くなっていると考えられる．すなわち，この発光強度分布の反相関はサイズ 4.6 nm の量子ドットから 6.3 nm の量子ドット中の双極子禁制準位 $E_{2,1,1}$ を介してのエネルギー移動が起きたことを示している．一方，第 5 図(c)に示すように，このような強度分布の相関は共鳴関係を満たさないサイズ 5.3 nm の量子ドット(第 4 図(b)のピーク C)からの発光強度分布では見られなかった．このような発光強度の空間分布の相関強度を表わしたのが **第 6 図** である．図中の縦軸と横軸は発光波長，明暗が相関強度を表わしている．縦軸と横軸の波長が同じ場所は自己相関になるので相関強度は 1 になる．また，相関強度 0 以下は反相関を意味する．図中の白破線はお互いに共鳴準位を持つ量子ドットの発光波長位置を表わしており，$(n_x, n_y, n_z)-(n_x, n_y, n_z)^*$ は共鳴する励起子準位を意味する．破線に沿った領域に強い反相関が現れている．このような反相関性は単なる量子ドットの空間分布だけでは説明できず，量子ドット間エネルギー移動が起きた証拠となる[10]．

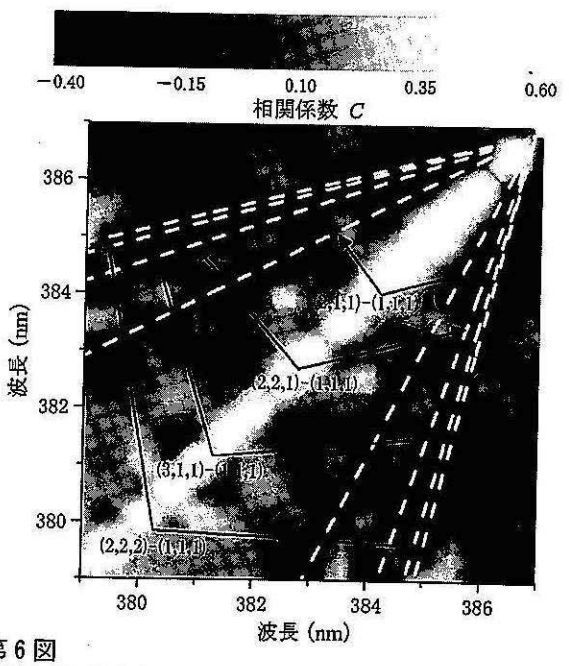

第 6 図
発光の強度分布の相関強度；横軸と縦軸はそれぞれ発光強度分布を測定した波長グレースケールで空間強度分布の相互相関強度を表わしている．相関強度 1 は完全に同じ分布を意味し，−1 は完全反相関を意味する．

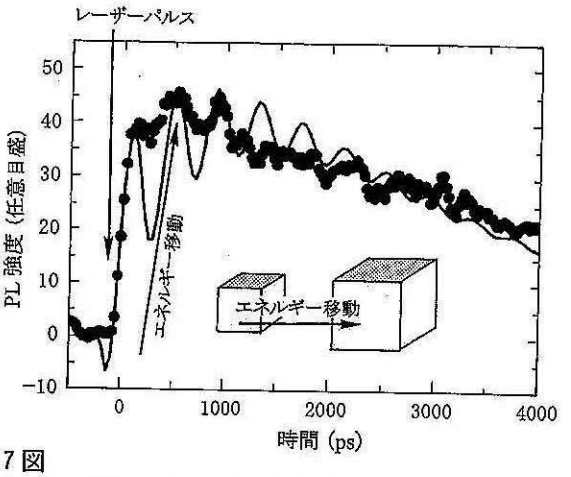

第 7 図
量子ドット間のエネルギー移動時間分解測定．
●：測定結果，実線：計算結果(相互作用 $U=20\,\mu$eV)．

第 7 図はエネルギー移動の時間発展を観測した結果である[17,19]．時刻 0 においてパルス幅 10 ps の励起光パルスが入射している．測定はサイズ 4.6 nm と 6.3 nm の CuCl 量子ドットが近接場相互作用が支配的になる距離にある系で行った．図中の縦軸は 6.3 nm の量子ドットに流れ込む励起子密度に対応している．図中の●は観測結果を，実線は近接場光相互作用 $U=20\,\mu$eV を与えたときのエネルギー移動の時間発展を計算した結果である．実験結果と計算結果はよく一致しており，両者はパルス光入射とともに立ち上がる．この立ち上がり時間がエネルギー移動に要する時間である．ピークを迎えた後，僅かに振動しながら信号は励起子の再結合によって減少する．僅かに観測される振動は二つの量子ドット間に生じる章動現象に対応し，計算と実験結果はこの点でもよく一致している．ここで有効相互作用 V_{eff}((14)式)を用

いて r だけ空間的に離れている二つの量子ドットに働くこの計算に用いた近接場光相互作用 $U(r)$ を示す．始状態，終状態を $|\phi_1\rangle=|A_e\rangle|B_g\rangle|0;k,\Omega(k)\rangle$, $|\phi_2\rangle=|A_g\rangle|B_e\rangle|0;k,\Omega(k)\rangle$ とする．ここで $|A_g\rangle$, $|A_e\rangle$ および $|B_g\rangle$, $|B_e\rangle$ はそれぞれ，4.6 nm の量子ドットに励起子がない真空状態，励起子基底状態と 6.3 nm の量子ドットの真空状態，励起子励起状態の 4 つに対応する．また，ここでは $|0;k,\Omega(k)\rangle$ は NaCl 結晶中の励起子ポラリトンを表わしており，その個数が 0 であることを意味する．これらを用いると量子ドット間の相互作用は

$$
\begin{aligned}
U&=\langle\phi_2|\hat{V}_{\mathrm{eff}}|\phi_1\rangle\\
&=-\frac{\mu_A\mu_B}{6\pi^2}\int_0^\infty d^3kf^2(k)\\
&\quad\times\left\{\left[\frac{1}{E(k)+E_A}+\frac{1}{E(k)+E_B}\right]e^{ik\cdot r}\right.\\
&\quad\left.+\left[\frac{1}{E(k)-E_A}+\frac{1}{E(k)-E_B}\right]e^{-ik\cdot r}\right\}
\end{aligned}
\tag{23}
$$

となる．ここで，μ_A, μ_B はそれぞれ二つの遷移双極子モーメント，$E(k)$ は波数 k を持つ励起子ポラリトンのエネルギーであり，励起子ポラリトンの有効質量 m_p とバルク結晶中の励起子エネルギー E_m を使って，

$$
E(k)=\frac{\hbar^2k^2}{2m_p}+E_m \tag{24}
$$

で与えられる．(23)式と(24)式より，伝搬光による相互作用を除いた，近接場光相互作用は

$$
\begin{aligned}
U(r)=\frac{\mu_A\mu_B}{3(\hbar c)^2}\sum_{\alpha=A}^{B}&[W_{\alpha+}Y(\Delta_{\alpha+}r)\\
&+W_{\alpha-}Y(\Delta_{\alpha-}r)]
\end{aligned}
\tag{25}
$$

と湯川関数；

$$
Y(\Delta_{\alpha\pm}r)=\frac{e^{-\Delta_{\alpha\pm}r}}{r},
$$

$$
\Delta_{\alpha\pm}=\frac{1}{\hbar c}\sqrt{2E_p(E_m\pm E_\alpha)} \tag{26}
$$

の和によって表わされる．ここで，E_p, E_α には CuCl 量子ドットの励起子エネルギーを E_m には環境の影響を取り込むため NaCl 結晶の励起子エネルギーを採用する[17]．**第 8 図**は(25)式によって求めた 4.6 nm と 6.3 nm の CuCl 量子ドット間に働く近接場光相互作用の量子ドット間距離依存性である．第 7 図のフィッティングから求めた相互作用エネルギー 20 μeV を持つのは量子ドット間隔が 10 nm のときであり，近接場顕微鏡を用いて得られる発光の空間強度分布より得た量子ドット間距離 20 nm 以下と一致している．このように湯川関数で近接電磁相互作用が表わされるということは，近接領域での電磁力は質量のない光子ではなく，質量をもったポラリトンの交換によって起こることを意味しており，物理的に大変興味深い．

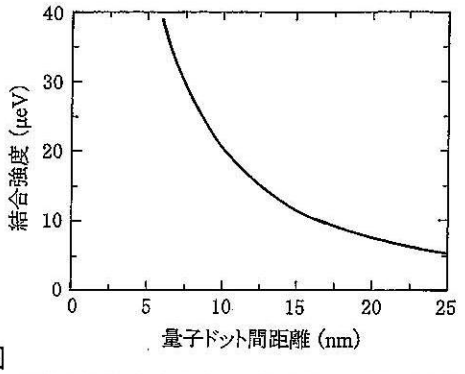

第 8 図
NaCl 中に成長させた 4.6 nm と 6.3 nm の立方体形状の CuCl 量子ドット間に働く近接場光相互作用の量子ドット間距離依存性．

§4 今後の展開（ナノフォトニックデバイス）

上で述べた近接場光相互作用による量子ドット間のエネルギー移動を制御することにより光の回折限界を超えたナノ寸法の光デバイスが可能となる[11,20]．**第 9 図**にわれわれが提案している光近接場スイッチを構成する 3 個の量子ドットとそれらのエネルギー準位図を示す．(22)式からわかるように，量子ドットの有効サイズが $1:\sqrt{2}:2$ である場合，第 9 図中の入力ドット中の励起子閉じ込め準位 $E_{1,1,1}$ と出力ドット中の $E_{2,1,1}$ 準位が共鳴し，同様に制御ドット中の $E_{2,2,2}$ 準位とも共鳴する．これら 3 個の量子ドットは光スイッチのそれぞれ入力，出力，制御端子と見なせる．このナノ寸法光スイッチのオフ動作状態は入力ドットに入力された励起エネルギーを制御ドットへ直接もしくは出力ドットを経由し緩和させ，制御ドットの発光によって入力エネルギーを消費させる．

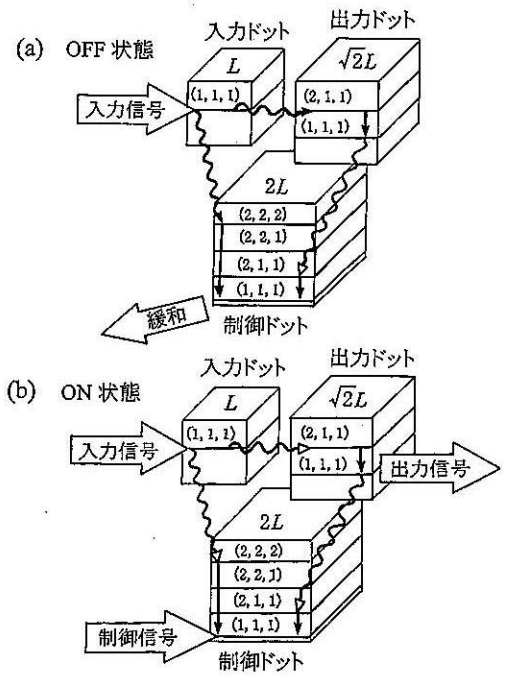

第9図
三つの量子ドットを用いたナノフォトニックスイッチの動作状態.
(a) OFF 状態, (b) ON 状態.

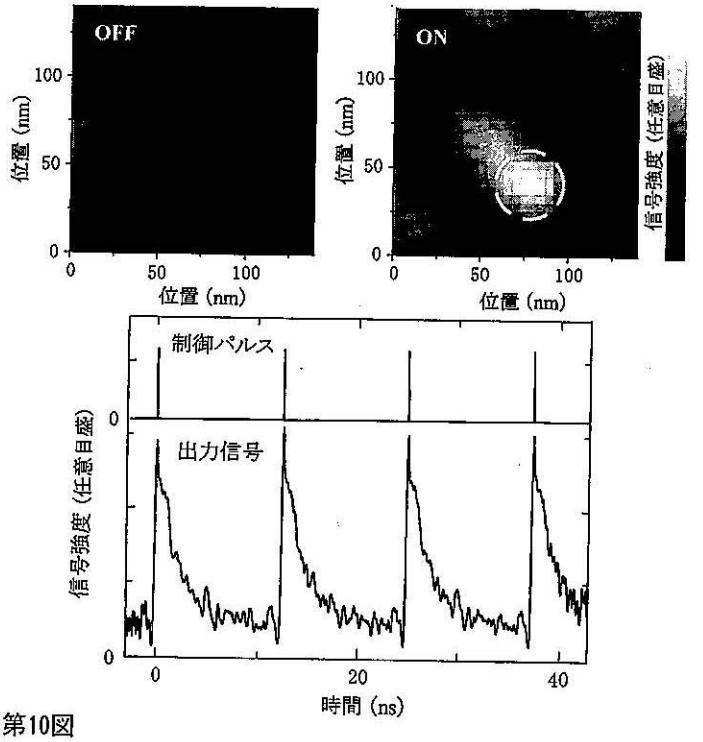

第10図
ナノフォトニックスイッチの動作実験結果, ON 状態と OFF 状態の出力光強度分布と出力信号の動特性.

第1表 ナノフォトニックスイッチと既存の代表的光スイッチの性能指数比較.

種　類	寸法 $V=L^3$	速度 T_{sw}	消費 energy/cycle E	ON/OFF 比 C	性能指数 $C/(V\cdot T_{sw}\cdot E)$
ナノフォトニックスイッチ	$(\lambda/10)^3$	～100 ps	1 photon	10	～1
Mach-Zehnder	$(n\lambda)^3$	10 ps	10^{-18}～10^{-17} J	10^2以上	10^{-2}～10^{-3}
$\chi^{(3)}$非共鳴	$(n\lambda)^3$	10 fs	10^6 photons	10^3以上	10^{-3}
$\chi^{(3)}$共　鳴	$(n\lambda)^3$	1 ns	10^3～10^4 photons	10^4以上	10^{-4}～10^{-5}
量子井戸 sub-level	$(n\lambda)^3$	100 fs	10^3～10^4 photons	10^4以上	10^{-1}～10^{-2}
光 MEMS	$(n\lambda)^3$	1 μs	10^{-18}～10^{-17} J	10^4以上	10^{-5}

この結果, 出力ドットから発光は押さえられる. よって, このデバイスの出力を 0 としたオフ動作が実現される(第 9 図(a)). オン動作は制御ドットを外部からの制御光で励起することで制御ドット準位を埋め, 制御ドットへのエネルギー移動を制限する. この結果入力エネルギーは出力ドットへエネルギー移動し, 出力ドットが発光することで実現する(第 9 図(b)). **第10図** にこのデバイスの ON 状態と OFF 状態の出力信号強度の近接場顕微鏡による空間分布測定と 80 MHz のパルス光でこのデバイスを駆動させた時の出力信号の時間変化を示す. 出力信号の空間分布は測定分解能によって広がっているが, 僅か 20 nm という寸法のこの光デバイスが動作するのは近接場光相互作用が量子ドット間に働くからである. また, 動特性のグラフは制御光パルスに同期した出力信号が得られていることを示している. 測定結果から得られたナノフォトニックスイッチの動特性と静特性を基に既存の光デバイスと性能指数比較した結果を **第 1 表** に示す. ここでサイズも含めた性能指数として, スイッチの寸法(体積), 速度, 消費エネルギーあたりのスイッチの ON/OFF 比を採用した. 寸法, 消費エネルギーの点で従来の光デバイスをはるかに凌駕し, 性能指数は10～100

倍ほど高い．特に消費エネルギーの小さいことは集積化の際重要な要素となる．既存の集積化電子デバイスの代表である典型的なCPUと比べ10^4～10^5も熱的に余裕があり，将来的には光CPUへの応用も期待できそうである．

量子ドット間に起きる近接場相互作用を介したエネルギー移動は光合成生物の光捕獲アンテナでも起きていると言う話にふれた．第11図(a)に動作原理を示す多数の量子ドットで構成されたデバイスは光捕獲アンテナのごとく，多数のサイズの小さい量子ドットで捕獲した光エネルギーをサイズの大きい一つの量子ドットに集めるナノ集光デバイスである．われわれはこのデバイスをあたかも雨水を集め溢れ出す泉のような動作をすることから“Optical Nanofountain”と名づけた[12]．第11図(b)に半径100 nmの光を1辺10 nmの立方体CuClに量子ドットに集めたOptical Nanofountainの実験結果を示す．図中中心の破線で囲んだ部分に10 nmの量子ドットが存在し，その周辺には数十個の6 nm–2 nmの量子ドットが存在している．この10 nmの量子ドットは単独で存在している場合と比べ約5倍明るく輝いている．これは周辺の小さな量子ドットから近接場光相互作用を介したエネルギー移動により励起エネルギーを得た結果である．

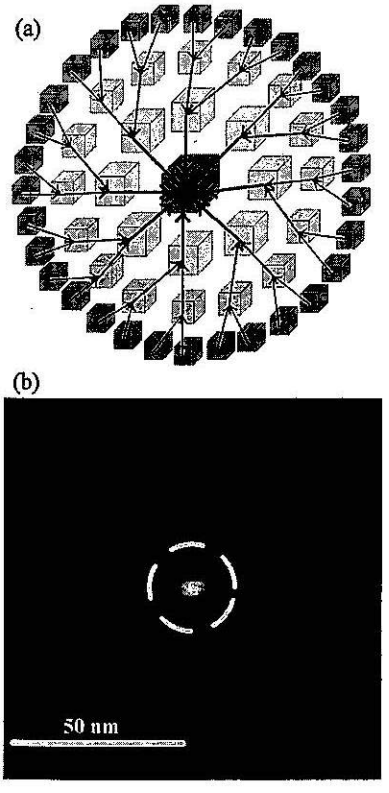

第11図
Optical Nanofountain：ナノ集光器．
(a) 概念図．(b) 近接場顕微鏡によるOptical Nanofountainの動作実験結果．

電子デバイスが100 nm以下になった現在，実用的な機能を有するような光デバイス(たとえば光交換機)もまたナノ寸法にならなければならないであろう．われわれはここで簡単に述べたナノフォトニックデバイスをどのようなシステムで運用するべきかについても研究を行っており，ナノフォトニックデバイスの特徴を生かした幾つかのシステムを提案している[21,22]．

§5 まとめ

本稿では近接場光という観点からナノ物質間の電磁相互作用について議論した．点電気双極子や長波長近似を使った光物性研究者にとって馴染みの深い従来の光学とは異なる部分が多いため，湯川関数で表わされる近接場光相互作用の導出に多くの誌面を割いた．これに基づき量子ドット間の励起エネルギー移動を議論し，実験結果との比較検討を行った．もちろん，個々の場合に対して煩雑な計算やナノ物質とその界面の状態を求めることができれば実験結果は既存の物理モデルでも説明可能かもしれない．しかし，ナノ物質を使った様々なアイデアが提案される状況において，近接場光相互作用の考え方を導入することで環境の効果を取り込んで簡単に相互作用の大きさを見積もることができるなど，その考え方の有効性はますます増大すると考えられる．本稿では触れなかったが，ごく最近，近接場光特有の非断熱光化学反応，すなわち伝搬する光では起き得ない物理現象なども報告されている．このユニークな光化学反応は既存の光化学では定量化が難しい様々な効果に起因していると考えられるが，近接場光相互作用という観点から定性的・定量的に実験結果が議論されている[23,24]．コヒーレントなレーザー光が分光を飛躍的に進歩させたように，そして，ピコ・フェムト秒短光パルスが新しい物理現象を引き出したように，近い将来，近接場光によって新し

い分光法や物理現象が発見されることを期待したい．ここで紹介した近接したナノ物質間に働く電磁相互作用によるエネルギー移動現象がその出発点になることを願いつつ筆をおくことにする．

本研究を進めるにあたり，理論面で多くの実りある議論や計算を行ってくださった科学技術振興機構 ERATO の三宮俊氏(現 (株) リコー)，小路口暁氏(現　奈良女子大)，貴重なコメントをくださった山梨大学：堀裕和氏，坂野斎氏に深く感謝いたします．また，実験に協力いただいた東京大学・東京工業大学・神奈川科学技術アカデミー，科学技術振興機構 ERATO・SORST の研究員・学生の皆様にお礼申し上げます．特に SORST 研究員八井崇氏には常に議論に参加していただき深い感謝の念を表したいと思います．

〔参考文献〕

1) R. P. Feynman: 29th the annual meeting of the American Physical Society, Pasadena, USA (1959); see, for example, http://www.feynmanonline.com/

2) L. Esaki, L. L. Chang, W. E. Howard and V. L. Rideout: Proc. Int. Conf. Phys. Semicond., Warsaw (1972) 431.

3) L. L. Chang, L. Esaki and R. Tsu: Appl. Phys. Lett. **24** (1974) 593.

4) Y. Guo ed.: *Nonlinear Photonics Nonlinearities in Optics, Optoelectronics and Fiber Communications*, Springer Series in Photonics, Vol. 8 (Springer-Verlag, 2002).

5) F. R. Waugh, M. J. Berry, D. J. Mar, R. M. Westervelt, K. L. Campman, and A. C. Gossard: Phys. Rev. Lett. **75** (1995) 705.

6) M. Ohtsu, K. Kobayashi, T. Kawazoe, S. Sangu, and T. Yatsui: IEEE J. Sel. Top. Quant. Electron **8** (2002) 839.

7) M. Ohtsu and K. Kobayashi: *Optical Near Fields: Introduction to Classical and Quantum Theories of Electromagnetic Phenomena at the Nanoscale* (Springer-Verlag, 2003).

8) M. Ohtsu and H. Hori: *Near-Field Nano-Optics: From Basic Principles to Nano-Fabrication and Nano-Photonics* (Kluwer Academic Pub., 1999).

9) M. Ohtsu ed.: *Optical and Electronic Process of Nano-Matters* (KTK Scientific, 2001).

10) T. Kawazoe, K. Kobayashi, J. Lim, Y. Narita, and M. Ohtsu: Phys. Rev. Lett. **88** (2002) 067404.

11) T. Kawazoe, K. Kobayashi, S. Sangu, and M. Ohtsu: Appl. Phys. Lett. **82** (2003) 2957.

12) T. Kawazoe, K. Kobayashi, and M. Ohtsu: Appl. Phys. Lett. **86** (2005) 103102.

13) K. Mukai, S. Abe, and H. Sumi: J. Phys. Chem. B **103** (1999) 6096.

14) C. R. Kagan, C. B. Murray, M. Nirmal, and M. G. Bawendi: Phys. Rev. Lett. **76** (1996) 1517.

15) S. A. Crooker, J. A. Hollingsworth, S. Tretiak, and V. I. Klimov: Phys. Rev. Lett. **89** (2002) 186802.

16) N. Sakakura and Y. Masumoto: Phys. Rev. B **56** (1997) 4051.

17) S. Sangu, K. Kobayashi, A. Shojiguchi, T. Kawazoe and M. Ohtsu: J. Appl. Phys. **93** (2003) 2937.

18) T. Suzuki, T. Mitsuyu, K. Nishi, H. Ohyama, T. Tomimasu, S. Noda, T. Asano, and A. Sasaki: Appl. Phys. Lett. **69** (1996) 4136.

19) K. Kobayashi, S. Sangu, T. Kawazoe, and M. Ohtsu: J. Lumin. (2005) in press.

20) T. Kawazoe, K. Kobayashi, S. Sangu, and M. Ohtsu: J. of Microscopy **209** (2002) 261.

21) S. Sangu, K. Kobayashi, A. Shojiguchi and M. Ohtsu: Phys. Rev. B **69** (2004) 115334.

22) M. Naruse, T. Miyazaki, F. Kubota, T. Kawazoe, K. Kobayashi, S. Sangu, and M. Ohtsu: Optics Letters (2005) in press.

23) T. Kawazoe, Y. Yamamoto, and M. Ohtsu: Appl. Phys. Lett. **79** (2001) 1184.

24) T. Kawazoe, K. Kobayashi, S. Takubo, and M. Ohtsu: J. of Chem. Phys. **122** (2005) 024715; K. Kobayashi, T. Kawazoe and M. Ohtsu: IEEE Trans. on Nanotech. (2005) in press.

近接場光による微細加工*

Nanofabrication using Optical Near-field

八井 崇** 大津元一***
Takashi YATSUI and Motoichi OHTSU

Key words nanophotonics, optical near-field, near-field desorption, self-assembly, size-dependent resonance

1. まえがき

従来の光技術では光の波動的性質を使っているが，この光の波は空間的に広がろうとする性質(回折)を持つ．従ってそれを凸レンズで集めても焦点面上での光のスポット径は波長程度以下にはならない．これが光リソグラフィなどの微細加工における加工可能最小寸法の限界を与えており，ブレークスルーのための革新技術が待望されている．この期待にこたえる技術がナノフォトニクスであり，それは「近接場光のエネルギー移動を活用してナノ寸法の光加工を行ったり光デバイス機能を発現する技術」と定義されている*1．

この技術では近接場光と呼ばれる小さな光を使うが，これは次章に概説するように物質表面近傍の，光の波長に比べ十分近い位置に発生する電磁場である．本稿では物質の寸法が波長に比べずっと小さい場合を考えるが，その表面に発生する近接場光のエネルギーを利用するとナノ寸法の光加工が可能となる．また，近接場光を信号の担い手として用い，そのエネルギーをナノ寸法物質間で移動させると，新しい光デバイス機能が発現する．この方法により光の波長より小さい寸法を持つ光デバイス，すなわちナノフォトニックデバイス[1]が実現する．

ナノフォトニクスは光の波長以下でナノ寸法の光加工や光デバイス動作を実現する．しかし，光の回折限界を超えたナノ寸法を実現するという「量的変革」がナノフォトニクスの本質ではないことに注意されたい．本質的なことは「物質間の近接場光のエネルギー移動の性質が伝搬光のエネルギー移動の性質とは異なることを用いて，伝搬光では原理的に不可能な形態の微細光加工，光デバイス機能を実現する」ことである．すなわち，光技術の「質的変革」を実現することが本質である．

本稿では近接場光に馴染みのない読者のために，まず2章で近接場光について概説した後，3章以降ではナノフォトニクスでのみ可能になるナノ寸法の光加工について列挙する．

2. 近接場光とその検出

近接場光とは物質表面近傍の，光の波長に比べ十分近い位置に発生する電磁場である．ここでは物質の寸法が波長に比べずっと小さい場合を考える．近接場光は①非伝搬，②エネルギーは物質表面から遠ざかるにつれ減少という2つの性質を持つ．

図1は近接場光の発生の様子を示している．すなわち半

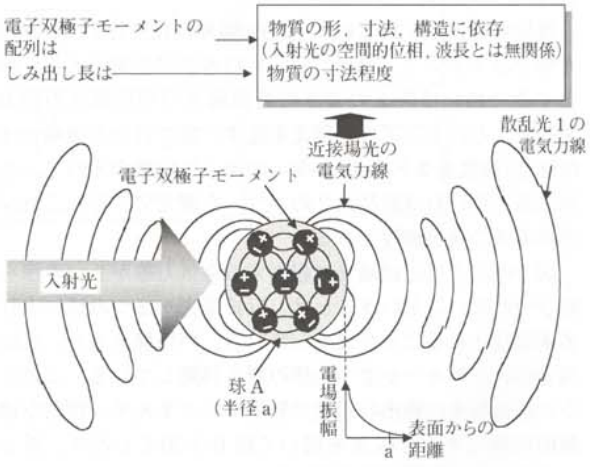

図1 近接場光の発生の様子

*原稿受付 平成17年12月27日
**科学技術振興機構 SORST(東京都町田市鶴間)
***東京大学大学院工学系研究科電子工学専攻(東京都文京区本郷)
八井 崇
2000年東京工業大学総合理工学研究科博士課程修了．2000年より科学技術振興事業団 ERATO 大津局在フォトンプロジェクト 研究員．2004年より科学技術振興機構 SORST 研究員．近接場光を用いた光デバイスの研究に従事．
大津元一
1978年東京工業大学大学院理工学研究科博士課程修了．同年同大学助手，助教授を経て，1991年同大学大学院総合理工学研究科教授．2004年より，東京大学大学院工学系研究科教授．1988年日本IBM科学賞，1998年井上学術賞，2004年紫綬褒章など受賞．

*1「ナノフォトニクス」は筆者(大津)が1993年頃命名したものであり，従来の光技術において伝搬光のエネルギー移動を利用して加工，光デバイス機能を発現させるのが「フォトニクス」であることに対応している．

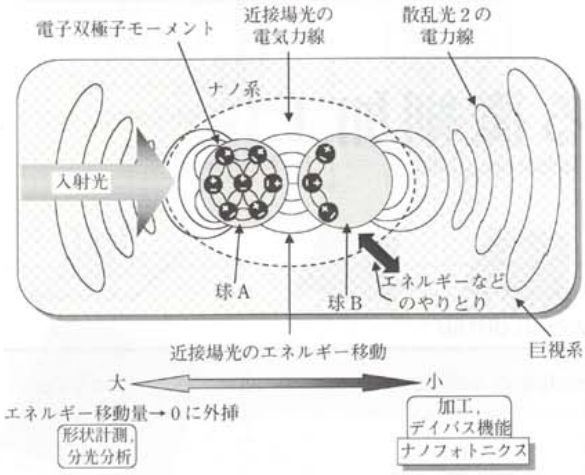

図2　近接場光の測定の様子．破線の楕円はナノ系と巨視系との間の境界を表す．

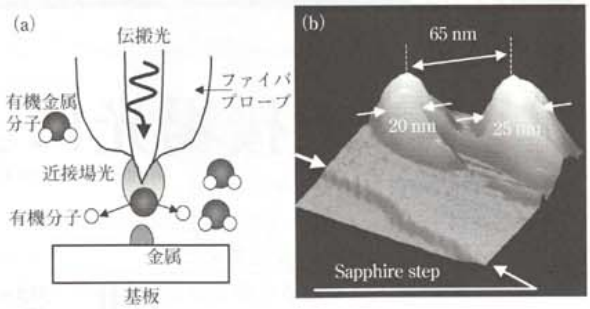

図3　(a)NFO－CVD．(b)隣接して堆積されたZn微粒子の堆積結果

径aの電気的に中性な物質(球A)に光が入射したとき，その中の多数の原子に時間的に振動する電気双極子モーメント誘起され，その電気双極子モーメントから電磁場が発生する．この電磁場を表す電気力線は電気双極子モーメント同士を結び，その一部は球Aの外にしみ出している．このしみ出した電気力線が表す光が近接場光である．この電気力線は電気双極子モーメントから発して電気双極子モーメントに終端しているので非伝搬であることを表している(性質①に対応)．その外側にある閉曲線状の電気力線は遠方へと回折しながら伝搬する光を表すが，これは従来の光技術で使われている光である(散乱光1と呼ぶ)．半径aが入射光の波長に比べずっと小さい場合，発生する多数の電気双極子モーメントの配列の仕方は入射光の空間的位相，波長とは無関係となり，球Aの形，寸法，構造に依存するので，近接光のしみ出し長は球Aの半径a程度となる(性質②に対応)．

近接場光は非伝搬なので，近接場光の発生(図1)のみの考察では不十分で，検出についての考察が必須である．検出するためには図2のように近接場光の中に第2の球Bを置くことによって近接場光を乱す．乱された近接場光は散乱光(散乱光2と呼ぶ)となって遠くに伝搬するので，光検出器を用いれば散乱光2のパワーを測定できる．これが近接場光の検出過程である．

図2のように近接場光に起因する電気力線が2つの球を結びつけているということは，近接場光が2つの球により多重散乱されることを意味している．いい換えると，近接場光のエネルギーが2つの球の間を移動している．このように近接場光の検出の過程で発生するエネルギー移動を積極的に利用すると球Aを用いて球Bを加工したり，新しい光デバイス機能を発現させたりすることができる．すなわち一方の球が他方の球の光学的特性，構造，形状を変化させる．近接場光はこのような応用に適している．

一方，物質の形状や構造を測定する顕微鏡，分光分析装置などへの応用では測定試料の状態を乱してはいけないので，近接場光のエネルギー移動が少ない状態下で用い，得られたデータの解析の際にはエネルギー移動がゼロの状態を推定する．しかし実際には，このような極限状態への外挿は非常に困難なので，無理のある使い方である．以上の関係を図2の下部に示す．

ナノフォトニクスで本質的なことは「物質間の近接場光のエネルギー移動の性質が伝搬光のエネルギー移動の性質とは異なることを用いて，伝搬光では原理的に不可能な形態の微細な光加工，光デバイス機能を実現する」ことである．これは近接場光の次の2つの性質に起因する．

(i) 近接場光エネルギーの空間局在性

(ii) 近接場光，微粒子からなるナノ寸法の系と熱浴(入射光，散乱光，基板などからなる巨視的寸法の系)とのエネルギー相互作用(図2参照)．

なお，これらの考え方は互いに共通する内容を別の表現で述べているに過ぎない．これらを統一的に記述するには波動光学の枠組みでは不十分で，特に微小物質との電磁気学的相互作用を取り入れ，さらに巨視系の中に埋もれたナノ系としての振る舞いを記述するために量子論が必要となる[2)～4)]．

以上で述べた近接場光の性質，現象は普遍的である．これらを利用することにより，光技術の「質的変革」を実現することがナノフォトニクスの本質である．波長に比べずっと小さな光技術を実現するという「量的変革」は，副次的な成果に過ぎない．次章ではナノフォトニクスの特徴を利用したナノ光加工について列挙する．

3. 近接場光によるナノ光加工

ナノ寸法のデバイス製作手法として，露光装置とエッチングを用いる加工法(トップダウン)と原子・分子を積み上げる加工法(ボトムアップ)が挙げられる．トップダウンは，近年X線などを用いたリソグラフィにより20 nm以下の精度の加工が可能であるが[5)]，「削る」ことによる加工が主となるため基板などの損傷が問題となる．これに対してボトムアップは「積み上げる」加工のため損傷は回避できる．近年，量子ドットレーザなどを作製するために自己組織化による方法が広く用いられているが[6)]，この方法では所望の寸法・位置に量子ドットを配置することや，異種ドットを隣接して配置することは困難である．

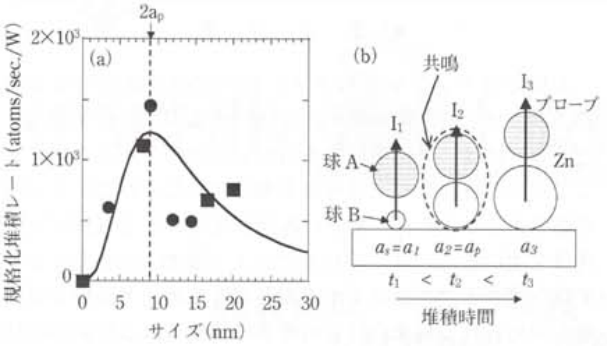

図4 (a)入射光パワーで規格化された堆積速度．横軸は堆積されたZn微粒子の基板面内寸法．実線は双極子間相互作用により求められた散乱光2の強度(図(b)のI_1～I_3)を示す．■印および●印は各々入射光パワーが：10 μW，5 μWの場合の測定結果である．(b)微粒子が堆積されその寸法が増加する様子の説明図．

これに対して，原料分子を光により解離し，堆積させる光化学気相堆積法(光CVD法)は，様々な材料を任意の場所に高精度に堆積することが可能である[7]．さらには，近接場光を用いることで，光の波長より遥かに小さな寸法の微細加工が可能である．

この近接場光CVD法(NFO-CVD)の例としてファイバプローブ先端に発生する近接場光により，金属Znを堆積する場合を説明する(図3(a))．Znの原料として有機金属分子を用い，これを光により解離し，析出したZn原子を基板に堆積する．この際，近接場光により吸着分子を選択的に解離する光源を用いることで[8]，30 nm以下のZn微粒子の作製が65 nmの間隔で可能となっている(図3(b))[9]．ここで，堆積速度の特性について考えるために，サファイヤ基板上に堆積されたZn微粒子の堆積速度の測定値を図4(a)に示す．この結果から，Zn微粒子の寸法がファイバプローブ先端の曲率直径である$2a_p$に一致したときに，堆積速度が極大となっていることがわかる．つまり，この堆積されたZn微粒子とファイバプローブ先端との近接場相互作用は，微粒子寸法が$2a_p$となったときに最も強くなり，それが堆積速度の極大となって現れている．この共鳴効果は，双極子間相互作用の理論から定量的に説明される．近似としてファイバプローブ先端とZn微粒子を，各々球Aおよび球B中の双極子により近似し(図4)，算出する[2]．ここで，球Aの直径を9 nm(＝$2a_p$)とし，Zn微粒子である球Bの大きさ($2a_s$)を変化させたときの，球同士での近接場により結合された双極子間相互作用から求められる散乱光強度(図2の散乱光強度2および図3(b)のI_1～I_3)を求めた結果を図4(a)の実線に示す．図4(a)に示されるように，堆積速度の実験結果と双極子間相互作用による散乱光強度との良い一致から，堆積過程におけるプローブ先端と微粒子との物質寸法に依存し共鳴する効果が観測されたことが確認できる[9]．

NFO-CVDでは，堆積速度がファイバプローブ先端の寸法に依存する共鳴効果を示すことが確認された．次に，これとは別に堆積物自身で生じる共鳴効果を用い，形成されるパターンの寸法精度をさらに向上させる手法について解説する．

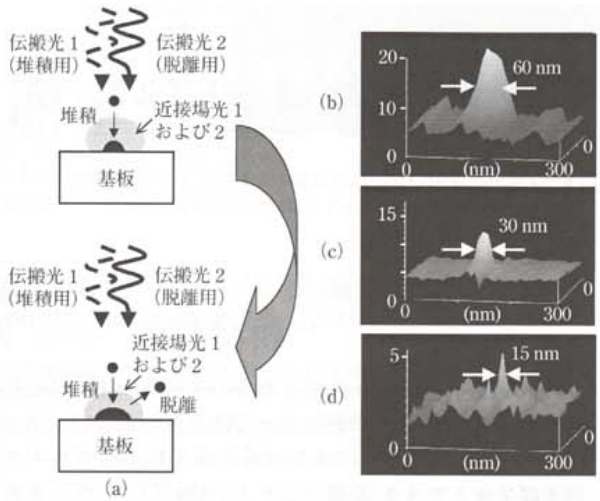

図5 (a)物質寸法に依存する光脱離法による寸法制御の原理図．(b)-(d)物質寸法に依存する光脱離法により作製されたZn微粒子の形状像．

そのためには図5(a)に示すように2種類の近接場光(近接場光1および2)を発生させる．近接場光1は光CVDによる堆積のために用いる．このとき同時に近接場光2を発生させて基板に照射し，堆積された物質を一部脱離させる．この脱離の現象は，堆積される金属微粒子が近接場光2を吸収し，この光エネルギー吸収量が金属微粒子同士の吸着エネルギーよりも大きくなる場合に発生する．この脱離の現象とそれによる寸法制御は次の過程により実現する[10]．

(1) 近接場光2により金属微粒子中の自由電子が振動する．同時に近接場光1により堆積が進むので，微粒子寸法が自由電子の平均自由行程より大きくなると，微粒子内部での電子の固有振動が立ちにくくなり，電子振動の固有振動周波数が変化するとともにスペクトル幅が広がる[11]．

(2) この固有振動周波数変化が近接場光2の周波数と一致するある特定の微粒子寸法になったとき，微粒子に吸収される近接場光2のエネルギーは極大をとる．すなわち物質寸法に依存した光共鳴吸収が起こる．

(3) この特定の寸法のときに脱離が顕著になり，図5(a)に示すように近接場光1による堆積とのつり合いにより，これ以上の寸法の増加が停止する[10][12]．これにより基板上に形成される物質の寸法は，近接場光2の光子エネルギーの値によって決まる．

図5(b)～(d)はサファイヤ基板上にNFO-CVDによりZnを堆積した実験結果であるが，近接場光1用の光源波長はいずれも325 nmである．一方近接場光2用の光源波長は各々325 nm(図5(b))，488 nm(図5(c))，633 nm(図5(d))である．

このように，同一ファイバプローブを用いてZnを堆積したにも関わらず，形成されたZn微粒子の寸法はこの光

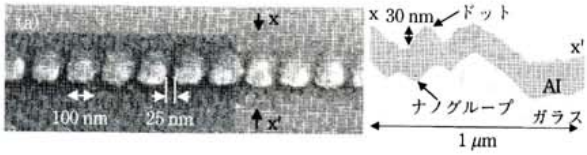

図6 プローブを用いない自己組織的作製法による(a)Al微粒子列の電子顕微鏡写真．(b)X-X'におけるAl堆積前(ガラス上)後(Al上)の断面図

子エネルギーに依存しており，各々60 nm，30 nm，15 nmとなっている[10]．

前述の結果によれば，形成されるパターンの寸法は近接場光の光子エネルギーの値によって決定されるので，ファイバプローブの代わりにほかの近接場光発生用デバイス(例えばフォトマスク)を使ってもよい(脱プローブ)．さらには，形状加工基板を近接場光発生用デバイスとして用いることで，フォトマスクなどが不要となり，マスクと基板との密着性などの問題点が回避できる．さらに，金属微粒子中での物質寸法に依存する光脱離は一般的な現象であるので，光CVD以外の様々な微細加工法にも応用が可能である．

金属微粒子薄膜を直接堆積する方法の一種であるスパッタリング法を例にとり，金属微粒子列の自己組織的作製例を紹介する．ここでは，堆積された微粒子を脱離するための近接場光発生用に，一部にナノ寸法の微細パターンを持つ基板用いる．また，本方法では金属微粒子を直接堆積させるため，堆積用の光源は必要とはならない．スパッタリングの際に伝搬光をこのような基板に照射すると，このパターンの端部に局所的に強い近接場光が発生する．これが先に述べた脱離を誘起し，寸法制御された金属微粒子がパターン近傍に形成される．その後引き続き伝搬光照射を続けても，この微粒子の表面では脱離の効果により成長進行しないため，これにより微粒子同士が繋がることなく第2の金属微粒子が高い寸法制御性にて形成される．これが繰り返され最後には寸法制御された金属微粒子の列が自己組織的に形成される．

図6(a)は，以上の手法によりナノグルーブを有するガラス基板上にされたAl微粒子の一次元配列である[13]．ここでは物質寸法に依存する光脱離を実現するためにスパッタリング中に532 nmの光を照射した．その結果，直径100 nmの半球状のAl微粒子が20 nm間隔で一列に形成されており，このような一次元配列は全長20 μmにわたり形成された．また，それらの断面図の比較(図6(b))より，微粒子列が形成された場所がナノグルーブ上であることも確認された．直径および間隔の値は，光子エネルギーおよびあらかじめ形成された基板パターン形状により，全長は照射スポット径及び基板パターン形状により決まる．

4. あとがき

本稿ではナノフォトニクスにおいてのみ観測可能な現象，およびそれを用いたナノ寸法の光加工について解説した．本方法は，光化学反応を利用したものであるため，ここで示した金属微粒子以外に半導体微結晶の作製にも応用可能である．さらに，形状に起因して局在する近接場光の性質を用いることは，これまでナノ寸法加工に必要とされていたプローブやマスクが不要となるため，多品種多量生産が求められる将来の社会的要求に答えられる革新的な技術である．

また，従来のナノ微細加工技術としては，半導体微細加工などに用いられている電子ビームリソグラフィーなどが一般であるが，これらの技術においても「加工する」ことと，デバイスとして「動作させる」こととは別の技術であり，ナノ寸法のデバイスを実現させるためには大きな技術的・機能的限界が存在する．これに対し，近接場光による加工は単にナノ寸法の微細加工が可能ということではなく，近接場光で動作するナノフォトニックデバイスを作製する手法としては，作製後デバイスとしての動作を保証する自己完結的手法であると期待される．

参考文献

1) M. Ohtsu, et al.; Nanophotonics: Design, fabrication, and operation of nanometric devices using optical near fields, IEEE J. Selec. Topics in Quant. Elect., **8**, (2002) 839.
2) 大津元一, 小林潔: 近接場光の基礎, オーム社 (2003).
3) M. Ohtsu and K. Kobayashi: Optical Near Fields, Springer-Verlag, Tokyo, (2003), 1-200.
4) 大津元一監修: ナノフォトニクスへの挑戦, 米田出版, 2003.
5) P. B. Fischer, et al.: Sub-50 nm high aspect-ratio silicon pillars, ridges, and trenches fabricated using ultrahigh resolution electron beam lithography and reactive ion etching, Appl. Phys. Lett., **62**, (1993) 1414.
6) D. Leonard, et al.: Direct formation of quantum-sized dots from uniform coherent islands of InGaAs on GaAs surfaces, Appl. Phys. Lett., **63**, (1993) 3203.
7) D. J. Ehrlich, et al.: Photodeposition of metal films with ultraviolet laser light, J Vac. Sci. Tech., **21**, (1982) 23.
8) T. Yatsui, et al.: Fabrication of nanometric single zinc and zinc oxide dots by the selective photodissociation of adsorption-phase diethylzinc using a nonresonant optical field, Appl. Phys. Lett., **81**, (2002) 3651.
9) 林定植 等: 近接場光化学気相堆積法によるZnナノ微粒子のサイズ制御, 第51回春季応物予稿集, No.3, (2004) 1137.
10) T. Yatsui, et al.: Regulating the size and position of deposited Zn nanoparticles by optical near-field desorption using size-dependent resonance, Appl. Phys. Lett., **83**, (2003) 1716.
11) C. Sönichsen, et al.: Drastic reduction of plasmon damping in gold nanorods, Phys. Rev. Lett., **88**, (2002) 077402.
12) K. F. MacDonald, et al.: Optical control of gallium nanoparticle growth, Appl. Phys. Lett., **80**, (2002) 1643.
13) 野村航 等: 金属ナノ微粒子堆積の光制御, 第50回春季応物予稿集, No.3, (2003) 1110.

[Ⅳ] PUBLISHED BOOKS

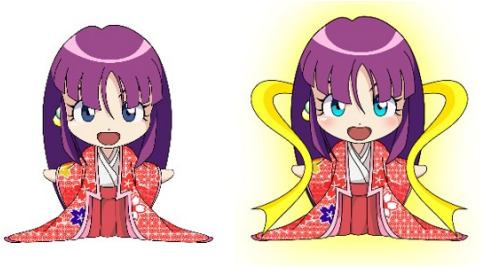

Motoichi Ohtsu (Ed.)

Progress in Nano-Electro-Optics IV

Characterization of Nano-Optical Materials and Optical Near-Field Interactions

With 123 Figures

Springer

Professor Dr. Motoichi Ohtsu
Department of Electronics Engineering
School of Engineering
The University of Tokyo
7-3-1 Hongo, Bunkyo-ku, Tokyo 113-8656, Japan
E-mail: ohtsu@ee.t.u-tokyo.ac.jp

ISSN 0342-4111

ISBN 3-540-23236-2 Springer Berlin Heidelberg New York

Library of Congress Cataloging-in-Publication Data

Progress in nano-electro-optics IV : characterization of nano-optical materials and optical near-field interactions / Motoichi Ohtsu (ed.). p.cm. – (Springer series in optical sciences ; v. 109)
Includes bibliographical references and index.
ISBN 3-540-23236-2 (alk. paper)
1. Electrooptics. 2. Nanotechnology. 3. Near-field microscopy. I. Ohtsu, Motoichi. II. Series.
TA1750 .P75 2002 621.381'045–dc21 2002030321

Springer is a part of Springer Science+Business Media.

springeronline.com

Printed in The Netherlands

Typesetting and prodcution: PTP-Berlin, Protago-TEX-Production GmbH, Berlin
Cover concept by eStudio Calamar Steinen using a background picture from The Optics Project. Courtesy of John T. Foley, Professor, Department of Physics and Astronomy, Mississippi State University, USA.
Cover production: *design & production* GmbH, Heidelberg

Printed on acid-free paper SPIN: 11320623 57/3141/YU 5 4 3 2 1 0

Contents

Motoichi Ohtsu (Ed.)

Progress in Nano-Electro-Optics III

Industrial Applications and Dynamics of the Nano-Optical System

With 186 Figures and 8 Tables

Springer

Professor Dr. Motoichi Ohtsu
The University of Tokyo
Department of Electronics Engineering
School of Engineering
7-3-1 Hongo, Bunkyo-ku
Tokyo 113-8656
Japan
E-mail: ohtsu@ee.t.u-tokyo.ac.jp

ISSN 0342-4111

ISBN 3-540-21050-4 Springer Berlin Heidelberg New York

Library of Congress Cataloging-in-Publication Data

Progress in nano-electro-optics III : industrial applications and dynamics of the nano-optical system / Motoichi Ohtsu (ed.). p.cm. – (Springer series in optical sciences ; v. 96)
Includes bibliographical references and index.
ISBN 3-540-21050-4 (alk. paper)
1. Electrooptics. 2. Nanotechnology. 3. Near-field microscopy. I. Ohtsu, Motoichi. II. Series.
TA1750 .P75 2002 621.381'045–dc21 2002030321

Springer is a part of Springer Science+Business Media

springeronline.com

Printed in Germany

Data prepared by the author using a Springer TEX macropackage
Data conversion by EDV-Beratung F. Herweg, Hirschberg
Cover concept by eStudio Calamar Steinen using a background picture from The Optics Project. Courtesy of John T. Foley, Professor, Department of Physics and Astronomy, Mississippi State University, USA.
Cover production: *design & production* GmbH, Heidelberg

Printed on acid-free paper SPIN 10985588 57/3141/di 5 4 3 2 1 0

Contents

New Photonics Technologies for the Information Age

The Dream of Ubiquitous Services

Shoichi Sudo
Katsunari Okamoto
Editors

Artech House, Inc.
Boston • London
www.artechhouse.com